Computational Investigation of Cyclic Peptide Nanotubes: Self-Assembly, Solvent Effects, and Transport Behavior of Water and Ions

A Thesis Submitted
in Partial Fulfillment of the Requirements
for the Degree of

DOCTOR OF PHILOSOPHY

by

Rimjhim Moral

to the

Department of Chemistry
Indian Institute of Technology Guwahati, India

2025

Dedicated with devotion to

Lord Shree Krishna, the guide, and
Lord Shiva, the protector...

Declaration

I hereby declare that the matter manifested in this thesis entitled *"Computational Investigation of Cyclic Peptide Nanotubes: Self-Assembly, Solvent Effects, and Transport Behavior of Water and Ions"* is the result of research carried out by me in the Department of Chemistry, Indian Institute of Technology Guwahati, India under the supervision of Prof. Sandip Paul.

In keeping with the general practice of reporting scientific observations, due acknowledgement has been made wherever the work described is based on the findings of other investigators.

Rimjhim Moral

IIT Guwahati

Certificate

It is certified that the work contained in this thesis entitled, *"Computational Investigation of Cyclic Peptide Nanotubes: Self-Assembly, Solvent Effects, and Transport Behavior of Water and Ions"* has been carried out by Ms. Rimjhim Moral for the Degree of Doctor of Philosophy under my supervision and the same has not been submitted elsewhere for a degree.

Prof. Sandip Paul
Thesis Supervisor
Department of Chemistry
Indian Institute of Technology Guwahati
Guwahati-781039, India

Acknowledgment

"A PhD is not just a degree, it's a test of patience, persistence, and passion for discovering the unknown."

This long journey of patience, persistence, and passion would not have been possible without the support of several individuals who, in various ways, extended their help and encouragement throughout.

First and foremost, I would like to express my sincere gratitude to my supervisor, Prof. Sandip Paul, for his excellent guidance, constant encouragement, and unwavering support throughout the years of my doctoral studies. His readiness to provide illuminating advice and engage in insightful discussions made this journey significantly smoother. I am also deeply thankful to him for granting me the freedom to pursue my ideas, and I could not have asked for a better advisor and mentor during my Ph.D. journey.

I am equally grateful to the members of my doctoral committee: Prof. Gopal Das, Prof. Lal Mohan Kundu, and Dr. Sunanda Chatterjee for periodically evaluating my work and providing valuable suggestions for its improvement. I also sincerely thank Prof. Aiyagari Ramesh for his thoughtful input during the early stages of my research. My heartfelt appreciation goes to all the faculty members and staff of the Department of Chemistry for their support at various stages of my doctoral work.I gratefully acknowledge the Ministry of Human Resource and Development (MHRD), India for financial assistance, and IIT Guwahati for offering the infrastructure and research facilities necessary for carrying out this work. In particular, I would like to acknowledge the PARAM-ISHAN and PARAM-KAMRUPA supercomputing facilities at IIT Guwahati, without which the timely completion of my dissertation would not have been possible.

No words are sufficient to thank my lab mates Aritra Daa, Madhusmita Baa, Sanjib, Mira, Anandita, Vanneikima, Balaram, and Srimila for their constant support, productive discussions, and for fostering a pleasant and collaborative lab environment. I will fondly remember all our "addas" and the frequent tea breaks at Sushil Daa's shop every couple of hours, which added a special rhythm to our days. A heartfelt thank you to my seniors Dr. Srijita Paul, Dr. Saikat Pal, Dr. Krishna Gopal Chattaraj, Dr. Rabindranath Paul, and Dr. Rituparna Roy for sharing their experiences and offering invaluable guidance during my Ph.D. years.

I take this opportunity to express my sincere gratitude and respect to all my teachers from school, college, and university who have contributed to shaping me both academically and personally. Their teachings, values, and guidance will always remain a guiding force in every stage of my life. I also extend my thanks to everyone I have crossed paths with, who in their own unique ways, encouraged me and inspired me to embark on this remarkable journey of pursuing a Ph.D. and exploring the unknown.

Above all, I owe everything to my family, whose unwavering support and unconditional love have been the foundation of this journey. I am profoundly grateful to my husband, Gourav, for being my constant source of strength, patience, and motivation. His quiet encouragement, belief in me, and steady presence made even the most challenging moments feel lighter. This achievement is as much his as it is mine.

My heartfelt thanks go to my mother and my sister, Munu, whose endless love and support have been the bedrock of my life. Their resilience, sacrifice, and unwavering belief in me have carried me through the toughest times. I am also deeply thankful to my extended family Khura, Khuri, Aita, Riya, and Risika for their continued blessings, warmth, and encouragement that have always uplifted my spirits and reminded me of the strength of family bonds.

Lastly, I fondly remember my Deuta, who I believe is watching over me from heaven. It was always his dream to see his daughter being called a "doctor." While it may not be in the field of medicine as he once imagined, I hope he would be proud to see me taking steady steps toward earning the title "Dr.", fulfilling his cherished wish in my own way.

Rimjhim Moral
2025

karmaṇy-evādhikāras te mā phaleṣhu kadāchana
mā karma-phala-hetur bhūr mā te saṅgo 'stvakarmaṇi

— *Shree Krishna, Bhagavad Gita*

Contents

1 Introduction **1**

1.1 Cyclic Peptides: A Brief Overview 2

1.2 Cyclic Peptide Nanotubes 4

1.3 Applications of Cyclic Peptide Nanotubes 8

1.3.1 CPNT as Antiviral Agents 8

1.3.2 CPNT as Antibacterial Agents 9

1.3.3 CPNT as Drug and Gene Delivery Vehicle 10

1.3.4 CPNTs as Artificial Ion and Molecular Channels 11

1.4 Methodology 14

1.4.1 Molecular Dynamics Theory 14

1.4.2 Simulation Setup 18

1.4.3 Analysis Methods 19

1.4.4 Present Work 22

2 Self-Assembly of Cyclic Peptides in Water: Influence of Salt Concentration and Temperature **31**

2.1 Introduction 33

2.2 Materials and Methods 35

2.2.1 System Setup 35

2.2.2 Simulation Protocols . . . 36
2.2.3 Simulation Analysis . . . 37
2.3 Results and Discussions . . . 38
2.3.1 Radial Distribution Functions . . . 40
2.3.2 Coordination Number Analysis . . . 46
2.3.3 Spacial Density Functions . . . 49
2.3.4 Preferential Interactions . . . 50
2.3.5 Cluster Analysis . . . 52
2.3.6 Hydrogen Bonding . . . 54
2.3.7 Dynamics of Hydrogen Bonds . . . 57
2.3.8 Association Constant . . . 60
2.3.9 Thermodynamics Behind the Self-Association of CPs . . . 61
2.3.10 Free Energy of Binding of the Self-Assembled CP Rings . . . 65
2.4 Conclusion . . . 66

3 Impact of Solvent Polarity and Amino Acid Composition on the Structural Stability of Cyclic Peptide Nanotubes 73

3.1 Introduction . . . 75
3.2 Materials and Methods . . . 76
3.2.1 System Setup . . . 76
3.2.2 Simulation Protocols . . . 78
3.2.3 Simulation Analysis . . . 80
3.3 Results and Discussions . . . 82
3.3.1 Stability of the CPNTs across Various Solvents . . . 84
3.3.2 Enhanced Stability of D$\underline{\text{L}}$K$\underline{\text{L}}_2$ Nanotubes over D$\underline{\text{K}}_4$ and W$\underline{\text{L}}_4$ . . . 95
3.3.3 Interaction of the Solvent Medium with CPNT . . . 97

3.3.4 Binding Free Energy of the CP rings of the CPNTs 99
3.4 Conclusion and Summary 101

4 Behavior of Cyclic Peptide Nanotubes in Deep Eutectic Solvents 107
4.1 Introduction 109
4.2 Materials and Methods 110
4.2.1 System Setup 110
4.2.2 Simulation Protocols 111
4.2.3 Simulation Analysis 113
4.3 Results and Discussions 114
4.3.1 Stability of the CPNT in DES 114
4.3.2 DES-CPNT interactions 122
4.3.3 DES-Water interactions 127
4.3.4 DES-DES interactions 128
4.3.5 Thermal Stability 131
4.4 Discussion 132
4.5 Conclusion 135

5 Interaction of Cyclic Peptide Nanotubes with Lipid Bilayers and Water Transport Dynamics 141
5.1 Introduction 143
5.2 Materials and Methods 145
5.2.1 Construction of Stable CPNT Structure 145
5.2.2 System Setup for Lipid Simulation 145
5.2.3 System Setup for Water Dynamics Calculation 148
5.3 Results and Discussions 149
5.3.1 Structural Stability of CPNTs in Different Lipid Bilayers 150

5.3.2 Effect of CPNTs over Lipid Bilayer Properties 158
5.3.3 CPNT as Water Channels 161
5.4 Conclusion 166

6 Ion Transportation Through Cyclic Peptide Nanotube Embedded in Lipid Bilayer 173

6.1 Introduction 175
6.2 Materials and Methods 177
6.2.1 System Setup 177
6.2.2 Simulation Protocols 178
6.3 Results and Discussions 181
6.3.1 PMF Profiles of the Ions Through the CPNT 181
6.3.2 Non-Bonded Interactions of the Ions with the Backbone of the CPNT and Channel Water 182
6.3.3 Cation Interactions with the CPNT Lumen 184
6.3.4 Radial Distributions of the Cations within the CPNT Channel . . . 186
6.3.5 Distribution of Water Along the Lumen of the CPNT in Presence of Cations 187
6.3.6 Effect of Cations on the Translational Dynamics of Water Inside the CPNT 188
6.3.7 Dipole Moment of Channel Water in the Presence of Cations 190
6.3.8 Effect of Confinement on Cation Hydration Shells 191
6.4 Summary and Conclusion 194

7 Summary and Our View on Cyclic Peptide Nanotubes 199

Chapter 1

Introduction

"All truths are easy to understand once they are discovered; the point is to discover them."

– Galileo Galilei

1.1 Cyclic Peptides: A Brief Overview

Among the vast diversity of biomolecules, linear peptides and proteins have long been regarded as the archetypal form of amino acid polymers. Their critical roles as structural components, signaling molecules, enzymes, and regulatory elements have made them the subject of extensive biochemical and structural investigations[1, 2]. Much of our knowledge of protein folding, function, and interactions are originated from the innumerous investigations into their structure-function relationships[3–5]. However, the world of peptides extend far beyond their linear configurations. A structurally and functionally distinctive class of peptides known as "Cyclic Peptides", also exists. Though less prevalent in nature compared to linear peptides, cyclic peptides exhibit a range of properties that make them particularly promising in pharmaceutical and nanotechnological applications[6].

One of the primary motivations for the increasing interest in cyclic peptides comes from the limitations inherent to linear peptides. The linear peptides often face poor susceptibility to proteolytic degradation, low oral bioavailability, and limited conformational rigidity, which restrict their therapeutic potential[7, 8]. In contrast, the closed ring conformation of cyclic peptides imposes constraints on the peptide backbone, thereby enhancing structure rigidity[9]. This rigidity not only enhances proteolytic resistance but also reduces entropic penalties during target binding, often resulting in higher binding affinities. Furthermore, many cyclic peptides show improved membrane permeability, which is a key parameter in the design of biologically active compounds[10].

Cyclic peptides (CPs) generally represent a unique and functionally rich class of polypeptides in which the linear peptide chain is closed to form a ring through chemical bond(s). This cyclization can occur between the N- and C- termini, between side chains, or as a combination of both, resulting in one or more macrocyclic rings. Several chemical pathways have been employed to achieve such cyclization[10, 11](Figure 1.1). These include:

- Disulfide linkage, formed between thiol groups of two cysteine residues, common in naurally occuring proteins;
- Head-to-tail cyclization, where the N-terminal amine (head) forms a peptide bond with the C-terminal carboxyl group (tail), forming a closed loop by removing the free ends;

- Bonding between the N-terminus and acidic side chains;
- Bonding between the C-terminus and basic side chains;
- Side chain-to-side chain bonding; and
- More complex modifications, such as thioether bridges found in lanthipeptides, where cysteine residues form bonds with serine or threonine.

Generally, cyclic peptides require a minimum of four amino acid residues in order to achieve structural integrity, a notable exception is the class of diketopiperazines[12]. They contains two just amino acids formed through head-to-tail cyclization resulting in a stable six-membered lactam ring.

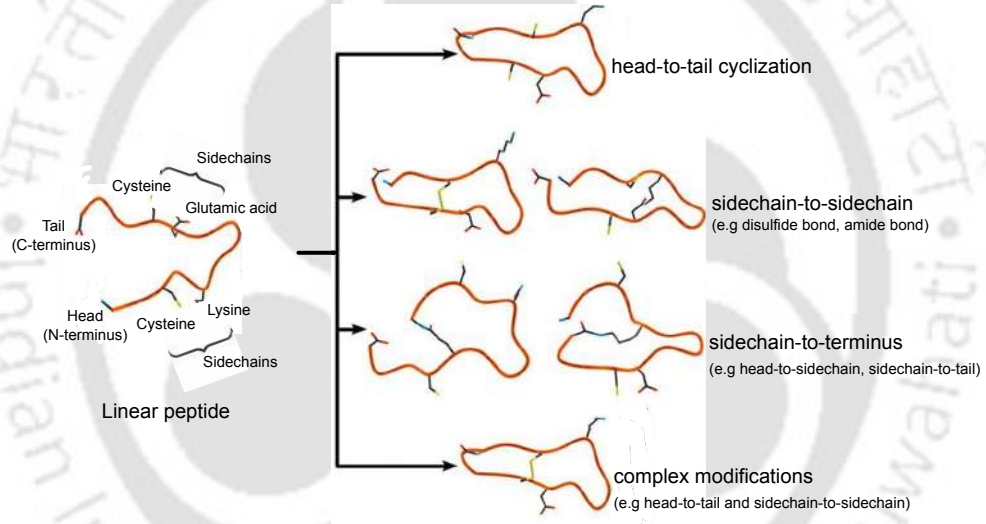

Figure 1.1: *Schematic representation of common modes of cyclization for a linear peptide chain constituting two cysteines, a lysine, and a glutamic acid. All other residues are not shown for clarity. The peptide backbone is shown in orange, carbon in black, nitrogen in blue, oxygen in red, and sulfur in yellow. Figure adapted from reference [11]*

Naturally occurring cyclic peptides further exemplify the functional and structural potential of this class. Notable examples include vancomycin[13], a glycopeptide antibiotic widely used against Gram-positive bacterial infections, and cyclosporin A[14], an immunosuppressive agent crucial in organ transplantation. Other naturally derived cyclic peptides such as bacitracin[15], gramicidin S[16], and theta-defensins[17] exhibit diverse biological activities, ranging from antimicrobial and antiviral functions to enzyme inhibition. These natural molecules serve not only as therapeutic agents but also as inspiration

for the design of synthetic analogs with enhanced efficacy and selectivity.

Due to their structural tunability and bioactive potential, cyclic peptides have found significant applications across several sectors. In the pharmaceutical industry, they are used as antibiotics, anticancer agents, immunosuppressants, and enzyme inhibitors[18–20]. In agriculture, they function as antifungal agents[21], while in diagnostics[22] and vaccine development[23], their stable and recognizable structures make them ideal scaffolds for molecular recognition.

In addition to these bioactive applications, cyclic peptides have also emerged as fundamental building blocks for the construction of supramolecular architectures. Their rigid backbone structure and tendency to form intermolecular hydrogen bonds, makes them ideal candidates for controlled self-assembly[24]. Within the realm of supramolecular chemistry, cyclic peptides have demonstrated the capacity to organize into a variety of architectures such as nanosheets[25, 26], vesicles[27], nanoparticles[28], hydrogels[29], conjugates[26], etc. depending on sequence composition, solvent environment, and chemical modification. Among these, the most intriguing and widely studied supramolecular architectures are the cyclic peptide nanotubes (CPNTs), formed by the ordered stacking of cyclic peptides through intermolecular hydrogen bonding. This leads to the next section, where we delve deeper into the structural characteristics, various design strategies, and functional implications of CPNTs.

1.2 Cyclic Peptide Nanotubes

As discussed above, cyclic peptides possess a remarkable property to self-assemble into nanotube like structures in aqueous environment and this has made them a holy grail for researchers in the fields of supramolecular chemistry and nanotechnology. The CPNTs are used extensively in the field of therapeutics[16, 18–20, 30, 31], agricultural sector[21], diagnostics[22], ion channels[32–38]etc. Numerous experimental and theoretical studies have been conducted in this context to investigate the stability and properties of self-assembled CPNTs[39–43]. These nanotubes are defined as hollow tubular-shaped supramolecular structures that are formed by non-covalent interactions (viz. hydrogen bonding, electrostatic, van der Waals interactions, etc.) between the cyclic peptide (CP) subunits to give rise to a flat ring conformation. These hollow cylindrical structures consist of cyclic di-, tri-, tetra-, hexa-, octa-, and decapeptides having different sequences

of amino acids, their enantiomers, and other functional side chains[44]. These CPNTs have several advantages over linear peptide nanotubes such as easy controlling of the radius of the tubular structure, tuning the surface characteristics by altering the number and type of amino acids, pH, and polymeric conjunctions[45, 46].

Mostly four types of CPNT stuctures have been studied so far[45, 47]: cyclic D,L-α -peptides, cyclic β-peptides, cyclic α-γ-peptides, and self-assembling heterocyclic peptides that incorporate ε-amino acids. Among them, nanotubes constructed from cyclic D,L-α-peptides have received the highest attention from the scientific community. Although the assembly of cyclic D,L-α-peptides was first proposed by De Santis et al. in 1974[48], the first structure of the self-assembled CPNT was reported experimentally by Ghadiri *et. al.* in the year 1993[49], marking a breakthrough in supramolecular peptide chemistry. They observed that, on protonation, CPs containing eight amino acid sequences in each unit, crystallized to form tubular structures of length up to hundreds of nanometers, having diameters of 7-8 Å (Figure 1.2). This early example belongs to the class of cyclic D,L-α-peptides. Subsequently, numerous investigations were carried out to elucidate the design and synthesis of CPNTs[47, 50–52].

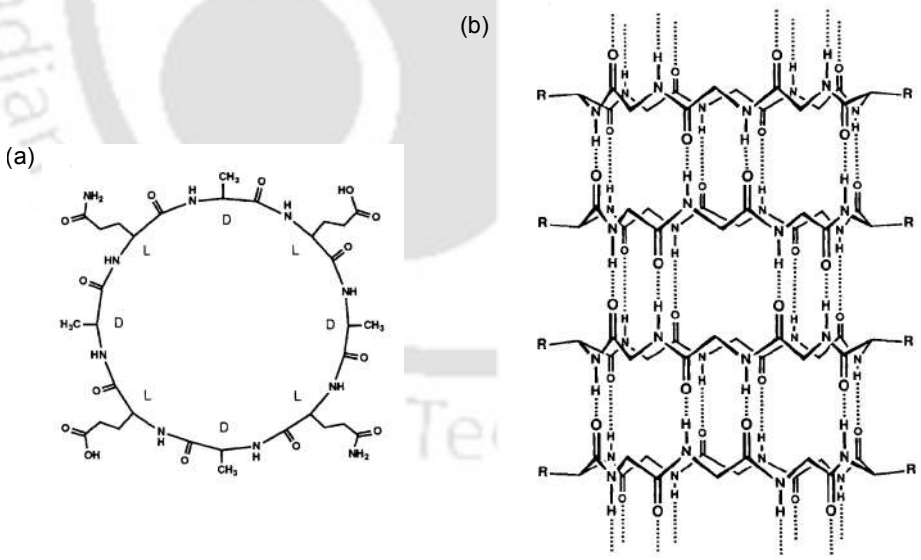

Figure 1.2: *(a)The primary structure of the cyclic peptide subunit, cyclo-[-(D-Ala-Glu-D-Ala-Gln)$_2$-], used by Ghadiri et. al., (b)The tubular structure reported by them (only the backbone structure is represented for clarity). Figure adapted from reference [49].*

Figure 1.3 shows the four structural classes of CPNTs alongwith their corresponding

CP subunits. One of the key features of the design principles of cyclic D,L-α CPNTs is that the CP subunit structures that assemble to form the nanotube is made up of an even number of alternating D- and L- amino acid residues(Figure 1.3a). These arrangements of amino acids tend to minimize the interactions between side chain-side chain as well as side chain-backbone of the nanotube by adopting a flat ring shaped conformation. By doing so, all the backbone amide groups tend to be in a perpendicular position with respect to the plane of the ring structure. In addition to that, the conformational as well as steric hindrance i.e. caused by the alternating amino acid residues compelled the side chain moieties to point outward from the center of the cyclic peptide ring. Thus, the lumen of the CPNTs becomes free from all the amino acid side chains making it a free tubular hollow-core cylindrical structure[51]. Owing to their well-characterized self-assembly behavior and structural simplicity, we focus our thesis on cyclic D,L-α-peptide nanotubes. Apart from the structure of the CP subunits, the ring stacking arrangement between two conjugate CPs also plays a vital role in the self-assembly of the nanotubes. The stacking interaction is mainly backbone-backbone intermolecular hydrogen-bonding which can be either parallel or antiparallel β-sheet like H-bonds. Molecular modeling, however, suggests a preference for antiparallel ring stacking arrangement over parallel one as that possess the best alignment between amide and carbonyl groups needed for nanotube formation[53].

The self assembling properties of cyclic β-peptide nanotubes (Figure 1.3b) closely resemble to those of cyclic D,L-α-peptides. In both cases, the amino acid side chains radiate equatorially from the peptide ring, resulting in the formation of well-defined tubular structure. However, the orientation of the amide and carbonyl groups presents an opposite unidirectional allocation along the longitudinal axis of the tube in cyclic β-peptide nanotubes, thus forming parallel stacking[47, 54]. The third type of CPNTs formed by cyclic α-γ-peptides (Figure 1.3c) differs from the other two classes and possesses nonequivalent faced rings that stack flat together with different hydrogen bonding patterns as γ-γ and α-α interactions[47, 52]. The last category involves self-assembling heterocyclic CPNTs (Figure 1.3d) that incorporate non canonical amino acids, such as ε-amino acids or other unnatural building blocks[55].

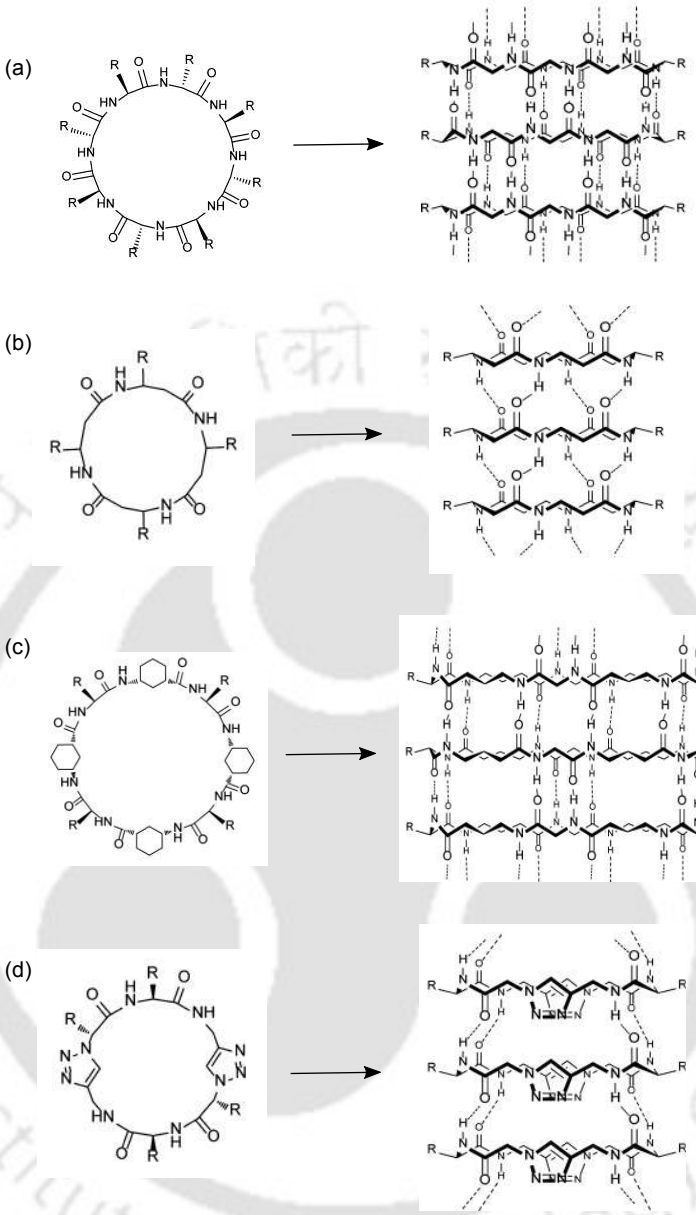

Figure 1.3: *Different types of CPNTs studied so far that are formed through β sheet stacking. (a) cyclic D,L-α-peptides; (b) cyclic β-peptides; (c) cyclic α-γ-peptides and; (d) heterocyclic peptides containing ε-amino acids. The N-H and C=O hydrogen bond donors and acceptors are aligned with tube lengths for all the cases and side chains (R) are omitted for clarity. Figure adapted from reference [47]*

Having outlines the major classes of CPNTs and their underlying self-assembly principles, it becomes evident that their self-assembling nature and ease of controlling structural properties have made them ideal candidates for a wide range of applications. In the fol-

lowing section, we explore how these nanotubes translate into function roles across various fields.

1.3 Applications of Cyclic Peptide Nanotubes

Although the applications of CPNTs cover a wide range, in this section we focus only on those related to cyclic D,L-α-CPNTs. This is because our thesis is mainly based on this specific class as mentioned above. We briefly highlight some of their important uses in different fields of medicinal chemistry and material science.

1.3.1 CPNT as Antiviral Agents

CPNTs constructed with alternating D- and L-amino acids exhibit significant antiviral activity against viruses. Their effectiveness is primarily influenced by their interaction with host cell membranes, particularly through disruption of endosomal acidification and prevention of viral escape from endosomes, rather than via conventional receptor-ligand mediated mechanisms. This unique, non-specific mode of action enables them to maintain activity across a broad range of viral strains[44].

Among the studied sequences, an eight-residue cyclic D,L-α-peptide, cyclo-(Ser-D-His-Lys-D-Arg-Lys-D-Trp-Leu-D-Trp), exhibited noteworthy activity against type A influenza virus, with an IC_{50} of approximately 5 μM[56]. Reversal of the sequence or substitution with its enantiomeric form did not significantly alter the antiviral efficacy, further confirming that the observed activity arises from membrane-level interactions rather than specific chiral recognition. Additionally, structure-activity relationship studies revealed that hydrophobic residues such as tryptophan play a critical role in membrane affinity and antiviral action. For instance, alanine substitutions at key hydrophobic positions led to a marked reduction in activity.

In another study, a library of 144 cyclic D,L-α-peptides was screened for anti-Hepatitis C activity[57]. One such sequence, cyclo-(D-Trp-Leu-D-Trp-Orn-D-Glu-Asn-D-Glu-Lys), displayed antiviral activity with an IC_{50} of 11 μM. Modifications to the arrangement of charged residues, particularly the introduction of negatively charged amino acids into hydrophobic regions, significantly attenuated the antiviral effect. Furthermore, N-methylation of peptide backbones, which disrupts intermolecular hydrogen bonding and stacking, was

found to abolish antiviral activity, underscoring the importance of supramolecular assembly in functional performance. Collectively, these findings suggest that CPNTs can function as robust membrane-active antiviral agents.

1.3.2 CPNT as Antibacterial Agents

In addition to their antiviral activity, CPNTs have been extensively investigated for their antibacterial potential, particularly in addressing the urgent need for new therapeutic strategies against antibiotic-resistant bacteria. Their mode of action deviates from conventional antibiotics by targeting bacterial membranes through physicochemical interactions, offering a mechanism less prone to resistance development.

The antibacterial activity of CPNTs is closely linked to their amphipathic character and the specific arrangement of amino acid residues along the peptide ring. Notably, six- and eight-residue cyclic D,L-α-peptides with balanced hydrophilic and hydrophobic segments have been shown to self-assemble into β-sheet-like hollow tubular structures that interact directly with bacterial membranes. This interaction, frequently described by the "carpet model", results in increased membrane permeability and rapid bacterial cell death[58]. Importantly, these peptides do not rely on binding to intracellular targets, which is advantageous in circumventing resistance mechanisms typically associated with traditional antibiotics. For example, the cyclic peptide cyclo-(D-Ser-Lys-D-Ser-Trp-D-Leu-Trp-D-Leu-Trp) demonstrated significant activity against methicillin-resistant *Staphylococcus aureus* (MRSA) and *Escherichia coli*, with a minimum inhibitory concentration (MIC) of 8 μM for both strains. Structural modification studies revealed that substituting polar or charged residues, such as replacing lysine with histidine and serine with glutamic acid, could dramatically reduce antibacterial activity. This reduction is attributed to decreased electrostatic interactions with the negatively charged bacterial membrane or increased electrostatic repulsion. Conversely, increasing the number of positively charged residues such as lysine or arginine was found to enhance antimicrobial activity, confirming the role of positive charge density in promoting bacterial membrane disruption[58]. The preservation of hydrophilic residues to design CPNTs with broad-spectrum antibacterial activity was also confirmed by other experimental finidngs[59, 60].

Beyond these conventional sequences, glycosylated CPNTs, where side chains are functionalized with carbohydrate moieties such as D-glucosamine, D-galactose, or D-mannose,

have also been developed. These modified CPNTs retained the ability to self-assemble and exhibited potent activity against both MRSA and vancomycin-resistant *Enterococcus faecalis* (VRE), with MIC values of 2.5-5 μM and 10-15 μM[61].

1.3.3 CPNT as Drug and Gene Delivery Vehicle

The unique structural features of CPNTs such as hollow tubular morphology, high aspect ratio, and large surface area have provided an ideal platform for encapsulating, protecting, and transporting therapeutic agents. Additionally, the amphiphilic character of CPNTs with tunable internal and external environments facilitates the incorporation of both hydrophilic and hydrophobic drug molecules, thereby expanding their utility across a wide range of pharmaceutical compounds.

Studies showed that with the addition of a highly hydrophobic cyclic peptide, cyclo-[Gln-(D-Leu-Trp)$_4$-D-Leu] increased the liposomal membrane release of anticancer drug 5-fluorouracil (5-FU)[62]. The permeation of drugs smaller than the internal diameter of CPNTs may occure through the channel of the nanotube in a dose-dependent manner. Further enhancement of delivery performance was achieved by surface modification of CPNTs with biocompatible polymers. For example, PEG-modified CPNTs loaded with doxorubicin displayed improved cellular uptake and increased cytotoxicity in MCF-7 and MCF-7/ADR breast cancer cells, suggesting involvement of endocytic pathways in cellular entry[63]. Similar success was observed with HEA-co-CEMA-conjugated CPNTs delivering ruthenium-based drugs to A2780 ovarian cancer cells, where conjugation altered intracellular distribution, leading to enhanced drug retention and activity[64].

Notably, in vivo studies have supported these in vitro findings. In mice with S180 tumors, intratumoral injection of 5-fluorouracil (5-FU) in combination with CPNTs led to a significant reduction in tumor volume and mass compared to treatment with 5-fluorouracil alone[62]. Histological analysis of treated tumor tissue revealed increased necrosis and vacuolization, indicating the enhanced therapeutic efficacy of the CPNT-assisted delivery strategy.

The transport behavior of the antitumor drug 5-fluorouracil (5-FU) through CPNT has been extensively investigated using molecular dynamics simulations. In one study, (Trp-D-Leu)$_4$-Gln-D-Leu-based cPNTs embedded in a hydrated DMPC bilayer exhibited a hopping mechanism for 5-FU translocation, wherein the drug moved through sequen-

tial potential energy minima along the nanotube axis, driven by alternating hydrophobic interactions and hydrogen bonding with the backbone amide and carbonyl groups of the cPNT [65]. An energy well near the nanotube exit further stabilized the transport process. In a separate study, classical and steered MD simulations combined with umbrella sampling revealed that 5-FU translocation through cyclo-[(D-Trp-L-Leu)$_5$]$_8$ and cyclo-[(L-Ala-D-Gln-L-ALa-D-Glu)$_2$-L-Ala-D-Gln]$_8$ CPNTs occurred via continuous formation and rupture of hydrogen bonds along the peptide backbone [66]. Free energy profiles showed favorable transport, with energy barriers of approximately –6.0 and –2.0 kcal mol^{-1} at specific regions of the nanotube, supporting the potential of CPNTs as effective drug delivery platforms for 5-FU.

Furthermore, CPNTs have garnered significant attention as non-viral vectors for gene delivery, owing to their favorable structural and physicochemical properties. Studies showed that cyclic octapeptide nanotubes, consisting of four L-lysines and four D-alanines with a guanidiniocarbonyl pyrrole moiety attached to one lysine residue, bound to calf thymus DNA via electrostatic interactions. The resulting aggregates indicated that these CPNTs could mediate gene delivery without relying on the endocytic pathway[67]. Another study demonstrated the use of cyclic peptide cyclo-(D-Trp-Tyr) to deliver plasmid DNA both orally and topically in murine models[68]. When administered orally, the CPNT/DNA complexes led to successful gene expression in multiple tissues, including the stomach, duodenum, liver, and kidney. In addition, these complexes have been employed in ocular gene delivery, where eye-drop formulations carrying caspase-3-targeting siRNA effectively suppressed gene expression in corneal tissue, resulting in a reduction of chemically induced apoptosis and inflammation[69]. The application of cPNTs in gene delivery thus offers several key advantages: enhanced protection of genetic material, facilitation of mucosal and epithelial transport, and efficient intracellular release with minimal immune response.

1.3.4 CPNTs as Artificial Ion and Molecular Channels

Natural ion channels are large and complex membrane proteins, which are very expensive, difficult to isolate, and sensible to denaturation. For this reason, artificial ion channels are an important alternative, as they can be produced by simple and inexpensive synthetic chemistry paths, allowing manipulation of characteristics and enhancement

of ion selectivity properties[37]. They can be used not only in curing channelopathies, but also for understanding the natural ion channel functions which pave the way for a wide range of applications in water treatment, biosensing, nanotechnologies and drug delivery[70]. The pioneering work by Ghadiri and co-workers demonstrated that CPNTs are capable of facilitating the transmembrane transport of cations such as Na^+ and K^+, with conduction rates surpassing those observed in natural ion channels like gramicidin A[71]. This seminal discovery generated widespread interest in elucidating the efficacy of these nanotubes in transporting various ions and small molecules. Owing to their tubular architecture and tunable properties, CPNTs have potential to act as artificial channels for ionic and molecular transport across lipid bilayers or synthetic membranes[72]. The transportion behaviors and mechanisms of different ions and molecules are not similar and are dependent of the radius[34, 36, 38], length[35], surface properties of the respective CPNTs[72, 73]. The transportation of ions and molecules also depends on the strength of the electric field[37, 74], the open-ended orientation of CPNTs on the membrane surface[75], the concentration of ions or molecules[32, 72, 76], the size of the molecules, and the temperature[37].

Molecular dynamics simulations and experimental studies have revealed that CPNTs enable the transport of a wide range of ionic and molecular species, including monovalent and divalent cations[36–38, 77] (e.g., Na^+, K^+, Ca^{2+}, $NH_4{}^+$), water molecules[34, 74, 77], and neutral gases such as O_2, CO_2, and NH_3[78]. Among these, Na^+ and K^+ exhibited favorable transport profiles, with low free energy barriers, due to smaller size and compatibility with the dimensions of typical peptide nanotubes. In contrast, ions like Ca^{2+} or $NH_4{}^+$, which possess stronger hydration energies, required CPNTs of larger diameters or enhanced polar interactions to enable effective permeation. Coming to water transportation through CPNT it was found that water diffusion was facilated by the larger radius of CPNTs with increasing diffusion coefficients of water molecules as we went from hexa-, octa-, to deca- cyclo-(Trp-D-Leu) CPNTs[34]. On the other hand, the osmotic permeability (Pf) of water in cyclo-(Trp-D-Leu)$_4$ was observed to be decreasing with the increasing length of the channel, thus indicating the relatively rapid transport in short channels[35]. Again in a study the water permeation coefficient of CPNT was reported to be highly comparable to the Human Aquaporin-2 (AQP2) channel protein. It was found that the mechanism of water transport took place as a two line 1-2-1-2 file fashion through the nanotube[79]. A later study showed that the choice of water model significantly influenced

the simulated water dynamics, with TIP3P yielding the highest water velocity, followed by TIP4P, TIP4P/2005, and OPC[80]. Interestingly, this trend remained consistent even in the confined environment of cPNTs, indicating minimal impact of confinement on the relative transport behavior of different water models. Additionally, the transport of small gas molecules such as O_2, CO_2, and NH_3 through cyclo-(Trp-D-Leu)$_4$ was shown to depend on the required external force, with NH_3 requiring the least due to its ability to form single or double water bridges via hydrogen bonding within the channel[78].

Beyond water, ions, and gases, several studies have shown that a variety of small organic molecules can also permeate through CPNTs. These include methane[73], methanol[72, 73], ethanol[73, 81], chloroform[72], β-D-glucose[82], lactic acid[83, 84], ascorbic acid[85], and glutamic acid[86]. Transport behaviors for these molecules have been systematically evaluated using molecular dynamics (MD) simulations, highlighting that molecular size, polarity, hydrogen bonding potential, and interaction with confined water or channel residues significantly influence permeation efficiency and selectivity within the nanotube environment.

Among these, relatively larger molecules such as methane, methanol, and ethanol were found to experience high energy barriers during translocation through narrow-diameter CPNTs such as cyclo-(Trp-D-Leu)$_4$, indicating size-restricted diffusion. These barriers, however, can be reduced by using CPNTs with wider internal radii[73]. For β-D-glucose, non-bonded interactions between glucose, water molecules, and the nanotube wall played a central role in facilitating its movement through the CPNT[82]. Lactic acid transport was found to be enantioselective: the S-enantiomer moved more efficiently along the nanotube walls, whereas the R-enantiomer displayed higher velocity along the central axis[83]. Interestingly, increasing the nanotube diameter further enhanced the mobility of the S-enantiomer compared to the R-form, suggesting the potential of CPNTs as chirality-selective channels[84]. The transport of L-ascorbic acid was investigated through two structurally distinct CPNTs: cyclo-(L-Gln-(D-Leu-L-Trp)$_4$-D-Leu-) and cyclo-(D-Ala-L-Ala)$_5$ embedded within a complex lipid bilayer system[85]. The study revealed that differences in nanotube architecture significantly influenced ascorbic acid's translocation due to variations in hydrogen bonding patterns, configurational entropy, and binding energy along the transport pathway. Finally, glutamic acid transport was shown to be strongly dependent on its protonation state[86]. MD simulations indicated that the anionic form encountered high energy barriers within the nanotube, while

the zwitterionic and cationic forms exhibited more favorable energetics. These differences were largely attributed to the electrostatic interactions between the charged species and the nanotube environment, rather than changes in diffusivity.

In summary, CPNTs demonstrate significant potential as artificial ion and molecular channels, owing to their well-defined internal cavities, tunable architecture, and versatile chemical functionality. A broad range of computational and experimental studies have established their ability to selectively transport diverse species including water, ions, gases, and small organic molecules through mechanisms governed by size exclusion, electrostatic interactions, hydrogen bonding, etc. These findings emphasize not only the structural adaptability of CPNTs but also their relevance in mimicking biological channels and contributing to the advancement of nanoscale transport technologies.

Given the vast possibilities offered by CPNTs in material science and nanotechnology, the present dissertation focuses on a detailed investigation of their structure, self-assembly, and functional applications. The subsequent chapters present our simulation-based studies and key findings in this regard. The following section introduces the fundamental concepts of molecular dynamics (MD) simulations, outlines the simulation protocols and analytical techniques employed throughout this work, and sets the stage for the system-specific analyses provided in later chapters. A brief overview of the individual chapters is also included at the end of this introductory chapter.

1.4 Methodology

The computational study of molecular systems is fundamentally rooted in mathematical formulations, which form the basis for generating and interpreting simulation data. To understand the results presented in this dissertation, it is essential to first introduce the theoretical framework and methods that underpin classical Molecular Dynamics (MD).

The following subsection outlines the basic principles of MD theory relevant to the present work.

1.4.1 Molecular Dynamics Theory

In this thesis, classical Molecular Dynamics (MD) simulation techniques have been employed to explore the structure and dynamics of biomolecular systems. MD has been

widely used in the study of proteins, nucleic acids, and small molecules such as amino acids, sugars, and drug-like compounds. In MD simulations, the potential energy of the system (U) is defined by both bonded interactions (such as bond stretching, angle bending, and torsional rotations) and non-bonded interactions (including van der Waals and electrostatic forces) among atoms and molecules in the condensed phase. These interactions are described through a mathematical framework known as a force field[87], which provides the parameterization necessary to model atomic interactions accurately.

The potential energy function in a classical MD simulation is expressed as the sum of bonded and non-bonded interaction terms:

$$U = U_{\text{bond}} + U_{\text{angle}} + U_{\text{dihedral}} + U_{\text{vdW}} + U_{\text{Coulomb}} \tag{1.1}$$

Here, U_{bond}, U_{angle}, and U_{dihedral} represent the bonded interactions arising from bond stretching, angle bending, and torsional rotations, respectively. The terms U_{vdW} and U_{Coulomb} denote the non-bonded van der Waals and electrostatic interactions between atoms. This potential energy function forms the basis for calculating interatomic forces that govern atomic motion throughout the simulation. In the bonded interaction terms, bond stretching and angle bending are typically modeled using harmonic potentials. These interactions include direct bonds between two atoms (1-2 interactions), bond angles involving three atoms (1-3 interactions), and torsional rotations involving four sequentially bonded atoms (1-4 interactions). The potential energy contributions for these terms are defined as follows:

$$U_{\text{bond}} = \sum_{\text{bonds}} K_b (b_{\text{ac}} - b_{\text{eq}})^2 \tag{1.2}$$

$$U_{\text{angle}} = \sum_{\text{angles}} K_\theta (\theta_{\text{ac}} - \theta_{\text{eq}})^2 \tag{1.3}$$

$$U_{\text{dihedral}} = \sum_{\text{dihedrals}} \frac{V_n}{2} \left[1 + \cos(n\phi - \delta)\right] \tag{1.4}$$

In these expressions, b, θ, and ϕ represent the bond length, bond angle, and dihedral angle, respectively. The subscript 'ac' refers to the actual (instantaneous) value, and 'eq'

denotes the equilibrium value. The parameters K_b, K_θ, and V_n are the force constants for bond stretching, angle bending, and dihedral rotation, respectively. The term n represents the multiplicity of the dihedral angle, and δ is the phase offset.

The non-bonded interactions are computed using two main terms: the Lennard-Jones potential (U_{vdW})[88], which accounts for van der Waals forces[89], and the Coulomb potential (U_{Coulomb})[90], which describes electrostatic interactions between particles bearing partial charges. These interactions are defined as:

$$U_{\text{vdW}} = \sum_i \sum_{j>i} 4\epsilon_{ij} \left[\left(\frac{\sigma_{ij}}{r_{ij}} \right)^{12} - \left(\frac{\sigma_{ij}}{r_{ij}} \right)^{6} \right] \tag{1.5}$$

$$U_{\text{Coulomb}} = \sum_i \sum_{j>i} \frac{q_i q_j}{4\pi\epsilon_0 r_{ij}} \tag{1.6}$$

In these equations, the double summation runs over all atom pairs i and j where $j > i$. The parameters σ_{ij} and ϵ_{ij} represent the Lennard-Jones diameter and well-depth energy between atom pairs, respectively. r_{ij} is the interatomic distance between atoms i and j, while q_i and q_j are the partial atomic charges. ϵ_0 denotes the electrical permittivity.

The aim of a MD simulation is to track the time evolution of atomic coordinates in a system. For an N-particle system, the total energy is described by the Hamiltonian:

$$H = \sum_{i=1}^{N} \frac{p_i^2}{2m_i} + U(\mathbf{r}^N) \tag{1.7}$$

where m_i and p_i are the mass and momentum of the i-th particle, respectively, and $U(\mathbf{r}^N)$ is the total potential energy of the system, incorporating all particle-particle interactions. The positions of all particles are represented by $\mathbf{r}^N = \{\mathbf{r}_1, \mathbf{r}_2, \ldots, \mathbf{r}_N\}$.

The motion of each particle is governed by Newton's second law:

$$\mathbf{a}_i = \frac{\mathbf{F}_i}{m_i} \tag{1.8}$$

where $\mathbf{F}_i$ is the force acting on particle i, and $\mathbf{a}_i$ is its acceleration.

This equation can be derived from the Lagrangian formulation. Assuming the total po-

tential energy U is a sum of pairwise interactions $u(r_{ij})$, the Lagrangian of the system is given by:

$$L = \frac{1}{2}\sum_{i=1}^{N} m_i \mathbf{v}_i^2 - \frac{1}{2}\sum_{i=1}^{N}\sum_{j\neq i} u(r_{ij}) \tag{1.9}$$

The Lagrange equations of motion are then obtained from:

$$\frac{d}{dt}\left(\frac{\partial L}{\partial \dot{q}_i}\right) - \frac{\partial L}{\partial \dot{q}_i} = 0 \tag{1.10}$$

As evident from this expression, the dynamics of the system are governed by a set of $3N$ second-order differential equations, where q_i denotes the generalized coordinates for each particle.

It is also possible to describe the dynamics of a system using Hamiltonian mechanics. The Hamiltonian (H) represents the total energy of the system and is expressed in terms of generalized coordinates $\mathbf{q}_k$ and conjugate momenta $\mathbf{p}_k$. The equations of motion in Hamiltonian form are given by:

$$\dot{\mathbf{q}}_k = \frac{\partial H}{\partial p_k} \tag{1.11}$$

$$\dot{\mathbf{p}}_k = -\frac{\partial H}{\partial q_k} \tag{1.12}$$

For a system with pairwise interaction potentials, the Hamiltonian can be written as:

$$H = \frac{1}{2}\sum_{i=1}^{N} m_i \mathbf{v}_i^2 + \frac{1}{2}\sum_{i=1}^{N}\sum_{j\neq i} u(r_{ij}) \tag{1.13}$$

Using the above expression, the Hamiltonian equations reduce to:

$$\frac{dr_i}{dt} = \frac{\mathbf{p}_i}{m_i} \tag{1.14}$$

$$-\dot{\mathbf{p}}_i = -\nabla \mathbf{u} = \mathbf{F}_i \tag{1.15}$$

where $i = 1, 2, \ldots, N$. These result in a system of $6N$ first-order differential equations, which can be solved numerically to simulate the time evolution of the system.

The equations of motion in molecular dynamics are solved numerically to obtain particle velocities and positions as a function of time. Typically, this is achieved using a finite difference approach. One of the most commonly used algorithms for this purpose is the Verlet algorithm[91]. Its popularity stems from its straightforward implementation and modest storage requirements. However, it has certain limitations, such as moderate precision and the absence of explicit velocity calculations.

To address these shortcomings, the leap-frog algorithm was developed[92], which calculates velocities at half-integer time steps. Despite this improvement, the leap-frog method suffers from a lack of synchronization between positions and velocities. As an alternative, the Velocity Verlet algorithm[93] offers better accuracy and synchrony by updating positions and velocities simultaneously. It employs the following relations:

$$r(t + dt) = r(t) + v(t)\, dt + \frac{1}{2} a(t)\, dt^2 \tag{1.16}$$

$$v(t + dt) = v(t) + \frac{1}{2}[a(t) + a(t + dt)]\, dt \tag{1.17}$$

To compute the velocities at time $t + dt$, the accelerations at both time steps t and $t + dt$ are required. In the present work, we have employed the Velocity Verlet algorithm for integrating the equations of motion due to its balance of accuracy, efficiency, and ease of implementation.

1.4.2 Simulation Setup

All initial systems were constructed using the PACKMOL program[94] with a packing tolerance of 2.0 Å. The topology and coordinate files for the packed systems were then generated using the LEaP module of AMBER18[95]. The molecular dynamics simulations were performed using the SANDER module implemented in AMBER18. Each system

was placed in a cubic simulation box with periodic boundary conditions (PBC) applied in all three spatial dimensions. Prior to the production runs, energy minimization was carried out to eliminate unfavorable atomic contacts. This process included a few initial steps using the steepest descent method followed by additional steps using the conjugate gradient method.

Subsequently, the systems were gradually heated from 0K to the target temperature under the canonical (NVT) ensemble. This was followed by equilibration in the isothermal-isobaric (NPT) ensemble at the desired temperature and pressure for a sufficient duration. Temperature and pressure control were maintained using the Langevin thermostat[96] with a collision frequency of $1 ps^{-1}$ and either the Berendsen barostat[97] or the Monte Carlo barostat[98] with a pressure relaxation time of 2 ps. SHAKE algorithm[99] with a tolerance of 10^{-5} Å was used to constrain the bond lengths involving hydrogen atoms. The particle mesh Ewald (PME)[100] method was applied to treat the long-ranged non-bonding electrostatic interactions and 10 Å cut off radius was employed for short-ranged non-bonding Lennard-Jones interactions. Each system was subjected to a sufficiently long NPT production run to ensure statistical convergence. Additional simulation details and protocol variations, specific to the objectives of individual studies, are described in the respective chapters of this thesis.

1.4.3 Analysis Methods

The trajectories of all systems were analyzed using the CPPTRAJ[101] module from the Amber18 package. In addition, few analyses were carried out using in-house scripts which would be discussed in respective chapters. Visualization was carried out using Visual Molecular Dynamics (VMD)[102] and UCSF-Chimera[103].

The radial distribution function (RDF), denoted as $g(r)$, described how the local particle density varied as a function of distance r from a reference particle. It was defined such that the average number of particles, $dN(r)$, found in a spherical shell of thickness dr at distance r from a given particle was given by[104]:

$$dN(r) = 4\pi r^2 \rho \, g(r) \, dr \tag{1.18}$$

where ρ was the average number density of the system. Equivalently, the RDF can be

expressed as

$$g(r) = \frac{1}{4\pi r^2 \rho} \frac{dN(r)}{dr} \tag{1.19}$$

A hydrogen bond was defined as formed when the following two conditions were simultaneously satisfied: (a) The distance between the donor atom (D) of one molecule and the acceptor atom (A) of another is within a cutoff of 3.5 Å , and (b) The H-D-A angle does not exceed 45° [105, 106]. The continuous hydrogen bond time correlation function (TCF) was applied to compute the lifespan of hydrogen bonds between backbone atoms in adjacent CP rings. The TCF was defined as[107–110]:

$$S_{HB}(t) = \frac{\langle h(0)H(t)\rangle}{\langle h(0)h(0)\rangle} \tag{1.20}$$

Here, h(t) was assigned a value of 1 when a hydrogen bond was present between two sites at time t=t, and 0 when it was not. The value of H(t) was considered to be 1 only if the hydrogen bond persisted between the two sites from t=0 to t=t; otherwise, H(t)=0. The $S_{HB}(t)$ was derived from the last 200 ps trajectory of the NVE simulations for each system. Subsequently, the amplitude-weighted average lifetime values[111],$<\tau_{HB}>$ were determined by employing triexponential fit to the decay curves.

The NAMD energy plugin in VMD[102] was used to calculate the non-bonded interaction energies for the systems under consideration. The preferential interaction parameter for CP-CP over CP-solvent (s) was determined by the use of Kirkwood-Buff integrals [112–116]. It is deduced as follows:

$$\tau^{cp}_{cp/s} = \rho_{cp}(G_{cp/cp} - G_{cp/s}) \tag{1.21}$$

where $G_{cp/cp}$ and $G_{cp/s}$ represent Kirkwood-Buff integrals, and they are derived from the radial distribution functions of CP around CP and solvent around CP respectively[115, 117]. ρ_{cp} denotes the number density of CP in the respective solvent[118]. A positive $\tau^{cp}_{cp/s}$ value indicates that CP prefers interacting with other CP molecules over solvent molecules, while its negative value suggests a greater affinity of CP units for solvent molecules.

The binding free energy of each CP ring within the nanotube structure, relative to the

two adjacent rings, was evaluated using Molecular Mechanics/Poisson-Boltzmann Surface Area (MM/PBSA)[119] and Molecular Mechanics/Generalized Born Surface Area (MM/GBSA)[120] methods. The Python script MMPBSA.py[119] was employed for these calculations. The final 20 ns of the trajectory was used, with solvent molecules and other CP rings stripped away. The binding free energy between each CP ring and its two neighboring rings was calculated using the following relations[121]:

$$\Delta G^{i}_{bind} = G_{complex} - (G^{i} + G^{j}_{complex}) \tag{1.22}$$

Here, G^{i} representes the energy of the ith CP ring in the nanotube, where i ranges from 1 to 6. $G^{j}_{complex}$ refers to the energy of the two neighboring rings, excluding the i ring, while $G_{complex}$ corresponds to the total energy of the three CP rings. The binding free energy, ΔG^{i}_{bind}, for each ring was determined using the following equation[121]:

$$\Delta G_{bind} = \Delta E_{vac} + \Delta G_{solv} \tag{1.23}$$

The first component, ΔE_{vac} *i.e* energy in vacuum consists of:

$$\Delta E_{vac} = \Delta E_{vdW} + \Delta E_{ele} \tag{1.24}$$

where, ΔE_{vdW} and ΔE_{ele} denotes the van der Waals and electrostatic energies, respectively. The second component of equation (5), ΔG_{solv}, representes the solvation energy and was determined as the sum of the polar solvation energy (ΔG_{pol}) and nonpolar solvation energy (ΔG_{np})[122]:

$$\Delta G_{solv} = \Delta G_{pol} + \Delta G_{np} \tag{1.25}$$

The ΔG_{pol} term was determined by solving either the Poisson-Boltzmann (PB) or Generalized Born (GB) equation, while the ΔG_{np} term was derived from the solvent accessible surface area (SASA) using the linear combination of pairwise overlaps (LCPO) method[123]. The relationship is expressed as[122, 124]:

$$\Delta G_{np} = \gamma SASA + \beta \tag{1.26}$$

The surface tension coefficient (γ) was set to be 0.005 kcal mol^{-1} Å $^{-2}$, and the offset (β) was -1.008 kcal mol^{-1}[122, 124].

1.4.4 Present Work

To fully unlock the potential of CPNTs in advanced materials science and biomedical research, a comprehensive understanding of their self-assembly behavior, structural stability under various environmental conditions, and their capabilities for molecular and ionic transport is essential. The present thesis employs classical molecular dynamics (MD) simulations as the primary computational tool to systematically investigate these aspects of CPNTs. These simulations enable us to probe the behavior of CPNTs at atomic resolution, providing insights that are often difficult to obtain through experiments alone. The studies presented herein are aimed at understanding how CPNTs behave across different solvent environments, how their interactions with lipid bilayers influence transport phenomena, and how their structural attributes contribute to selective transport mechanisms.

The thesis is organized into seven chapters, each dealing with a distinct but interconnected aspect of CPNT research. The current chapter (**Chapter 1**) introduces the concept of cyclic peptide nanotubes, their origin, structural features, and various applications, with a special emphasis on their role as biomimetic channels. A brief description of the basic principles of MD simulations, the simulation protocols adopted in the present work, and the analysis techniques employed are also provided in this chapter. Thereafter, **Chapter 2** investigates the process of self-assembly of cyclic peptides in aqueous environments and explores how external factors such as salt concentration and temperature influence their aggregation behavior. Through detailed simulation studies, the chapter identifies key thermodynamic and structural parameters that govern the formation and stability of nanotubes. **Chapter 3** extends the investigation to probe how the polarity of the solvent and sequence variation in the cyclic peptides impact the overall structural integrity and morphology of CPNTs, offering insight into how subtle changes in chemical environment and peptide composition can tune their architecture. In **Chapter 4**, the solvent study is further broadened by exploring the behavior of CPNTs in deep eutec-

tic solvents (DESs), which are gaining limelights as green and tunable alternatives to conventional organic solvents. The simulations assess structural stability, role of hydration, and thermal resilience of CPNTs in DES, thereby illuminating their performance in less conventional but industrially relevant environments. **Chapter 5** shifts the focus to more biologically relevant systems by examining how CPNTs interact with various lipid bilayer membranes. This chapter specifically addresses the insertion of CPNTs into lipid bilayers and investigates water transport behavior through the nanotube lumen when embedded in realistic membrane environments. **Chapter 6** builds on this by analyzing ion transportion through CPNTs embedded in yeast lipid bilayer. The chapter elucidates ion selectivity mechanisms, changes in water dynamics, and the influence of ionic size and charge on transport efficiency. Finally, **Chapter 7** presents a comprehensive summary of the findings across all the previous chapters and discusses future directions for advancing CPNT-based nanomaterials in functional applications.. Collectively, the thesis offers a thorough exploration of CPNTs, from fundamental structural behavior to applied transport properties.

References

(1) Sewald, N.; Jakubke, H.-D., *Peptides: chemistry and biology*; John Wiley & Sons: 2015.

(2) R Zuconelli, C.; Brock, R.; JW Adjobo-Hermans, M. *Curr. Med. Chem.* **2017**, *24*, 1862–1873.

(3) Nölting, B.; Andert, K. *Proteins:Struct. Funct. Bioinf.* **2000**, *41*, 288–298.

(4) Hosseinkhani, H.; Hong, P.-D.; Yu, D.-S. *Chem. Rev.* **2013**, *113*, 4837–4861.

(5) Cheng, R. P.; Gellman, S. H.; DeGrado, W. F. *Chem. Rev.* **2001**, *101*, 3219–3232.

(6) Koehnke, J.; Naismith, J.; Van der Donk, W. A., *Cyclic Peptides: From Bioorganic Synthesis to Applications*; Royal Society of Chemistry: 2017; Vol. 6.

(7) Haggag, Y. A.; Donia, A. A.; Osman, M. A.; El-Gizawy, S. A. *Biomed. J.* **2018**, *1*, 6659–6662.

(8) Wang, L.; Wang, N.; Zhang, W.; Cheng, X.; Yan, Z.; Shao, G.; Wang, X.; Wang, R.; Fu, C. *Signal Transduction Targeted Ther.* **2022**, *7*, 48.

(9) Duffy, F.; Maheshwari, N.; Buchete, N.-V.; Shields, D. *Cyclic Peptide Design* **2019**, 73–95.

(10) Tapeinou, A.; Matsoukas, M.-T.; Simal, C.; Tselios, T. *Pept. Sci.* **2015**, *104*, 453–461.

(11) Empting, M. In *Cyclic Peptides: From Bioorganic Synthesis to Applications*; The Royal Society of Chemistry: 2017, pp 1–14.

(12) Martins, M. B.; Carvalho, I. *Tetrahedron* **2007**, *63*, 9923–9932.

(13) Levine, D. P. *Clin. Infect. Dis.* **2006**, *42*, S5–S12.

(14) Kahan, B. D. *N. Engl. J. Med.* **1989**, *321*, 1725–1738.

(15) Johnson, B. A.; Anker, H.; Meleney, F. L. *Science* **1945**, *102*, 376–377.

(16) Gause, G. F.; Brazhnikova, M. G. *Nature* **1944**, *154*, 703–703.

(17) Conibear, A. C.; Craik, D. J. *Angew. Chem. Int. Ed.* **2014**, *53*, 10612–10623.

(18) Loll, P. J.; Axelsen, P. H. *Annu. Rev. Biophys. Biomol. Struct.* **2000**, *29*, 265–289.

(19) Liu, S.; Gu, W.; Lo, D.; Ding, X.-Z.; Ujiki, M.; Adrian, T. E.; Soff, G. A.; Silverman, R. B. *J. Med. Chem.* **2005**, *48*, 3630–3638.

(20) Jin, L.; Harrison, S. C. *Proc Natl Acad Sci* **2002**, *99*, 13522–13526.

(21) Lee, D. W.; Kim, B. S. *Plant Pathol. J.* **2015**, *31*, 1.

(22) Choi, J.-S.; Joo, S. H. *Biomol. Ther.* **2019**, *28*, 18.

(23) Jarząb, A.; Witkowska, D.; Ziomek, E.; Setner, B.; Czajkowska, A.; Dorot, M.; Szewczuk, Z.; Gamian, A. *Vaccine* **2018**, *36*, 4641–4649.

(24) Wu, C.; Wang, H. *Chem. Bio. Chem* **2023**, *24*, e202300018.

(25) Insua, I.; Cardellini, A.; Díaz, S.; Bergueiro, J.; Capelli, R.; Pavan, G. M.; Montenegro, J. *Chem. Sci.* **2023**, *14*, 14074–14081.

(26) Song, Q.; Cheng, Z.; Kariuki, M.; Hall, S. C.; Hill, S. K.; Rho, J. Y.; Perrier, S. *Chem. Rev.* **2021**, *121*, 13936–13995.

(27) Mandal, D.; Tiwari, R. K.; Shirazi, A. N.; Oh, D.; Ye, G.; Banerjee, A.; Yadav, A.; Parang, K. *Soft Matter* **2013**, *9*, 9465–9475.

(28) Sun, L.; Fan, Z.; Wang, Y.; Huang, Y.; Schmidt, M.; Zhang, M. *Soft Matter* **2015**, *11*, 3822–3832.

(29) Shaikh, H.; Rho, J. Y.; Macdougall, L. J.; Gurnani, P.; Lunn, A. M.; Yang, J.; Huband, S.; Mansfield, E. D.; Peltier, R.; Perrier, S. *Chem. Eur. J.* **2018**, *24*, 19066–19074.

(30) Sandhu, P.; Xu, X.; Bondiskey, P. J.; Balani, S. K.; Morris, M. L.; Tang, Y. S.; Miller, A. R.; Pearson, P. G. *Antimicrob. Agents Chemother.* **2004**, *48*, 1272–1280.

(31) Dewan, V.; Liu, T.; Chen, K.-M.; Qian, Z.; Xiao, Y.; Kleiman, L.; Mahasenan, K. V.; Li, C.; Matsuo, H.; Pei, D.; Musier-Forsyth, K. *ACS Chem. Biol.* **2012**, *7*, 761–769.

(32) Garcia-Fandino, R.; Amorin, M.; Castedo, L.; Granja, J. R. *Chem. Sci.* **2012**, *3*, 3280–3285.

(33) Sánchez-Quesada, J.; Kim, H. S.; Ghadiri, M. R. *Angew. Chem., Int. Ed.* **2001**, *40*, 2503–2506.

(34) Liu, J.; Fan, J.; Tang, M.; Cen, M.; Yan, J.; Liu, Z.; Zhou, W. *J. Phys. Chem. B* **2010**, *114*, 12183–12192.

(35) Liu, J.; Fan, J.; Cen, M.; Song, X.; Liu, D.; Zhou, W.; Liu, Z.; Yan, J. *J. Chem. Inf. Model.* **2012**, *52*, 2132–2138.

(36) Yan, X.; Fan, J.; Yu, Y.; Xu, J.; Zhang, M. *J. Chem. Inf. Model.* **2015**, *55*, 998–1011.

(37) Carvajal-Diaz, J. A.; Cagin, T. *J. Phys. Chem. B* **2016**, *120*, 7872–7879.

(38) Zhang, M.; Fan, J.; Xu, J.; Weng, P.; Lin, H. *J. Mol. Model.* **2016**, *22*, 1–12.

(39) Asthagiri, D.; Bashford, D. *Biophys. J.* **2002**, *82*, 1176–1189.

(40) Jishi, R. A.; Flores, R. M.; Valderrama, M.; Lou, L.; Bragin, J. *J. Phys. Chem. A* **1998**, *102*, 9858–9862.

(41) Lewis, J. P.; Pawley, N. H.; Sankey, O. F. *J. Phys. Chem. B* **1997**, *101*, 10576–10583.

(42) Sánchez-Quesada, J.; Isler, M. P.; Ghadiri, M. R. *J. Am. Chem. Soc.* **2002**, *124*, 10004–10005.

(43) Tarek, M.; Maigret, B.; Chipot, C. *Biophys. J.* **2003**, *85*, 2287–2298.

(44) Hsieh, W.-H.; Liaw, J. *J. Food Drug Anal.* **2019**, *27*, 32–47.

(45) Hamley, I. W. *Angew. Chem. Int. Ed.* **2014**, *53*, 6866–6881.

(46) Yanlian, Y.; Ulung, K.; Xiumei, W.; Horii, A.; Yokoi, H.; Shuguang, Z. *Nano Today* **2009**, *4*, 193–210.

(47) Chapman, R.; Danial, M.; Koh, M. L.; Jolliffe, K. A.; Perrier, S. *Chem. Soc. Rev.* **2012**, *41*, 6023–6041.

(48) De Santis, P.; Morosetti, S.; Rizzo, R. *Macromolecules* **1974**, *7*, 52–58.

(49) Ghadiri, M. R.; Granja, J. R.; Milligan, R. A.; McRee, D. E.; Khazanovich, N. *Nature* **1993**, *366*, 324–327.

(50) Khazanovich, N.; Granja, J. R.; McRee, D. E.; Milligan, R. A.; Ghadiri, M. R. *J. Am. Chem. Soc.* **1994**, *116*, 6011–6012.

(51) Hartgerink, J. D.; Granja, J. R.; Milligan, R. A.; Ghadiri, M. R. *J. Am. Chem. Soc.* **1996**, *118*, 43–50.

(52) Amorín, M.; Castedo, L.; Granja, J. R. *J. Am. Chem. Soc.* **2003**, *125*, 2844–2845.

(53) Silk, M. R.; Newman, J.; Ratcliffe, J. C.; White, J. F.; Caradoc-Davies, T.; Price, J. R.; Perrier, S.; Thompson, P. E.; Chalmers, D. K. *Chem. Commun.* **2017**, *53*, 6613–6616.

(54) Seebach, D.; Matthews, J. L.; Meden, A.; Wessels, T.; Baerlocher, C.; McCusker, L. B. *Helv. Chim. Acta.* **1997**, *80*, 173–182.

(55) Van Maarseveen, J. H.; Horne, W. S.; Ghadiri, M. R. *Org. Lett.* **2005**, *7*, 4503–4506.

(56) Horne, W. S.; Wiethoff, C. M.; Cui, C.; Wilcoxen, K. M.; Amorin, M.; Ghadiri, M. R.; Nemerow, G. R. *Bioorg. Med. Chem.* **2005**, *13*, 5145–5153.

(57) Montero, A.; Gastaminza, P.; Law, M.; Cheng, G.; Chisari, F. V.; Ghadiri, M. R. *Chem. Biol.* **2011**, *18*, 1453–1462.

(58) Fernandez-Lopez, S.; Kim, H.-S.; Choi, E. C.; Delgado, M.; Granja, J. R.; Khasanov, A.; Kraehenbuehl, K.; Long, G.; Weinberger, D. A.; Wilcoxen, K. M.; Ghadiri, M. R. *Nature* **2001**, *412*, 452–455.

(59) Fletcher, J. T.; Finlay, J. A.; Callow, M. E.; Callow, J. A.; Ghadiri, M. R. *Chem.-Eur. J.* **2007**, *13*, 4008–4013.

(60) Dartois, V.; Sanchez-Quesada, J.; Cabezas, E.; Chi, E.; Dubbelde, C.; Dunn, C.; Granja, J.; Gritzen, C.; Weinberger, D.; Ghadiri, M. R.; Jr Parr, T. R. *Antimicrob. Agents Chemother.* **2005**, *49*, 3302–3310.

(61) Motiei, L.; Rahimipour, S.; Thayer, D. A.; Wong, C.-H.; Ghadiri, M. R. *Chem. Commun.* **2009**, 3693–3695.

(62) Chen, J.; Zhang, B.; Xia, F.; Xie, Y.; Jiang, S.; Su, R.; Lu, Y.; Wu, W. *Nanoscale* **2016**, *8*, 7127–7136.

(63) Wang, Y.; Yi, S.; Sun, L.; Huang, Y.; Lenaghan, S. C.; Zhang, M. *J. Biomed. Nanotechnol.* **2014**, *10*, 445–454.

(64) Blunden, B. M.; Chapman, R.; Danial, M.; Lu, H.; Jolliffe, K. A.; Perrier, S.; Stenzel, M. H. *Chem. -Eur. J.* **2014**, *20*, 12745–12749.

(65) Liu, H.; Chen, J.; Shen, Q.; Fu, W.; Wu, W. *Mol. Pharmaceutics* **2010**, *7*, 1985–1994.

(66) Vijayaraj, R.; Van Damme, S.; Bultinck, P.; Subramanian, V. *Phys. Chem. Chem. Phys.* **2013**, *15*, 1260–1270.

(67) Li, M.; Ehlers, M.; Schlesiger, S.; Zellermann, E.; Knauer, S. K.; Schmuck, C. *Angew. Chem. Int. Ed.* **2016**, *55*, 598–601.

(68) Hsieh, W.-H.; Chang, S.-F.; Chen, H.-M.; Chen, J.-H.; Liaw, J. *Mol. Pharm.* **2012**, *9*, 1231–1249.

(69) Lee, Y.-H.; Chang, S.-F.; Liaw, J. *Pharm.* **2015**, *7*, 122–136.

(70) Zheng, S.-p.; Huang, L.-b.; Sun, Z.; Barboiu, M. *Angew. Chem. Int. Ed.* **2021**, *60*, 566–597.

(71) Ghadiri, M. R.; Granja, J. R.; Buehler, L. K. *Nature* **1994**, *369*, 301–304.

(72) Montenegro, J.; Ghadiri, M. R.; Granja, J. R. *Acc. Chem. Res.* **2013**, *46*, 2955–2965.

(73) Xu, J.; Fan, J. F.; Zhang, M. M.; Weng, P. P.; Lin, H. F. *J. Mol. Model.* **2016**, *22*, 1–12.

(74) Li, H.; Fan, J. F.; Li, R.; Yu, Y.; Yan, X. L. *J. Mol. Model.* **2014**, *20*, 1–11.

(75) Dehez, F.; Tarek, M.; Chipot, C. *J. Phys. Chem. B* **2007**, *111*, 10633–10635.

(76) García-Fandiño, R.; Granja, J. R. *J. Phys. Chem. C* **2013**, *117*, 10143–10162.

(77) Shan, T.; Zhao, X.; Liang, H. *Mater. Res. Express* **2020**, *7*, 065010.

(78) Li, R.; Fan, J.; Li, H.; Yan, X.; Yu, Y. *J. Phys. Chem. B* **2013**, *117*, 14916–14927.

(79) Maroli, N.; Kolandaivel, P. *J. Biomol. Struct. Dyn.* **2020**, *38*, 186–199.

(80) Calvelo, M.; Lynch, C. I.; Granja, J. R.; Sansom, M. S. P.; Garcia-Fandiño, R. *ACS Nano* **2021**, *15*, 7053–7064.

(81) Li, R.; Fan, J.; Li, H.; Yan, X.; Yu, Y. *J. Chem. Phys.* **2015**, *143*.

(82) Khavani, M.; Izadyar, M.; Housaindokht, M. R. *J. Mol. Graph. Model.* **2017**, *71*, 28–39.

(83) Farrokhpour, H.; Mansouri, A.; Najafi Chermahini, A. *J. Phys. Chem. C* **2017**, *121*, 8165–8176.

(84) Farrokhpour, H.; Mansouri, A.; Rajabi, A. R.; Najafi Chermahini, A. *J. Biomol. Struct. Dyn.* **2019**, *37*, 691–701.

(85) Joozdani, F. A.; Taghdir, M. *J. Mol. Liq.* **2022**, *349*, 118136.

(86) Kim, N.; Lee, J. H.; Song, Y.; Lee, J.-H.; Schatz, G. C.; Hwang, H. *J. Phys. Chem. B* **2023**, *127*, 6061–6072.

(87) Ponder, J. W.; Case, D. A. *Adv. Prot. Chem.* **2003**, *66*, 27–85.

(88) Jones, J. E. *Proc. R. Soc. London, Ser. A* **1924**, *106*, 463–477.

(89) Waals, J. D., *Thermodynamische theorie der capillariteit in de onderstelling van continue dichtheidsverandering*; 8; J. Müller: 1893; Vol. 1, p 1.

(90) De Coulomb, C. A., *Collection de Mémoires relatifs a la Physique*; Gauthier-Villars: 1889; Vol. 4.

(91) Verlet, L. *Phys. Rev.* **1967**, *159*, 98–103.

(92) Hockney, R. W. *Methods Comput. Phys.* **1970**, *20*, 135–211.

(93) Swope, W. C.; Andersen, H. C.; Berens, P. H.; Wilson, K. R. *J. Chem. Phys.* **1982**, *76*, 637–649.

(94) Martínez, L.; Andrade, R.; Birgin, E. G.; Martínez, J. M. *J. Comput. Chem.* **2009**, *30*, 2157–2164.

(95) Case, D. A. et al. Amber 18., University of California: San Francisco, CA, 2018.

(96) Hünenberger, P. H. *Adv. Polym. Sci.* **2005**, 105–149.

(97) Berendsen, H. J.; Postma, J. v.; Van Gunsteren, W. F.; DiNola, A.; Haak, J. R. *J. Chem. Phys.* **1984**, *81*, 3684–3690.

(98) Åqvist, J.; Wennerström, P.; Nervall, M.; Bjelic, S.; Brandsdal, B. O. *Chem. Phys. Lett.* **2004**, *384*, 288–294.

(99) Ryckaert, J.-P.; Ciccotti, G.; Berendsen, H. J. *J. Comput. Phys.* **1977**, *23*, 327–341.

(100) Essmann, U.; Perera, L.; Berkowitz, M. L.; Darden, T.; Lee, H.; Pedersen, L. G. *J. Chem. Phys.* **1995**, *103*, 8577–8593.

(101) Roe, D. R.; Cheatham III, T. E. *J. Chem. Theory Comput.* **2013**, *9*, 3084–3095.

(102) Humphrey, W.; Dalke, A.; Schulten, K. *J. Mol. Graphics* **1996**, *14*, 33–38.

(103) Pettersen, E. F.; Goddard, T. D.; Huang, C. C.; Couch, G. S.; Greenblatt, D. M.; Meng, E. C.; Ferrin, T. E. *J. Comput. Chem.* **2004**, *25*, 1605–1612.

(104) Allen, M. P.; Tildesley, D. J., *Computer Simulation of Liquids*, 2nd; Oxford University Press: Oxford, 2017.

(105) Moral, R.; Paul, S. *Phys. Chem. Chem. Phys.* **2023**, *25*, 5406–5422.

(106) Moral, R.; Paul, S. *Langmuir* **2023**, *40*, 882–895.

(107) Stillinger, F. H. *Science* **1980**, *209*, 451–457.

(108) Luzar, A.; Chandler, D. *Nature* **1996**, *379*, 55–57.

(109) Luzar, A.; Chandler, D. *Phys. Rev. Lett.* **1996**, *76*, 928.

(110) Paul, R.; Mitra, A.; Paul, S. *J. Chem. Phys.* **2021**, *154*, 244504.

(111) Bandyopadhyay, S.; Chakraborty, S.; Bagchi, B. *J. Am. Chem. Soc.* **2005**, *127*, 16660–16667.

(112) Kirkwood, J. G.; Buff, F. P. *J. Chem. Phys.* **1951**, *19*, 774–777.

(113) Ben-Naim, A. Y., *Statistical thermodynamics for chemists and biochemists*; Springer Science & Business Media: 2013.

(114) Ben-Naim, A., *Molecular theory of solutions*; OUP Oxford: 2006.

(115) Smith, P. E. *J. Phys. Chem. B* **2006**, *110*, 2862–2868.

(116) Smith, P. E. *Biophys. J.* **2006**, *91*, 849–856.

(117) Matteoli, E.; Mansoori, G. A., *Fluctuation theory of mixtures*; Taylor & Francis New York: 1990.

(118) Devi, M.; Paul, S. *Phys. Chem. Chem. Phys.* **2022**, *24*, 14452–14471.

(119) Miller III, B. R.; McGee Jr, T. D.; Swails, J. M.; Homeyer, N.; Gohlke, H.; Roitberg, A. E. *J. Chem. Theory Comput.* **2012**, *8*, 3314–3321.

(120) Hou, T.; Wang, J.; Li, Y.; Wang, W. *J. Chem. Inf. Model.* **2011**, *51*, 69–82.

(121) Vijayaraj, R.; Van Damme, S.; Bultinck, P.; Subramanian, V. *Phys. Chem. Chem. Phys.* **2012**, *14*, 15135–15144.

(122) Roy, R.; Paul, S. *J. Phys. Chem. B* **2020**, *124*, 10913–10929.

(123) Weiser, J.; Shenkin, P. S.; Still, W. C. *J. Comput. Chem.* **1999**, *20*, 217–230.

(124) Devi, M.; Paul, S. *ACS Chem. Neurosci.* **2024**, *15*, 3202.

Chapter 2

Self-Assembly of Cyclic Peptides in Water: Influence of Salt Concentration and Temperature

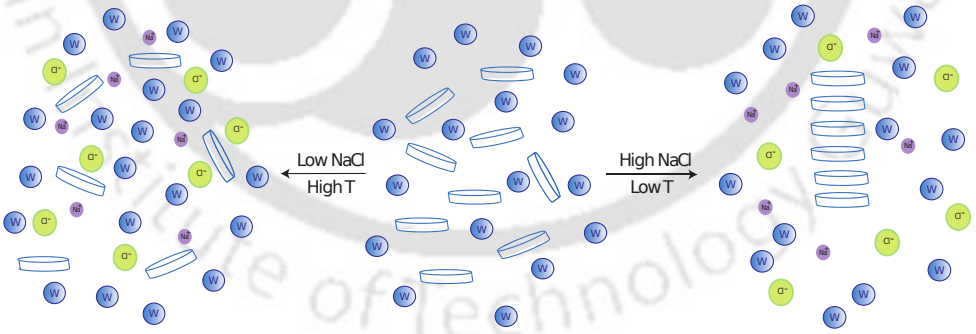

Overview

It is found in the literature that the cyclic peptides (CPs) possess the property to self-assemble in water to form cyclic peptide nanotubes (CPNTs) and are used extensively in the field of nanotechnology. Several factors influence the formation and stability of these nanotubes in water. However, an extensive study of the contribution of several important factors is still lacking. The purpose of this study is to explore the importance of temperature and salt (NaCl) on the association tendency of CPs. Furthermore, the self-association behavior of CPs in aqueous solutions at various temperatures are also thoroughly discussed. Cyclo-[(Asp-D-Leu-Lys-D-Leu)$_2$] is considered for this study and a series of classical molecular dynamics (MD) simulations at three different temperatures, viz. 280 K, 300 K, and 320 K, both in pure water and in various concentrations of NaCl salt are carried out. The calculations of radial distribution functions, preferential interaction parameters, cluster formation and hydrogen bonding properties suggest a strong dependence of NaCl concentration in the association propensity of CPs. Low NaCl concentration hinders CP association while high NaCl concentration facilitates the association of CPs. Besides this, the association of CPs is found to be enhanced at low temperature. Furthermore, the thermodynamics of CP association is predominantly found to be enthalpy driven in both presence and absence of salt. No crossover between enthalpy and entropy in CP association is observed. In addition, the MM-GBSA method is used to investigate the binding free energies of the CP rings that self-assembled to form nanotube like structures at all three temperatures.

2.1 Introduction

As discussed in Chapter 1, cyclic peptide nanotubes (CPNTs) are a class of supramolecular architectures formed through the spontaneous stacking of cyclic peptides (CPs) via parallel or antiparallel hydrogen bonding. Their hollow tubular structure, structural rigidity, and tunable internal environment make them attractive candidates for a wide range of applications in the field of therapeutics[1–6], agricultural sector[7], diagnostics[8], ion channels[9–15]etc. The first structure of the self-assembled cyclic peptide nanotube (CPNT) was reported by Ghadiri *et. al.* in the year 1993[16]. They observed that, on protonation, CPs containing eight amino acid sequences in each unit, crystallized to form tubular structures of length up to hundreds of nanometers, having diameters of 7-8 Å . Subsequently, numerous investigations were carried out to elucidate the design and synthesis of CPNTs[17–20].

Although a plethora of studies on the application of CPNTs have been reported in recent times[21], a thorough investigation of the peptide self-assembly mechanisms remains lacking. There are several factors that can affect the molecular behavior of the cyclic peptides in solution. Some of these physicochemical factors include: (i) amino acid sequence of the cyclic peptide subunit; (ii) concentration of the cyclic peptide subunit; (iii) role of temperature; (iv) pH; (v) nature of the solvent; (vi) effect of salt, etc. Out of these factors, effects of amino acid sequence[22, 23] and solvent polarity[23–25] on the stability of CPNTs were studied by various scientists. The CPNTs composed of non-polar amino acid residues were found to be highly stable in aqueous medium in comparison to polar amino acid chains[22]. Moreover, the stacking of multiple CPs provides higher mechanical stability to the self-assembled CPNTs[24].

It is well-known that the presence of salt in aqueous solution containing peptide and proteins also alter the behavior of peptide and protein aggregation[26–28]. For example, ionic salts can affect the solubility of peptides and proteins, thus inducing the process of salting peptides and proteins in and out of solutions[26, 29]. The effect of ions was ordered by Hofmeister and his coworkers in a series which is popularly known as 'Hofmeister series'[30]. The series was arranged according to their ability to aggregate the protein (salting-out) or to increase the solubility of the protein (salting-in) in solution. The study of the influence of salt ions on the self-association of biological molecules is pivotal because

salt ions are a necessary element of all living organisms. In fact, the study of formation of specific structures or conformation of biological macromolecules is technically incomplete without considering the ionic environment in water[31]. Pritzker and Chen investigated the effect of NaCl on the self-assembly of an ionic-complimentary peptide EAK 16-II and discovered that as salt concentration rises below a critical self-assembly concentration, the radius of the peptide fibrils formed enhanced[29]. On the other hand, Ghosh and her team studied the effect of three chloride salts with different cations on the aggregation propensity of a charged hexapeptide VEALYL in water. They discovered that adding NaCl to the aqueous peptide solution caused the largest aggregate to form when compared to the other salt systems, KCl and $MgCl_2$[32]. In addition to salt, peptide assembly is a spontaneous process governed by thermodynamics and kinetics based on various intermolecular non-covalent interactions. These interactions can be hydrogen bonding, π-π stacking, van der Waals, electrostatic and hydrophobic interactions[33]. Out of these, hydrogen-bonding and hydrophobic interactions are dependent on temperature. It is reported that high temperatures may break the intermolecular hydrogen bonds but at the same time can increase the hydrophobic effect[33]. Again, from a thermodynamic standpoint, the contribution of enthalpy and entropy to peptide self-association is a matter of discussion. Since enthalpy and entropy are largely governed by temperature, the thermodynamics stability of peptide self-assembly is assumed to be predominantly influenced by temperature. As a matter of fact, in addition to salt, temperature plays a key role in the self-association of cyclic peptides. However, a detailed study of the influence of these two prime factors on the formation of CPNTs still remains unexplored; that is one of the prime interests of the current manuscript. In addition, we focus to unveil the entropy and enthalpy contributed free energy of association that can further guide the cyclic peptides to nanotubes formation.

In this chapter, the effect of NaCl salt on the association propensity of (D$\underline{\text{L}}$K$\underline{\text{L}}$)$_2$ cyclic peptide with varying salt concentration is explored. Further, the influence of temperature on the self-assembly of (D$\underline{\text{L}}$K$\underline{\text{L}}$)$_2$ that results in the formation of nanotubes like structures is studied. We choose this particular cyclic peptide because (D$\underline{\text{L}}$K$\underline{\text{L}}$)$_2$ is well reported to form nanotubes in water with antiparallel stacking[34]. The cyclic peptide (D$\underline{\text{L}}$K$\underline{\text{L}}$)$_2$ *i.e* cyclo[(Asp-D-Leu-Lys-D-Leu)$_2$] comprises of both hydrophilic and hydrophobic amino acid side chains in alternating positions (Figure 2.1) which is suggested in studies to enhance the stability of the nanotubes formed in polar solvents[24]. Our study begins by

examining the effect of NaCl on the association behavior of cyclic peptides at 300 K. This is done by varying the concentration of NaCl from a lower to a moderately higher one. We subsequently proceed to investigate the effect of temperature on cyclic peptide association both in pure water and in the presence of NaCl. For that, we consider three temperatures, viz. 280 K, 300 K, and 320 K. Finally, we provided a comprehensive comparative study of the free energies of binding of the CP rings that self-assembled leading to the formation of nanotube like structures at different temperatures.

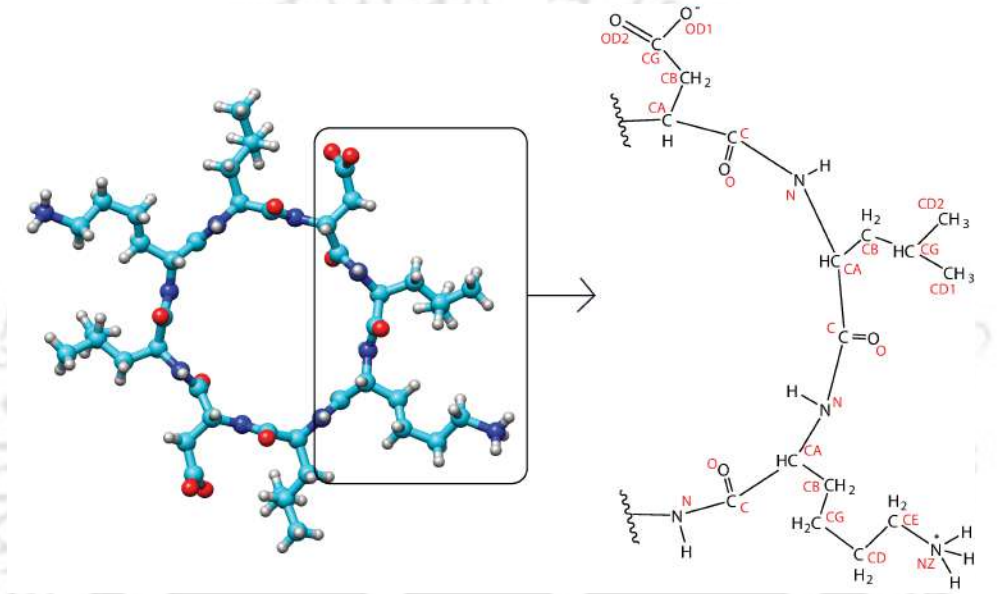

Figure. 2.1: *Molecular Structure of cyclo[(Asp-D-Leu-Lys-D-Leu)]$_2$. The atom namings are provided in red for all the three amino acid side chains along with the backbone atoms of the cyclic peptide. The naming of H-atoms are omitted for visual clarity.*

2.2 Materials and Methods

2.2.1 System Setup

The initial crystal structure of cyclo-[(Asp-D-Leu-Lys-D-Leu)$_2$] was taken from Cambridge Crystallographic Data Centre (CCDC Deposition Number: 1520676)[34]. The Na^+ and Cl^- ions were added by the LEAP module of Amber18 package[35]. The three-point transferable intermolecular potential (TIP3P)[36] model for water was used for all the simulations. The ff14SB Force Field[37] was employed for cyclic peptide. For Na^+ and Cl^- ions, the force field parameters developed by Li, Merz, and co-workers[38] were

considered. The initial configurations of all the systems used in this study were prepared using the PACKMOL program[39]. For all simulations, the molecules are packed in a cubic box. As we aim to observe the effect of salt ions and temperature on self-association of CPs, therefore the concentration of CPs was chosen to facilitate the formation of CPNTs. In order to explore the behavior of salt ions in varied concentrations, we used three distinct concentrations of NaCl ranging from a lower to a much greater value. The detailed information of all the systems considered for our investigation is summarized in Table 2.1. Note that, the concentrations of NaCl and the cyclic peptide in different systems were expressed in molality. This was done to ensure that the concentrations of the various species were the same at all three temperatures.

Table. 2.1: *The table below contains the necessary information for all of the systems considered in the study. Here, N_{CP}, N_{Wat} and N_{NaCl} represent the number of cyclic peptide [(D$\underline{L}$K$\underline{L}$)$_2$], water molecules (TIP3P), and NaCl molecules in the systems respectively. C_{NaCl} and C_{CP} denote the concentrations of cyclic peptide and NaCl in different systems (expressed in molality).*

T(K)	System	N_{CP}	N_{Wat}	N_{NaCl}	Final Box Length (Å)	C_{NaCl}(m)	C_{CP}(m)
280	A0	90	5000	0	63.317	0	1.0
	A1	90	5000	62	63.543	0.68	1.0
	A2	90	5000	308	64.860	3.42	1.0
	A3	90	5000	658	65.523	7.31	1.0
300	B0	90	5000	0	63.605	0	1.0
	B1	90	5000	62	63.884	0.68	1.0
	B2	90	5000	308	64.594	3.42	1.0
	B3	90	5000	658	65.671	7.31	1.0
320	C0	90	5000	0	63.934	0	1.0
	C1	90	5000	62	64.180	0.68	1.0
	C2	90	5000	308	64.915	3.42	1.0
	C3	90	5000	658	66.082	7.31	1.0

2.2.2 Simulation Protocols

Initially, a series of MD simulations of cyclic peptides in pure water and at various aqueous NaCl concentrations (Table 2.1) were carried out at all three different temperatures. The cyclic peptide rings were placed randomly in the simulation box alongwith water molecules. All the simulations were performed adopting periodic boundary conditions (PBC) in all three directions in order to remove the edge effect. To attain a reasonable initial structure and to remove unfavorable contacts, minimization of all the

systems were carried out for 10000 steps (in the SANDER module of AMBER18) using 5000 steps in steepest descent method followed by 5000 steps in conjugate gradient method. After that, each system was heated gradually from 0 K to the desired temperature for a total of 150 ps in canonical ensemble (NVT), succeeded by equilibration at that temperature for 1 ns. Subsequently, the systems were run for 4 ns in an NPT (isothermal-isobaric) ensemble by targeting the desired temperature and pressure of 1.0 atm using the Langevin thermostat[40] with a collision frequency of 1 ps and Berendsen barostat[41] with a pressure relaxation time of 2 ps. The covalent bonds involving the hydrogen atoms were constrained or fixed without affecting the other degrees of freedom by employing the SHAKE algorithm[42]. Simulations were performed using a timestep of 2 fs and all short-ranged non-bonded interactions were restricted within a cut-off distance of 10.0 Å . The Particle Mesh ewald (PME)[43] method was employed to estimate the long-ranged electrostatic interactions. Finally, productive MD runs were performed for 500 ns for each system in NPT ensemble at the desired temperature and pressure of 1 atm.

2.2.3 Simulation Analysis

For analyzing the trajectories, CPPTRAJ[44] module of Amber18 package was used whenever required. The rest of the analyses were done using some in-house FORTRAN 95 codes. Visual Molecular Dynamics (VMD)[45] and UCSF-Chimera[46] were used for visualization purposes. Majority of the analyses were carried out over the entire 500 ns trajectory of the systems except for calculating dynamics of hydrogen bonding and binding energies of the CP rings. The structural properties of the CP association were discussed first, followed by hydrogen bond properties. Following that, we went over the thermodynamics of CP ring association in depth. We concluded our discussion by calculating the free energy of CP ring binding. The following section and subsections of the paper provided a thorough explanation of all of the analysis techniques and their results.

2.3 Results and Discussions

The formation of CPNT like structures by self-association of cyclic peptides in pure water systems (A0, B0, and C0) and in highest salt concentration systems (A3, B3, and C3) at all three temperatures are shown in Figure 2.2. Here, the self-assembly of at least four CP rings are highlighted. It is clear from the snapshots that as the temperature rises, the probability of self-assembly of CP rings decreases in both the presence and absence of salt. The self-association of CPs to form nanotube like structures in pure water systems is highest at 280 K, followed by 300 K. At 320 K, the stacking of CP rings that leads to the creation of nanotubes is not as apparent. The same pattern is observed in the presence of NaCl. At all three temperatures, however, the addition of salt stimulates the self-assembly of CP rings. Again, to gain insight into the formation of these nanotube like structures, snapshots of the systems A3, B3, and C3 at different time frames are shown in Figure 2.3. The figure shows that the CP rings are initially randomly distributed in the box and gradually some of them self-assembled over the course of the simulation. The nanotube-like assembly remains stable at 280 K throughout the simulation time. However, the self-assembly CPNT is less stable at 300 K, and the nanotube structure tends to break after 200 ns. The stability of the nanotube structure is very low at high temperatures (320 K), and self-assembly is not properly formed. Although the snapshots provide a preliminary understanding of the behavior of CP rings in the presence and absence of NaCl at different temperatures, it is essential to elucidate the modulation of NaCl towards the association of CPs to the formation of CPNTs at different temperatures in detail. For this reason, the current section is divided into several subsections in which we explain each analysis and its result exhaustively.

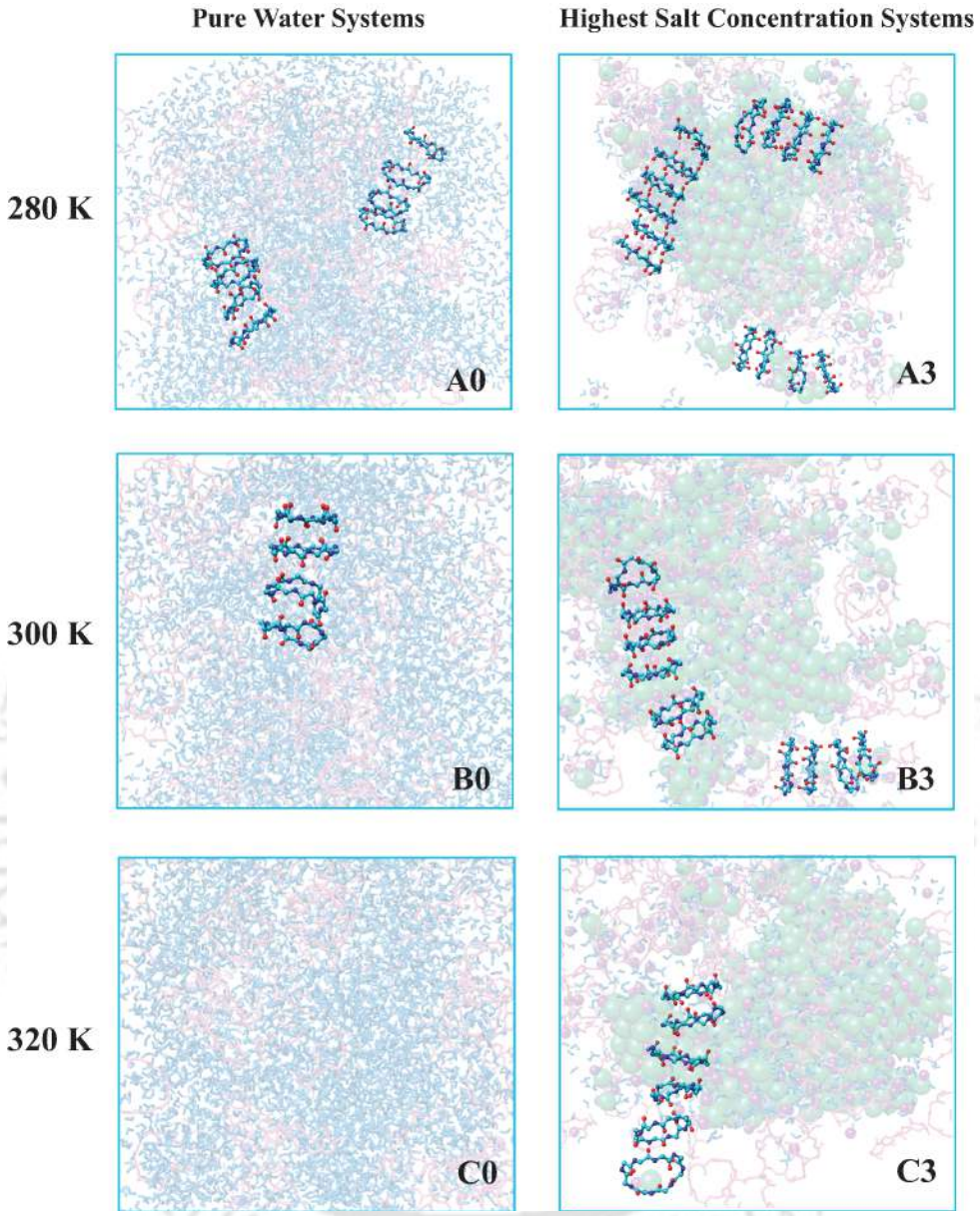

Figure. 2.2: *Snapshots showing the self-assembly of CP rings in pure water systems (A0, B0, and C0) and highest salt concentration systems (A3, B3, and C3) at three temperatures viz. 280 K, 300 K, and 320K.*

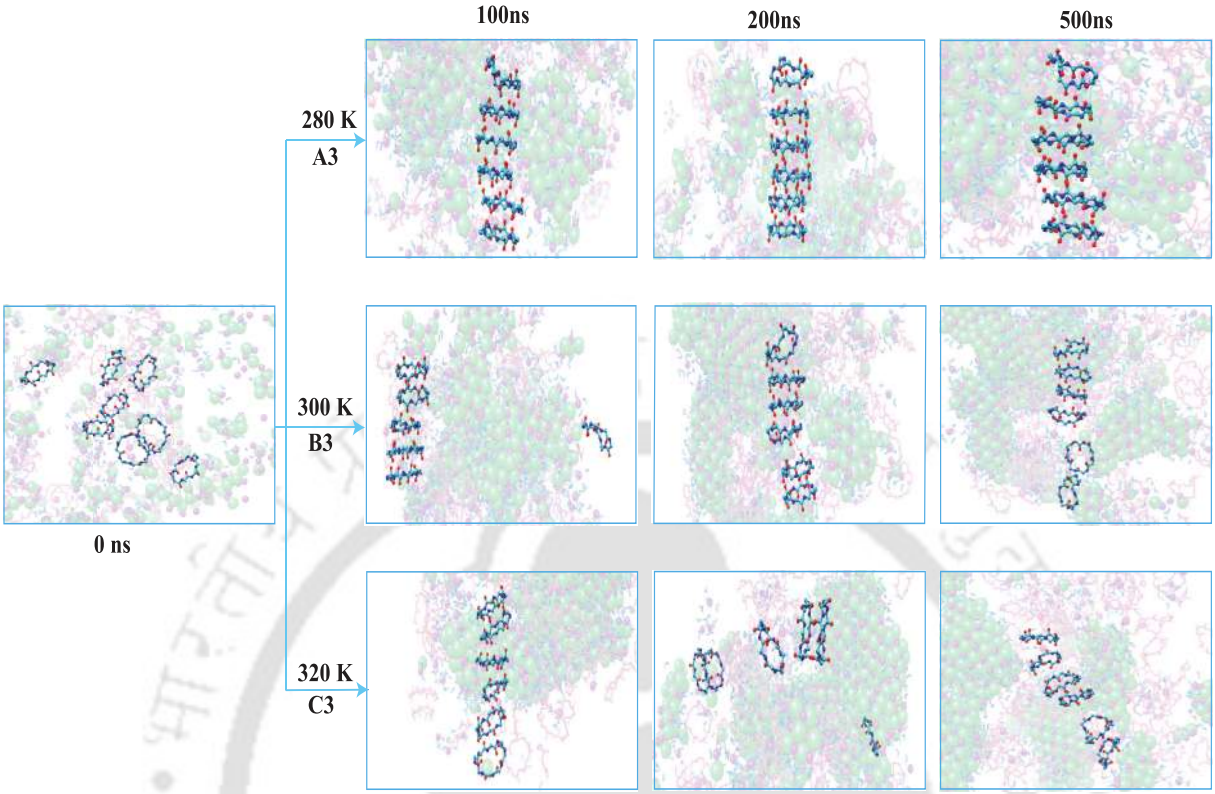

Figure. 2.3: *Snapshots of cyclic peptide nanotube (CPNT) like structures formed in the systems (A3, B3, C3) at 280 K, 300 K, and 320 K at 0ns, 100ns, 200ns, and 500ns respectively.*

2.3.1 Radial Distribution Functions

To understand the role of salt and temperature on the self-association of CPs, we thoroughly studied the intermolecular interactions of CP molecules as well as their interactions with water and with the ions (Na^+ and Cl^-). The radial distribution function (rdf), a useful tool for defining the average structure of molecules assembled around a reference molecule, is employed for this purpose[47, 48].

Effect of Salt (NaCl)

Figure 2.4(a) shows the rdfs of CP around a reference CP molecule at 300 K for B0, B1, B2 and B4 systems. For this, we have considered center of mass of each CP. Further, we have presented schematic diagrams (Figure 2.4 (b) and (c)) explaining the probable

mechanisms behind the trend of the distribution curves.

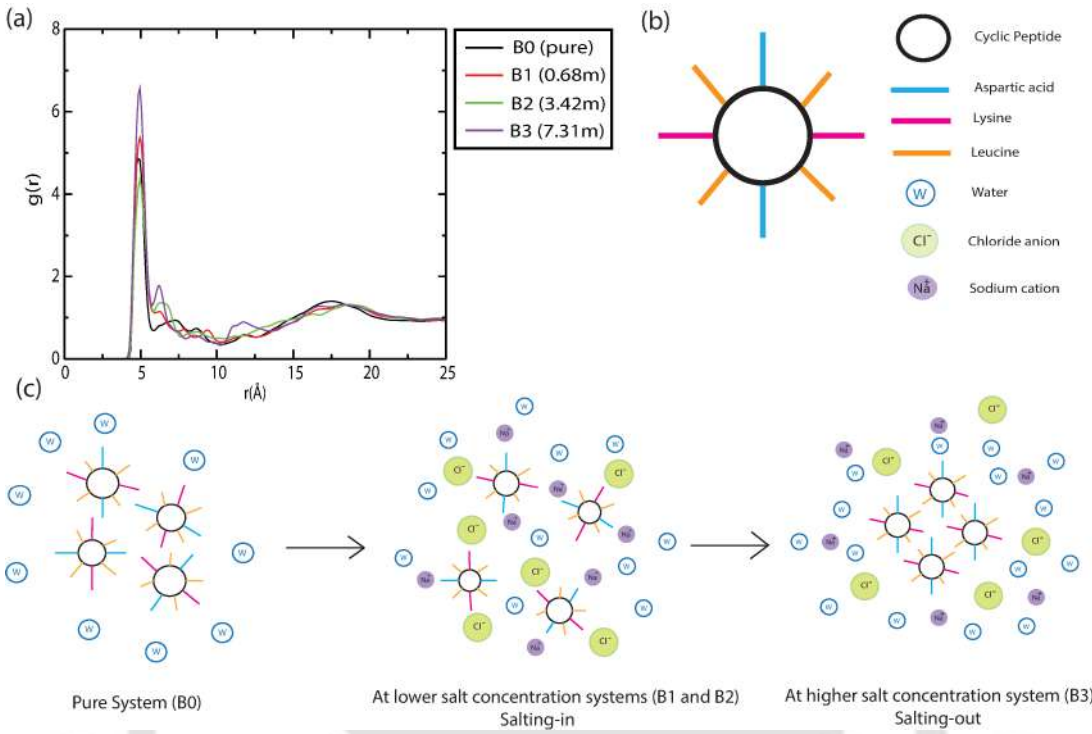

Figure. 2.4: *(a) Radial distribution functions of CP around a reference CP molecule at 300 K calculated using center of mass of CP. (b) the schematic representation of all the species present in the systems B0-B3, (c) the schematic representation of salting in and salting out mechanisms in the systems B0-B3.*

The first peak (Figure 2.4(a)), observed at a distance range of 4.85-4.95 Å signifies the interaction between different CPs molecules present in the first co-ordination shell of a reference CP molecule. It is intriguing to observe that on addition of salt, the height of the first peak of g(r) changes although the concentration of CP remains the same for all the systems. For lower salt concentration *i.e.* for B1 system, the first peak height is more that for the pure system, B0 . However, the peak height decreases for B2 system and again increases for B3 system (Figure 2.4(a)). One possible explanation for this trend can be that on addition of small amount of salt (B1 system), the salt ions mask charged sites of few CP rings. As a result, the remaining CPs tend to aggregate a little as the solvent around them is hydrophilic (water). On further addition of salt (B2 system), the salt ions mask the charged sites of almost all the CPs (Figure 2.4(c)). Now, the water molecules create a hydration shell around the CP molecules which results in increased solubility of the CPs in water. This leads to a decrease in peptide-peptide interactions and the phenomenon responsible for this is known as the salting-in effect[49, 50] as shown

in Figure 2.4(c). However, on increasing salt concentration further (B3 system), the additional salt ions interact more with water. This results in less availability of solvent (water) for interaction with peptides as the number of water molecules remains constant throughout. This ultimately leads to the increased intermolecular interaction of CPs resulting in more association of CPs. This phenomenon of salting-out is indicated by a higher first peak height of the distribution function[49] (Figure 2.4(a) inset). Additionally, for B3 system, several consecutive peaks of low intensities are observed at higher r-values which attribute to strong CP-CP correlations in this system. Apart from the first peak, the first minimum also holds significance in the study of the association of molecules. The first minimum of the distribution function has been reported to correspond to the ordered arrangement of solute molecules in the second solvation shell[51]. Furthermore, the second peak (Figure 2.4(a)) which corresponds to the probability of the number of solute molecules in the second solvation shell, shifts to a shorter distance as we move from systems B0 to B3 which suggests that the CP-CP association becomes more compact as the salt concentration increases. Almost similar results are obtained for the rdfs of CP around CP at 280 K and 320 K (Figure 2.5(a and b)). At lower salt concentrations [(A1, A2) and (C1, C2)], the 1st peak height of the rdfs remains almost same or a minor change from that of pure systems at that respective temperatures (A0 and C0) indicating fewer association of CPs. On the other hand, at higher NaCl concentrations (A3 and C3) the 1st peak height increases significantly for both the temperatures implying high association of CP molecules.

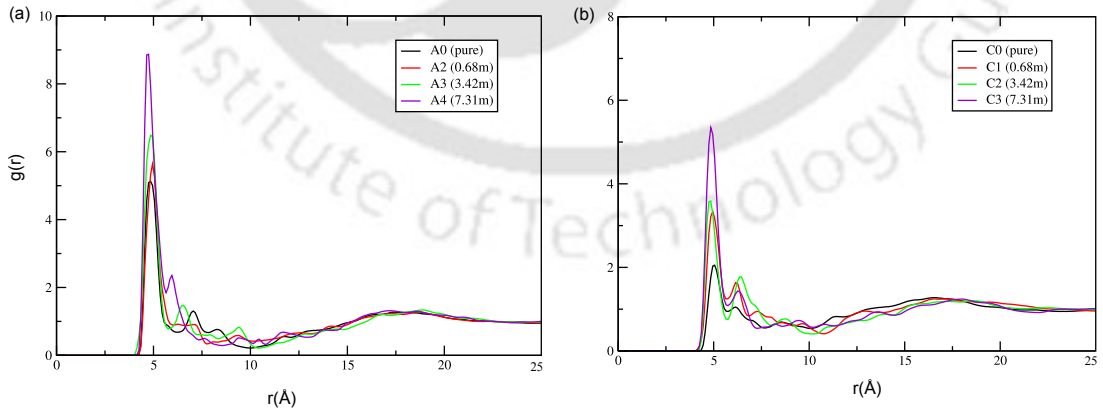

Figure. 2.5: *Radial distribution functions of CP around a reference CP molecule calculated using center of mass of CP at (a) 280 K and (b) 320 K.*

To support the above explanation, we further computed the distribution functions of

Na^+ and Cl^- around the hydrophilic amino acid side chains of the CP molecule at 300 K. For this, OD1 atom of aspartic acid side chain and NZ atom of lysine are considered (Figure 2.1). From the first and second peak heights in Figure 2.6(a) it can be seen that the interaction of Na^+ with the OD1 atom of aspartic acid decreases gradually as the concentration of NaCl rises. This implies that on increasing salt concentration, the cations tend to interact more with water molecules. However, the distribution trend of Cl^- around NZ atom of lysine (Figure 2.6(b)) is different. The interaction of anion is more with the NZ atom in the B2 system followed by B3 and then B1. This is because at lower salt concentrations, anions (Cl^-) surround or mask the charged atom of NZ, and this masking is more pronounced in the system B2. The second peak around 5.30-5.40 Å for B1 system implies the second co-ordination shell formation around NZ atom whereas for B2 and B3 system, it appears at 6.65 Å and 6.75 Å respectively. The formation of the second co-ordination shell of NZ atom for B2 and B3 systems is at a greater distance due to more hydration around the charged lysine sites.

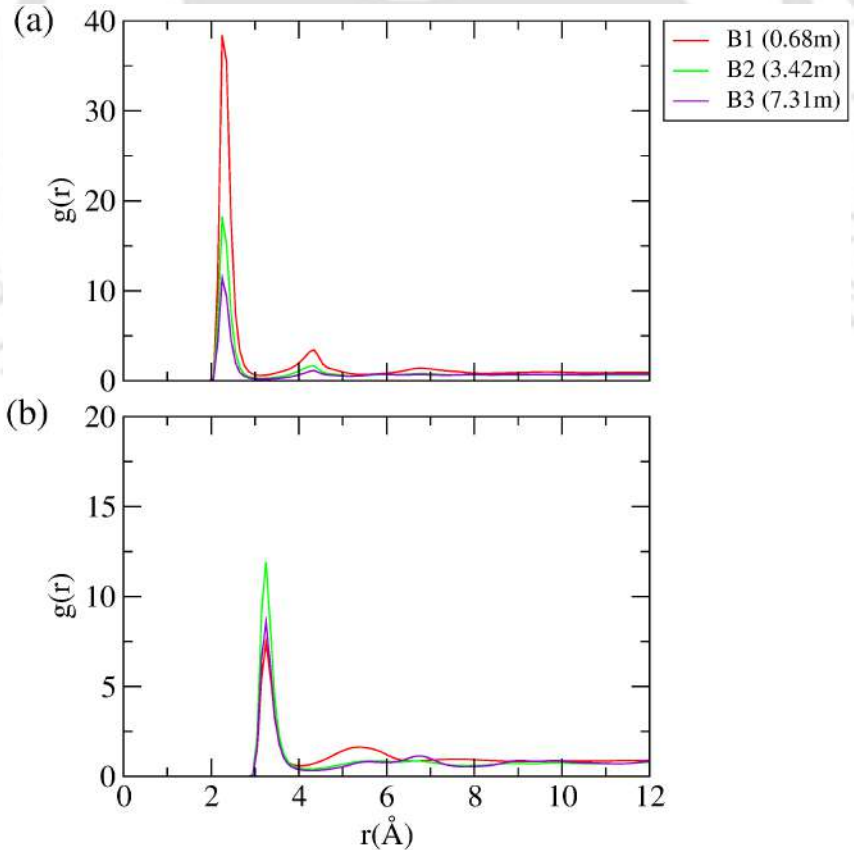

Figure. 2.6: *Site-site radial distribution functions of ions around selective atomic sites of cyclic peptide for the systems B1-B3 at 300 K. (a) Na^+ around OD1 atom of CP, (b) Cl^- around NZ atom of CP.*

In addition to that, different types of amino acids present in the CP molecule exhibit different hydration patterns around themselves. As discussed in Section 1, the cyclic peptide (D$\underline{\text{L}}$K$\underline{\text{L}}$)$_2$ contains aspartic acid and lysine which are hydrophilic, and leucine which is hydrophobic in nature. So, to get an insight into the behavior of water around different types of amino acids, the distribution functions of oxygen atom of water around different sites of amino acid side chains are evaluated and they are depicted in Figure 2.7. The appearance of the first peaks at 2.65 Å and 2.85 Å in Figure 2.7(a) and 2.7(b) respectively, indicate the presence of strong hydrogen bonding interactions between water molecules and the charged sites of the CP molecules. It is to be noted that, with increasing salt concentration, there is a decrease in the first peak height which implies that interaction between water molecules and charged sites decreases with increasing NaCl concentration. Coming to Figure 2.7(c), the peak at 3.75 Å suggests well defined arrangement of water surrounding the methyl residues of leucine side chain in the first hydration shell. The trend of the first peak height reveals that the access of the non-polar hydrophobic leucine side chains to the solvent increases with increasing salt concentrations. Thus, it can be speculated that the electrostatic interactions between the hydrophilic sites of CPs and water molecules in presence of salt ions drive the association of CPs[52].

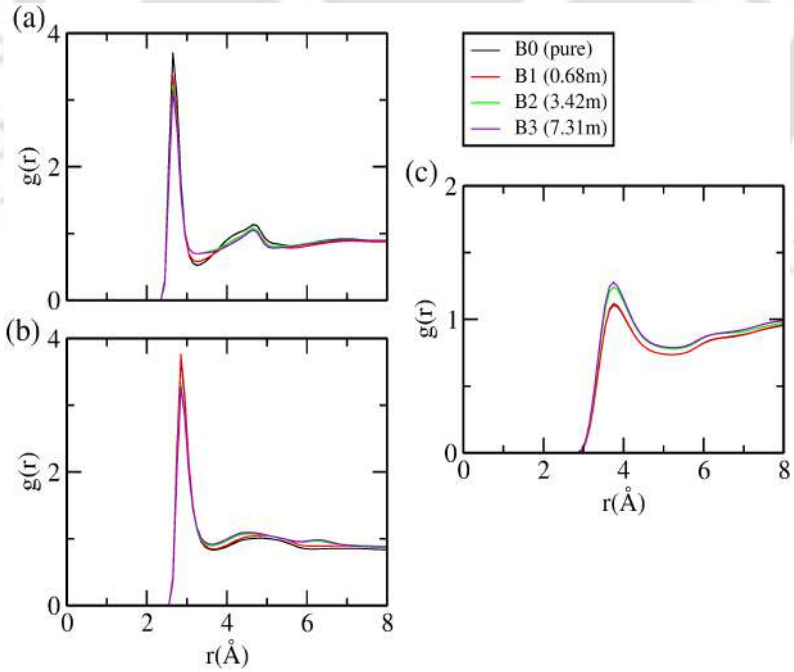

Figure. 2.7: *Site-site radial distribution function of (a) water around OD1 (hydrophilic) atom of CP , (b) water around NZ (hydrophilic) atom of CP, and (c) water around CD2 (hydrophobic) atom of CP for all the systems B0-B3 at 300 K.*

Effect of Temperature

To study the influence of temperature at the molecular level, we have computed the rdfs of CP-CP molecules that involve the center of masses of the peptides for both pure water and the highest salt concentration (7.31m of NaCl) systems at three different temperatures (Figure 2.8).

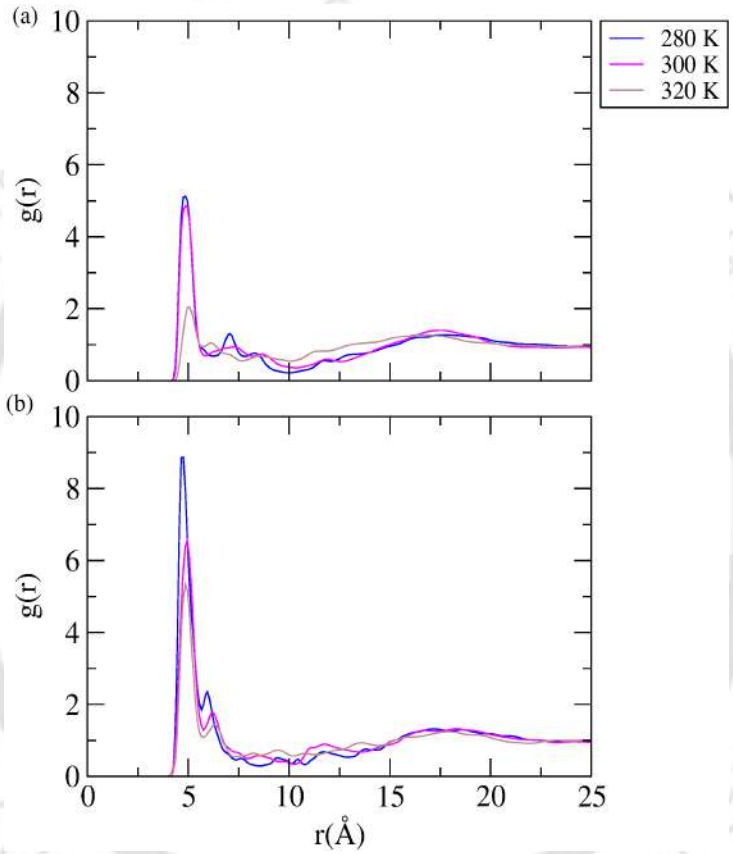

Figure. 2.8: *Radial distribution functions (rdfs) of CPs around CPs for (a) pure systems (A0, B0, C0) and (b) salt systems (A3, B3, C3) at 280 K, 300 K, and 320 K. Here, the center of mass of CP is used to calculate rdf plots.*

It can be seen that the first peak appears within the range of 4.85-4.95 Å which suggests the aggregation tendency of the CPs. However, as temperature rises, the peak height decreases both in the presence and absence of salt. This indicates that the tendency of association of CP molecules decreases as we raise the temperature. A distinct second peak at 7.05 Å is observed for pure water system at 280 K but is not so prominent at both 300 K and 320 K. However, for the salt systems, a noticable second peak is present at all the temperatures suggesting the formation of well-defined second solvation shell in

presence of salt. For all temperatures, the peak height is greater for salt systems than for pure water systems, indicating higher aggregation in the presence of salt.

2.3.2 Coordination Number Analysis

The radial distribution functions provide information about the distribution of various species around a reference atom. In this section, we evaluate the number of solvent molecules (water in this case) present in the first hydration shell of various atomic sites of a reference CP molecule in order to gain insight into its solvation pattern. The first minima of the corresponding rdfs, g(r), are used to accomplish this. Then, using the following equation, we calculate the coordination number values around each atomic site of interest:[53, 54]

$$\eta_{\alpha\beta} = 4\pi\rho_{\beta}\int_{r_1}^{r_2} r^2 g_{\alpha\beta}(r)dr \tag{2.1}$$

In equation (1), the number of atoms of type β that surrounds the atom of type α is denoted by $\eta_{\alpha\beta}$. Both types of atoms are assumed to be present in a shell of radius extending from r_1 to r_2 having a number density of ρ_{β} in the system. Now, for the evaluation of the first shell coordination number, the value of r_1 will be zero and that of r_2 will be considered from the distance of the first minimum of the respective radial distribution function plot. Table 2.2 reports the first shell hydration number (coordination number) values of different atomic sites of CP at 300 K calculated using the above equation. Furthermore, the hydration number values are normalized to the volume of the pure CP-water (B0) system's box, and they are shown in parentheses of the same table. This is done to represent the reduction of number density of solvent (water in this case) in salt solutions as the volume of the simulation box is not same for all the systems [see Table 2.1]. It is seen from the table that with the addition of salt, the hydration number values are decreased for the hydrophilic sites *i.e* for OD1 and NZ atoms. This indicates the elimination of water molecules from the first hydration shell because of the association of the CP molecules. For the hydrophobic sites (CG and CD2), there is almost no change in the number of water molecules in the first hydration shell with the addition of salt. Nevertheless, for both hydrophilic and hydrophobic sites, the difference in the number of first hydration shell water molecules (calculated from equation 2.1) from the expected

values (calculated from the normalized number density) increases as salt concentration increases. It is to be noted that hydrophobic sites appear to be more hydrated than hydrophilic sites.

Table. 2.2: *Co-ordination (hydration) number around different hydrophilic and hydrophobic atomic sites of CP molecule in the considered systems at 300 K. The normalized values of hydration numbers are presented in parenthesis for each site.*

Systems	OD1	NZ	CG	CD2
B0	2.77	3.66	5.18	5.08
B1	2.58(2.60)	3.63(3.62)	5.13(5.18)	5.03(5.07)
B2	2.42(2.53)	3.26(3.41)	5.40(5.65)	5.31(5.56)
B3	2.25(2.47)	3.03(3.33)	5.23(5.75)	5.13(5.64)

Similar results are obtained from the systems at 280 K (Table 2.3) and 320 K (Table 2.4). The reason for this could be that strong electrostatic interactions between interfacial water molecules near hydrophilic sites disrupt their tetrahedral structures, resulting in fewer water molecules near those sites. Weak surface-water interactions of hydrophobic sites, on the other hand, result in less perturbation of hydrogen bonds between water, resulting in less randomization and reorientation of solvent molecules near those sites. In turn, this causes the formation of a caging network around the hydrophobic groups. As a result, the water density around the hydrophobic sites is relatively higher[55].

Table. 2.3: *Co-ordination (hydration) number around different hydrophilic and hydrophobic atomic sites of CP molecule in the considered systems at 280 K. The normalized values of hydration numbers are presented in parenthesis for each site*

System	OD1	NZ	CG	CD2
A0	2.85	3.92	5.73	5.63
A1	2.61 (3.01)	3.79 (4.29)	5.60 (6.14)	5.56 (6.17)
A2	2.29 (2.56)	3.42 (3.82)	5.41 (5.97)	5.29 (5.84)
A3	2.12 (2.33)	3.29 (3.61)	5.14 (5.62)	5.02 (5.60)

Table. 2.4: *Co-ordination (hydration) number around different hydrophilic and hydrophobic atomic sites of CP molecule in the considered systems at 320 K. The normalized values of hydration numbers are presented in parenthesis for each site.*

System	OD1	NZ	CG	CD2
C0	2.71	3.51	4.89	4.81
C1	2.30 (2.56)	3.49 (3.82)	4.87 (5.37)	4.82 (5.31)
C2	2.17 (2.34)	3.31 (3.66)	5.10 (5.63)	5.05 (5.58)
C3	2.32 (2.59)	3.43 (3.80)	5.33 (5.88)	5.31 (5.87)

The co-ordination number of CP around CP molecules are also evaluated and plotted with respect to simulation time (Figure 2.9) for all the systems at 300 K. From the graph we can state that at highest salt concentration (B3), the number of CP molecules present in the first co-ordination shell of a CP molecule is highest indicating high association of CP molecules in B3 system. It is followed by B1, B2, and B0 systems where the coordination number values are almost similar.

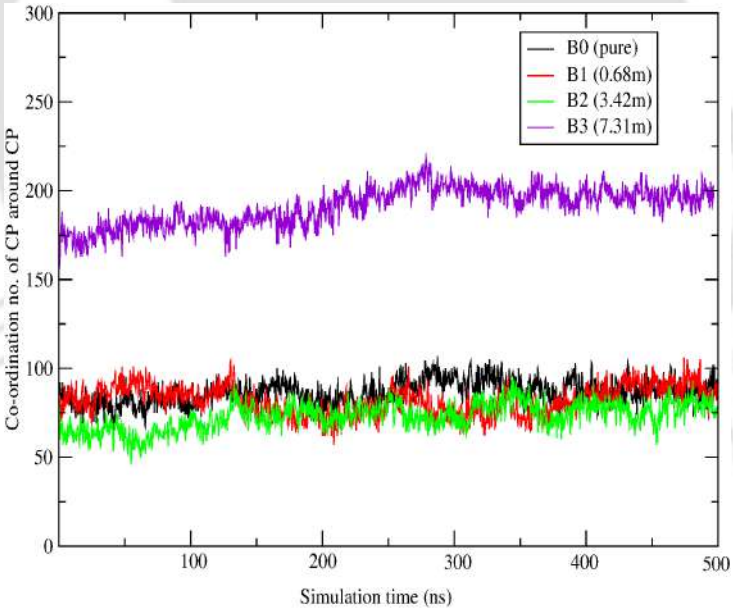

Figure. 2.9: *The co-ordination number of CP around CP molecules versus simulation time for the systems B0, B1, B2, and B3 at 300 K.*

2.3.3 Spacial Density Functions

To substantiate the aforementioned results, we generated the spatial density functions (SDFs) using the TRAVIS software package [56]. The SDF, $g(\mathbf{r})$, represents the normalized local number density of solvent or solute molecules around a reference molecule and is defined as[57]:

$$g(\mathbf{r}) = \frac{\rho(\mathbf{r})}{\rho_0},$$

where $\rho(\mathbf{r})$ is the local number density at position $\mathbf{r}$ and ρ_0 is the bulk number density. These density plots reveal the three-dimensional probabilistic arrangement of molecules around a reference molecule in the system. Accordingly, SDFs provide valuable insights into the structural organization and preferential orientations of molecules, making them a powerful tool for visualizing the distribution of cyclic peptides (CPs) at different temperatures. Figure 2.10 presents representative spatial density maps of CP molecules within the solvation shell of a reference CP at an isovalue of 0.8, for both pure water systems and the systems with the highest salt concentration at all three temperatures. As one continuously moves from lower to higher temperature, the distribution of density of CP molecules around the reference CP gradually reduces. The trend is similar for both pure water systems (A0, B0, C0) and salt solution systems (A3, B3, C3). Based on these findings, it is clear that the aggregation or self-association property of CPs decreases with increasing temperature. Additionally, one can observe a significant rise in density distribution of CP around CP in the salt systems with respect to its pure water counterparts at 280 K and 300 K. However, for 320 K, there is no such prominent difference in density maps in C0 and C3 systems which indicates the marginal influence of salt in the aggregation tendency of CPs at higher temperature.

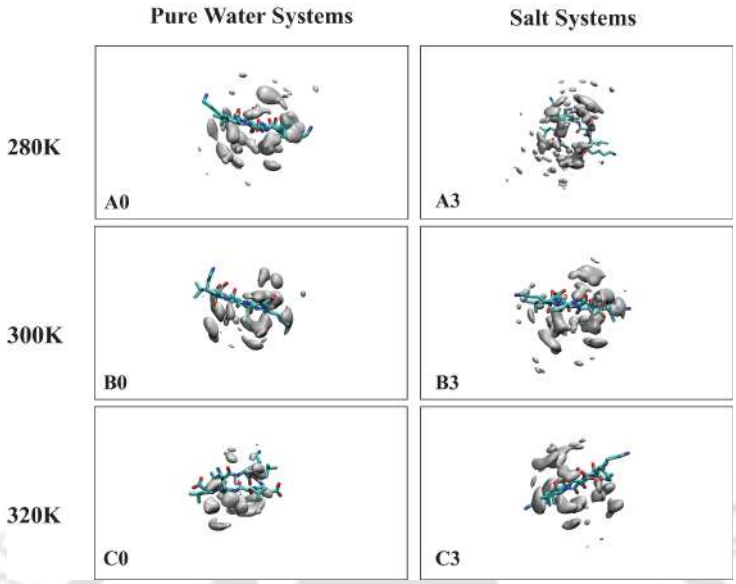

Figure. 2.10: *Spatial density distribution of CP around a reference CP for pure (A0, B0, C0) and salt solution systems (A3, B3, C3) at 280 K, 300 K, and 320 K.*

2.3.4 Preferential Interactions

From the previous subsections, it is quite obvious that there is an inherent inclination of CP molecules to interact among themselves depending upon the appropriate salt concentration in aqueous solutions. To substantiate our previous analyses, we have further computed the preferential interaction parameters of CPs for CPs over water for all the systems at 300 K, followed by the interaction parameters of sodium and chloride ions with the selective atomic sites of CP molecules over water. The Kirkwood-Buff theory[58–63], which employs statistical thermodynamic procedure, is used for this. The theory behind this interaction parameter calculation is already described in Chapter 1 (Section 1.4.3).

A positive value of the interaction parameter, $\tau^{cp}_{cp/w}$ value indicates a CP's preference for like molecules over water, whereas a negative $\tau^{cp}_{cp/w}$ value indicates a CP's affinity for water molecules. The former is known as "preferential binding", while the latter is known as "preferential hydration"[64].

In Figure 2.11(a), the variation of the preferential interaction parameter, $\tau^{cp}_{cp/w}$ is shown as a function of distance for each system at 300 K. The preferential interaction parameter, $\tau^{cp}_{cp/w}$, is positive for all the systems which suggest more affinity of CP molecules to associate with themselves over water. The preference is highest for the B3 system, which

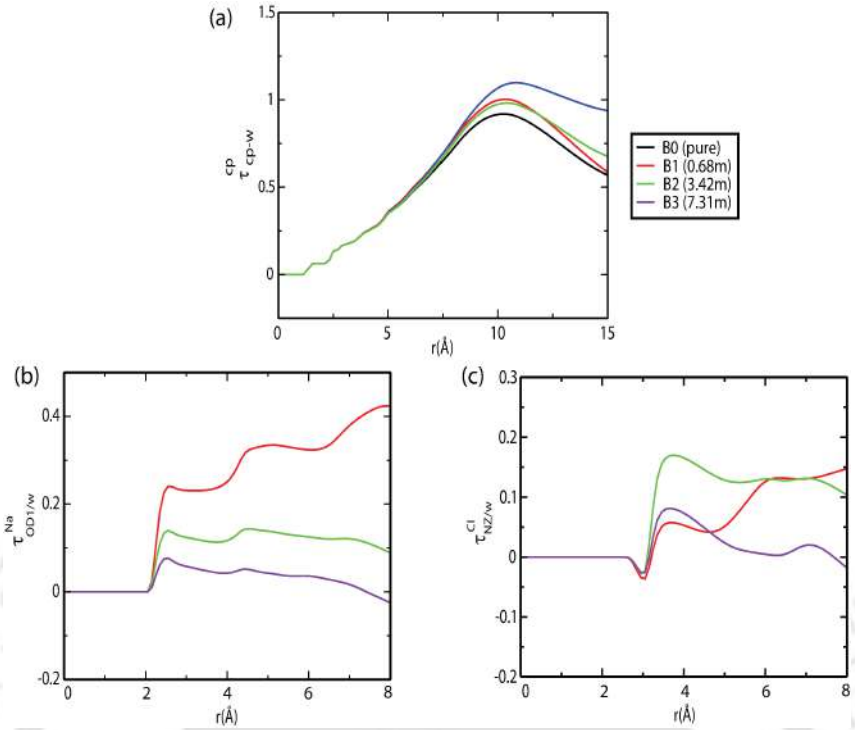

Figure. 2.11: *Preferential interaction parameters (a) ($\tau^{cp}_{cp/w}$) of CP for CP over water, (b) ($\tau^{Na}_{OD1/w}$) of Na^+ with OD1 atom of CP over water, and (c) ($\tau^{Cl}_{NZ/w}$) of Cl^- with NZ atom of CP over water in all the different systems considered at 300 K.*

has the highest salt concentration, followed by the systems B2, B1, and B0. The reason for almost similar values of $\tau^{cp}_{cp/w}$ in B1 and B2 systems can be well explained from the fact that in these systems, salt ions promote salting-in mechanism which results in the lesser association of CP molecules and so the preference of CPs for CPs is comparable to the B0 system (discussed above).

Furthermore, we have calculated the preferential interaction parameter of ions with the specific atomic sites of CP over water molecules to better understand the role of ions on CP association. Figure 2.11(b) and 2.11(c) depict the variation of preferential interaction parameters with distance for Na^+ with OD1 atom of aspartic acid and Cl^- with NZ atom of lysine side chain of (DLKL)$_2$ respectively. Figure 2.8(b) shows that the value of $\tau^{Na}_{OD1/w}$ decreases as we move from B1 to B3 system indicating that the interaction of Na^+ ions with the CP molecules decreases as the salt concentration increases. The trend of $\tau^{Cl}_{NZ/w}$ versus distance (Figure 2.11(c)), on the other hand, is somewhat different. For lower concentrations of NaCl (B1 and B2 systems), the $\tau^{Cl}_{NZ/w}$ value is higher as compared to high concentration NaCl system (B3) which indicates that Cl^- ions prefer CP molecules

more as compared to water in lower NaCl concentrations. Therefore, this trend supports the theory that the salting-in effect of Cl^- anion predominates in the B1 and B2 systems, resulting in a lower association of CPs, whereas in the B3 system, the salting-out effect of Cl^- anion prevails, resulting in a higher association of CPs. Thus, it can be speculated that the Cl^- anion induces salting-in and salting-out behavior in CP association in water.

2.3.5 Cluster Analysis

It is clear from the description above that salt addition alters self-association of CP molecules in water. Temperature is another factor that modifies how CP rings assemble themselves. In this section, we discuss about how temperature and salt affect the cluster formation during simulations. The cluster formation here means the self-assembly of CP rings to form nanotube like structures. We use the first minima of the rdf curves calculated between the center of masses of CP molecules as a cutoff limit for the cluster formation investigation. Stoddard clustering algorithm[65] is used for calculating the cluster sizes. Figure 2.12 depicts the formation of the maximum possible number of CP rings that self-assembled to form nanotube (C_{max}) over time for systems with pure and salt concentrations at 300 K. For each system's trajectory, we have omitted the first 10 ns of simulation time in order to obtain an equal number of frames. As can be observed, the average number of CP rings forming nanotube ranges from 2.32 for the pure water system (B0) to 3.92 for the B3 system.

Further, to examine the role of temperature on cluster formation, we have calculated maximum number of CP rings that formed nanotube (C_{max}) versus simulation time for pure water systems (A0, B0, C0) and highest salt concentration systems (A3, B3, C3) at three different temperatures (Figure 2.13). It is evident from the graphs that at lower temperature the number of CP rings to form nanotube is more and is highest in the A3 system (*i.e.* 5.87). With rise in temperature, this number decreases in both pure water and salt systems.

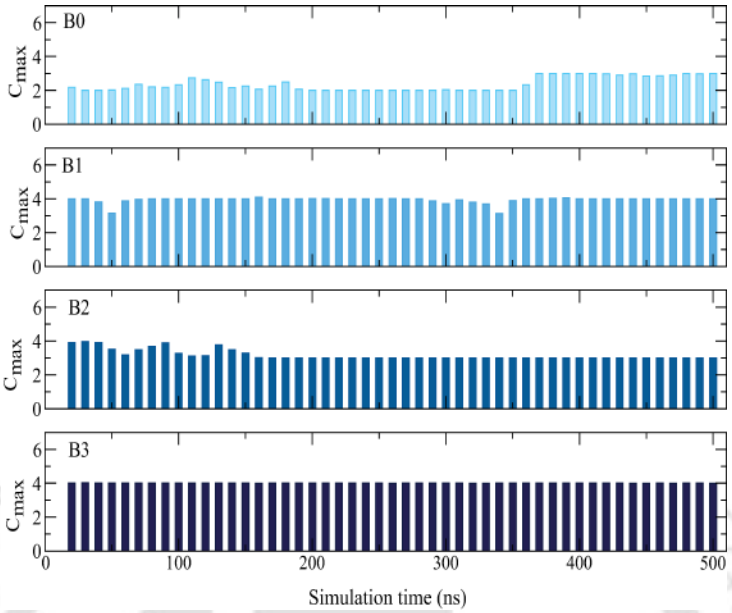

Figure. 2.12: *Maximum number of CP rings forming nanotube like structures (C_{max}) versus simulation time in all the different systems (B0, B1, B2, B3) considered at 300 K.*

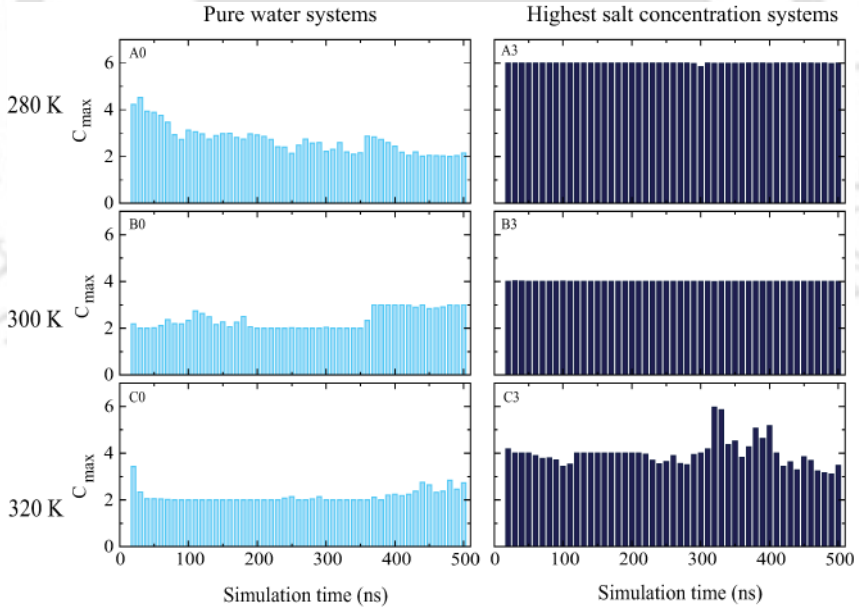

Figure. 2.13: *Maximum number of CP rings forming nanotube like structures (C_{max}) versus simulation time in pure (A0, B0, C0) and highest salt solution systems (A3, B3, C3) at 280 K, 300 K, and 320 K.*

2.3.6 Hydrogen Bonding

When CP molecules are added to water, they have the possibility to form hydrogen bonds among themselves as well as with solvent water molecules. The backbone carbonyl oxygen atom of the CP molecule can act as hydrogen bond acceptor and backbone amide nitrogen atom can act as both hydrogen bond donor and acceptor. Besides, the two equivalent carboxyl oxygens (OD1 and OD2) of aspartic acid side chain and terminal NZ atom of lysine can act as hydrogen bond acceptor and donor respectively. All these four atoms can form hydrogen bonds with water. In addition, hydrogen bonds between water molecules are also present, with the oxygen atom of the water molecule acting as both a hydrogen bond acceptor and a donor. Thus, in aqueous solution of cyclic peptide $(D\underline{L}K\underline{L})_2$, we can have five types of hydrogen bonds, *i.e.*, water-water (HB_{W-W}), backbone carbonyl oxygen-water (HB_{O-W}), backbone amide nitrogen-water (HB_{N-W}), two equivalent carboxyl oxygen atoms of aspartic acid-water (HB_{OD1-W}) and amide nitrogen of lysine-water (HB_{NZ-W}). The two geometric criteria that we adopt to define hydrogen bonds are: (a) the distance between the donor atom (D) of one molecule and the acceptor atom (A) of another molecule should fall within the cutoff distance (r_{cut}), and simultaneously (b) the angle H-D-A should be less than or equal to some cutoff angle (r_{angle}). In the current study, r_{cut} distance is considered as the first minimum of the respective site-water rdf and the maximum r_{angle} as 45°[47, 48, 66] . Table 2.5 shows the total number of hydrogen bonds that are formed between water-water and water with different atomic sites of CP in all the systems at 300 K.

Table. 2.5: *The average number of hydrogen bonds formed between water-water (per water) and site-water (per atom of CP) in all the systems considered at 300 K. Here, O and N are the backbone atoms of the CP while OD1 and NZ are the side chain atoms of aspartic acid and lysine respectively.*

System	HB_{W-W}	HB_{O-W}	HB_{N-W}	HB_{OD1-W}	HB_{NZ-W}
B0	3.00	0.78	0.36	1.75	1.45
B1	2.90	0.73	0.35	1.55	1.43
B2	2.74	0.72	0.34	1.44	1.21
B3	2.58	0.71	0.33	1.32	1.14

From the table, it is observed that for all the systems hydrogen bonds formed between water-water dominates and they are found to be decreasing modestly from 3.00 (B0) to

2.58 (B3) with increase in salt concentrations. It is worth noting that the average number of hydrogen bonds per water between water molecules in all the systems (B0-B3) is found to be lower than that in pure TIP3P water *i.e.* 3.16[67]. The presence of large CP molecules in the system causes some of the water-water hydrogen bonds to rupture. Also, the hydrogen bonds formed between backbone atoms of CP (*i.e.* O and N) with water is lesser in comparison to that of side chain OD1 and NZ atoms with water. Moreover, the average number of hydrogen bonds between different sites of CP with water is also found to be decreasing from B0 to B3 system. However, this decrease is not so prominent for the hydrogen bonds formed between water and backbone atoms of CP molecule. For 280 K (Table 2.6) and 320 K (Table 2.7), the similar trends are observed. This indicates that as salt concentration increases, the hydrogen bonding tendency of different sites of CP with water decreases. This implies a rise in the interaction of CPs among themselves, which results in the self-association of CP molecules.

Table. 2.6: *The average number of hydrogen bonds formed between water-water (per water) and site-water (per atom of CP) in all the systems considered at 300 K. Here, O and N are the backbone atoms of the CP while OD1 and NZ are the side chain atoms of aspartic acid and lysine respectively.*

System	HB_{W-W}	HB_{O-W}	HB_{N-W}	HB_{OD1-W}	HB_{NZ-W}
A0	3.01	0.82	0.36	1.83	1.49
A1	2.92	0.77	0.35	1.65	1.47
A2	2.67	0.72	0.33	1.42	1.16
A3	2.48	0.69	0.28	1.26	1.06

Table. 2.7: *The average number of hydrogen bonds formed between water-water (per water) and site-water (per atom of CP) in all the systems considered at 300 K. Here, O and N are the backbone atoms of the CP while OD1 and NZ are the side chain atoms of aspartic acid and lysine respectively.*

System	HB_{W-W}	HB_{O-W}	HB_{N-W}	HB_{OD1-W}	HB_{NZ-W}
C0	2.94	0.72	0.34	1.63	1.30
C1	2.87	0.69	0.33	1.47	1.32
C2	2.67	0.67	0.32	1.26	1.19
C3	2.50	0.68	0.32	1.25	1.12

Again we have studied the average number of hydrogen bond formed as a function of time between two adjacent CP rings that self-assembled to form nanotube like structures. Figure 2.14 shows the evolution of the hydrogen bonds between backbone atoms of the

adjacent CP rings at three different temperatures *i.e.* 280 K, 300 K, and 320 K for the systems (A3, B3, C3) with highest salt concentrations as it is found that self-assembly is highly favored in these systems. Maximum of 8 number of hydrogen bonds are observed to be formed between the backbone atoms of two adjacent CP rings. It is to be noted that the number of hydrogen bonds that are formed between adjacent CP rings is highest at 280 K and with increase in temperature, the values decrease between all the six CP rings that are considered.

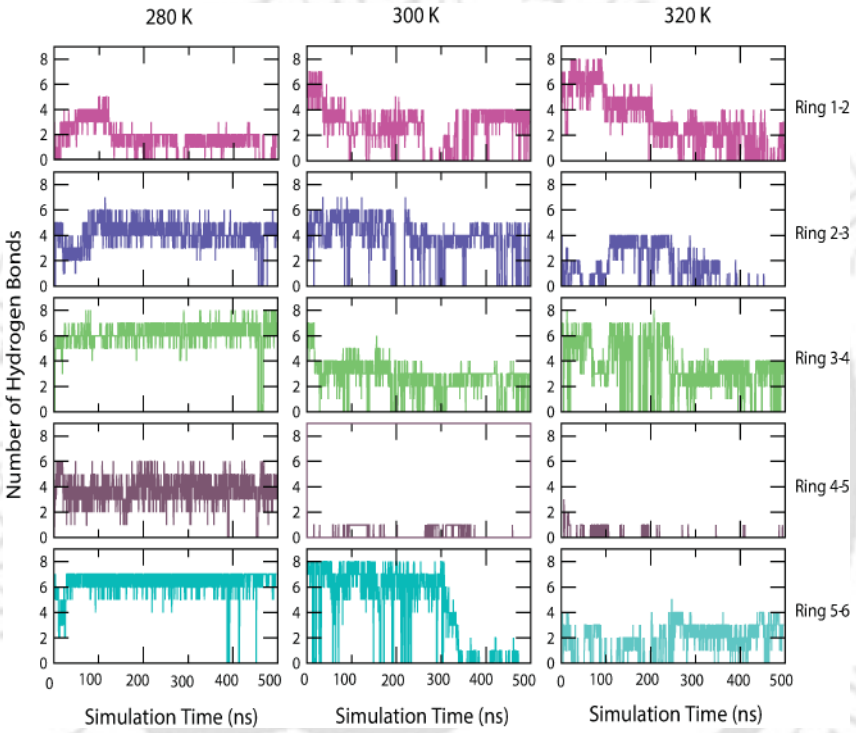

Figure. 2.14: *The number of hydrogen bonds with respect to simulation time formed between the backbone atoms of adjacent CP rings of the self-assembly nanotube like conformation at 280 K, 300 K, and 320 K in A3, B3, and C3 systems respectively.*

Nature of Hydrogen Bonding Leading Association of CP Rings:

As mentioned in Section 2.1, the nature of ring stacking arrangement between two CP molecules plays an essential part in their self-association. Out of parallel and antiparallel backbone-backbone intermolecular hydrogen-bonding, the later is more favorable in the formation of CPNTs[34]. Figure 2.15 shows the formation of antiparallel hydrogen bonding between the backbone atoms of adjacent CP rings that associates to form nanotube like structures. This finding goes well with the experimental results reported by Silk *et. al.*[34].

A slight orientation of the adjacent CP rings provides the amide and carbonyl groups the optimum alignment for creating hydrogen bonds between them. This is true for all the six CP rings leading to the formation of antiparallel hydrogen bonds.

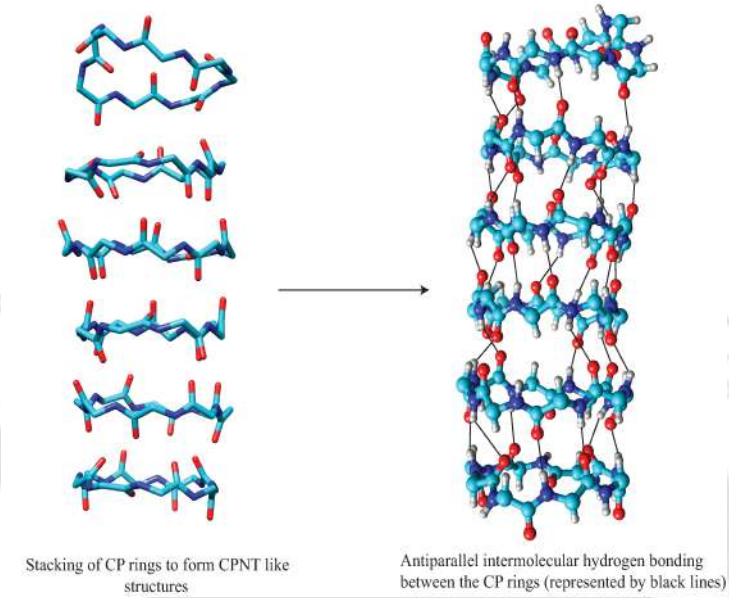

Figure. 2.15: *Antiparallel hydrogen bonding formed between the adjacent CP rings that self-assembled to form CPNT like structures.*

2.3.7 Dynamics of Hydrogen Bonds

In this section we investigate the dynamics of hydrogen bonds that are formed between the donor and acceptor sites of CP molecule in presence of salt and at different temperatures. A type of time correlation function (TCF) known as the continuous hydrogen bond correlation function, (S(t)) is used to efficiently calculate the dynamics of the hydrogen bonds formed. The theory behind this correlation function is described in Chapter 1 (Section 1.4.3).

To calculate the dynamic properties of the hydrogen bonds formed between different sites of the CP rings, we extracted six CP molecules from the final configuration of our previous 500 ns NPT simulation that tend to form nanotube-like structures and then equilibrated them for another 10 ns under NVT in the same water and salt environment. This NVT equilibration was performed to keep the system volume constant. Following that, these equilibrated systems were subjected to an additional 45 ns production run in

a micro-canonical ensemble (NVE). The coordinates of the final 200 ps run were recorded at 10 fs intervals. The S(t) was evaluated using this last 200 ps trajectory of the NVE simulation. We have then fitted the decay curves using triexponentials to obtained the lifetime values. The amplitude-weighted average lifetimes[68], $<\tau_{HB}>$ are reported in Table 2.8 and Table 2.9.

We start our discussion with the continuous hydrogen bond TCFs for the systems B0, B1, B2 and B3 at 300 K. Here, we have only reported the lifetime of the hydrogen bonds that are formed between backbone atoms of the CP molecules for better understanding as there are many possible sites in a CP molecule to undergo hydrogen bond formation with another like molecule. Figure 2.16 shows the decay functions S(t) versus time of the top five most dominant hydrogen bonds that are formed between the backbone atoms of the adjacent CP rings. Because the top five hydrogen bond pairs with the highest lifetime values are found to be dissimilar in all four systems, the curves are numbered with decreasing lifetime values for each system for convenience. In Table. 2.8, we have reported the top three hydrogen bonding pairs alongside their lifetime values,($<\tau_{HB}>$) for each system under consideration. It can be observed that for all the systems the bonding pairs having highest lifetimes are different which is obvious as the systems are very dynamic in nature and the hydrogen bonding sites between two CP molecules are not similar and are constantly changing throughout all the systems. Hence, it is not apt to compare the values of all the systems and comment on the association tendency of CP molecules based on lifetime of hydrogen bonds alone that are formed.

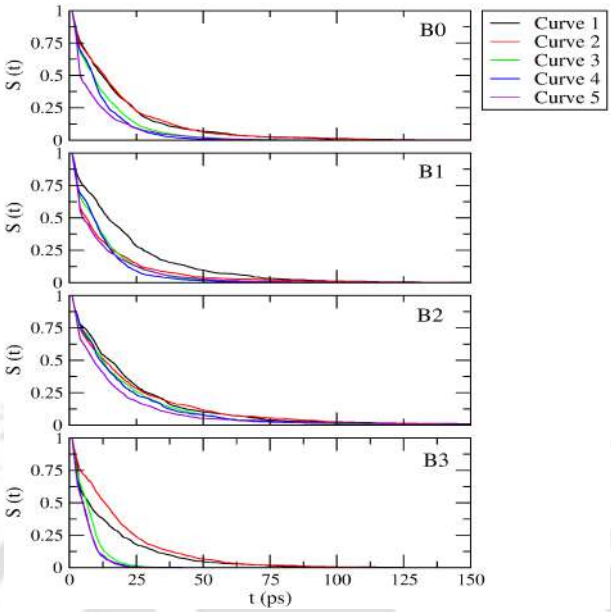

Figure. 2.16: *The top five continuous hydrogen bond correlation functions for the backbone hydrogen bonding pairs between CP molecules having highest lifetime values for the systems B0, B1, B2, and B3 at 300 K.*

Table. 2.8: *The lifetime values (<τ_{HB}>) of the continuous hydrogen bonds S(t) that are formed between different pairs of the backbone atoms of the CP molecules for all the systems at 300 K. The three backbone pairs of each system having highest lifetime values are reported here. All the lifetime values are expressed in ps.*

System	Curve No.	Bonding Pair	Lifetime value(<τ_{HB}>)
B0	1	$CP5_{(LEU@O)}$-$CP4_{(LYS@N-H)}$	19.93
	2	$CP6_{(LEU@O)}$-$CP1_{(LEU@N-H)}$	18.66
	3	$CP2_{(LYS@O)}$-$CP1_{(LYS@N-H)}$	8.55
B1	1	$CP4_{(LEU@O)}$-$CP5_{(LEU@N-H)}$	23.26
	2	$CP4_{(LEU@O)}$-$CP5_{(LEU@N-H)}$	10.81
	3	$CP4_{(LYS@O)}$-$CP3_{(LYS@N-H)}$	8.86
B2	1	$CP4_{(LEU@O)}$-$CP2_{(LEU@N-H)}$	24.84
	2	$CP2_{(LEU@O)}$-$CP4_{(LEU@N-H)}$	18.29
	3	$CP3_{(LYS@O)}$-$CP4_{(LYS@N-H)}$	14.61
B3	1	$CP2_{(LEU@O)}$-$CP4_{(LEU@N-H)}$	11.87
	2	$CP2_{(LYS@O)}$-$CP1_{(LYS@N-H)}$	11.20
	3	$CP4_{(LEU@O)}$-$CP2_{(LEU@N-H)}$	6.66

The top three continuous hydrogen bond lifetimes of the pure water system (A0, B0,

C0) and highest salt concentration systems (A3, B3, C3) at 280 K, 300 K, and 320 K are reported in Table. 2.9. It can be seen that the lifetimes of the hydrogen bonds formed between CP molecules are decreasing with the rise in temperature both in presence and absence of salt. This is agreement with the fact that as temperature rises, hydrogen bonds break, resulting in increased vibrational motion[54].

Table. 2.9: *The lifetime values ($<\tau_{HB}>$) of the continuous hydrogen bonds S(t) that are formed between different pairs of the backbone atoms of the CP molecules for pure water systems (A0, B0, C0) and highest salt systems (A3, B3, C3) at 280 K, 300 K, and 320 K. The three backbone pairs of each system having highest lifetime values are reported here. All the lifetime values are expressed in ps.*

Temp (K)	Systems	Bonding Pair	Lifetime value ($<\tau_{HB}>$)
280 K	A0	$CP3_{(ASP@O)}$-$CP4_{(ASP@N-H)}$	25.00
		$CP3_{(LYS@O)}$-$CP4_{(LYS@N-H)}$	20.01
		$CP3_{(LYS@O)}$-$CP4_{(LYS@N-H)}$	11.08
	A3	$CP6_{(LYS@O)}$-$CP5_{(LYS@N-H)}$	24.54
		$CP4_{(ASP@O)}$-$CP3_{(ASP@N-H)}$	23.50
		$CP6_{(LEU@O)}$-$CP2_{(LEU@N-H)}$	18.95
300 K	B0	$CP5_{(LEU@O)}$-$CP4_{(LYS@N-H)}$	19.93
		$CP6_{(LEU@O)}$-$CP1_{(LEU@N-H)}$	18.66
		$CP2_{(LYS@O)}$-$CP1_{(LYS@N-H)}$	8.55
	B3	$CP2_{(LEU@O)}$-$CP4_{(LEU@N-H)}$	11.87
		$CP2_{(LYS@O)}$-$CP1_{(LYS@N-H)}$	11.20
		$CP4_{(LEU@O)}$-$CP2_{(LEU@N-H)}$	6.66
320 K	C0	$CP5_{(LEU@O)}$-$CP2_{(LYS@N-H)}$	10.08
		$CP1_{(LEU@O)}$-$CP5_{(ASP@N-H)}$	10.00
		$CP5_{(LYS@O)}$-$CP6_{(LYS@N-H)}$	8.59
	B3	$CP1_{(LYS@O)}$-$CP2_{(LYS@N-H)}$	9.76
		$CP4_{(ASP@O)}$-$CP3_{(ASP@N-H)}$	8.90
		$CP4_{(LYS@O)}$-$CP3_{(LYS@N-H)}$	8.23

2.3.8 Association Constant

To comprehend the role of salt and temperature on the self-association of CPs, we further evaluated the association constant, K_a for all the systems that are under consideration. The association constant, K_a can be defined from the following equation[69]:

$$K_a = 4\pi \int_0^{r_a} r^2 e^{-W(r)/k_B T} dr \tag{2.2}$$

where r_a is the position in the PMF curve (W(r)) where the energy barrier exists. It is to be noted that, the higher the value of K_a, the more will be the association of the CPs in solution. Table 2.10 illustrates the values of K_a for all the systems at all three temperatures

Table. 2.10: *Values of association constants (K_a) for CP-CP association at different temperatures for both pure and salt solution systems.*

Temp (K)	Systems	Ka × $10^2(M^{-1})$
280 K	A0	14.52
	A1	15.09
	A2	14.42
	A3	20.54
300 K	B0	12.63
	B1	15.72
	B2	12.24
	B3	17.38
320 K	C0	6.32
	C1	11.05
	C2	9.39
	C3	21.09

The table shows that as temperature rises, the association propensity of CPs decreases for both pure and salt systems which is as per expectation. Again, when comparing pure and salt systems at a given temperature, the self-association of CPs is found to be greater in salt systems. Again, at a particular temperature the association constant values go well with the rdf trends as explained earlier.

2.3.9 Thermodynamics Behind the Self-Association of CPs

The examination of enthalpy and entropy contributions to the free energy of CP association is crucial for understanding the thermodynamics of self-association of CPs. The potential of mean force (PMF), $W(r)$, represents the free energy profile as a function of the center-of-mass distance, r, between two cyclic peptides (CPs). It quantifies the reversible work required to bring two CP molecules from infinite separation to a distance r in the solution. The PMF can be derived from the radial distribution function (RDF),

$g_{\mathrm{cp-cp}}(r)$, according to the following relation [48]:

$$W(r) = -k_{\mathrm{B}}T \ln g_{\mathrm{cp-cp}}(r) \tag{2.3}$$

where k_B and T represents the Boltzmann constant and absolute temperature, respectively, and $g_{cp-cp}(r)$ is the radial distribution function calculated between CP-CP involving the center of masses of CP molecules. After that, the entropy is being computed from the PMFs of the three temperatures with the help of finite difference temperature derivative:[70–72]

$$-\Delta S(r) = \frac{1}{2}\left[\frac{\delta W(r, T+\delta T)}{\delta T} - \frac{\delta W(r, T-\delta T)}{\delta T}\right] \tag{2.4}$$

Here, the value of δT is 20 K. After obtaining the value of $\Delta S(r)$ from the above equation, the corresponding value of enthalpy ($\Delta H(r)$) can be calculated by using the following equation:

$$\Delta H(r) = W(r) + T\Delta S(r) \tag{2.5}$$

The enthalpy and entropy derived from PMFs provide a reaction coordinate resolved picture of the thermodynamics of CP association, capturing both solute-solute interactions and solvent mediated effects along the center of mass separation. Compared to other popular approaches such as normal mode or quasi harmonic analyses[73], which primarily estimate conformational entropy near local minima, or endpoint methods like MM-PBSA[74], which give overall binding free energies with approximate entropic contributions, PMF-based decomposition offers the advantage of mapping distance-dependent energetic and entropic changes, thus providing more detailed insight into the association process.

Figure 2.17(a) and 2.17(b) portray the contributions of entropy (-T$\Delta S(r)$) and enthalpy ($\Delta H(r)$) to the PMF (W(r)) at 300 K for pure water and salt solution systems respectively. By observing the two figures, we arrive at the following considerations: (a) Two distinct minima are present in both the PMF plots. The first minimum of the curves at 4.85 Å and 4.95 Å for pure and salt systems respectively is the contact minimum (CM)

which corresponds to the distance where no solvent molecule, or even a portion of one, comes between the solute molecules. The second minimum, known as the solvent separated minimum (SSM), appears at 7.25 Å for pure water system and at 6.25 Å for the salt solution. The SSM represent the distances at which exactly one water molecule can be accommodated between two solutes[75]. Further, the stability of the contact minima are more than the solvent separated minima for both the systems. (b) The contribution of entropy and enthalpy towards the stability of self-association of CPs are in opposite directions to each other. The intersolute distances, or CP-CP distances, determine the proportion of each contribution. (c) In pure water, enthalpy plays a key role in stabilizing both CM and SSM (Table. 2.11). (d) With the addition of salt, the entropic contribution at CM increases, whereas the enthalpic contribution at both CM and SSM becomes less favorable.

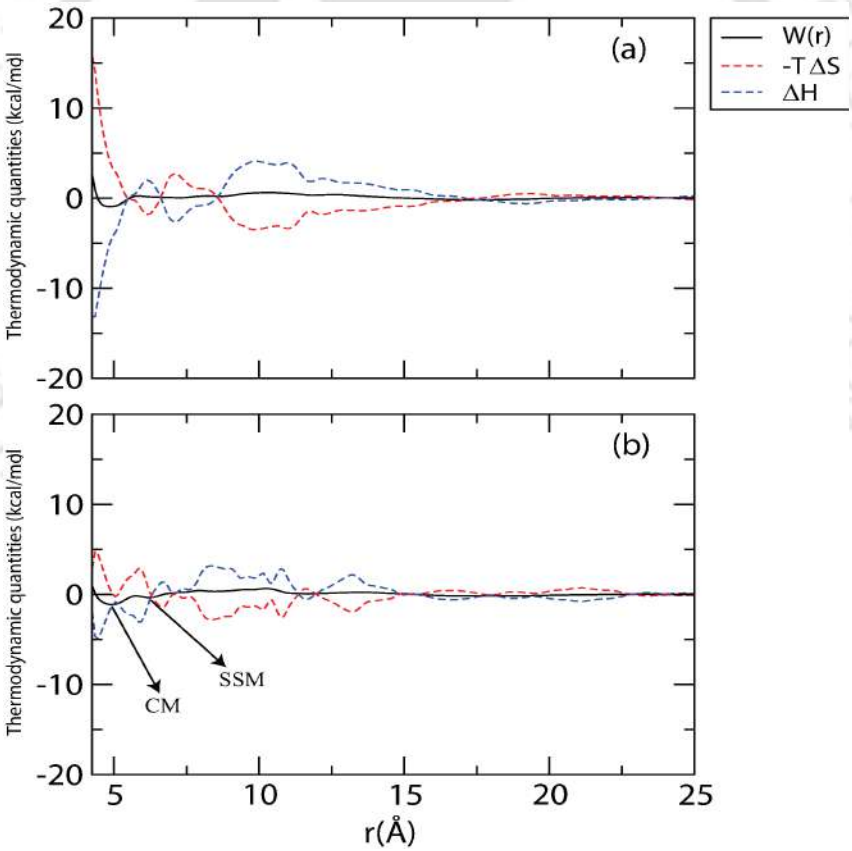

Figure. 2.17: *Enthalpy and entropy contribution to CP-CP PMF for (a) pure (B0) and (b) salt solution systems (B3) at 300 K. All the thermodynamic quantities are expressed in kcal/mol.*

The change in the contributions of entropy and enthalpy to free energy at 300 K can

Table. 2.11: *The values of W(r), ΔH, and -TΔS because of the interactions among the CP molecules at 300 K. Here, CM, SSM, and r represent respectively, the contact minima, solvent separated minima, and distance at which CM and SSM appear. All the energy values are expressed in kcal/mol units, and the distances are is Å .*

System		r	W(r)	-T$\Delta S(r)$	$\Delta H(r)$
B0	CM	4.85	-0.95	4.13	-5.08
	SSM	7.25	-0.02	2.50	-2.45
B3	CM	4.95	-1.13	-0.12	-1.17
	SSM	6.25	-0.34	0.13	-0.47

be explained by the fact that CP, due to its large size, cannot fit inside the cavity of a liquid water hydrogen-bonded network. This causes some of the water-water hydrogen bonds that are closer to the surface of the CP molecules to break. As a result, entropy is increased by the release of these well organized water molecules around CP molecules. On the other hand, when CP molecules are added to water, new hydrogen bonds are formed between the CP and water molecules, which results in an increase in enthalpy.

From Table 2.11 and Figure 2.17 it is observed that the presence of salt in aqueous CP solution has very little effect on the thermodynamics of CP association. Previously, it was reported that the hydrophobic interactions that are induced by salt for methane like small molecules is enthalpic in nature, whereas for large-scale length hydrophobic moiety the salting out effect is entropic in nature[76, 77]. This difference in the origin of thermodynamic properties is supported by different salting out mechanisms for molecules irrespective of sizes. Mancera[76], in his paper, proposed that the presence of salt reduces hydrogen bonds between water-water, resulting in a decrease in system's enthalpy. Moreover, Zangi *et. al.*[77] observed that for large solutes, the salting out phenomenon is entropic in the presence of NaCl. They explained that because Na^+ and Cl^- ions have high charge densities, water molecules tend to cluster around them, which results in the formation of hydration complexes. Because of this, the less hydrophobic molecules are driven aside from the solvent, resulting in a decrease in the available surface area of water-accessible solute molecules. Hence, the salting out phenomenon is believed to possess an entropic origin. Nevertheless, we find that both in pure water and in salt solution the self-association of CPs is mostly enthalpic in nature and we do not observe any enthalpy-entropy crossover.

2.3.10 Free Energy of Binding of the Self-Assembled CP Rings

In this subsection, the binding free energy of each CP ring in the self-assembly structure with respect to the adjacent two rings is evaluated with the help of Molecular Mechanics/Generalized Born Surface Area (MM/GBSA)[78] using the Python script *MMPBSA.py*[79]. To calculate the free energy of binding, we extracted the most stable stacking conformation from the entire 500 ns simulation and then ran a production simulation with the self-assembled rings restrained in position for another 20ns. Finally, the solvent water molecules, salt ions, and other CP rings that do not self-assembled are stripped out, and the binding free energy of each CP ring with respect to the other two adjacent rings of the self-assembly is evaluated using the following relations:[22] It is to be noted that for the terminal CP rings (Ring 1 and Ring 6) we considered only one adjacent ring *i.e.* Ring 2 and Ring 5 respectively.

Table 2.12 illustrates the binding free energy ($\Delta G^i_{binding}$) of each ring (CP subunit) of the nanotube formed at all the three temperatures.

Table. 2.12: *The values of binding free energy (ΔG^i_{bind}) and standard error of mean of each CP rings forming self-assembly at 280 K, 300 K, and 320 K. All the units are expressed in kcal mol^{-1}.*

CP rings	280 K		300 K		320 K	
	ΔG^i_{bind}	Std. Err. of Mean	ΔG^i_{bind}	Std. Err. of Mean	ΔG^i_{bind}	Std. Err. of Mean
Ring 1	-16.10	0.01	-15.71	0.01	-12.85	0.01
Ring 2	-50.15	0.01	-44.74	0.01	-29.28	0.02
Ring 3	-70.23	0.02	-57.40	0.01	-36.01	0.01
Ring 4	-64.98	0.02	-34.59	0.01	-28.14	0.01
Ring 5	-59.77	0.02	-48.00	0.01	-23.53	0.01
Ring 6	-35.69	0.01	-32.06	0.01	-18.62	0.01

Results obtained from the GB method indicate that the binding free energies of the CP rings forming self-assembly are more favorable in case of low temperature and the values of ΔG_{bind} become less negative as the temperature is increased. This indicates higher stability of the self-assembled structure at 280 K and the tendency of self-assembly of CPs reduces with raise in temperature. Furthermore, the binding energies of each CP ring at the core regions are more favorable than that of the terminal CP rings of the nanotube like structures that are formed at all three temperatures. Based on this observation, we can speculate that multiple stacking of the CP rings can result in mechanical stability in

the core region of the self-assembled structures.

2.4 Conclusion

The present chapter elucidates the influence of NaCl and temperature on the self-association of CPs to form nanotube like structures in aqueous solution using classical MD simulation. To investigate the role of NaCl, we have prepared four systems, each comprising 90 CPs, one in pure water and three others in various salt concentrations for three different temperatures (280 K, 300 K, and 320 K). The behavior of the salt ions towards CP self-association are discussed elaborately for the systems at 300 K. From the CP-CP center of mass distribution plot it is found that at lower salt concentrations the CP molecules tend to get solvated by water which in turn implies less association among themselves in comparison to pure water system. However, at a high concentration of NaCl, the CP molecules get more associated. It is observed that the Cl^- ions interact more with the negatively charged NZ atom of lysine side chain of the CP molecule at lower salt concentrations. But, with increasing salt ions, they prefer to interact more with water leaving the CPs to associate among themselves. The same conclusion is derived from the preferential interaction parameter of CP for CP over water and that of ions for CP over water. At low salt concentration systems (B1 and B2) the value of the preferential interaction parameter of CP for like molecules over water is low as compared to that of the pure water system (B0). However, at a high salt concentration (B3), the preferential interaction parameter value is more than the pure water system. Moreover, the preference of Na^+ ions for CP over water decreases as we move from B0 to B3 system. But, the preference of Cl^- ions for CP over water is more for the low salt concentration systems (B1 and B2) as compared to the high salt B3 system. Thus, it can be concluded that, at low concentration of NaCl salt, salting in phenomenon takes place inducing fewer the association of CP molecules. However, at high salt concentration, the association of CP molecules increases suggesting salting out phenomenon. The same conclusion can be drawn from the cluster analysis. We can see an increase in maximum cluster size for the highest salt system (B3) compared to pure water (B0) and the other two lower salt systems (B1 and B2) at 300 K. Again, the co-ordination number around different hydrophilic and hydrophobic atomic sites of CP molecule reveals that with increasing in NaCl concentration, water gets expelled out from the hydrophilic sites while hydrophobic sites get more

hydrated. Also, increasing salt concentration leads to a decrease in hydrogen bonds of different atomic sites of CP with water. This ultimately indicates more association of CPs at high salt concentration in comparison to pure water. The hydrogen bond lifetime values obtained from the continuous hydrogen bond TCF calculated between CP molecules indicates that for all the systems the pair of sites contributing maximum lifetime values are not similar and changes throughout. Apart from that, the nature of hydrogen bonding between two adjacent CP rings is found to be antiparallel which goes in agreement with the previous experimental reports.

Again, to study the effect of temperature, we have considered two systems each, CPs in pure water (A0, B0, C0) and CPs in water at the highest salt concentration (A3, B3, C3) at three different temperatures (280 K, 300 K, and 320 K). The radial distribution functions, spatial density plots, and association constant values reveal that for both pure and salt systems, the association of CPs among themselves decreases with a rise in temperature. Furthermore, the association of CPs is found to be mostly enthalpic in nature in both pure water and salt solution at 300 K and no crossover between enthalpy and entropy is observed. Moreover, the binding free energies between the CP rings that tends to form nanotube like structures with six subunits at all three temperatures are calculated using MM-GBSA methodology. From the results it is quite evident that the self-assembly of CP rings is more favourable at lower temperature (280 K) as compared to those formed at 300 K and 320 K and the process is enhanced in presence of salt.

References

(1) Jin, L.; Harrison, S. C. *Proc Natl Acad Sci* **2002**, *99*, 13522–13526.

(2) Gause, G. F.; Brazhnikova, M. G. *Nature* **1944**, *154*, 703–703.

(3) Loll, P. J.; Axelsen, P. H. *Annu. Rev. Biophys. Biomol. Struct.* **2000**, *29*, 265–289.

(4) Sandhu, P.; Xu, X.; Bondiskey, P. J.; Balani, S. K.; Morris, M. L.; Tang, Y. S.; Miller, A. R.; Pearson, P. G. *Antimicrob. Agents Chemother.* **2004**, *48*, 1272–1280.

(5) Dewan, V.; Liu, T.; Chen, K.-M.; Qian, Z.; Xiao, Y.; Kleiman, L.; Mahasenan, K. V.; Li, C.; Matsuo, H.; Pei, D.; Musier-Forsyth, K. *ACS Chem. Biol.* **2012**, *7*, 761–769.

(6) Liu, S.; Gu, W.; Lo, D.; Ding, X.-Z.; Ujiki, M.; Adrian, T. E.; Soff, G. A.; Silverman, R. B. *J. Med. Chem.* **2005**, *48*, 3630–3638.

(7) Lee, D. W.; Kim, B. S. *Plant Pathol. J.* **2015**, *31*, 1.

(8) Choi, J.-S.; Joo, S. H. *Biomol. Ther.* **2019**, *28*, 18.

(9) Garcia-Fandino, R.; Amorin, M.; Castedo, L.; Granja, J. R. *Chem. Sci.* **2012**, *3*, 3280–3285.

(10) Sánchez-Quesada, J.; Kim, H. S.; Ghadiri, M. R. *Angew. Chem., Int. Ed.* **2001**, *40*, 2503–2506.

(11) Liu, J.; Fan, J.; Tang, M.; Cen, M.; Yan, J.; Liu, Z.; Zhou, W. *J. Phys. Chem. B* **2010**, *114*, 12183–12192.

(12) Liu, J.; Fan, J.; Cen, M.; Song, X.; Liu, D.; Zhou, W.; Liu, Z.; Yan, J. *J. Chem. Inf. Model.* **2012**, *52*, 2132–2138.

(13) Yan, X.; Fan, J.; Yu, Y.; Xu, J.; Zhang, M. *J. Chem. Inf. Model.* **2015**, *55*, 998–1011.

(14) Carvajal-Diaz, J. A.; Cagin, T. *J. Phys. Chem. B* **2016**, *120*, 7872–7879.

(15) Zhang, M.; Fan, J.; Xu, J.; Weng, P.; Lin, H. *J. Mol. Model.* **2016**, *22*, 1–12.

(16) Ghadiri, M. R.; Granja, J. R.; Milligan, R. A.; McRee, D. E.; Khazanovich, N. *Nature* **1993**, *366*, 324–327.

(17) Khazanovich, N.; Granja, J. R.; McRee, D. E.; Milligan, R. A.; Ghadiri, M. R. *J. Am. Chem. Soc.* **1994**, *116*, 6011–6012.

(18) Hartgerink, J. D.; Granja, J. R.; Milligan, R. A.; Ghadiri, M. R. *J. Am. Chem. Soc.* **1996**, *118*, 43–50.

(19) Chapman, R.; Danial, M.; Koh, M. L.; Jolliffe, K. A.; Perrier, S. *Chem. Soc. Rev.* **2012**, *41*, 6023–6041.

(20) Amorín, M.; Castedo, L.; Granja, J. R. *J. Am. Chem. Soc.* **2003**, *125*, 2844–2845.

(21) Hsieh, W.-H.; Liaw, J. *J. Food Drug Anal.* **2019**, *27*, 32–47.

(22) Vijayaraj, R.; Van Damme, S.; Bultinck, P.; Subramanian, V. *Phys. Chem. Chem. Phys.* **2012**, *14*, 15135–15144.

(23) Khavani, M.; Izadyar, M.; Housaindokht, M. R. *J. Mol. Liq.* **2020**, *314*, 113660.

(24) Vijayaraj, R.; Van Damme, S.; Bultinck, P.; Subramanian, V. *J. Phys. Chem. B* **2012**, *116*, 9922–9933.

(25) Vijayakumar, V.; Vijayaraj, R.; Peters, G. H. *J. Mol. Model.* **2016**, *22*, 1–12.

(26) Marlow, G. E.; Perkyns, J. S.; Pettitt, B. M. *Chem. Rev.* **1993**, *93*, 2503–2521.

(27) Von Hippel, P. H.; Schleich, T. *Acc. Chem. Res.* **1969**, *2*, 257–265.

(28) Robinson, D. R.; Jencks, W. P. *J. Am. Chem. Soc.* **1965**, *87*, 2470–2479.

(29) Hong, Y.; Pritzker, M. D.; Legge, R. L.; Chen, P. *Colloids Surf. B* **2005**, *46*, 152–161.

(30) Hofmeister, F. *Pathol. Pharmakol* **1888**, *24*, 247–260.

(31) Jelesarov, I.; Dürr, E.; Thomas, R. M.; Bosshard, H. R. *Biochem.* **1998**, *37*, 7539–7550.

(32) Ghosh, S.; Baul, U.; Vemparala, S. *The Journal of Chemical Physics* **2019**, *151*, 074901.

(33) Whitesides, G. M.; Grzybowski, B. *Science* **2002**, *295*, 2418–2421.

(34) Silk, M. R.; Newman, J.; Ratcliffe, J. C.; White, J. F.; Caradoc-Davies, T.; Price, J. R.; Perrier, S.; Thompson, P. E.; Chalmers, D. K. *Chem. Commun.* **2017**, *53*, 6613–6616.

(35) Case, D. A. et al. Amber 18., University of California: San Francisco, CA, 2018.

(36) Jorgensen, W. L.; Chandrasekhar, J.; Madura, J. D.; Impey, R. W.; Klein, M. L. *J. Chem. Phys.* **1983**, *79*, 926–935.

(37) Maier, J. A.; Martinez, C.; Kasavajhala, K.; Wickstrom, L.; Hauser, K. E.; Simmerling, C. *J. Chem. Theory Comput.* **2015**, *11*, 3696–3713.

(38) Li, P.; Song, L. F.; Merz Jr, K. M. *J. Chem. Theory Comput.* **2015**, *11*, 1645–1657.

(39) Martínez, L.; Andrade, R.; Birgin, E. G.; Martínez, J. M. *J. Comput. Chem.* **2009**, *30*, 2157–2164.

(40) Hünenberger, P. H. *Adv. Polym. Sci.* **2005**, 105–149.

(41) Berendsen, H. J.; Postma, J. v.; Van Gunsteren, W. F.; DiNola, A.; Haak, J. R. *J. Chem. Phys.* **1984**, *81*, 3684–3690.

(42) Ryckaert, J.-P.; Ciccotti, G.; Berendsen, H. J. *J. Comput. Phys.* **1977**, *23*, 327–341.

(43) Essmann, U.; Perera, L.; Berkowitz, M. L.; Darden, T.; Lee, H.; Pedersen, L. G. *J. Chem. Phys.* **1995**, *103*, 8577–8593.

(44) Roe, D. R.; Cheatham III, T. E. *J. Chem. Theory Comput.* **2013**, *9*, 3084–3095.

(45) Humphrey, W.; Dalke, A.; Schulten, K. *J. Mol. Graphics* **1996**, *14*, 33–38.

(46) Pettersen, E. F.; Goddard, T. D.; Huang, C. C.; Couch, G. S.; Greenblatt, D. M.; Meng, E. C.; Ferrin, T. E. *J. Comput. Chem.* **2004**, *25*, 1605–1612.

(47) Sharma, B.; Paul, S. *J. Phys. Chem. B* **2015**, *119*, 6421–6432.

(48) Sharma, B.; Paul, S. *J. Chem. Phys.* **2013**, *139*, 194504.

(49) Klement, K.; Wieligmann, K.; Meinhardt, J.; Hortschansky, P.; Richter, W.; Fändrich, M. *J. Mol. Biol.* **2007**, *373*, 1321–1333.

(50) Hyde, A. M.; Zultanski, S. L.; Waldman, J. H.; Zhong, Y.-L.; Shevlin, M.; Peng, F. *Org. Process Res. Dev.* **2017**, *21*, 1355–1370.

(51) Chattaraj, K. G.; Paul, S. *J. Chem. Phys.* **2019**, *150*, 064501.

(52) Zapadka, K. L.; Becher, F. J.; Gomes dos Santos, A.; Jackson, S. E. *Interface focus* **2017**, *7*, 20170030.

(53) Das, S.; Paul, S. *J. Phys. Chem. B* **2016**, *120*, 173–183.

(54) Paul, R.; Mitra, A.; Paul, S. *J. Chem. Phys.* **2021**, *154*, 244504.

(55) Head-Gordon, T.; Sorenson, J. M.; Pertsemlidis, A.; Glaeser, R. M. *Biophys. J.* **1997**, *73*, 2106–2115.

(56) Brehm, M.; Thomas, M.; Gehrke, S.; Kirchner, B. *J. Chem. Phys.* **2020**, *152*, 164105.

(57) Yokogawa, D.; Sato, H.; Sakaki, S. *J. Chem. Phys.* **2005**, *123*, 211102.

(58) Kirkwood, J. G.; Buff, F. P. *J. Chem. Phys.* **1951**, *19*, 774–777.

(59) Matteoli, E.; Mansoori, G. A., *Fluctuation theory of mixtures*; Taylor & Francis New York: 1990.

(60) Ben-Naim, A. Y., *Statistical thermodynamics for chemists and biochemists*; Springer Science & Business Media: 2013.

(61) Ben-Naim, A., *Molecular Theory of Solutions*; Oxford University Press: 2006.

(62) Smith, P. E. *J. Phys. Chem. B* **2006**, *110*, 2862–2868.

(63) Smith, P. E. *Biophys. J.* **2006**, *91*, 849–856.

(64) Timasheff, S. N. *Proc. Natl. Acad. Sci.* **2002**, *99*, 9721–9726.

(65) Stoddard, S. D. *J. Comput. Phys.* **1978**, *27*, 291–293.

(66) Devi, M.; Paul, S. *Phys. Chem. Chem. Phys.* **2022**, *24*, 14452–14471.

(67) Ong, E. E.; Liow, J.-L. *Fluid Phase Equilibr.* **2019**, *481*, 55–65.

(68) Bandyopadhyay, S.; Chakraborty, S.; Bagchi, B. *J. Am. Chem. Soc.* **2005**, *127*, 16660–16667.

(69) Paul, S.; Paul, S. *RSC Adv.* **2014**, *4*, 34267–34280.

(70) Smith, D. E.; Haymet, A. *J. Chem. Phys.* **1993**, *98*, 6445–6454.

(71) Lüdemann, S.; Abseher, R.; Schreiber, H.; Steinhauser, O. *J. Am. Chem. Soc.* **1997**, *119*, 4206–4213.

(72) Head-Gordon, T. *J. Am. Chem. Soc.* **1995**, *117*, 501–507.

(73) Ma, J. *Structure* **2005**, *13*, 373–380.

(74) Wang, C.; Greene, D.; Xiao, L.; Qi, R.; Luo, R. *Front. Mol. Biosci.* **2018**, *4*, 87.

(75) Sobolewski, E.; Makowski, M.; Czaplewski, C.; Liwo, A.; Ołdziej, S.; Scheraga, H. A. *J. Phys. Chem. B* **2007**, *111*, 10765–10774.

(76) Mancera, R. L. *J. Phys. Chem. B* **1999**, *103*, 3774–3777.

(77) Zangi, R.; Hagen, M.; Berne, B. *J. Am. Chem. Soc.* **2007**, *129*, 4678–4686.

(78) Hou, T.; Wang, J.; Li, Y.; Wang, W. *J. Chem. Inf. Model.* **2011**, *51*, 69–82.

(79) Miller III, B. R.; McGee Jr, T. D.; Swails, J. M.; Homeyer, N.; Gohlke, H.; Roitberg, A. E. *J. Chem. Theory Comput.* **2012**, *8*, 3314–3321.

Chapter 3

Impact of Solvent Polarity and Amino Acid Composition on the Structural Stability of Cyclic Peptide Nanotubes

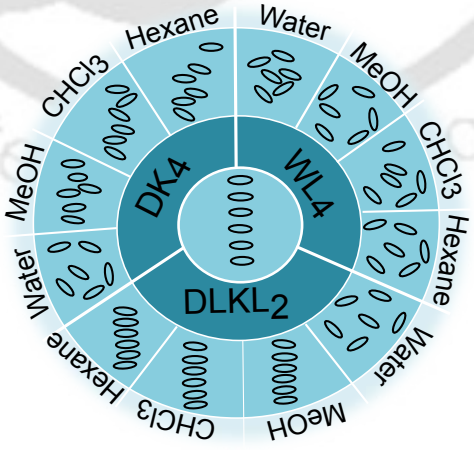

Overview

The formation and stability of cyclic peptide nanotubes (CPNTs) are influenced by multiple factors. This chapter explores the stability of CPNTs in various solvents with varying polarity, focusing on three specific peptide sequences: D$\underline{\text{K}}_4$, W$\underline{\text{L}}_4$, and D$\underline{\text{L}}$K$\underline{\text{L}}_2$. Using molecular dynamics simulations, the effect of solvent polarity and peptide composition on the stability of CPNTs is assessed through the determination of electrostatic, van der Waals, and hydrogen bonding interactions. The binding free energy between adjacent cyclic peptide rings is analyzed via MM/GBSA and MM/PBSA methods, revealing that D$\underline{\text{L}}$K$\underline{\text{L}}_2$, an amphiphilic peptide, exhibits greater stability than D$\underline{\text{K}}_4$ and W$\underline{\text{L}}_4$ in non-polar solvents. The introduction of leucine residues in D$\underline{\text{L}}$K$\underline{\text{L}}_2$ reduces intramolecular hydrogen bonding and electrostatic interactions, promoting stronger inter-peptide backbone hydrogen bonds and maintaining the nanotube's structural integrity. Hydrogen bond lifetimes, computed using corresponding time correlation function, indicate the longest-lasting hydrogen bonds occur in all the solvent environments except water, further contributing to the stability of D$\underline{\text{L}}$K$\underline{\text{L}}_2$ nanotubes. Additionally, deformation from circularity in the peptide rings, analyzed using ellipticity values, highlights the degree of structural distortion across solvents, with D$\underline{\text{K}}_4$ showing the highest deviation due to stronger intramolecular interactions. These findings offer valuable insights into the roles of solvent and peptide composition in the self-assembly and stability of CPNTs, which have significant implications for their potential applications in nanotechnology and biomedicine.

3.1 Introduction

The formation of CPNTs is driven by intermolecular forces including electrostatic, van der Waals, hydrogen bonds and hydrophobic interactions[1–3]. The process of self-association is profoundly dependent on several key factors, including the amino acid sequence of the peptide, the concentration of the peptides, temperature, the nature of the solvent, and the pH of the environment[4–8]. These factors collectively influence the stability and morphology of the resulting nanotube structures. For example, specific sequences of amino acids can promote or inhibit certain interactions that are essential for maintaining the tubular architecture, while the choice of solvent and pH can alter the peptide's conformational behavior, thus affecting the self-assembly process[4, 6].

Solvent polarity is one of the most influential factors in determining nanotube stability. Polar solvents, such as water, often destabilize certain nanotube structures by disrupting intramolecular and intermolecular hydrogen bonds that are critical to maintaining their shape. In contrast, nonpolar solvents, like chloroform, tend to stabilize hydrophobic nanotubes by minimizing solvent interference with internal bonding. Izadyar et al. demonstrated this phenomenon through computational studies, showing that nonpolar solvents enhance the structural integrity of heterocyclic peptide nanotubes, whereas polar solvents can cause nanotube shortening and instability due to competition for hydrogen bonding[9]. Other studies have similarly underscored the importance of solvent choice in stabilizing nanotubes. Adler-Abramovich et al. investigated the chemical stability of peptide nanotubes in various solvent environments and found that organic solvents, including ethanol and dimethyl sulfoxide (DMSO), enhance nanotube stability compared to aqueous solutions [10]. These findings indicate that solvent properties, such as their ability to form hydrogen bonds or their hydrophobicity, directly influence the nanotube's ability to maintain its ordered structure. Again, Vijayakumar and his team investigated the stability of $[(WQWE)_2]_8$ nanotube in polar and non-polar solvents using molecular dynamics (MD) simulations and Gibbs free energy calculations. They found that the CPNT was more stable in non-polar (nonane) environments, with tryptophan contributing to enhanced stability by forming side chain hydrogen bonds[6].

Again, the stability of CPNTs, is highly influenced by the specific amino acid components of the peptide rings. Amino acid residues influence the nature of hydrogen bonding,

hydrophobic interactions, and steric effects, all of which are crucial for determining the overall structural integrity and stability of the nanotube. Vijayaraj and his co-workers has reported that the CPNTs composed of polar side chains are less stable in aqueous enviornmnet compared to CPNTs with non-polar amino acids[4]. The hydrophobic residues increase nanotube stability, particularly in non-polar environments, by reducing solvent interference with the hydrogen bonding network[7]. Studies have found that tryptophan residues contributed to enhanced nanotube stability by forming stabilizing side chain-side chain hydrogen bonds, particularly in non-polar environments[6].

In this chapter, we investigate the stability of three CPNTs with distinct amino acid compositions in four different solvent environments of varying polarity, using molecular dynamics (MD) simulations. Each CPNT is characterized by a unique amino acid profile: one composed entirely of hydrophilic residues, another consisting solely of hydrophobic residues, and the third featuring an amphiphilic design, combining both hydrophilic and hydrophobic residues. By selecting solvents with different polarities, we aim to understand how these varying compositions respond to changes in the solvent environment, shedding light on their structural stability. Unlike previous studies that have primarily focused on short-term stability or limited solvent environments, our work extends the simulation period to a longer duration, allowing for a comprehensive analysis of the long-term behavior of these CPNTs. This extended time frame enables us to observe more subtle effects of solvent interactions on the stability of the nanotubes, such as non bonded interactions, persistent structural deformations, and shifts in the hydrogen bonding networks. The results of this investigation offer new insights into how different amino acid compositions impact the overall stability of CPNTs in diverse solvent conditions, providing valuable data that has been missing in previous studies.

3.2 Materials and Methods

3.2.1 System Setup

The starting structure of the CPNT was taken from our previous study (Chapter 2). The nanotube was made up of six cyclic peptide rings of cyclo-[(Asp-D-Leu-Lys-D-Leu)$_2$] ([D$\underline{\text{L}}$K$\underline{\text{L}}_2$]$_6$). This nanotube was formed by spontaneous assembly of maximum of six D$\underline{\text{L}}$K$\underline{\text{L}}_2$ rings in water in presence of NaCl salt as described in the previous chapter

and is shown in Figure 3.1. The nanotube was stable in water + NaCl medium for a period of 500 ns and hence we have taken the same self-assembled nanotube structure to investigate the role of solvents on its stability. For that we selected four solvents with varying polarities: hexane, chloroform, methanol, and water. Hexane is the most non-polar of these solvents, followed by chloroform, with methanol being polar, and water being the most polar. Again, to examine the influence of the amino acid compositions of the nanotube on its stability in different solvents, we mutated the CP subunits firstly by hydrophilic amino acids: [(Asp-D-Lys)$_4$] (D$\underline{\text{K}}_4$), secondly by hydrophobic amino acids: [(Trp-D-Leu)$_4$] (W$\underline{\text{L}}_4$). (Figure 3.1).

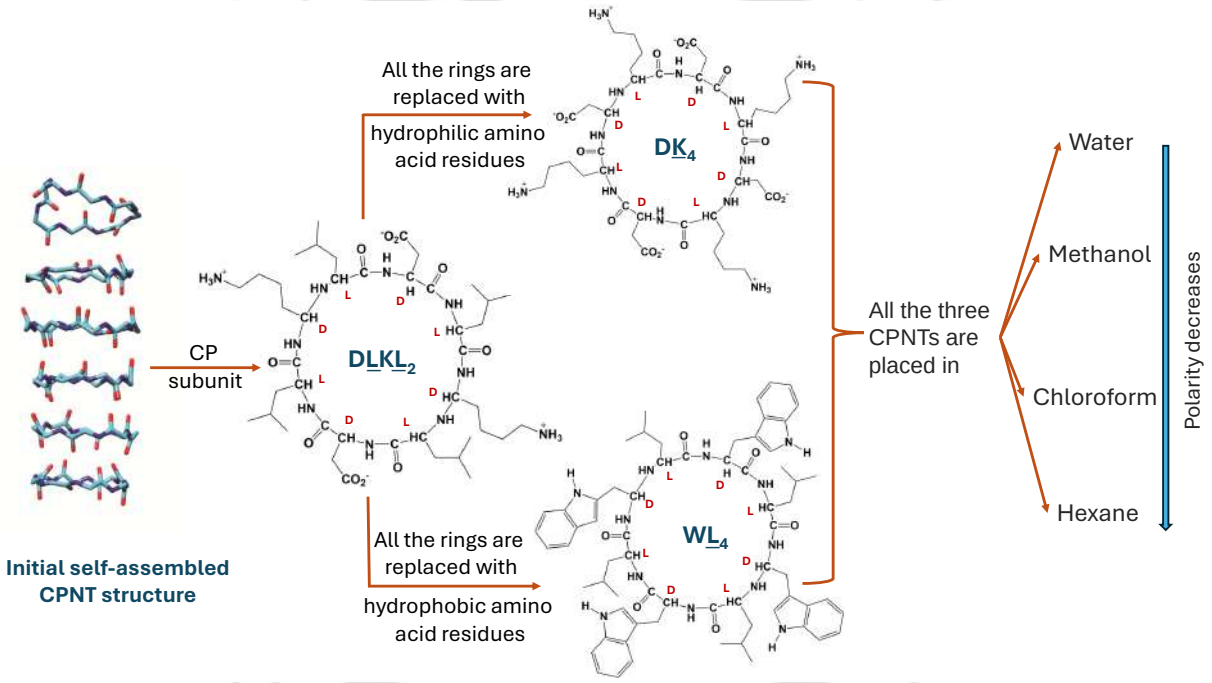

Figure 3.1: *Schematic representation of the D$\underline{\text{L}}$K$\underline{\text{L}}_2$ ring mutation with D$\underline{\text{K}}_4$ and W$\underline{\text{L}}_4$, placed in different solvent media with varying polarity. The initial self-assembled D$\underline{\text{L}}$K$\underline{\text{L}}_2$ nanotube structure is also shown. The chemical structures of D$\underline{\text{L}}$K$\underline{\text{L}}_2$, D$\underline{\text{K}}_4$, and W$\underline{\text{L}}_4$ rings are also presented for comparison.*

An alternating sequence of D- and L-amino acids is crucial to maintain the hollow tubular core structure of CPNTs[11]. The original crystal structure of D$\underline{\text{L}}$K$\underline{\text{L}}_2$ (CCDC 1520676)[1] inherently possesses the required alternating D- and L-stereochemistry. Consequently, all three CPNTs studied retain the hollow tubular core structure. To clearly indicate the D- and L-amino acids, the D-amino acids in all three CPNTs have been

underlined.

3.2.2 Simulation Protocols

For our simulations, we used the TIP3P water model[12] for water and ff14SB force field[13] for the cyclic peptides. Methanol and chloroform models were obtained from AMBER parameters[14–16]. For hexane, the ground state geometry was optimized with the HF/6-31G* method using Gaussian09[17], and atomic charges were fitted to electrostatic potentials using the RESP (restrained electrostatic potential)[18] module of the AMBER18 package[19]. The rest of the parameters of hexane were generated with the General AMBER Force Field[20] using the ANTECHAMBER[16] module. The CPNTs were completely solvated in a cubic box with solvent molecules (water, methanol, and chloroform) distributed at 15 Å distances from the solute atoms using the tleap module of AMBER18[19]. For hexane, the initial configurations of the systems were prepared using the PACKMOL program[21]. Finally, each of the three CPNTs was simulated in all four solvents, resulting in a total of 12 systems. To ensure comprehensive results, each system was simulated three times, with the runs labeled as Run 1, Run 2, and Run 3, respectively. The number of solvent molecules in all systems was adjusted to maintain a constant CP concentration across all, enabling a valid comparison of results. Accordingly, the total number of solvent molecules added to each system were 6733 for water, 2934 for methanol, 1500 for chloroform, and 1000 for hexane. Detailed specifications for all systems are provided in Table 3.1.

Table. 3.1: *Overview of all the systems investigated in this study. Here, D$\underline{K}_4$ corresponds to [(Asp-D-Lys)$_4$], W$\underline{L}_4$ to (Trp-D-Leu)$_4$, and D$\underline{L}K\underline{L}_2$ to (Asp-D-Leu-Lys-D-Leu)$_2$. C_{CP} refers to the molar concentration of the cyclic peptides.*

CPNT	Solvent	Run	No. of CP rings	No. of solvent	Box Length (Å)	C_{CP} (M)
6 × D$\underline{K}_4$	Water	1	6	6733	59.52	0.047
		2	6	6733	59.55	0.047
		3	6	6733	59.45	0.047
	Methanol	1	6	2934	59.92	0.046
		2	6	2934	59.99	0.046
		3	6	2934	59.93	0.046
	Chloroform	1	6	1500	59.35	0.047
		2	6	1500	59.41	0.047
		3	6	1500	59.41	0.047
	Hexane	1	6	1000	60.66	0.044
		2	6	1000	60.59	0.044
		3	6	1000	60.70	0.044
6 × W$\underline{L}_4$	Water	1	6	6733	59.90	0.046
		2	6	6733	59.89	0.046
		3	6	6733	59.88	0.046
	Methanol	1	6	2934	60.30	0.045
		2	6	2934	60.26	0.045
		3	6	2934	60.25	0.045
	Chloroform	1	6	1500	59.74	0.046
		2	6	1500	59.75	0.046
		3	6	1500	59.69	0.046
	Hexane	1	6	1000	60.96	0.043
		2	6	1000	60.92	0.043
		3	6	1000	60.88	0.043
6 × D$\underline{L}K\underline{L}_2$	Water	1	6	6733	59.58	0.047
		2	6	6733	59.64	0.047
		3	6	6733	59.61	0.047
	Methanol	1	6	2934	60.04	0.045
		2	6	2934	60.08	0.045
		3	6	2934	59.99	0.045
	Chloroform	1	6	1500	59.43	0.047
		2	6	1500	59.46	0.047
		3	6	1500	59.50	0.047
	Hexane	1	6	1000	60.73	0.044
		2	6	1000	60.73	0.044
		3	6	1000	60.67	0.044

All the systems were subjected to energy minimization in two stages: first, 5000 steps of the steepest descent method were performed, followed by 5000 steps of the conjugate gradient method to resolve any potential bad contacts. These minimizations were carried out using the SANDER module of AMBER18[19]. The systems were then gradually heated from 0 K to the targeted temperature of 300 K over 150 ps in an NVT ensemble followed by 1 ns equilibration in the same ensemble. Each system was subsequently equilibrated for 4 ns at 300 K and 1 atm in an NPT ensemble. Following that, each system underwent a production run under NPT conditions for 500 ns, with coordinates recorded at 4 ps intervals. The leap-frog algorithm was used to integrate the equations of motion and a 2 fs time step was used for it. To maintain constant pressure, the Berendsen barostat[22] with a 2 ps coupling constant was utilized. The Langevin thermostat[23] with a 1 ps^{-1} collision frequency was used to maintain the desired temperature. The SHAKE algorithm[24] was used to constrain covalent bonds involving hydrogen atoms. For short-ranged nonbonded interactions, a 10 Å cutoff distance was considered. Electrostatic interactions were evaluated with the help of particle mesh Ewald (PME) algorithm[25]. Periodic boundary conditions were enforced along all three directions.

To investigate hydrogen bond dynamics, selected systems were equilibrated under NVT conditions for 10 ns to fix the simulation box volume after the NPT run. Following equilibrations, production runs were performed in a micro-canonical (NVE) ensemble for 45 ns. The coordinates were recorded at 10 fs intervals during the last 200 ps of the NVE run to capture the ultrafast dynamics of hydrogen bonds formed between the CP rings of the nanotubes.

3.2.3 Simulation Analysis

The trajectories of all systems were analyzed using the CPPTRAJ[26] module from the Amber18 package. In addition, few analyses were carried out using in-house scripts. Visualization was carried out using Visual Molecular Dynamics (VMD)[27] and UCSF-Chimera[28].

To analyze the structural variations of the CPNTs in different solvents, the root mean square deviation (RMSD) values for both backbone and sidechain atoms of the CP units (relative to their initial geometry from the simulation trajectories) were calculated. Additionally, root mean square fluctuation (RMSF) was evaluated to assess the atomic po-

sitional fluctuations of the Cα atoms within the CP units. To evaluate the compactness of the nanotube structures across various solvents, the radius of gyration (R_g) was also determined. For the spatial density plots, the last 10 ns of the trajectory were used. These plots illustrated the three-dimensional probability distribution of the CP rings around a reference CP ring, which was typically positioned in the middle of the nanotube. An isovalue of 0.5 was applied for all the density plots.

The criteria considered to calculate hydrogen bonds is already discussed in Chapter 1 (Section 1.4.3) The frequency of hydrogen bonds was determined by counting the number of occurrences of each specific hydrogen bond number throughout the trajectory. The continuous hydrogen bond time correlation function (TCF) was applied to compute the lifespan of hydrogen bonds between backbone atoms in adjacent CP rings.

The NAMD energy plugin in VMD[27] was used to calculate the non-bonded interaction energies for the systems under consideration. Further, to assess the deformation of CP rings from their ideal circular structure, a parameter called ellipticity was calculated. Ellipticity was defined as the ratio of the largest (D_{max}) to the smallest (D_{min}) diameter of a CP ring[29]:

$$ellipticity = \frac{D_{max}}{D_{min}} \tag{3.1}$$

In this context it is worth mentioning that the diameter of a CP ring was defined as the distance between two opposite atoms within the ring. Since each CP ring has 24 backbone atoms, there are 12 possible diameters that can be measured. D_{max} and D_{min}, respectively, represent the highest and lowest diameters obtained from these measurements. The ellipticity value quantifies the deviation from a perfect circular shape. It also indicates the extent of deformation of the CP ring.

The preferential interaction parameter for CP-CP over CP-solvent (s) was determined by the use of Kirkwood-Buff integrals [30–34]. for solvent molecules. The binding free energy of each CP ring within the nanotube structure, relative to the two adjacent rings, was evaluated using Molecular Mechanics/Poisson-Boltzmann Surface Area (MM/PBSA)[35] and Molecular Mechanics/Generalized Born Surface Area (MM/GBSA)[36] methods. The Python script MMPBSA.py[35] was employed for these calculations. The final 20 ns of the trajectory was used, with solvent molecules and other CP rings stripped away.

3.3 Results and Discussions

The stability of the tubular structure of the three CPNTs in various solvents after a 500 ns for Run 1 is illustrated in Figure 3.2. Initial observations from the snapshots indicate that the CPNTs generally maintained their tubular structure in non-polar solvents (chloroform and hexane), with the exception of the W$\underline{L}_4$ nanotube. Additionally, amphiphilic CPNT (D$\underline{L}$K$\underline{L}_2$) appears to exhibit greater stability compared to those that are entirely hydrophilic or hydrophobic. The same observations can be drawn from the other two Runs (2 and 3) which are shown in Figure 3.3 and Figure 3.4 respectively. To delve deeper into the influence of amino acid sequences on the stability of CPNTs and to understand their behaviour in both polar and non-polar solvents, we examine various aspects in detail in the upcoming sections.

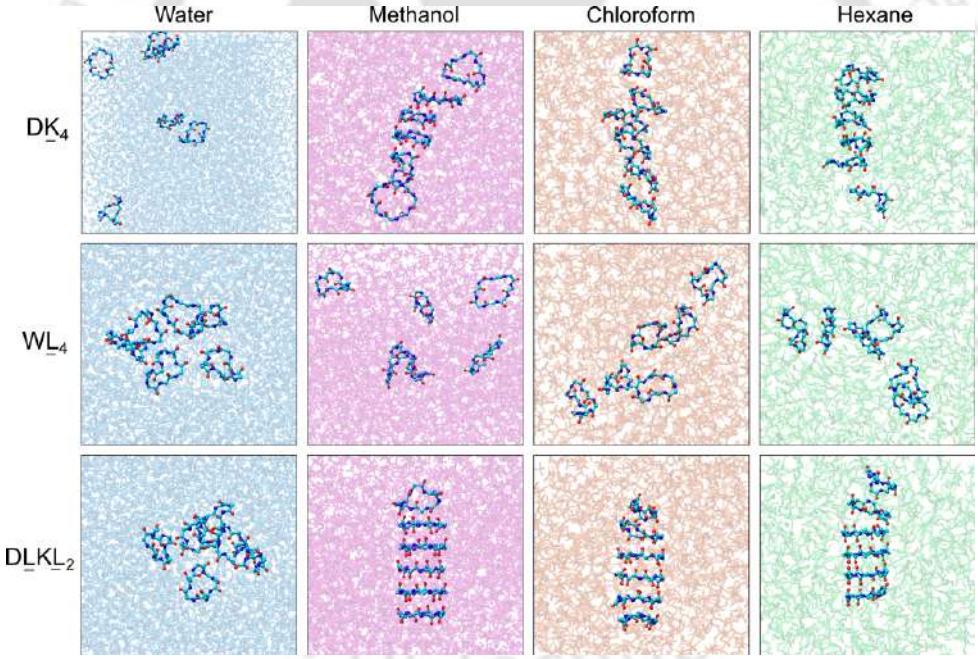

Figure 3.2: *Snapshots of three CPNTs after 500 ns of simulation in four different solvents for Run 1.*

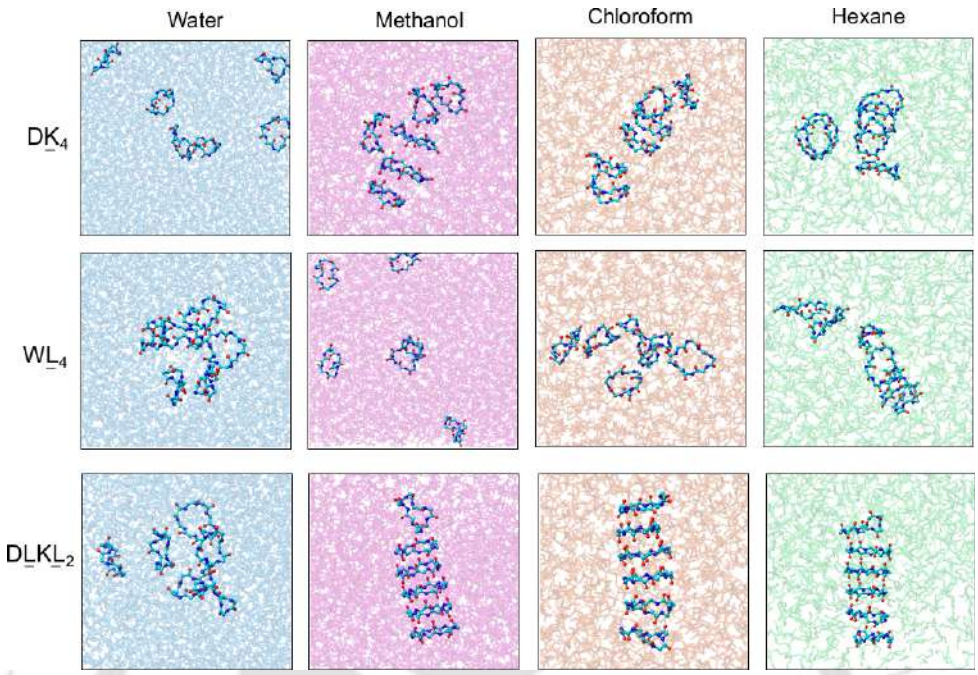

Figure 3.3: *Snapshots of three CPNTs after 500 ns of simulation in four different solvents for Run 2.*

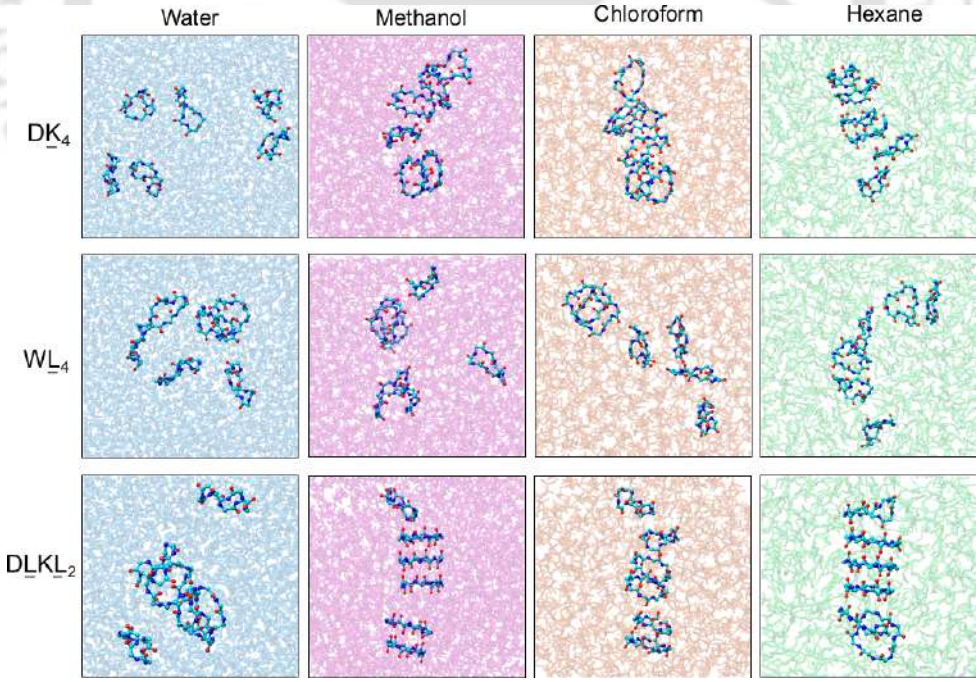

Figure 3.4: *Snapshots of three CPNTs after 500 ns of simulation in four different solvents for Run 3.*

3.3.1 Stability of the CPNTs across Various Solvents

At first, the structural stability of the three CPNTs in different solvents is evaluated by determining the root mean square deviation (RMSD) and radius of gyration (R_g). Figure 3.5 shows the average RMSD values of the backbone atoms of the respective CPNTs for Run 1, 2 and, 3 in different solvent environments, along with the variation of R_g over time. For the D$\underline{K}_4$ and D$\underline{L}K\underline{L}_2$ nanotubes, the average RMSD values are highest in water, followed by methanol, chloroform, and hexane, while the W$\underline{L}_4$ nanotube does not follow this trend. Similarly, the average of the R_g values of all the three simulation runs of respective CPNTs in different solvents over the simulation time suggests that the tubular structures of both D$\underline{K}_4$ and D$\underline{L}K\underline{L}_2$ nanotubes remain more compact in non-polar solvents (a pattern not observed for the W$\underline{L}_4$ nanotube).

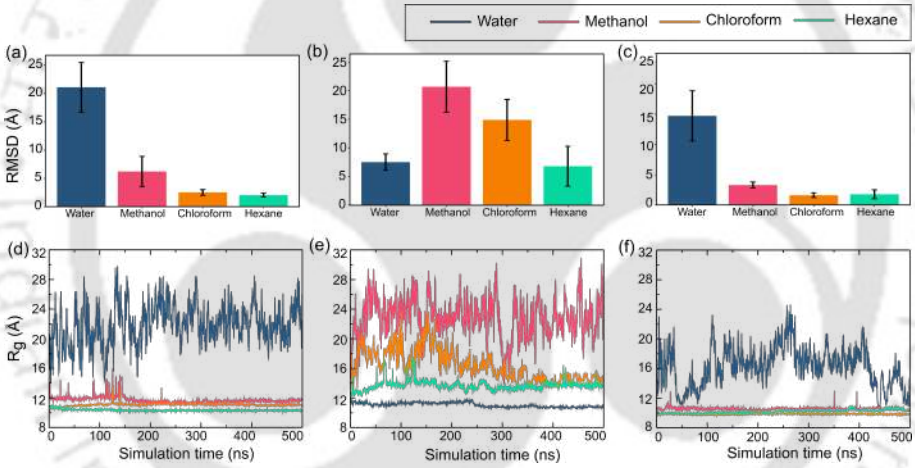

Figure 3.5: *Average root mean square deviation (RMSD) of backbone atoms of (a) D$\underline{K}_4$, (b) W$\underline{L}_4$, and (c) D$\underline{L}K\underline{L}_2$ in different solvents along with the radius of gyration (Rg) of backbone atoms of (d) D$\underline{K}_4$, (e) W$\underline{L}_4$, and (f) D$\underline{L}K\underline{L}_2$ over time across all solvents.*

The variation of RMSD of all the atoms of the CPNTs versus simulation time for Run 1, 2 and 3 and the root mean square fluctuation (RMSF) of Cα atoms in all solvent media for all the three runs are presented in Figures 3.6 and 3.7 respectively. The fluctuation of the Cα atoms of the CP rings of nanotube D$\underline{L}K\underline{L}_2$ is lower in all solvents except water in all the simulation replica runs. The same trend is followed for D$\underline{K}_4$ nanotube in all the simulation runs. However, this trend does not hold for the W$\underline{L}_4$ nanotube. Furthermore, the R_g values versus time for all the three runs for all the systems are shown in Figure 3.8.

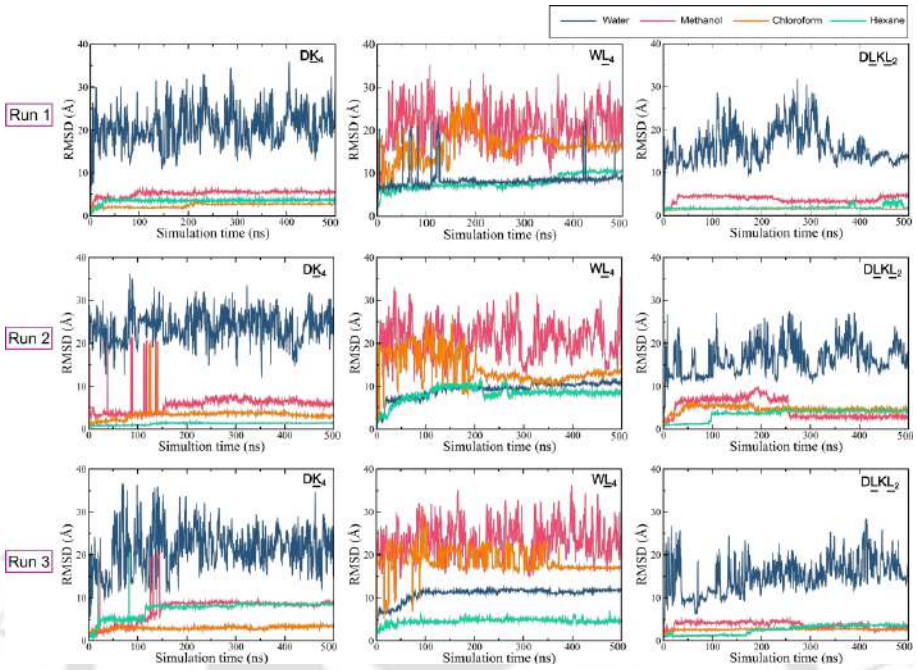

Figure 3.6: *Root mean square deviation (RMSD) of all the atoms of $D\underline{K}_4$, $W\underline{L}_4$, and $D\underline{L}K\underline{L}_2$ versus time accross all the solvent media for Run 1, 2, and 3.*

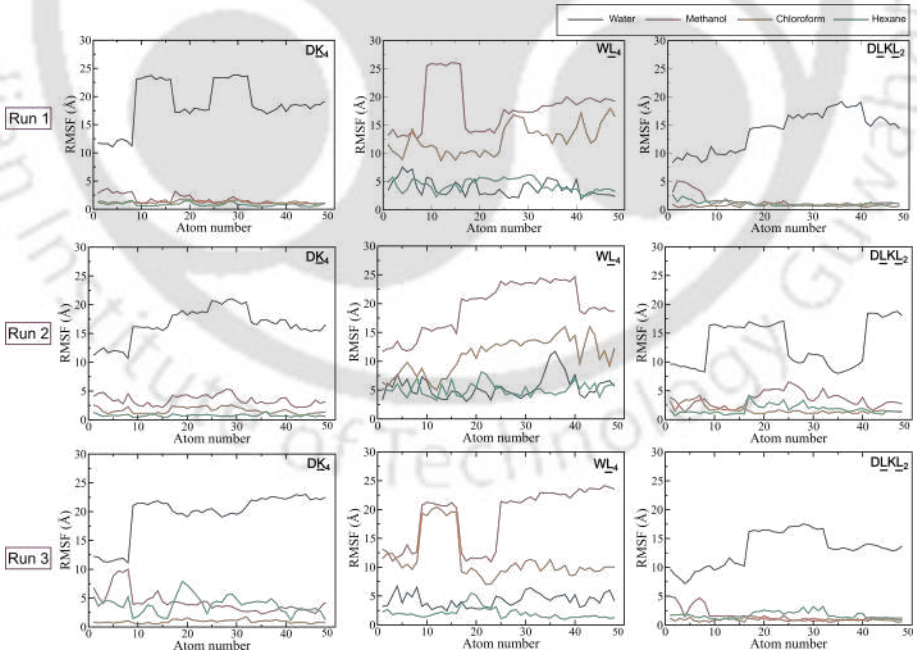

Figure 3.7: *Root mean square fluctuation (RMSF) of the C-α atoms of $D\underline{K}_4$, $W\underline{L}_4$, and $D\underline{L}K\underline{L}_2$ accross all the solvent media for Run 1, 2, and 3.*

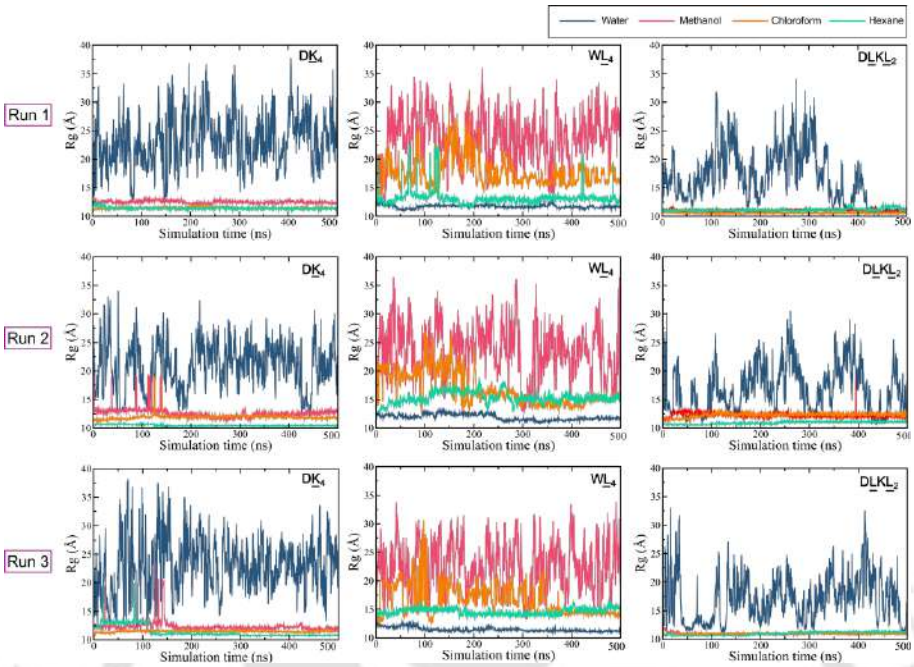

Figure 3.8: *Radius of gyration (R_g) of all the atoms of D$\underline{K}_4$, W$\underline{L}_4$, and D$\underline{L}$K$\underline{L}_2$ accross all the solvent media for Run 1, 2, and 3.*

The trend of RMSD versus time, R_g versus time and RMSF of Cα atoms is consistent across all the simulation replicas for the three CPNTs, confirming the validity of the results. Additionally, snapshots (Figure 3.2) clearly show that the W$\underline{L}_4$ nanotube loses its tubular structure in all solvent media. The lower RMSD and R_g values of W$\underline{L}_4$ in water are attributed to its tendency to form aggregates due to the high hydrophobicity of the W$\underline{L}_4$ rings. This aggregation is further supported by spatial density plots of CP around a reference CP molecule (Figure 3.9), where the density distribution around a CP ring is higher for the W$\underline{L}_4$ nanotube in water compared to the D$\underline{K}_4$ and D$\underline{L}$K$\underline{L}_2$ nanotubes. In methanol (a less polar solvent) and in non-polar solvents like chloroform and hexane, the CP density distribution for the amphiphilic D$\underline{L}$K$\underline{L}_2$ nanotube reflects the preservation of its tubular structure, indicating its stability. For the D$\underline{K}_4$ nanotube, the density of CP rings around a reference CP is minimal in water, and in other solvents, the CP rings do not maintain the tubular nanotube structure as effectively as observed in the D$\underline{L}$K$\underline{L}_2$ nanotube. The same observations can be drawn from the other two runs (2 and 3) which are presented in Figure 3.10 and Figure 3.11 respectively.

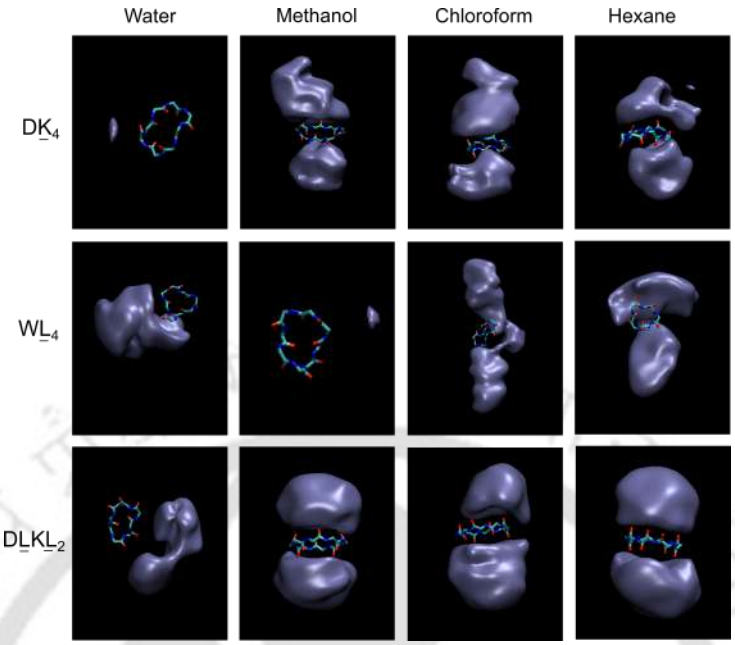

Figure 3.9: *Spatial density plots of CP rings around a reference CP ring for the three CPNTs across all solvent media for Run 1.*

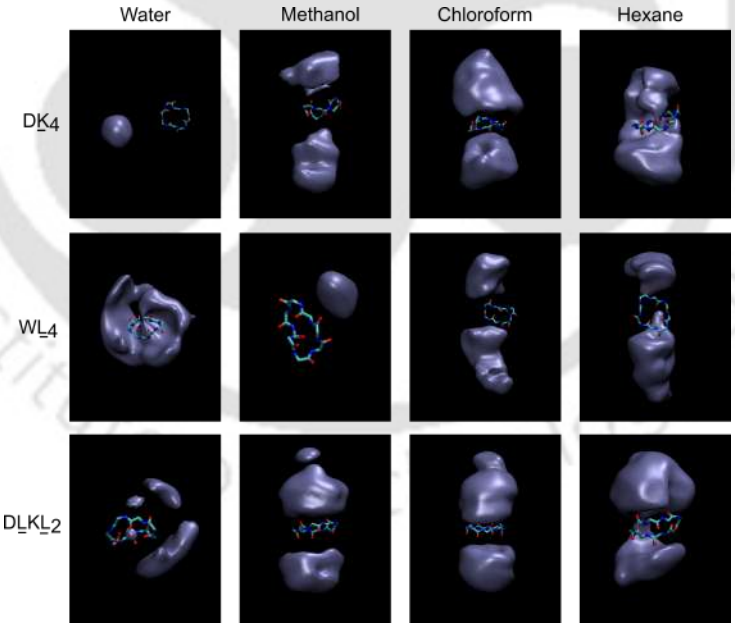

Figure 3.10: *Spatial density plots of CP rings around a reference CP ring for the three CPNTs across all solvent media for Run 2.*

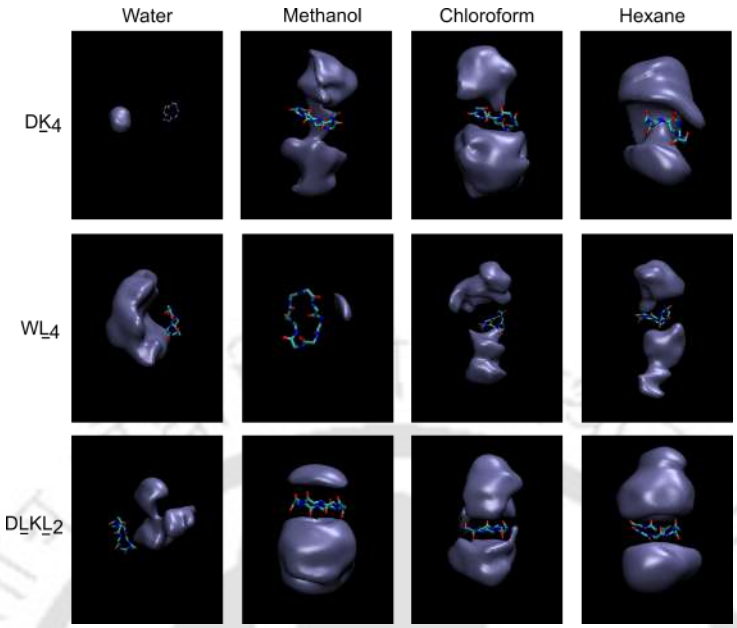

Figure 3.11: *Spatial density plots of CP rings around a reference CP ring for the three CPNTs across all solvent media for Run 3.*

The predominant factor behind the stability of the CPNTs is the intermolecular hydrogen bonds that are formed between the adjacent CP subunits[1]. The frequency of occurance of total number of hydrogen bonds between the backbone-backbone and side chain-side chain atoms of the three CPNTs in different solvents are shown in Figure 3.12. Each CP-unit can form at most 8 hydrogen bonds between the backbone atoms of the adjacent CP rings, and thus, accounting to maximum of 40 backbone-backbone H-bonds between 6 CP rings. As can be seen in Figure 3.12, the D$\underline{\text{L}}$K$\underline{\text{L}}_2$ nanotube forms the most number of backbone-backbone hydrogen bonds, reaching a maximum of 35 in methanol, followed by 30 in chloroform and 28 in hexane. The backbone-backbone H-bond is less for all nanotubes in water as water interacts with the backbone atoms of the CP rings. Additionally, the side chain-side chain hydrogen bonding provides extra stability to the D$\underline{\text{L}}$K$\underline{\text{L}}_2$ nanotube in all the solvent media except for water. The hydrophilic D$\underline{\text{K}}_4$ nanotube follows the similar trend but with the highest number of side chain-side chain hydrogen bonds due to its hydrophilic amino acid residues. On the contrary, W$\underline{\text{L}}_4$ nanotube has least number of backbone-backbone hydrogen bonds and almost negligible side chain-side chain hydrogen bonds in all the solvent media.

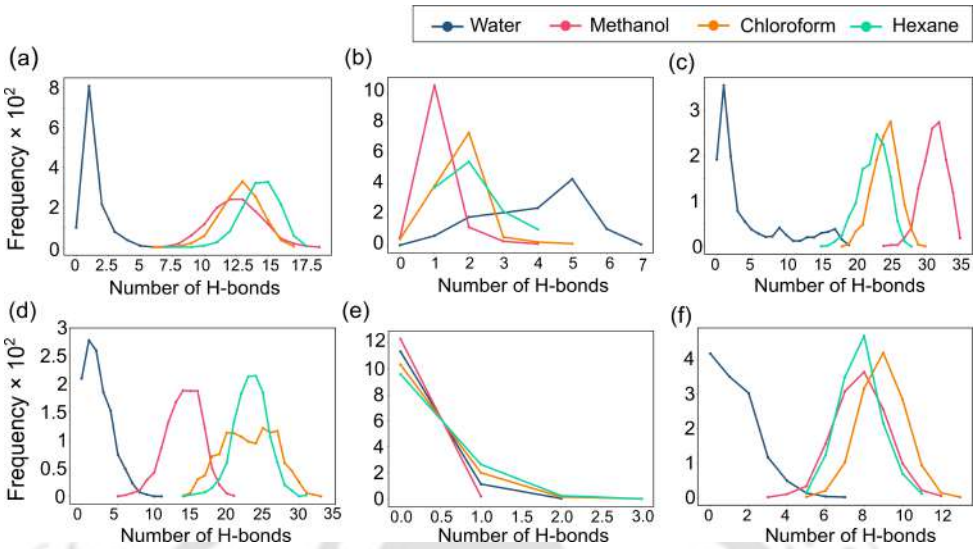

Figure 3.12: *Frequency of the number of hydrogen bonds formed between the backbone atoms for Run 1 of (a) D$\underline{K}_4$, (b) W$\underline{L}_4$, and (c) D$\underline{L}K\underline{L}_2$, and between the sidechain atoms of (d) D$\underline{K}_4$, (e) W$\underline{L}_4$, and (f) D$\underline{L}K\underline{L}_2$, respectively.*

As mentioned above that the number of backbone-backbone hydrogen bonds is high for CP rings in case of D$\underline{L}$K$\underline{L}_2$ in methanol, chloroform and hexane solvents. We have further evaluated the number of backbone-backbone hydrogen bonds between two adjacent CP rings in all the three solvents and plotted it against simulation time (Figure 3.13). This will shed some light on why D$\underline{L}$K$\underline{L}_2$ maintains its tubular structure in these solvent environments. In methanol, the number of hydrogen bonds remains consistently within the range of 7 to 8 throughout the entire trajectory for nanotube gaps 3-4, 4-5, and 5-6 (Figure 3.13(a)) indicating a stable nanotube structure. However, the number of hydrogen bonds is slightly lower for gap 2-3, with the least amount observed in gap 1-2. Notably, the number of hydrogen bonds in gap 1-2 represents the average number of hydrogen bonds between CP rings 1 and 2 (Figure 3.13(d)), and this pattern applies similarly to other gaps. In chloroform, gap 5-6 exhibits fewer hydrogen bonds compared to the other gaps (Figure 3.13(b)). In hexane, rings 1 and 2 are loosely bonded to the rest of the CP rings, as indicated by the lower number of hydrogen bonds in gaps 1-2 and gap 2-3 (Figure 3.13(c)). This leads us to conclude that the terminal rings form fewer hydrogen bonds and are more prone to detachment from the nanotube structure.

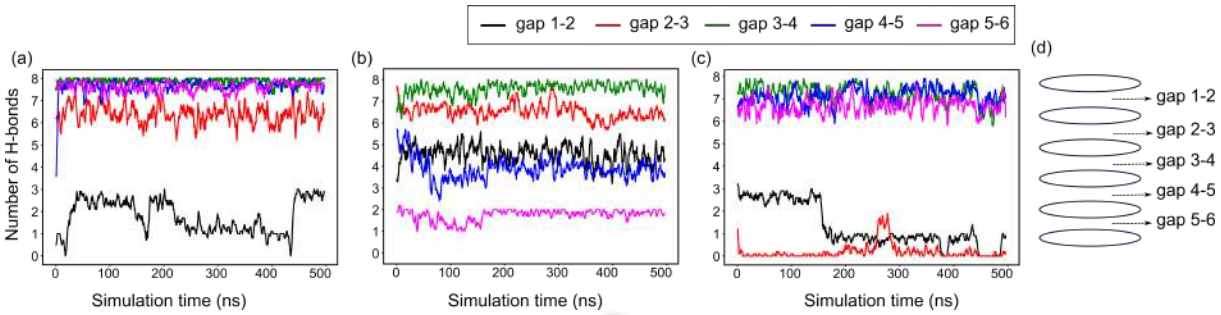

Figure 3.13: *Number of hydrogen bonds formed between the backbone atoms of adjacent CP rings for Run 1 of D$\underline{L}$K$\underline{L}_2$ over time in (a) methanol, (b) chloroform, and (c) hexane, along with (d) a schematic representation of the gap numbers in a CPNT.*

Again these intermolecular hydrogen bonds can be both parallel and antiparallel. In our previous study[37], we confirmed the presence of antiparallel hydrogen bonding between adjacent CP rings of D$\underline{L}$K$\underline{L}_2$ nanotube, consistent with the findings of Silk et. al.[1]. Given that the initial self-assembled structure of D$\underline{L}$K$\underline{L}_2$ nanotube features antiparallel hydrogen bonds between CP rings, the mutated D$\underline{K}_4$ and W$\underline{L}_4$ nanotubes also posses the same hydrogen bonding arrangements initially. Figure 3.14 illustrates the antiparallel hydrogen bonds in the D$\underline{L}$K$\underline{L}_2$ nanotube after 500 ns in methanol, chloroform and, hexane respectively. Similar representations are not shown for the other two nanotubes as they fail to maintain their tubular stacking in all the solvents.

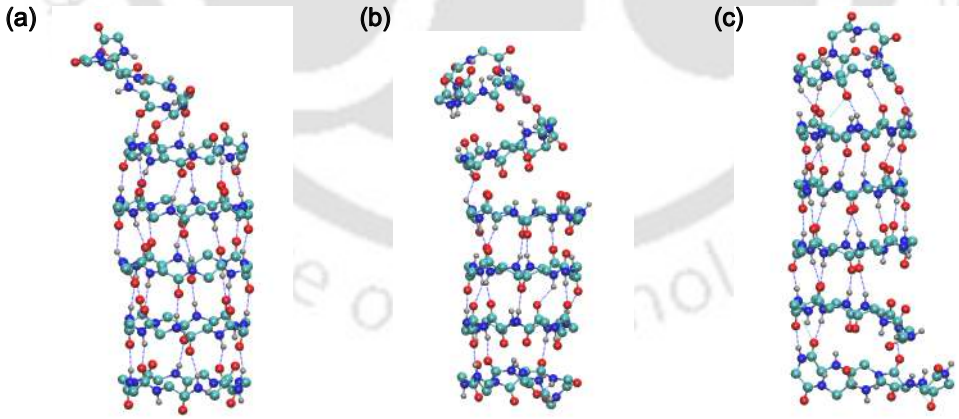

Figure 3.14: *Antiparallel hydrogen bonding (represented by blue dashed lines) between the backbone atoms of adjacent CP rings of D$\underline{L}$K$\underline{L}_2$ after 500 ns in (a) methanol, (b) chloroform, and (c) hexane.*

Additionally, the lifespan of hydrogen bonds formed between adjacent CP rings is

calculated using the continuous hydrogen bond correlation function ($S_{HB}(t)$). Given the presence of multiple hydrogen bonding sites between two CP rings, Table 3.2 highlights the top three hydrogen bonding pairs between the backbone atoms of adjacent CP rings in the D$\underline{L}$K$\underline{L}_2$ nanotube, focusing on those with the longest lifetimes in each solvent environment. The table reveals that hydrogen bond lifetimes are shorter in water in comparison to other solvents, suggesting that the CPNT struggles to maintain its tubular structure in the former medium. In contrast, the backbone hydrogen bond lifetimes are longer and relatively consistent across the other solvents. However, the specific bonding pairs with the highest lifetimes vary across systems, which is expected given the dynamic nature of these interactions. The decay functions $S_{HB}(t)$ versus time for the three most dominant hydrogen bonds formed between the backbone atoms of adjacent CP rings in D$\underline{L}$K$\underline{L}_2$ for Run 1 are presented in Figure 3.15

Table. 3.2: *The lifetimes ($<\tau_{HB}>$) of continuous hydrogen bonds S(t) between various backbone atom pairs in D$\underline{L}$K$\underline{L}_2$ across different solvents for Run 1. The table highlights the three pairs with the longest lifetimes in each solvent alongwith the corresponding amino acid residue numbers (as superscipts). Lifetime values are given in picoseconds (ps).*

Solvent	Bonding CP pairs	Bonding amino acids	Lifetime value ($<\tau_{HB}>$)
Water	CP3-CP4	^{6}LEU@O-^{4}LYS@N-H	10.47
	CP4-CP5	^{4}LYS@O-^{6}LEU@N-H	9.91
	CP3-CP6	^{5}LEU@O-^{1}LEU@N-H	9.49
Methanol	CP3-CP2	^{8}LEU@O-^{8}LEU@N-H	24.33
	CP5-CP4	^{6}LEU@O-^{5}LEU@N-H	20.85
	CP5-CP4	^{4}LEU@O-^{7}LEU@N-H	18.88
Chloroform	CP2-CP3	^{2}LEU@O-^{6}LEU@N-H	24.20
	CP3-CP2	^{2}LEU@O-^{6}LEU@N-H	18.23
	CP4-CP3	^{2}ASP@O-^{7}ASP@N-H	13.95
Hexane	CP3-CP4	^{7}ASP@O-^{2}ASP@N-H	23.08
	CP4-CP5	^{1}LEU@O-^{2}LEU@N-H	16.57
	CP5-CP4	^{2}LEU@O-^{1}LEU@N-H	13.99

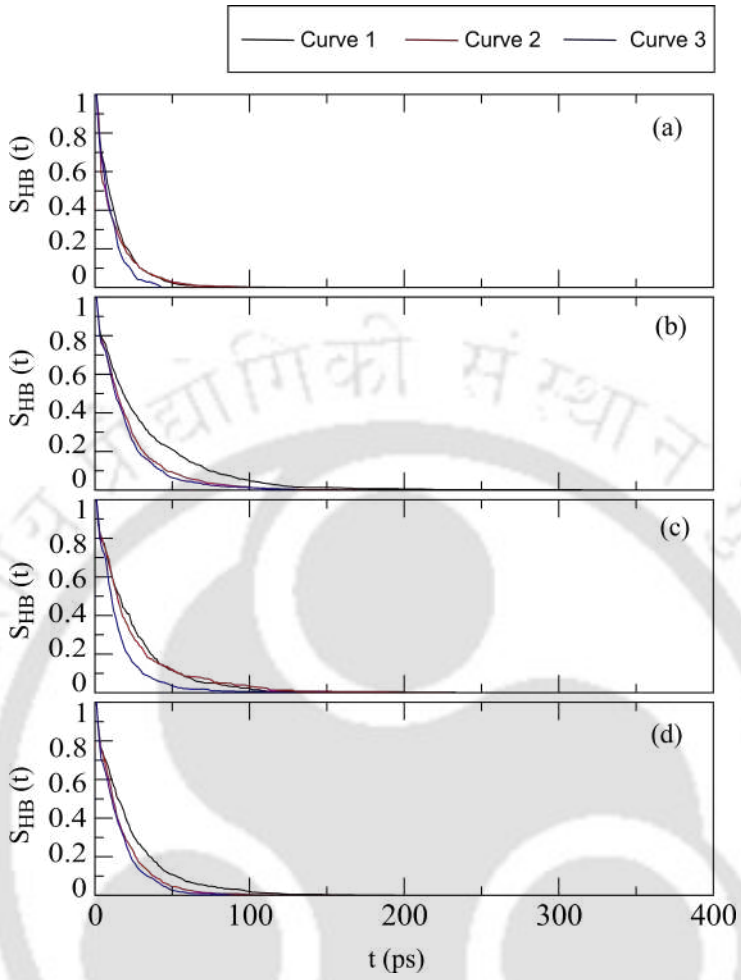

Figure 3.15: *The top three continuous hydrogen bond correlation functions for the backbone hydrogen bonding pairs between CP molecules of $DLKL_2$ having the highest lifetime values in (a) water, (b) methanol, (c) chloroform, and (d) hexane. The curves are numbered according to the decreasing lifetime values.*

To further understand the stability of the nanotubes in different solvent environments, we broke down the total non-bonded interaction energies between the CP rings of the three CPNTs into electrostatic and van der Waals components. Figure 3.16 illustrates the electrostatic and van der Waals energies between the gaps of adjacent CP rings in each solvent. The more negative electrostatic energy values for D$\underline{\text{K}}_4$ and D$\underline{\text{L}}$K$\underline{\text{L}}_2$, compared to van der Waals energy suggest that electrostatic interactions are more significant in contributing to the stability of these nanotubes. Moreover, the electrostatic interaction energy of D$\underline{\text{L}}$K$\underline{\text{L}}_2$ in methanol, chloroform, and hexane follows a distinct pattern (Figure 3.16(c)).

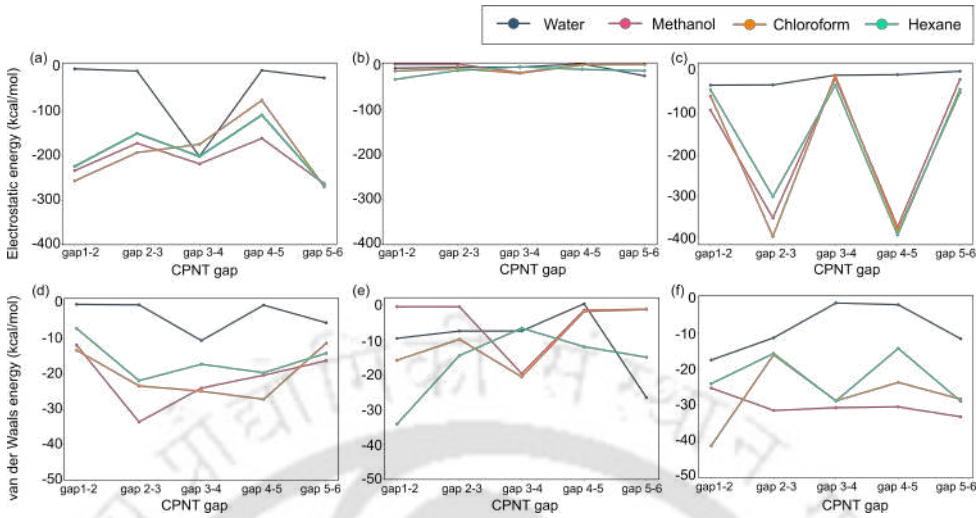

Figure 3.16: *Average electrostatic interaction energy between adjacent CP rings of (a) D$\underline{K}_4$, (b) W$\underline{L}_4$, and (c) D$\underline{L}$K$\underline{L}_2$, along with the average van der Waals interaction energy between adjacent CP rings of (d) D$\underline{K}_4$, (e) W$\underline{L}_4$, and (f) D$\underline{L}$K$\underline{L}_2$ for Run 1 across different solvent media.*

To understand the reason behind this, we further analyzed the electrostatic and van der Waals interaction energies between the backbone-backbone and side chain-side chain atoms of the adjacent CP rings of D$\underline{L}$K$\underline{L}_2$ in these solvents, as shown in Figure 3.17. While both the backbone-backbone and side chain-side chain atoms of the adjacent CP rings exhibit favorable van der Waals interactions (Figure 3.17(c and d)), the electrostatic contributions from the backbone atoms are unfavorable (Figure 3.17(a)). However, the side chain-side chain interactions in gaps 2-3 and 4-5 display favorable electrostatic interactions (Figure 3.17(b)), which are crucial for stabilizing the tubular nanotube structure across all these solvents. These favorable electrostatic interactions take place between the positively charged lysine and negatively charged aspartic acid residues in rings 2 and 3, and rings 4 and 5 of the D$\underline{L}$K$\underline{L}_2$ nanotube, providing additional stability to the structure.

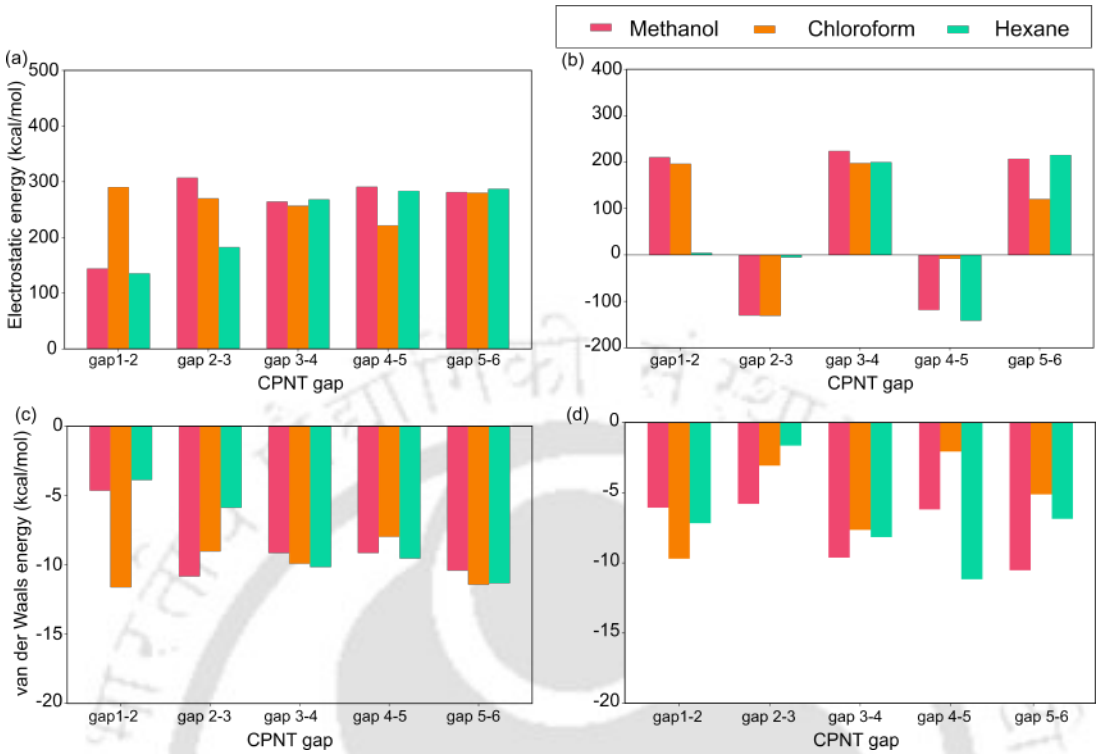

Figure 3.17: *Average electrostatic interaction energy between (a) the backbone atoms and (b) the sidechain atoms of adjacent CP rings of D$\underline{L}$K$\underline{L}_2$, along with the average van der Waals interaction energy between (c) the backbone atoms and (d) the sidechain atoms of adjacent CP rings of D$\underline{L}$K$\underline{L}_2$ for Run 1 in different solvent environments.*

So far, we have focused on the stability of the tubular structure of the three CPNTs in various solvent environments. However, for a nanotube to be truly stable, the circular structure of each CP ring that constitutes the nanotube must also remain largely intact. In a vacuum, a CP ring is expected to maintain a circular structure, but it may undergo slight deformation in an actual solvent environment. This deformation of the CP ring is quantified by measuring ellipticity (Equation 3.1). Figure 3.18 shows the average ellipticity of all six CP rings forming the three CPNTs across different solvent environments. The extent of deformation of each CP ring from a perfect circular structure is indicated by how much the ellipticity value deviates from 1.0. In MD simulations, an ellipticity value of 1.4 or less is generally considered a minor deformation[29]. Figure 3.18 (d) shows the snapshots of the deformed CP rings with ellipticity values 1.15, 1.24, 2.01, 2.28, and 2.50 respectively. Both hydrophilic D$\underline{K}_4$ and hydrophobic W$\underline{L}_4$ nanotubes exhibit significant deviations from the circular structure of their CP subunits and lack a consistent pattern

across all solvents. In the amphiphilic D$\underline{L}$K$\underline{L}_2$ nanotube, all CP rings, except 1 and 2 in water, show substantial deformation from a circular structure. However, in other solvents, aside from the terminal rings (CP1 and CP6), the D$\underline{L}$K$\underline{L}_2$ rings experience only minor deformation, indicating a stable nanotube conformation. This suggests that D$\underline{L}$K$\underline{L}_2$, in addition to maintaining its tubular structure in all solvents except highly polar water, also retains the circular structure of its CP subunits, making it a strong candidate for a stable CPNT.

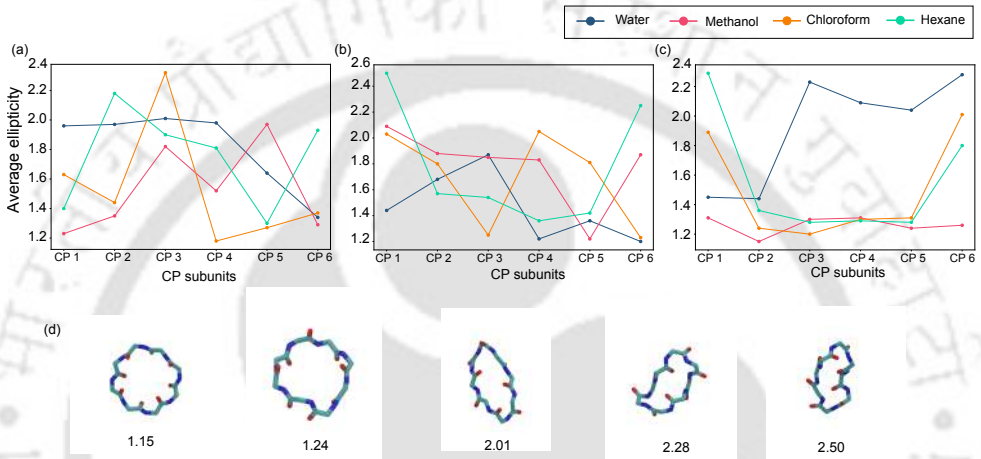

Figure 3.18: *Average ellipticity of the CP rings for Run 1 of (a) D$\underline{K}_4$, (b) W$\underline{L}_4$, and (c) D$\underline{L}$K$\underline{L}_2$ over time across all solvent media. (d) Snapshots showing the deformed CP rings with respective ellipticity values.*

3.3.2 Enhanced Stability of D$\underline{L}$K$\underline{L}_2$ Nanotubes over D$\underline{K}_4$ and W$\underline{L}_4$

Till now we have observed that the D$\underline{L}$K$\underline{L}_2$ nanotube consistently demonstrates superior stability across various solvents (except water) compared to D$\underline{K}_4$ and W$\underline{L}_4$ nanotubes. This enhanced stability is largely due to the intermolecular hydrogen bonding patterns and electrostatic interactions between the adjacent CP rings in those media. It is well reported that the stacking of CP rings is driven by hydrogen bonds, particularly those between NH and CO groups of adjacent CP rings[1, 3]. These backbone-backbone interactions are crucial for maintaining the nanotube's structure, and in D$\underline{L}$K$\underline{L}_2$, they are supplemented by sidechain-sidechain hydrogen bonds that further stabilize the tubular conformation (Figure 3.12). In contrast, the W$\underline{L}_4$ nanotube, which is hydrophobic, lacks significant sidechain hydrogen bonding, and its backbone-backbone hydrogen bonds are

minimal (Figure 3.12). This weak bonding leads to a loss of the tubular structure in W$\underline{L}_4$.

While the D$\underline{K}_4$ nanotube also forms sufficient backbone-backbone and sidechain-sidechain hydrogen bonds, it is less stable than D$\underline{L}$K$\underline{L}_2$ due to the hydrophilic nature of its CP rings. D$\underline{K}$'s charged amino acids, arranged alternately, promote strong intramolecular hydrogen bonds between aspartic acid and lysine residues. This intramolecular bonding reduces the number of interpeptide backbone hydrogen bonds, which weakens the overall nanotube structure. Additionally, the electrostatic interactions within D$\underline{K}_4$'s CP rings are high, leading to significant deformation of the circular shape of the rings, as evidenced by the high ellipticity values observed for D$\underline{K}_4$ in all solvents (Figure 3.18).

The introduction of leucine between aspartic acid and lysine in the D$\underline{L}$K$\underline{L}_2$ nanotube mitigates these effects. Leucine, being hydrophobic in nature, reduces intramolecular hydrogen bonding, particularly in the inner CP rings, allowing for more robust interpeptide backbone hydrogen bonding and thereby enhancing the stability of the D$\underline{L}$K$\underline{L}_2$ nanotube. This modification also reduces intramolecular electrostatic interactions, helping to preserve the circular shape of the CP rings in all solvents except water (Figure 3.18). The importance of these interactions in maintaining stability is illustrated in Figure 3.19 (a) and (b), which show the intramolecular hydrogen bonds and electrostatic interactions within the six CP rings of D$\underline{L}$K$\underline{L}_2$ and D$\underline{K}_4$ in methanol, respectively. As depicted, D$\underline{L}$K$\underline{L}_2$ has minimal intramolecular hydrogen bonds, particularly in the inner CP rings, whereas D$\underline{K}_4$ exhibits a higher number of intramolecular hydrogen bonds. Additionally, the electrostatic interactions among the amino acid residues within each CP ring are more pronounced in D$\underline{K}_4$ compared to D$\underline{L}$K$\underline{L}_2$.

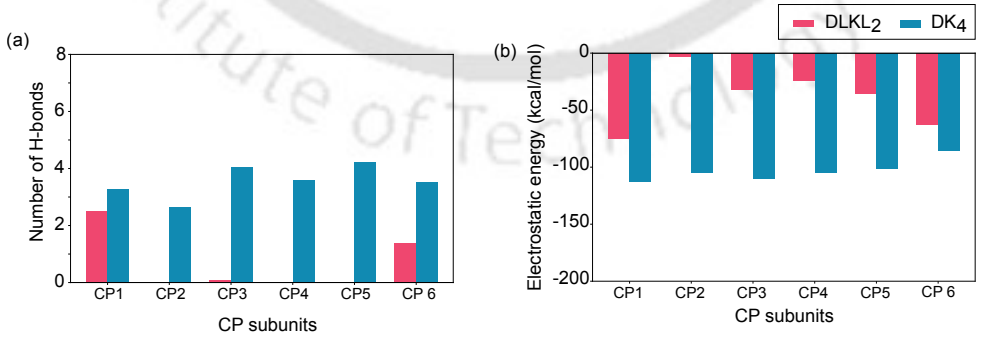

Figure 3.19: *(a) Average number of hydrogen bonds formed within the CP rings, and (b) average electrostatic interaction energy within the CP rings of D$\underline{L}$K$\underline{L}_2$ and D$\underline{K}_4$ nanotubes for Run 1 in methanol.*

3.3.3 Interaction of the Solvent Medium with CPNT

It has become evident by now that CPNTs exhibit greater stability in methanol, chloroform, and hexane compared to water. In this section, we will examine how different solvent molecules interact with the CPNTs. Figure 3.20 (a)-(c) displays the variation of the preferential interaction parameter, $\tau^{cp}_{cp/s}$ with respect to distance, which measures the preference of CP subunits to interact with each other over solvent molecules for the D$\underline{\text{K}}_4$, W$\underline{\text{L}}_4$, and D$\underline{\text{L}}$KunderlineL$_2$ nanotubes, respectively. The positive $\tau^{cp}_{cp/s}$ values across all systems indicate that CP rings consistently prefer interactions with each other rather than with solvent molecules in every solvent. Notably, for the D$\underline{\text{K}}_4$ and D$\underline{\text{L}}$K$\underline{\text{L}}_2$ nanotubes, $\tau^{cp}_{cp/s}$ is significantly higher in methanol, chloroform, and hexane, highlighting the strong tendency of CP rings to interact among themselves rather than with the solvent. Conversely, the W$\underline{\text{L}}_4$ nanotube shows the highest $\tau^{cp}_{cp/s}$ value in water, reflecting the increased aggregation of hydrophobic W$\underline{\text{L}}_4$ rings in this environment, as discussed earlier.

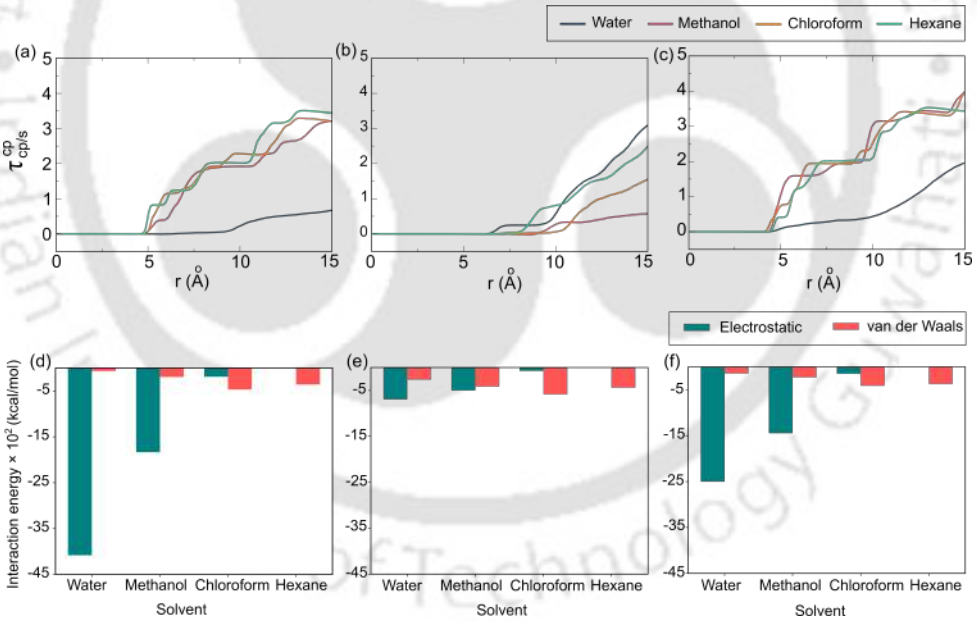

Figure 3.20: *Preferential interaction parameter ($\tau^{cp}_{cp/s}$) of CP for CP over solvent molecules for (a) D$\underline{\text{K}}_4$, (b) W$\underline{\text{L}}_4$, and (c) D$\underline{\text{L}}$K$\underline{\text{L}}_2$, along with the average electrostatic and van der Waals interaction energy between different solvents and CP rings of (d) D$\underline{\text{K}}_4$, (e) W$\underline{\text{L}}_4$, and (f) D$\underline{\text{L}}$K$\underline{\text{L}}_2$ nanotubes for Run 1.*

Again, D$\underline{\text{K}}_4$, the most hydrophilic nanotube, exhibits the highest electrostatic interactions with water, the most polar solvent, while D$\underline{\text{L}}$K$\underline{\text{L}}_2$ shows intermediate levels, and

W$\underline{L}_4$ displays the lowest interaction (Figure 3.20 (d)-(f)). A similar trend is observed in methanol. However, as we transition from polar to non-polar solvents, van der Waals interactions become more evident compared to electrostatic interactions in peptide-solvent interactions. Furthermore, the number of hydrogen bonds formed between the CPNTs and different solvent media, is highest in case of D$\underline{K}_4$, whereas W$\underline{L}_4$ forms the fewest across all solvents (Table 3.3). D$\underline{L}$K$\underline{L}_2$, due to its amphiphilic nature, shows an intermediate number of hydrogen bonds compared to the other two CPNTs. As anticipated, the number of hydrogen bonds decreases from polar to non-polar solvents. Additionally, the sidechains of D$\underline{K}_4$, being hydrophilic, form the highest number of hydrogen bonds with solvents, particularly water and methanol, compared to the other two CPNTs (Figure 3.21).

Table. 3.3: *Average number of hydrogen bonds formed between the respective CPNTs with all the different solvents considered in this study. Here, both backbone and side chain atoms of the CPNTs are considered for calculating hydrogen bond count.*

	Run	Water	Methanol	Chloroform	Hexane
D$\underline{K}_4$	1	303.98	167.08	32.46	5.96
	2	302.16	167.62	30.91	6.05
	3	310.26	184.74	31.73	7.30
W$\underline{L}_4$	1	126.96	73.61	15.16	3.76
	2	135.26	74.15	15.59	3.61
	3	124.97	72.46	17.43	3.34
D$\underline{L}$K$\underline{L}_2$	1	194.30	103.01	19.15	3.44
	2	189.48	112.84	21.90	3.58
	3	189.99	103.95	22.30	4.00

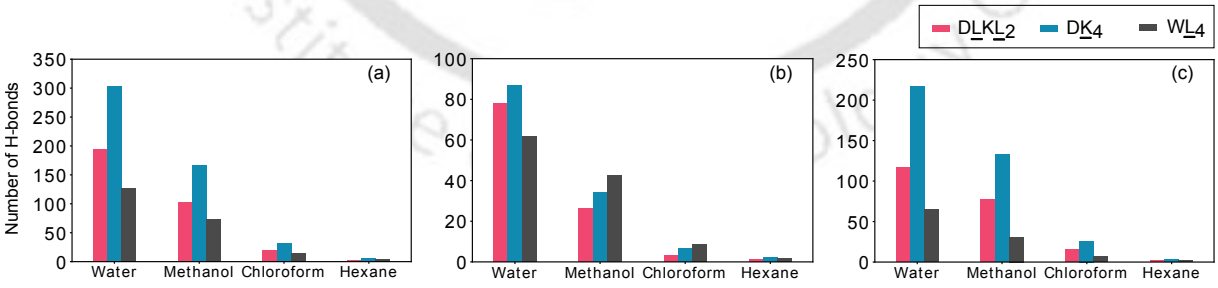

Figure 3.21: *Average H-bonds formed between all atoms and the solvent (a), backbone atoms and the solvent (b), and sidechain atoms and the solvent (c) of the three CPNTs for Run 1.*

3.3.4 Binding Free Energy of the CP rings of the CPNTs

In this subsection, we assess the free energy of binding of each CP ring within the CPNT relative to its adjacent rings to understand how the solvent environment influences the binding affinity of the CP subunits. For the inner CP rings, the adjacent rings are those immediately above and below. For the terminal rings, only one adjacent ring is considered: CP 2 for CP 1, and CP 5 for CP 6. Table 3.4 displays the binding free energy values (ΔG^i_{bind}) for each CP ring of the D$\underline{\text{L}}$K$\underline{\text{L}}_2$ nanotube, calculated using both the MMGBSA and MMPBSA methods across all the solvents considered in this study.

As discussed above, the D$\underline{\text{L}}$K$\underline{\text{L}}_2$ nanotube is unstable in water, which is reflected in the low ΔG^i_{bind} values for all CP rings in this solvent. In contrast, the ΔG^i_{bind} values in other solvent environments are significantly negative, indicating stronger binding affinity in other three solvents. Furthermore, the inner CP rings show more negative binding energy values compared to the terminal rings, suggesting that the terminal rings are more loosely bound than the inner rings of the D$\underline{\text{L}}$K$\underline{\text{L}}_2$ nanotube.

Table. 3.4: *Binding free energy (ΔG^i_{bind}) values of each CP rings of D$\underline{L}$K$\underline{L}_2$. Units are expressed in kcal mol^{-1}. The standard error of ΔG^i_{bind} for each CP rings are given in parentheses.*

	Water	Methanol	Chloroform	Hexane
MMGBSA				
CP 1	-19.47 (± 0.03)	-26.62 (± 0.04)	-41.33 (± 0.04)	-18.85 (± 0.05)
CP 2	-25.16 (± 0.04)	-75.71 (± 0.06)	-90.81 (± 0.07)	-63.30 (± 0.08)
CP 3	-5.41 (± 0.02)	-82.22 (± 0.06)	-80.28 (± 0.07)	-75.74 (± 0.07)
CP 4	-4.43 (± 0.03)	-87.20 (± 0.06)	-82.71 (± 0.06)	-80.13 (± 0.06)
CP 5	-8.41 (± 0.04)	-85.92 (± 0.06)	-71.74 (± 0.09)	-77.91 (± 0.06)
CP 6	-3.75 (± 0.02)	-37.16 (± 0.03)	-25.10 (± 0.03)	-30.99 (± 0.03)
MMPBSA				
CP 1	-5.99 (± 0.03)	-16.76 (± 0.06)	-14.09 (± 0.05)	-7.64 (± 0.05)
CP 2	-7.61 (± 0.07)	-35.81 (± 0.09)	-44.17 (± 0.08)	-32.07 (± 0.09)
CP 3	-0.81 (± 0.02)	-31.63 (± 0.08)	-44.87 (± 0.07)	-50.88 (± 0.08)
CP 4	2.14 (± 0.05)	-41.95 (± 0.09)	-63.84 (± 0.07)	-43.00 (± 0.07)
CP 5	1.20 (± 0.05)	-41.21 (± 0.08)	-46.97 (± 0.08)	-37.82 (± 0.07)
CP 6	-0.31 (± 0.02)	-20.34 (± 0.04)	-3.38 (± 0.04)	-12.02 (± 0.04)

Similarly, for the D$\underline{K}_4$ nanotube, the binding free energy values are lowest in water, as D$\underline{K}_4$, being hydrophilic, prefers interacting with water over binding with itself (Table 3.5). In the other three solvents, the ΔG^i_{bind} values are strongly negative, similar to D$\underline{L}$K$\underline{L}_2$, indicating strong binding affinity. However, the inner CP rings (CP 3 and CP 4) exhibit lower binding energy compared to their adjacent rings in chloroform and hexane, which disrupts the tubular stacking conformation of the nanotube. For the hydrophobic W$\underline{L}_4$ nanotube, the ΔG^i_{bind} values do not follow a consistent trend, indicating that the tubular structure of W$\underline{L}_4$ is compromised in all solvent environments (Table 3.6).

Table. 3.5: *Binding free energy (ΔG^i_{bind}) values of each CP rings of DK_4. Units are expressed in kcal mol^{-1}. The standard error of ΔG^i_{bind} for each CP rings are given in parentheses.*

	Water	Methanol	Chloroform	Hexane
MMGBSA				
CP 1	0.04 (± 0.02)	-26.26 (± 0.04)	-26.98 (± 0.03)	-36.92 (± 0.05)
CP 2	0.18 (± 0.03)	-70.21 (± 0.04)	-70.21 (± 0.07)	-74.32 (± 0.05)
CP 3	-26.72 (± 0.03)	-82.76 (± 0.03)	-82.86 (± 0.05)	-84.24 (± 0.06)
CP 4	-26.66 (± 0.03)	-66.73 (± 0.03)	-64.30 (± 0.06)	-64.94 (± 0.07)
CP 5	0.28 (± 0.02)	-50.61 (± 0.07)	-75.98 (± 0.05)	-80.71 (± 0.05)
CP 6	0.08 (± 0.04)	-21.59 (± 0.03)	-44.85 (± 0.02)	-48.90 (± 0.02)
MMPBSA				
CP 1	0.60 (± 0.03)	-15.61 (± 0.06)	-31.31 (± 0.04)	-41.55 (± 0.03)
CP 2	0.71 (± 0.02)	-38.00 (± 0.05)	-46.91 (± 0.08)	-46.86 (± 0.08)
CP 3	-37.92 (± 0.03)	-47.62 (± 0.08)	-31.90 (± 0.06)	-30.48 (± 0.04)
CP 4	-37.44 (± 0.03)	-38.88 (± 0.08)	-24.02 (± 0.06)	-33.10 (± 0.06)
CP 5	1.17 (± 0.04)	-33.89 (± 0.07)	-37.77 (± 0.07)	-56.33 (± 0.06)
CP 6	0.65 (± 0.02)	-17.92 (± 0.04)	-28.44 (± 0.03)	-38.70 (± 0.03)

Table. 3.6: *Binding free energy (ΔG^i_{bind}) values of each CP rings of WL_4. Units are expressed in kcal mol^{-1}. The standard error of ΔG^i_{bind} for each CP rings are given in parentheses.*

	Water	Methanol	Chloroform	Hexane
MMGBSA				
CP 1	-12.57 (± 0.05)	-1.37 (± 0.03)	-6.06 (± 0.03)	-35.00 (± 0.03)
CP 2	-19.33 (± 0.04)	-1.38 (± 0.05)	-17.65 (± 0.04)	-55.44 (± 0.06)
CP 3	-25.50 (± 0.03)	-13.98 (± 0.04)	-38.09 (± 0.03)	-43.58 (± 0.04)
CP 4	-22.29 (± 0.03)	-16.23 (± 0.05)	-26.02 (± 0.05)	-32.82 (± 0.03)
CP 5	-23.68 (± 0.03)	-2.20 (± 0.05)	0.09 (± 0.04)	-35.24 (± 0.05)
CP 6	-20.35 (± 0.01)	0.01 (± 0.03)	-0.06 (± 0.02)	-25.28 (± 0.02)
MMPBSA				
CP 1	-3.48 (± 0.06)	0.93 (± 0.03)	-0.34 (± 0.02)	-17.75 (± 0.03)
CP 2	-4.28 (± 0.05)	0.93 (± 0.05)	-8.11 (± 0.04)	-29.06 (± 0.07)
CP 3	-9.02 (± 0.04)	-4.90 (± 0.04)	-19.95 (± 0.03)	-15.43 (± 0.05)
CP 4	-9.51 (± 0.03)	-5.24 (± 0.05)	-11.76 (± 0.04)	-6.12 (± 0.04)
CP 5	-8.60 (± 0.03)	0.17 (± 0.04)	0.70 (± 0.04)	-13.34 (± 0.04)
CP 6	-6.90 (± 0.01)	0.57 (± 0.03)	0.63 (± 0.03)	-9.92 (± 0.03)

3.4 Conclusion and Summary

Cyclic peptides (CPs) can self-assemble into cyclic peptide nanotubes (CPNTs), which have diverse applications in the field of nanotechnology. The formation and stability of these nanotubes are affected by several factors. In this chapter, we have thoroughly investigated the tendency to retain the tubular structure of cyclic peptide nanotubes (CPNTs) composed of the amphiphilic D$\underline{\text{L}}$K$\underline{\text{L}}_2$ ((Asp-D-Leu-Lys-D-Leu)$_2$), hydrophilic D$\underline{\text{K}}_4$ ((Asp-D-Lys)$_4$), and hydrophobic W$\underline{\text{L}}_4$ ((Trp-D-Leu)$_4$) peptides in four different solvent environments: water, methanol, chloroform, and hexane. Our findings reveal that the stability and structural integrity of these CPNTs are significantly influenced by the nature of the solvent and the specific interactions within the peptide subunits.

The D$\underline{\text{L}}$K$\underline{\text{L}}_2$ nanotube exhibits the least fluctuation and compactness variation across solvents, confirming its stability over the other two nanotubes. Additionally D$\underline{\text{L}}$K$\underline{\text{L}}_2$ maintains a more circular and tightly packed conformation compared to D$\underline{\text{K}}_4$ and W$\underline{\text{L}}_4$, whose structures are more prone to deformation, particularly in polar solvents. The structural

differences between these CPNTs are further highlighted with the help of hydrogen bond formation which plays a significant role in the stability of CPNTs. D$\underline{L}$K$\underline{L}_2$ nanotube consistently forms a moderate number of hydrogen bonds among the CP subunits, with the lifespan of these bonds being almost identical in all solvents other than water. D$\underline{K}_4$ forms numerous but less effective hydrogen bonds, leading to less stable assemblies, while W$\underline{L}_4$, with minimal side chain-side chain interactions, exhibits the fewest backbone hydrogen bonds, further contributing to its instability. Notably, the terminal rings of D$\underline{L}$K$\underline{L}_2$ are loosely hydrogen bonded to adjacent subunits, compared to the inner rings. This observation aligns with the findings of Vijayaraj et al.[3], who reported that the overall stability of a CPNT is governed by the length of the core region, i.e., the number of hydrogen bonds between the inner rings.

Additionally, an antiparallel hydrogen bonding arrangement predominates between the CP rings of D$\underline{L}$K$\underline{L}_2$ in all solvents. This observation aligns with previous studies by Silk et al.[1, 38], who reported similar behavior in this specific nanotube. They further noted that the incorporation of hydrophobic amino acids enhances the stability of CP dimers through inter-CP side chain interactions, although an increase in the number of hydrophobic amino acids reduces aqueous solubility. Our findings support and extend these observations, confirming their relevance in the context of CPNTs in various solvent environments.

Moreover, this study demonstrates that the presence of leucine in D$\underline{L}$K$\underline{L}_2$ plays a crucial role in enhancing the stability of the nanotube by reducing disruptive intramolecular interactions and promoting more stable inter-ring hydrogen bonding. The amphiphilic design of D$\underline{L}$K$\underline{L}_2$ provides a balanced interplay between hydrophilic and hydrophobic interactions, making it more stable across a range of solvent environments compared to D$\underline{K}_4$ and W$\underline{L}_4$. Finally, the binding free energy estimation, calculated using both MM/GBSA and MM/PBSA methods, shows that D$\underline{L}$K$\underline{L}_2$ nanotubes exhibit strong stability in all solvents except water, with highly negative binding free energy values. In contrast, D$\underline{K}_4$ and W$\underline{L}_4$ show less stability, with W$\underline{L}_4$ failing to maintain its tubular structure across all solvents. The higher stability of D$\underline{L}$K$\underline{L}_2$ is attributed to its amphiphilic nature, where leucine residues disrupt excessive intramolecular interactions, allowing for more efficient interpeptide hydrogen bonding and reducing electrostatic stress, especially in the inner rings. D$\underline{K}_4$'s high intramolecular hydrogen bonding and electrostatic interactions, particularly between aspartic acid and lysine, contribute to its reduced stability and deformation,

as observed through its higher ellipticity values, indicating a deviation from the ideal circular shape of CP rings. In conclusion, the amphiphilic D$\underline{L}$K$\underline{L}_2$ nanotube demonstrates superior stability in all solvents except pure water, while the D$\underline{K}_4$ and W$\underline{L}_4$ nanotubes fail to maintain their tubular structures in any solvent.

Overall, this chapter provides valuable insights into the impact of molecular architecture and solvent conditions on the self-assembly and stability of CPNTs. These findings hold significant implications for the design and development of CPNTs as nanocarriers in drug and gene delivery, nanomaterial fabrication, and various other biomedical applications.

References

(1) Silk, M. R.; Newman, J.; Ratcliffe, J. C.; White, J. F.; Caradoc-Davies, T.; Price, J. R.; Perrier, S.; Thompson, P. E.; Chalmers, D. K. *Chem. Commun.* **2017**, *53*, 6613–6616.

(2) Calvelo, M.; Lamas, A.; Guerra, A.; Amorín, M.; Garcia-Fandino, R.; Granja, J. R. *Chem. Eur. J.* **2020**, *26*, 5846–5858.

(3) Vijayaraj, R.; Sundar Raman, S.; Mahesh Kumar, R.; Subramanian, V. *J. Phys. Chem. B* **2010**, *114*, 16574–16583.

(4) Vijayaraj, R.; Van Damme, S.; Bultinck, P.; Subramanian, V. *Phys. Chem. Chem. Phys.* **2012**, *14*, 15135–15144.

(5) Khavani, M.; Izadyar, M.; Housaindokht, M. R. *J. Mol. Liq.* **2020**, *314*, 113660.

(6) Vijayakumar, V.; Vijayaraj, R.; Peters, G. H. *J. Mol. Model.* **2016**, *22*, 1–12.

(7) Vijayaraj, R.; Van Damme, S.; Bultinck, P.; Subramanian, V. *J. Phys. Chem. B* **2012**, *116*, 9922–9933.

(8) Insua, I.; Montenegro, J. *J. Am. Chem. Soc.* **2019**, *142*, 300–307.

(9) Izadyar, M.; Khavani, M.; Housaindokht, M. R. *Phys. Chem. Chem. Phys.* **2015**, *17*, 11382–11391.

(10) Adler-Abramovich, L.; Reches, M.; Sedman, V. L.; Allen, S.; Tendler, S. J.; Gazit, E. *Langmuir* **2006**, *22*, 1313–1320.

(11) Ghadiri, M. R.; Granja, J. R.; Milligan, R. A.; McRee, D. E.; Khazanovich, N. *Nature* **1993**, *366*, 324–327.

(12) Jorgensen, W. L.; Chandrasekhar, J.; Madura, J. D.; Impey, R. W.; Klein, M. L. *J. Chem. Phys.* **1983**, *79*, 926–935.

(13) Maier, J. A.; Martinez, C.; Kasavajhala, K.; Wickstrom, L.; Hauser, K. E.; Simmerling, C. *J. Chem. Theory Comput.* **2015**, *11*, 3696–3713.

(14) Jorgensen, W. L. *J. Am. Chem. Soc.* **1981**, *103*, 335–340.

(15) Cieplak, P.; Caldwell, J.; Kollman, P. *J. Comput. Chem.* **2001**, *22*, 1048–1057.

(16) Wang, J.; Wang, W.; Kollman, P. A.; Case, D. A. *J. Mol. Graphics Modell.* **2006**, *25*, 247–260.

(17) Frisch, M. J.; Trucks, G. W.; Schlegel, H. B.; Scuseria, G. E.; Robb, M. A.; Cheeseman, J. R.; et al. Gaussian 09, Revision A.02.; Gaussian, Inc., Wallingford, CT, 2009.

(18) Bayly, C. I.; Cieplak, P.; Cornell, W.; Kollman, P. A. *J. Phys. Chem.* **1993**, *97*, 10269–10280.

(19) Case, D. A. et al. Amber 18., University of California: San Francisco, CA, 2018.

(20) He, X.; Man, V. H.; Yang, W.; Lee, T.-S.; Wang, J. *J. Chem. Phys.* **2020**, *153*, 114502.

(21) Martínez, L.; Andrade, R.; Birgin, E. G.; Martínez, J. M. *J. Comput. Chem.* **2009**, *30*, 2157–2164.

(22) Berendsen, H. J.; Postma, J. v.; Van Gunsteren, W. F.; DiNola, A.; Haak, J. R. *J. Chem. Phys.* **1984**, *81*, 3684–3690.

(23) Hünenberger, P. H. *Adv. Polym. Sci.* **2005**, 105–149.

(24) Ryckaert, J.-P.; Ciccotti, G.; Berendsen, H. J. *J. Comput. Phys.* **1977**, *23*, 327–341.

(25) Essmann, U.; Perera, L.; Berkowitz, M. L.; Darden, T.; Lee, H.; Pedersen, L. G. *J. Chem. Phys.* **1995**, *103*, 8577–8593.

(26) Roe, D. R.; Cheatham III, T. E. *J. Chem. Theory Comput.* **2013**, *9*, 3084–3095.

(27) Humphrey, W.; Dalke, A.; Schulten, K. *J. Mol. Graphics* **1996**, *14*, 33–38.

(28) Pettersen, E. F.; Goddard, T. D.; Huang, C. C.; Couch, G. S.; Greenblatt, D. M.; Meng, E. C.; Ferrin, T. E. *J. Comput. Chem.* **2004**, *25*, 1605–1612.

(29) Lin, H.; Fan, J.; Weng, P.; Si, X.; Zhao, X. *J. Phys. Chem. A* **2017**, *121*, 6863–6873.

(30) Kirkwood, J. G.; Buff, F. P. *J. Chem. Phys.* **1951**, *19*, 774–777.

(31) Ben-Naim, A. Y., *Statistical thermodynamics for chemists and biochemists*; Springer Science & Business Media: 2013.

(32) Ben-Naim, A., *Molecular theory of solutions*; OUP Oxford: 2006.

(33) Smith, P. E. *J. Phys. Chem. B* **2006**, *110*, 2862–2868.

(34) Smith, P. E. *Biophys. J.* **2006**, *91*, 849–856.

(35) Miller III, B. R.; McGee Jr, T. D.; Swails, J. M.; Homeyer, N.; Gohlke, H.; Roitberg, A. E. *J. Chem. Theory Comput.* **2012**, *8*, 3314–3321.

(36) Hou, T.; Wang, J.; Li, Y.; Wang, W. *J. Chem. Inf. Model.* **2011**, *51*, 69–82.

(37) Moral, R.; Paul, S. *Phys. Chem. Chem. Phys.* **2023**, *25*, 5406–5422.

(38) Silk, M. R.; Price, J. R.; Mohanty, B.; Leiros, H.-K. S.; Lund, B. A.; Thompson, P. E.; Chalmers, D. K. *Chem. Eur. J.* **2021**, *27*, 14489–14500.

Chapter 4

Behavior of Cyclic Peptide Nanotubes in Deep Eutectic Solvents

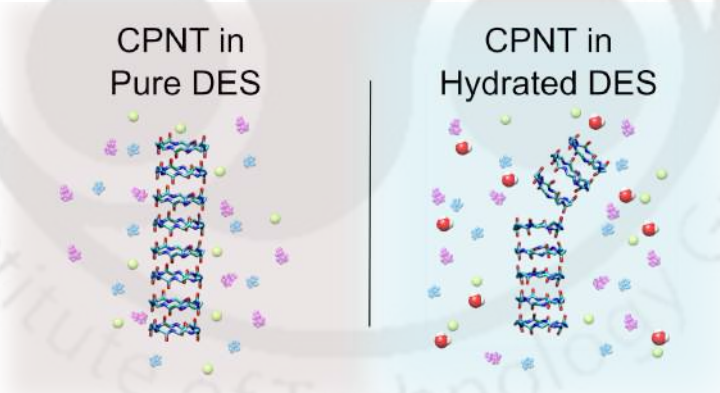

Overview

Cyclic peptide nanotubes (CPNTs) hold significant promise as nanostructures for drug delivery and materials science, yet their stability in diverse solvent environments remains a critical challenge. Deep eutectic solvents (DESs)-eco-friendly, sustainable alternatives to conventional solvents-have shown remarkable potential in enhancing biomolecular stability and functionality. This study pioneers an investigation into the interactions between CPNT and two DESs, reline (choline chloride-urea) and glyceline (choline chloride-glycerol), employing molecular dynamics simulations to unravel the structural behavior of CPNTs in pure and hydrated DES media. Key findings indicate that CPNT retains its tubular conformation in pure DESs, with glyceline providing slightly greater structural stability than reline, owing to stronger bonded and non-bonded interactions within the nanotube. This stability is primarily maintained through backbone-backbone hydrogen bonding, while side-chain contributions are negligible. The addition of water disrupts the tubular conformation of the CPNT by interfering with DES-CPNT interactions, as evidenced from broadened free energy basins and altered radial distribution patterns. Hydration also alters the DES structure itself, leading to reduced viscosity and enhanced solvent diffusion. Furthermore, temperature-dependent simulations indicate that elevated temperatures negatively impact CPNT stability, particularly in reline systems, due to reduction in intermolecular hydrogen bonds. As the first comprehensive study in this area, these findings lay the groundwork for future research into the applications of CPNTs in green solvents, opening up new possibilities for advancements in nanotechnology, chemistry and biomaterials.

4.1 Introduction

In the preceding chapter, the influence of solvent polarity and amino acid sequence variation on the structural stability of CPNTs was explored using conventional solvent systems. While those studies provided crucial insights into how solvent environments modulate CPNT behavior, they were largely confined to polar and non-polar molecular solvents. To further broaden this understanding and evaluate CPNT performance in more complex and application-relevant media, the current chapter investigates their behavior in alternative solvent systems. This includes an in-depth study of their structural and dynamic properties in deep eutectic solvents (DESs), thereby extending the scope of solvent-dependent stability and functionality explored so far.

Deep eutectic solvents (DESs) have recently emerged as a promising class of green solvents, offering advantages such as low volatility, biodegradability, adjustable viscosity, and affordability[1, 2]. They are typically formed by mixing hydrogen bond donors (HBDs) and hydrogen bond acceptors (HBAs), resulting in a eutectic mixture with a melting point substantially lower than that of the individual components[3, 4]. Thanks to their versatile physicochemical characteristics, DESs have been investigated for diverse uses, including drug delivery[5], food processing[6], biotechnology[7], energy storage[8], catalysis[9], and advanced materials development[10, 11]. In the biological domain, DESs are being explored as non-aqueous or co-solvents that can improve protein function, structural integrity, and long-term stability[12–15]. More recently, they have gained attraction in nanoscience for tuning the surface and morphological features of nanomaterials[16–18]. Their ability to act as reaction media or stabilizing agents under mild conditions has proven useful in the synthesis and manipulation of nanostructures[17, 19]. Despite these advances, studies involving DES-nanotube systems are still limited. Current efforts have largely focused on the dispersion of carbon nanotubes in DESs[20], the confinement of DESs within carbon and boron nitride nanotubes[21, 22], and interfacial interactions[20, 23]. However, peptide-based nanotubes in DES environments remain completely unstudied, leaving a notable gap and a promising direction for future research.

This chapter aims to bridge this gap by investigating the stability and behavior of cyclic peptide nanotubes (CPNTs) in two widely studied DES systems: reline (choline chloride-urea) and glyceline (choline chloride-glycerol). Both reline and glyceline are

known for their biocompatibility, non-toxicity[24, 25], and chemical inertness with water, making them ideal candidates for studying CPNT stability and behaviour in green solvent environments[26–29]. Specifically, we investigate the following key aspects:

(a) The stability of the CPNT in two different DES environments, Reline and Glyceline,

(b) The role of HBD and HBA components in each DES, analyzing their influence on the structural behavior and stability of CPNT,

(c) The effect of water incorporation into the DES medium, assessing how hydration alters the conformation and overall integrity of the CPNT, and

(d) The impact of temperature variations on the DES-CPNT systems, focusing on structural stability and molecular interactions under different thermal conditions.

By addressing these objectives, this study offers the first detailed examination of the interaction between CPNT and DES, providing valuable insights into their potential applications in various nanotechnology and biomaterials domains.

4.2 Materials and Methods

4.2.1 System Setup

The CPNT used in this study comprises eight stacked units of the cyclic peptide cyclo-[(Asp-D-Leu-Lys-D-Leu)$_2$] (D$\underline{\text{L}}$K$\underline{\text{L}}_2$) . The individual D$\underline{\text{L}}$K$\underline{\text{L}}_2$ subunit was obtained from the Cambridge Crystallographic Data Centre (CCDC ID: 1520676)[30]. The nanotube was constructed by aligning and stacking eight such subunits using PACKMOL software[31] (Figure 4.1a). In consistent with our previous chapters, the stacking of the CPNT followed an antiparallel arrangement between the adjacent CP rings. To assess the structural stability of the nanotube in deep eutectic solvents (DES), two widely studied DESs, reline and glyceline, were chosen. Reline is composed of choline chloride (HBA) and urea (HBD) mixed at a ratio of 1:2. Glyceline is formed by mixing choline chloride (HBA) with glycerol (HBD) at a ratio of 1:2. The structures of all the components of these two DESs are also depicted in Figure 4.1b.

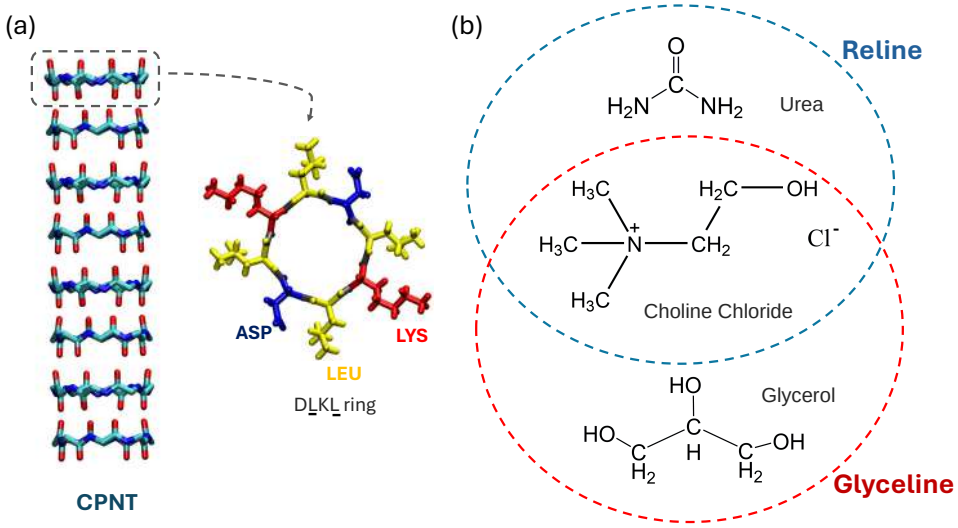

Figure 4.1: *(a) Initial conformation of the 8 × DLKL$_2$ nanotube alongwith the structure of the DLKL$_2$ ring and (b) the components of the two DESs studied.*

Additionally, the influence of hydration was examined by varying the DES-to-water ratio, where the number of water molecules was determined based on the percentage weight of DES relative to water (% w/w). The thermal stability of the DLKL$_2$ nanotube in DES was also analyzed over a range of temperature. The details of all the constructed systems, including solvent compositions are summarized in Table 4.1. To enhance the reliability of the findings, each system was subjected to three independent 500 ns simulation runs, allowing for a more comprehensive assessment of CPNT behavior across different conditions.

4.2.2 Simulation Protocols

For carrying out the simulations, ff14SB force field[32] was employed for the CPNT, while TIP3P[33] model was used for water. Again the parameters for the Cl^- ions were generated using the TIP3P specific AMBER adapted Joung and Cheatham force fields[34]. The DES components - urea, glycerol, and choline were optimized using the Gaussian 09 package[35] with HF/6-31G* as basis set[36, 37]. Partial charges for these molecules were derived using the restrained electrostatic potential (RESP) method[38]. The general AMBER force field (GAFF)[39–41] was applied to urea, glycerol, and choline. To address the common issue of overestimated electrostatic potentials in ionic liquid and DES

Table. 4.1: *Detailed composition of the investigated systems. Here, N_{Ure}, N_{Gly}, N_{Col}, N_{Cl}, and N_{Wat} represent the number of urea, glycerol, choline, chloride, and water molecules, respectively. C_{DES} denotes the concentration of DES, specifically reline and glyceline, in weight percentage.Temperature is reported in Kelvin. Box length here represents the final box length after 500 ns simulation for all the systems.*

System	N_{Ure}	N_{Gly}	N_{Col}	N_{Cl}	N_{Wat}	Temp(K)	C_{DES} (w %)	Box Length (Å)
R0	1000	-	500	500	-	300	100	56.66
R1	1000	-	500	500	801	300	90	58.98
R2	1000	-	500	500	3090	300	70	64.86
R3	1000	-	500	500	7209	300	50	73.47
R350	1000	-	500	500	-	350	100	57.22
R400	1000	-	500	500	-	400	100	57.84
R450	1000	-	500	500	-	450	100	58.28
G0	-	1000	500	500	-	300	100	61.85
G1	-	1000	500	500	999	300	90	64.22
G2	-	1000	500	500	3852	300	70	70.48
G3	-	1000	500	500	8987	300	50	79.65
G350	-	1000	500	500	-	350	100	62.51
G400	-	1000	500	500	-	400	100	63.18
G450	-	1000	500	500	-	450	100	63.91

simulations[42–44], a charge scaling approach was implemented[44, 45]. Following the methodology of Perkins et al.[44–46], which has shown good agreement with experimental results, the charges on the different atomic sites of choline chloride were reduced by 20 % [28, 29].

The molecular dynamics simulations were executed using AMBER18 package[47], with system initialization performed via PACKMOL. This process involved placing the cyclic peptide nanotube (CPNT) at the center of the box and solvent molecules are added randomly within a cubic simulation box. The systems then underwent a thorough energy minimization protocol, consisting of 5000 steps each of steepest descent and conjugate gradient methods, implemented through AMBER18's SANDER module[47]. System preparation involved a gradual temperature increase from 0 K to the target value in an NVT ensemble, followed by equilibration phases in NVT (1 ns) and NPT (4 ns) ensembles. The production run was carried for 500 ns under NPT conditions, with structural data recorded at 4 ps intervals. The simulations employed the leap-frog algorithm with a 2 fs time step for integrating equations of motion. Pressure regulation utilized the Berendsen barostat[48] (2 ps coupling constant), while temperature control was achieved via the Langevin thermostat[49] (1 ps^{-1} collision frequency). The SHAKE algorithm[50] constrained hydrogen-involved covalent bonds. A 10 Å cutoff was applied for short-ranged

non-bonded interactions, with long-ranged electrostatic interactions were managed by the application of particle mesh Ewald method[51]. The simulations implemented periodic boundary conditions in all the three directions.

For hydrogen bond lifetime analysis, selected systems underwent additional NVT equilibration of 10 ns to stabilize box volume after the previous 500 ns NPT simulation. This was followed by NVE ensemble production runs of 25 ns. The final 200 ps of these runs were sampled at 10 fs intervals to capture rapid hydrogen bond fluctuations between the CP rings of the CPNT.

4.2.3 Simulation Analysis

This section outlines the computational methodologies employed to analyze the structures and dynamical behaviors of cyclic peptide nanotubes (CPNTs) in deep eutectic solvents (DES). The molecular dynamics (MD) simulations were processed using CPPTRAJ[52], a module from the Amber18 package, while additional analyses were performed using in-house scripts. The visualization of simulation trajectories was conducted through Visual Molecular Dynamics (VMD)[53]. All graphical representations were plotted with Matplotlib[54].

To quantify structural variations of CPNTs in different DES environments, the root mean square deviation (RMSD) of backbone atoms was computed relative to their initial configurations. Furthermore, number density plots were generated using the MDAnalysis[55, 56] toolkit to examine molecular distributions. Spatial density plots were constructed from the full 500 ns trajectory using VMD[53] software, providing three-dimensional probability distributions of DES components around the CPNT, with an isovalue threshold set at 0.5. To evaluate non-bonded interaction energies, the NAMD energy plugin in VMD[53] was utilized.

The criteria considered to calculate hydrogen bonds is already discussed in Chapter 1 (Section 1.4.3) The frequency of hydrogen bonds was determined by counting the number of occurrences of each specific hydrogen bond number throughout the trajectory. The continuous hydrogen bond time correlation function (TCF) was applied to compute the lifespan of hydrogen bonds between backbone atoms in adjacent CP rings.

To investigate the retention of the CPNT tubular conformation, the free energy land-

scapes using the SASA and Rg values were generated using Gaussian kernel density estimation. To investigate the average structure of molecules surrounding a reference molecule, radial distribution function (rdf) was used. However, when comparing systems with different densities, it is essential to account for the density variations. To achieve this, the rdfs, g(r) were multiplied by a density factor ρ resulting in density-weighted rdfs for the various interacting pairs[57, 58]. For water-DES rdfs, the density factor corresponds to the number of water molecules in the system divided by the system's box volume. For rdfs involving DES components, the density factor is determined by the most abundant DES component in the system, divided by the particular system's box volume. Again, to evaluate the coordination number around specific atomic sites, the equation 2.1 was used (Chapter 2).

The diffusion coefficient values (D) reported for the hydrated DES systems correspond to those of the choline component in both reline and glyceline and were calculated using the Einstein's equation:

$$D = \lim_{\Delta t \to \infty} \frac{\langle \Delta r^2 \rangle}{2d\Delta t} \tag{4.1}$$

Here, d is the dimensionality of the co-ordinate system.

Viscosity was estimated using the Stokes-Einstein equation[59]:

$$\eta = \frac{k_{\mathrm{B}} T}{6\pi D r} \tag{4.2}$$

Here, where η is the viscosity, k_B is the Boltzmann constant, T is the temperature, D is the diffusion coefficient of choline, and r is the hydrodynamic radius of the choline ion.

4.3 Results and Discussions

4.3.1 Stability of the CPNT in DES

Our previous studies have shown that D$\underline{\mathrm{L}}$K$\underline{\mathrm{L}}_2$ has a strong tendency to self-assemble into nanotube-like structures in aqueous salt solution.[60]. Additionally, this nanotube has been found to remain stable in non-polar solvents such as chloroform and hexane[61]. However, the behavior of CPNTs in deep eutectic solvent (DES) environments remains

unexplored, and no prior evidence exists regarding their structural stability in these solvents. Figure 4.2 presents snapshots of the 8 × DLKL$_2$ nanotube after three independent simulations of 500 ns in hydrated and dehydrated reline and glyceline solvents. Initial observations suggest that the tubular structure of the CPNT is retained in both pure reline (R0) and glyceline (G0). However, as the water content in the DES increases, the stability of the nanotube gradually decreases. This effect is more pronounced in reline, where a progressive disruption of the CPNT rings is observed from system R1 to R3. In glyceline, the tubular structure remains intact in G1 but begins to break in G2 and G3.

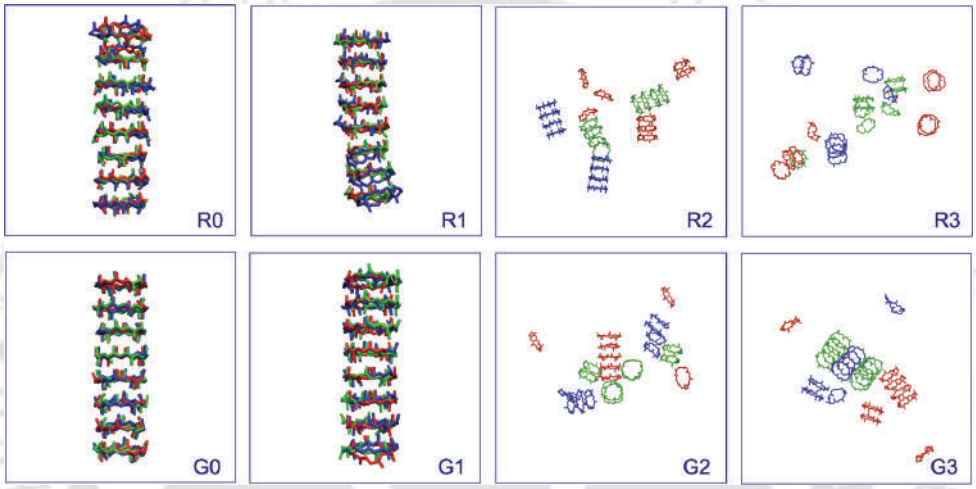

Figure 4.2: *Snapshots of the CPNT after three independent 500 ns simulation run in all the systems studied. Here, colour red, blue, and green represents simulation run 1, 2, and 3 respectively.*

The enhanced stability of the CPNT in pure DES and at low water content is further supported by the variation in root mean square deviation (RMSD) values of the backbone atoms over the simulation time (Figure 4.3). In reline medium, the average RMSD values for R0, R1, R2, and R3 systems are 0.92 ± 0.26, 1.17 ± 0.50, 10.42 ± 1.95, and 19.97 ± 2.63 respectively. In glyceline medium, the these values are 0.71 ± 0.08, 0.86 ± 0.16, 10.78 ± 2.50, and 20.15 ± 2.39 for the systems G0, G1, G2, and G3 respectively. Clearly, in both DESs, the retention of the tubular structure decreases as the water percentage in DES increases, highlighting the destabilizing effect of hydration on CPNT integrity.

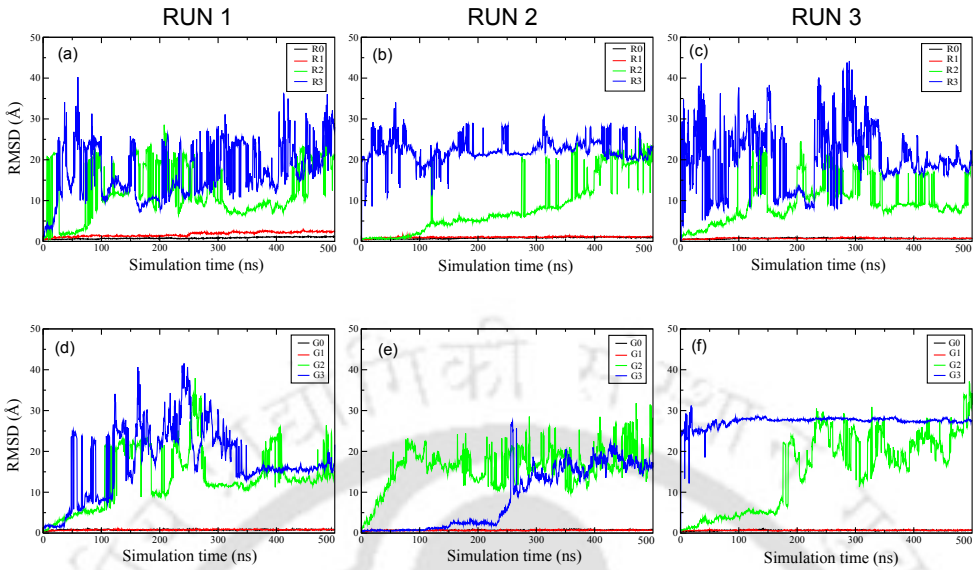

Figure 4.3: *Root mean square deviation (RMSD) of all the backbone atoms of the CPNT versus time across all the hydrated and dehydrated (a)-(c) reline and (d)-(f) glyceline systems for Run 1, 2, and 3.*

Furthermore, the 2D density profiles of the backbone atoms of the CPNT along the YZ plane (Figure 4.4) align with the RMSD trend, offering additional evidence of structural disruption with the increase in water content in DES. Notably, the backbone atoms display a more orderly stacking arrangement in G0 compared to the slight deformation observed in R0, indicating a solvent-dependent difference in nanotube stability. With increasing water content, the number density of CPNT backbone atoms gradually decreases in the YZ plane, and the tubular conformation nearly disappears in the R3 and G3 systems.

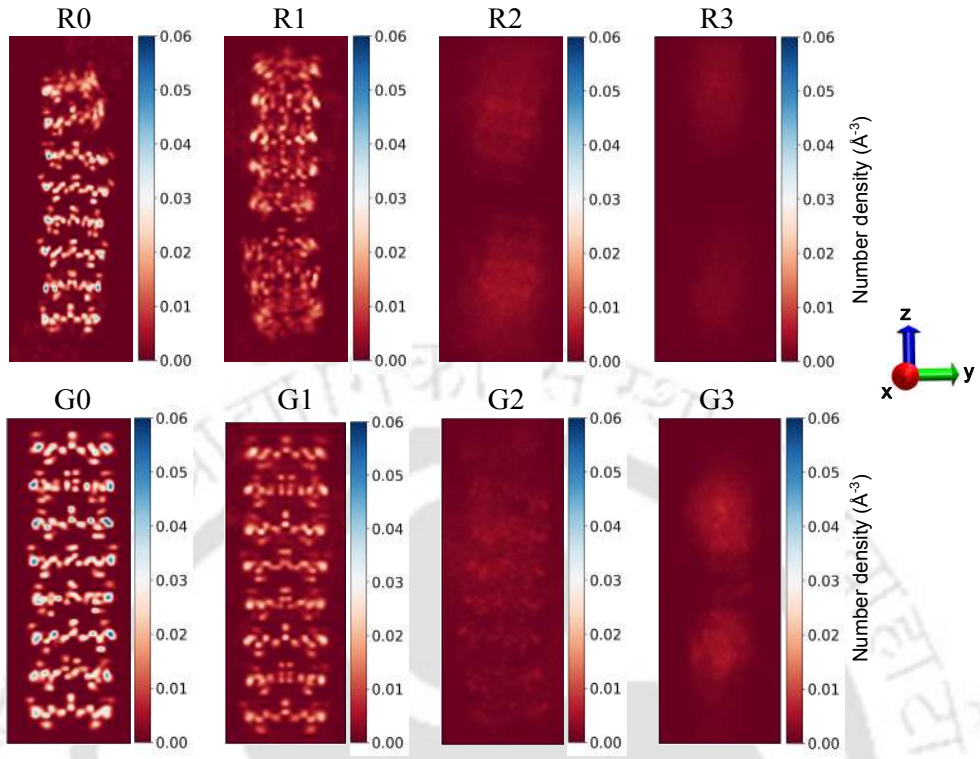

Figure 4.4: *Number density plots of the backbone rings of the CPNT along the X-axis across all the systems in reline and glyceline. The color bar indicates the number density in* $Å^{-3}$*. The axes orientations are given for reference.*

Additionally, to ensure that the stability of the CPNT is not influenced by the duration of the simulation, we extended the simulations for systems R0 and G0 to 1 μs. The retention of the tubular structure of the CPNT (Figure 4.5) even after a significantly longer timescale confirms that our findings are not dependent on simulation length.

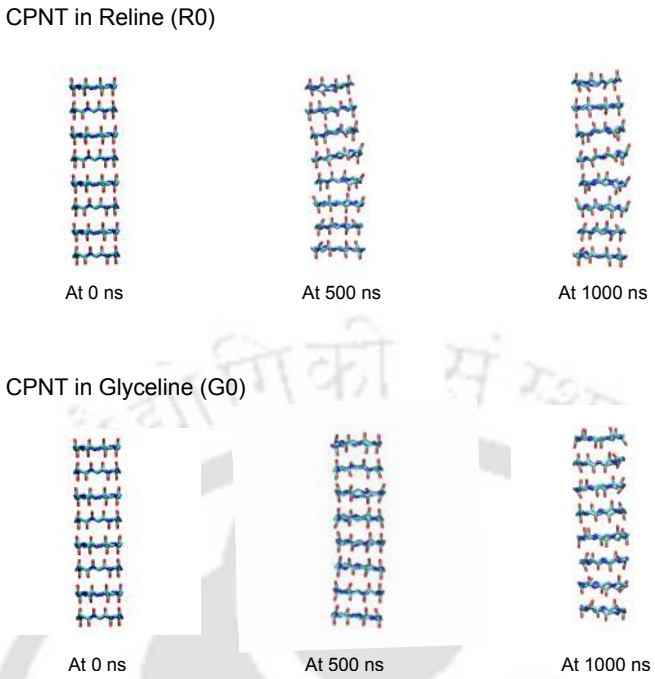

Figure 4.5: *Snapshots of the CPNT at different time frames for the systems R0 and G0.*

Hydrogen bonding between the backbone atoms of CP rings plays a crucial role in maintaining nanotube stability, with studies highlighting both parallel and antiparallel arrangements[30, 62–64]. Initially, the CPNT exhibits an antiparallel hydrogen bonding arrangement. Notably, this antiparallel arrangement is preserved in the CPNT after simulation (Figure 4.6a). This holds true for both R0 and G0 systems. Again, each CP ring consists of eight amino acid residues, allowing for a maximum of eight hydrogen bonds (H-bonds) to form between the backbone atoms of adjacent CP rings. Figure 4.6(b and c) shows the average number of H-bonds present in between the gaps of the CPNT in reline and glyceline systems. In pure DES systems (R0 and G0), the average H-bond number varies between 6 to 8 for all the gaps, indicating strong intermolecular bonded interactions that contribute to the stability of the nanotube. In terms of non-bonded interactions, van der Waals forces contribute favorably in all gaps of the CPNT for both R0 and G0 systems (Figure 4.7). In contrast, electrostatic interactions are consistently unfavorable across all gaps in these systems. As the water content increases, the average number of H-bonds in most of the gaps decreases in both DESs, reflecting a reduction in structural integrity. Additionally, the H-bond count is slightly higher in glyceline compared to reline, suggesting that the CPNT is more stable in glyceline than

in reline. An intriguing observation is the near absence of side chain-side chain H-bonds in pure DES environments, which gradually increase with increase in water content in DES (Figure 4.6(d and e)). This finding suggests that the stability of the CPNT in R0 and G0 is predominantly driven by backbone-backbone H bonding. This is in contrast to previous studies[62, 65], where side chain-side chain interactions were also reported to play a crucial role in CPNT stability alongside backbone-backbone H-bonding. This difference can be attributed to the strong and preferential hydrogen bonding of the side chains with the deep eutectic solvent (DES) components which will be discussed elaborately in the later part of the study. Furthermore, the overall number of backbone-backbone H-bonds between CP rings decreases with increasing water percentage in DESs (Figure 4.6(d and e)), whereas the trend is completely opposite for side chain-side chain H-bonding.

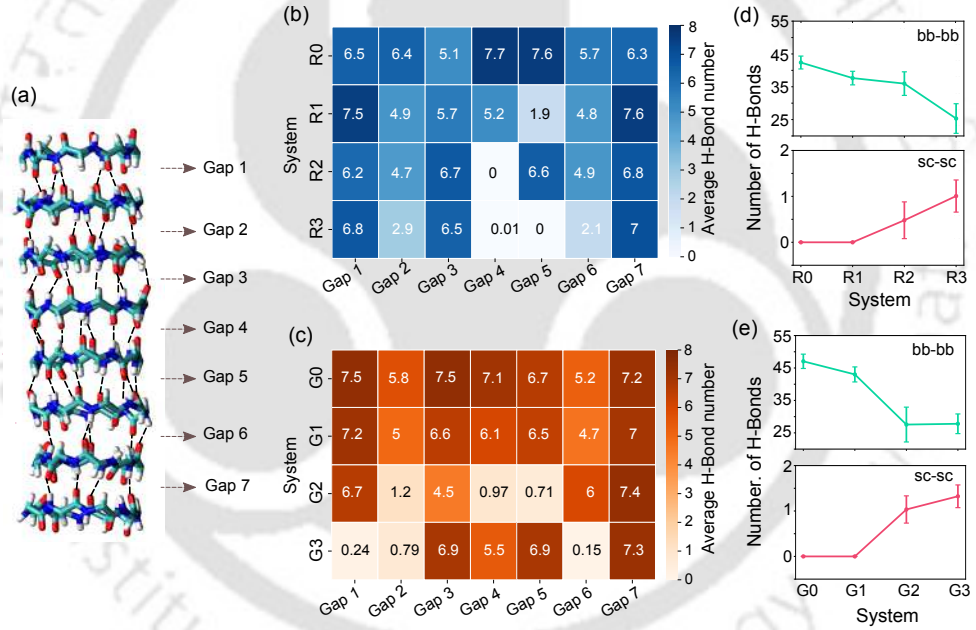

Figure 4.6: *(a) Antiparallel hydrogen bonding arrangement between CP rings in G0 system after a 500 ns simulation, represented by dotted black lines, along with the gap numbers of the CPNT. Average number of hydrogen bonds present in between the gaps of the CPNT in (b) reline systems and (c) glyceline systems, with the color bar indicating the average hydrogen bond values. Total number of hydrogen bonds between backbone-backbone (bb-bb) and side chain-side chain (sc-sc) atoms of the CPNT in (d) reline and (e) glyceline systems.*

Table 4.2 highlights the lifetimes of the top three backbone-backbone hydrogen bonds between adjacent CP rings in the CPNT across all systems. The CPNT is most stable

in pure DES media (R0 and G0), where the hydrogen bond lifetimes are the highest. As the water percentage increases in both reline and glyceline systems, the nanotube gradually breaks down, and this degradation is reflected in the decreasing lifetimes of the key hydrogen bond contributors. This trend indicates the weakening of the nanotube structure as water concentration rises, leading to the eventual breakdown of the CPNT.

Table. 4.2: *The top three lifetimes (<τ_{HB}>) of continuous hydrogen bonds S(t) between the adjacent CP rings in D$\underline{L}$K$\underline{L}_2$ in all the systems. Lifetime values are given in picoseconds (ps).*

System	Bonding CP pairs	Lifetime value (<τ_{HB}>)	System	Bonding CP pairs	Lifetime value (<τ_{HB}>)
R0	Ring3(LEU)-Ring2(LEU)	38.83	G0	Ring7(LEU)-Ring6(LEU)	39.34
	Ring5(LEU)-Ring6(LEU)	25.41		Ring2(LEU)-Ring3(LEU)	38.45
	Ring4(LEU)-Ring5(LEU)	21.27		Ring3(LEU)-Ring2(LEU)	36.95
R1	Ring1(LYS)-Ring2(LYS)	32.98	G1	Ring4(LEU)-Ring5(LEU)	26.29
	Ring4(LEU)-Ring5(LEU)	29.24		Ring3(LYS)-Ring4(LYS)	21.78
	Ring5(LEU)-Ring4(LEU)	22.12		Ring6(LYS)-Ring5(LYS)	21.56
R2	Ring8(LYS)-Ring7(LYS)	20.96	G2	Ring2(LEU)-Ring3(LEU)	22.90
	Ring6(LEU)-Ring7(LEU)	17.56		Ring6(LEU)-Ring7(LEU)	21.45
	Ring7(LYS)-Ring8(LYS)	17.28		Ring3(LEU)-Ring2(LEU)	17.91
R3	Ring1(LYS)-Ring2(LYS)	16.10	G3	Ring4(LYS)-Ring3(LYS)	21.72
	Ring5(LYS)-Ring6(LYS)	14.49		Ring1(LYS)-Ring2(LYS)	17.63
	Ring3(ASP)-Ring4(ASP)	12.18		Ring6(ASP)-Ring5(ASP)	14.69

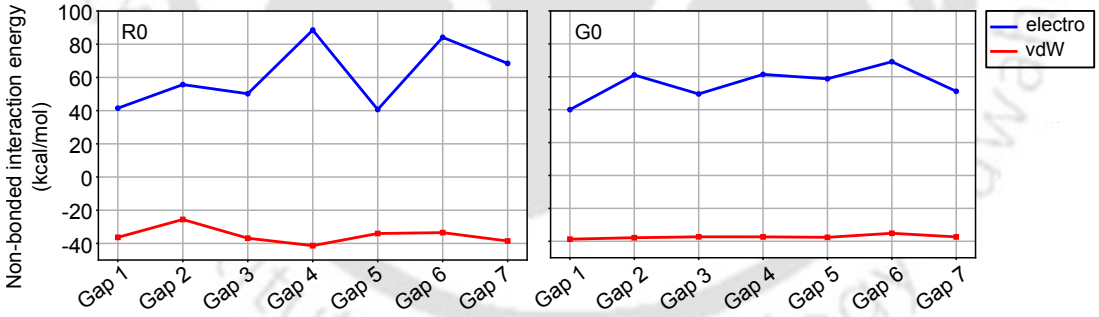

Figure 4.7: *Electrostatic and van der Waals contributions to the non-bonded interaction energy between the gaps of the CPNT in R0 and G0 systems.*

To further support the retention of the tubular conformation of CPNT in pure DES media, free energy landscapes were generated using solvent-accessible surface area (SASA) and radius of gyration (Rg) of the cyclic peptide rings across all systems. SASA indicates the degree of exposure of the CPNT to the solvent, while Rg reflects its structural compactness. Figure 4.8 displays the free energy profiles of the CPNT in both DESs, with and without water, highlighting the influence of hydration on conformational stability.

In pure DES systems, the CPNT adopts a compact conformation, evident from sharp, localized free energy minima at low SASA and Rg values. The G0 system shows a more compact state than R0, with minima around 4200 Å^2 SASA and 11.8-12.0 Å Rg for G0, and 4300-4400 Å^2 SASA and 12.2-12.6 Å Rg for R0. Figure 4.9 shows magnified free energy plots for the systems R0 and G0. Even at low water content (R1 and G1), the CPNT largely maintains its compact structure. However, as the water content increases, the free energy basins broaden and shift toward higher SASA and Rg values, indicating that the CPNT adopts more expanded, flexible, and solvent-exposed conformations. This transition reflects a gradual disruption of the nanotube's compact tubular structure in both DES environments.

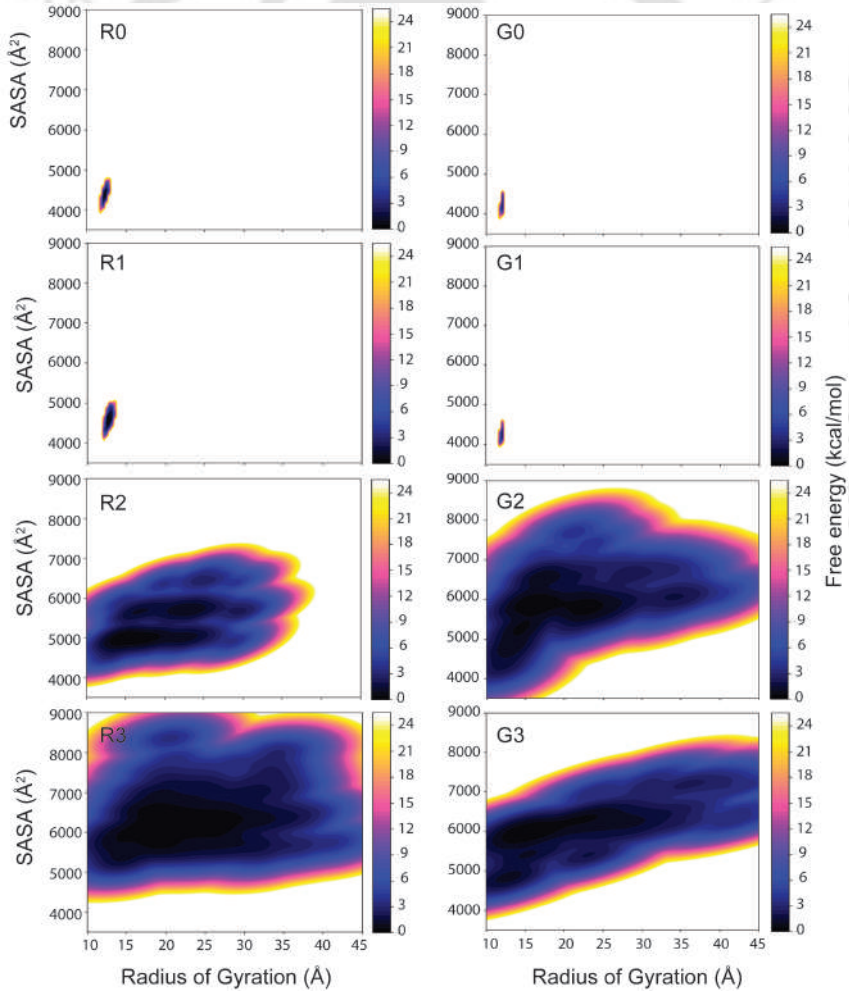

Figure 4.8: *Free energy profile (in kcal/mol) plotted against the solvent acccessible surface area (SASA) and radius of gyration (Rg) of the CPNT in all the pure and hydrated DES systems.*

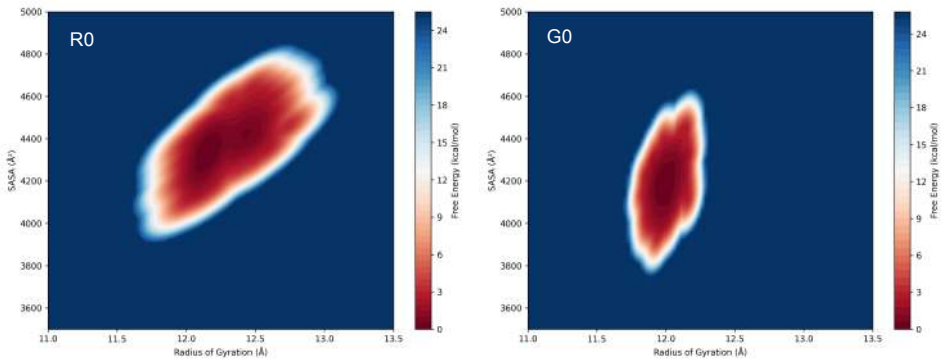

Figure 4.9: *Free energy profile (in kcal/mol) plotted against the solvent acccessible surface area (SASA) and radius of gyration (Rg) of the CPNT in R0 and G0 systems.*

4.3.2 DES-CPNT interactions

As DES consists of both HBA and HBD components, understanding their interactions with the CPNT is crucial. Figure 4.10(a and b) presents the number density distributions of reline and glyceline components around the CPNT in the XY plane for systems R0 and G0, respectively. The results indicate that each DES component interacts differently with specific sites on the CPNT. A high-density solvation shell is observed around the CPNT for all components of both DESs suggesting strong interactions with the nanotube. In the case of reline (Figure 4.10(a)), urea exhibits a uniform interaction across all CPNT sites, while choline shows preferential accumulation at certain locations. Chloride ions (Cl^-) form localized density regions around the CPNT, suggesting their accumulation near the nanotube. Similarly, in glyceline (Figure 4.10(b)), glycerol displays a high density uniform distribution near the CPNT, slightly less in comparison to urea in reline. Also, choline chloride in glyceline exhibits more preferential accumulation near certain sites of CPNT surface. The positively charged choline interacts predominantly with the negatively charged aspartic acid (Asp) residues of the CPNT, whereas Cl^- preferentially associates with positively charged lysine (Lys) residues. The spatial density plots (Figure 4.10(c, d)) further illustrate the arrangement of choline and Cl^- ions around specific amino acid residues of the CP rings. In glyceline, these interactions are more distinctly localized around the Asp and Lys residues (Figure 4.10(d)) compared to reline (Figure 4.10(c)), indicating a stronger preferential association of choline with Asp and Cl^- with Lys residues of the CP rings in the glyceline system. Notably, a small number of molecules from each component of both reline and glyceline systems enter inside the hollow tube of

the CPNT. This presence suggests that, despite the primary interactions of DES molecules occurring on the outer surface of the CPNT, some DES molecules diffuse into the nanotube's confined environment. This can be observed in Figure 4.10, where the density distributions highlight the presence of these molecules inside the CPNT.

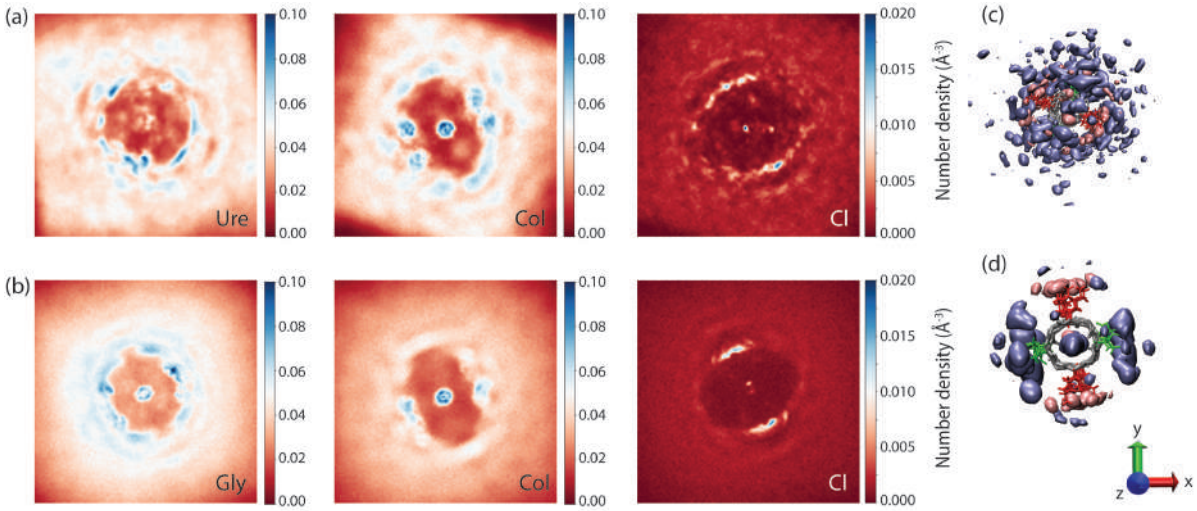

Figure 4.10: *Number density plots of the various components in the XY plane around the CPNT for (a) reline (R0) and (b) glyceline (G0) system. Ure, Col, Cl, and Gly represent urea, choline, chloride, and glycerol, respectively. The color bar indicates the number density in* $Å^{-3}$*. Spatial density distributions of choline and chloride around the CPNT are shown for (c) reline (R0) and (d) glyceline (G0) systems. In these plots, grey represents the CPNT backbone, green denotes aspartic acid residues, red denotes lysine residues, ice blue indicates choline density, and pink represents chloride density. The axes orientations are given for reference.*

As the water content increases in both DES systems, the dense solvation shell of DES components surrounding the CPNT gradually dissipates as evident from Figures 4.11 and 4.12. Consequently, the interactions between the components of DES and the nanotube weaken with the rise in water percentage in both the DES environments.

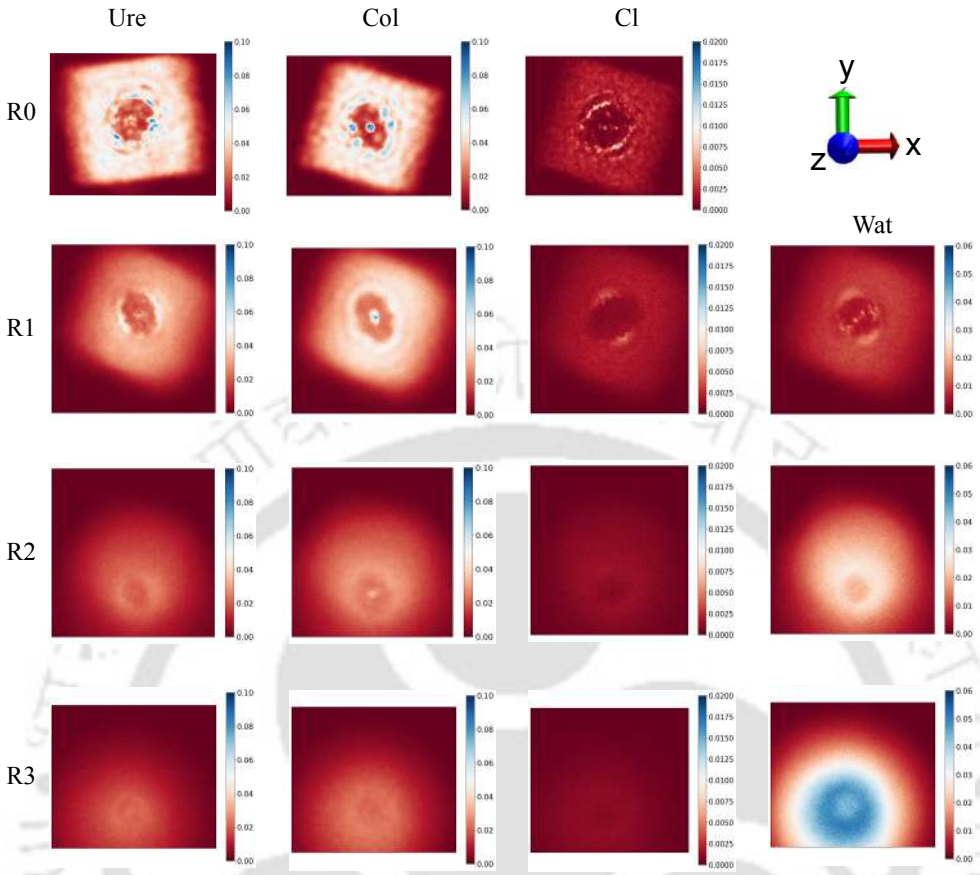

Figure 4.11: *Number density distributions of reline components and water around the CPNT in the XY plane for all the systems.The color bar indicates the number density in* $Å^{-3}$. *The axes orientations are given for reference.*

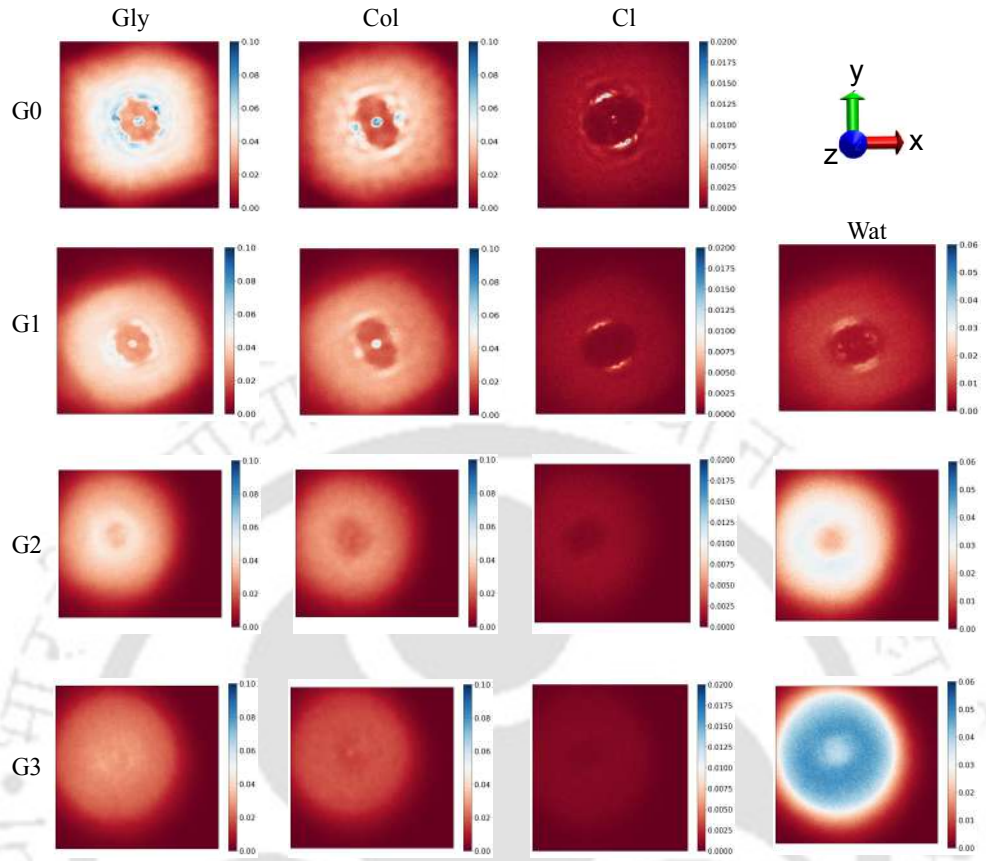

Figure 4.12: *Number density distributions of glyceline components and water around the CPNT in the XY plane for all the systems. The color bar indicates the number density in* $Å^{-3}$*. The axes orientations are given for reference.*

Figure 4.13 presents a detailed analysis of the interactions between the CPNT and components of reline and glyceline in the systems R0 and G0 respectively. The first shell coordination numbers of DES components around specific atoms of hydrophilic (Asp and Lys) and hydrophobic (Leu) amino acid side chains of the nanotube indicate stronger overall interactions in reline compared to glyceline (Figure 4.13a). This enhancement arises from both bonded and non-bonded interactions. In terms of bonded interactions, hydrogen bonding patterns show that all DES components preferentially form hydrogen bonds with the CPNT's side chains rather than its backbone, a trend consistent across both reline and glyceline (Figure 4.13b). Notably, urea in reline, due to its smaller size and higher polarity, establishes more hydrogen bonds with the CPNT than the bulkier glycerol in glyceline. Non-bonded interactions are dominated by electrostatic forces rather than van der Waals interactions, particularly for charged species such as chloride and

choline (Figure 4.13c). These electrostatic interactions play a key role in shaping the overall CPNT-DES interaction landscape. An exception to this trend is observed in the interaction of chloride ions with the NZ atom of lysine, where glyceline exhibits a higher coordination number than reline. This is further reflected in the non-bonded interaction plots, which show stronger electrostatic interactions between chloride ions and the CPNT in glyceline compared to reline.

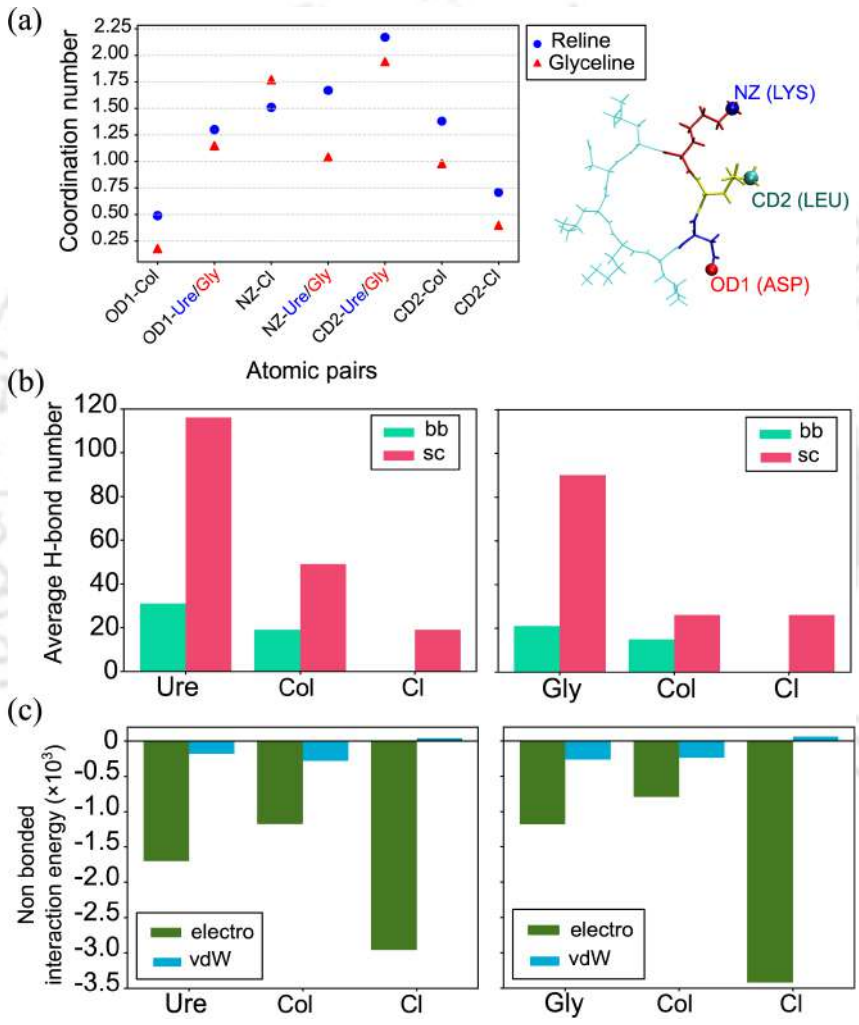

Figure 4.13: *(a) The first shell coordination number of the components of reline and glyceline around different atomic sites of the CPNT. The atomic sites of the CP ring are illustrated next to the plot. (b) Average number of hydrogen bonds formed between the components of reline and glyceline with the backbone (bb) atoms and side chain (sc) atoms of the CPNT. (c) Electrostatic and van der Waals contributions to the non-bonded interaction energy between the components of the two DESs and the CPNT. All plots correspond to systems R0 and G0. Interaction energy is expressed in kcal/mol.*

4.3.3 DES-Water interactions

With the addition of water into the DES systems, the interactions between the DES components and water increase. Figure 4.14(a and b) shows the density-weighted radial distribution functions (RDFs), g(r)ρ, of water around the different components of the DESs. The RDFs consistently demonstrate that all components (urea, glycerol, choline, and chloride) become more hydrated as the water concentration increases in both reline and glyceline. This is evident from the increasing peak heights in the RDFs with higher water content. The chloride-water RDF exhibits the most significant increase in the first peak height with increasing water concentration. This indicates a very strong and preferential hydration of chloride ions as water is added. This is in agreement with previous studies that shows that the hydration of chloride anions is stronger compared to choline cations and urea molecules in aqueous reline solutions[44, 66]. The sharp peak in the chloride-water RDF also suggests the formation of a well-defined hydration shell around the chloride ions.

As the components of both reline and glyceline become increasingly hydrated with the addition of water, a notable enhancement in both bonded and non-bonded interactions occurs between the DES components and water (Figure 4.14(c and d)). Specifically, the number of hydrogen bonds formed between water and the hydrogen bond donor (HBD) components: urea in reline and glycerol in glyceline increases more rapidly as the hydration level of the DESs rises. This rise in hydrogen bonding indicates a strong affinity between water and these HBD components. Furthermore, the electrostatic contributions to non-bonded interactions are more pronounced compared to van der Waals forces. Among these interactions, chloride-water interactions are particularly significant for both DESs (Figure 4.14d), highlighting the strong electrostatic attraction between chloride ions and water molecules. This increased interaction between water and the DES components leads to a disruption of the original DES structures. As water molecules become more prevalent, they increasingly compete with the DES components for interactions, thereby altering the solvent's structural integrity and properties. This competition for interactions not only affects the stability of the DESs but also impacts the behavior and stability of the CPNT within these environments.

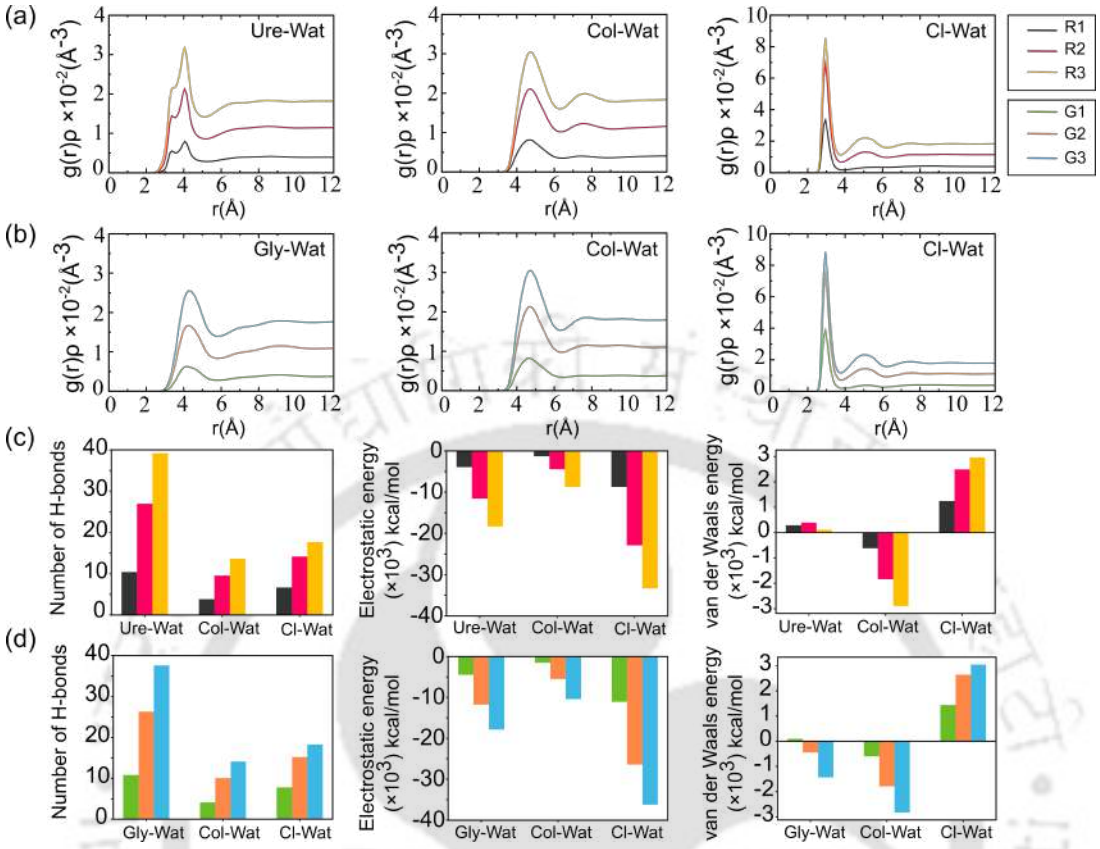

Figure 4.14: *Density-weighted radial distribution function of water around the components of (a) reline and (b) glyceline in all hydrated DES systems. Hydrogen bond count, electrostatic and van der Waals contributions to the non-bonded interactions between water and the components of (c) reline and (d) glyceline in all hydrated DES systems.*

4.3.4 DES-DES interactions

This section examines the interactions among different components of reline and glyceline. Figure 4.15(a and b) presents the density-weighted RDFs for various interacting pairs within both DESs. To assess how the presence of the nanotube influences these interactions, these RDFs are further compared with their counterparts in pure reline and glyceline systems, where the CPNT is absent. The RDFs between interacting pairs in systems R0 and G0 (with CPNT) closely resemble those of the respective pure DES systems (without CPNT). This similarity indicates that the presence of the CPNT does not significantly alter the structural properties of the DESs. However, the addition of water to the DESs introduces competition between water molecules and DES components for interactions. As water content increases, the peaks of all the RDFs decrease. This reduction reflects

a decrease in the number of respective DES components in the first solvation shell The second solvation shell gradually flattens as we progress from R0 to R3 and G0 to G3. This flattening indicates the disruption of the second solvation shell. These observations align with previous studies that reported that water addition significantly impacts DES properties[67, 68].

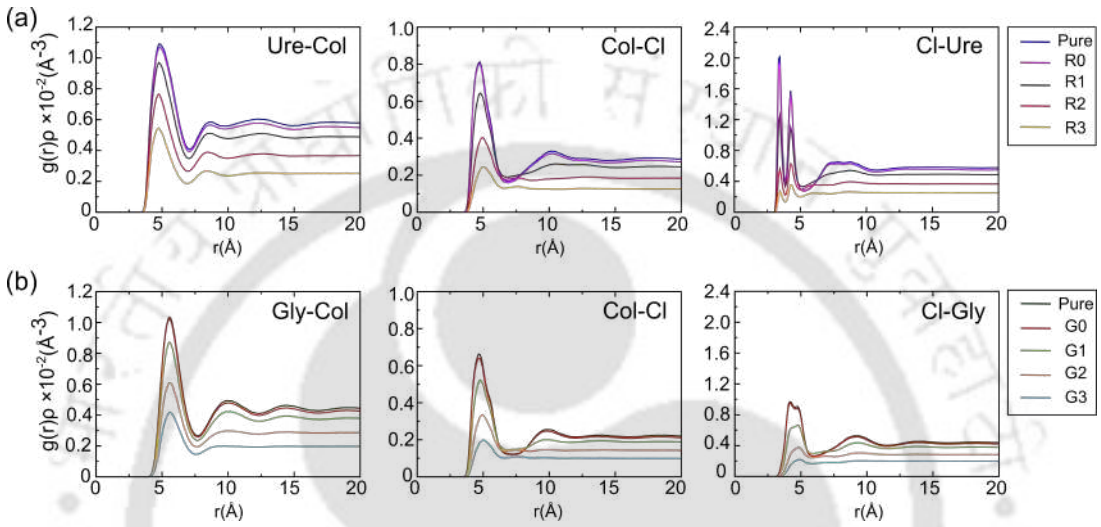

Figure 4.15: *Density-weighted radial distribution function of the various interacting pairs of (a) reline and (b) glyceline across all the systems studied. Here, "Pure" refers to the respective DES systems without the presence of the CPNT and water.*

The gradual changes in RDFs with increasing water content suggest a progressive disruption of the original DES structure, with water molecules increasingly competing for interactions with DES components. This trend is also reflected in the decreasing bonded and non-bonded interaction profiles between DES components with rising water concentration (Figure 4.16).

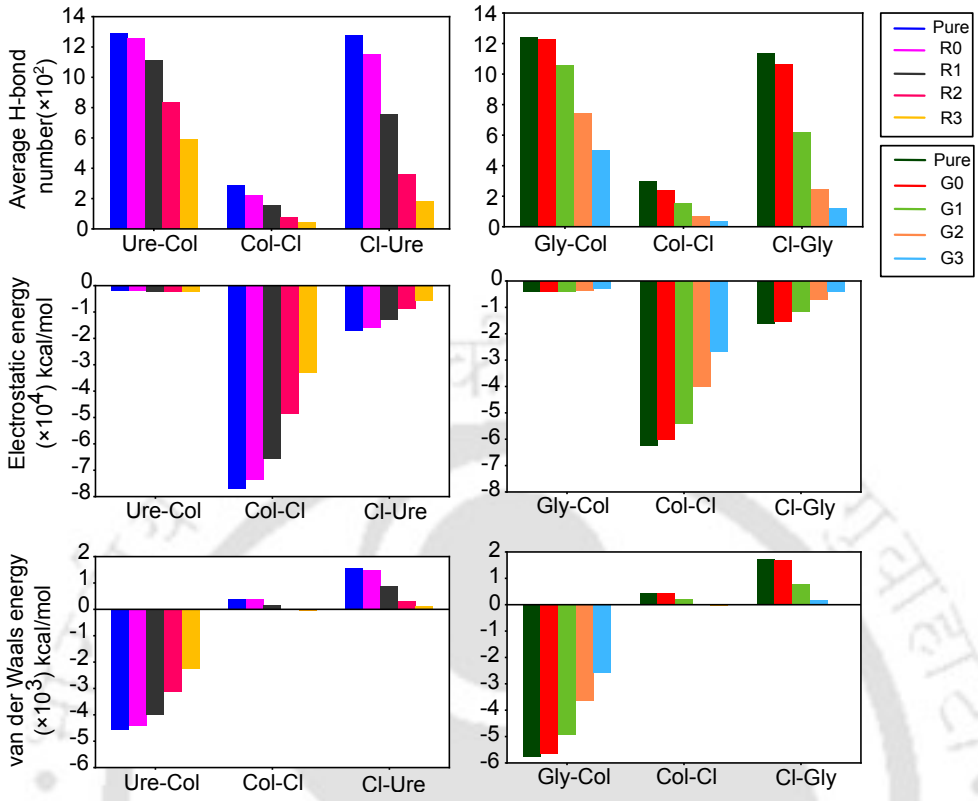

Figure 4.16: *Average number of hydrogen bonds, electrostatic and van der Waals interaction energies between the DES components across all the systems in reline and glyceline.*

Additionally, as the water percentage increases, the diffusion coefficient of both the DESs rises while their viscosity decreases, reflecting enhanced molecular mobility and a less structured solvent environment (Figure 4.17).

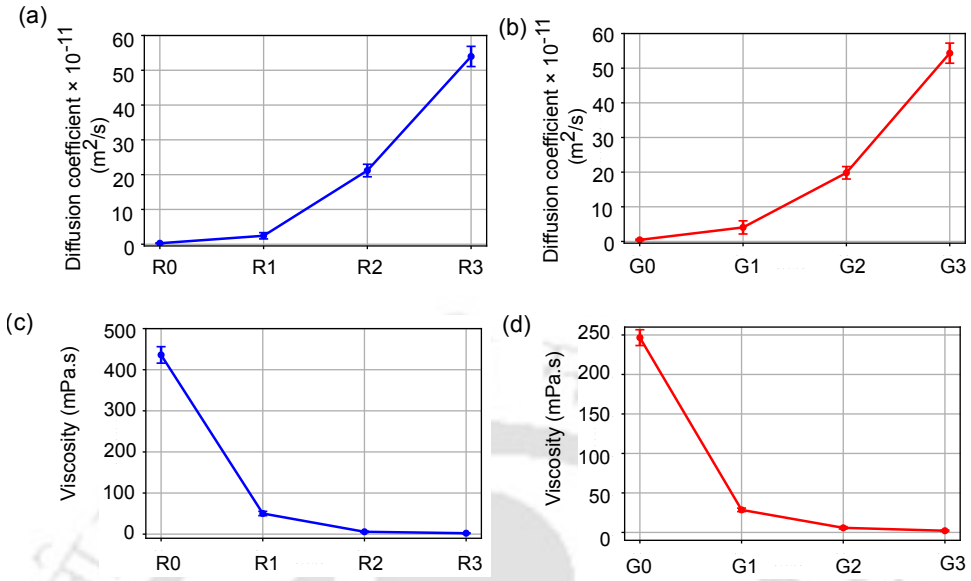

Figure 4.17: *Change in diffusion coefficient values (in m^2/s) of choline in (a) reline systems, and (b) glyceline systems. Also, change in viscosity (in mPa.s) of (c) reline systems, and (d) glyceline systems.*

4.3.5 Thermal Stability

Temperature significantly influences the structural stability of CPNT and this is already highlighted in our previous study[60]. Figure 4.18(a) shows the snapshot of the CPNT after 500 ns in reline and glyceline at four different temperatures. Here, R300 and G300 refers to the systems R0 and G0 respectively. In glyceline, the CPNT maintains its structural integrity over a broad temperature range, remaining stable from 300 K up to 350 K without significant deformation. However, in reline, the nanotube starts to lose its stability at 350 K, where it splits into two distinct parts. With a further increase in temperature, the structural disruption becomes more pronounced, leading to a gradual disintegration of the CPNT. Thus, at elevated temperatures, the nanotube loses its well-defined tubular conformation. Also, the CPNT destabilizes more in reline than in glyceline under thermal stress. This suggests that the nature of the DES medium plays a crucial role in determining the thermal stability of CPNT. This temperature induced instability is further supported by the analysis of hydrogen bond number within the CPNT. Figure 4.18(b) presents the average number of hydrogen bonds present in between the gaps of the CPNT over a range of temperature in pure reline and glyceline. At elevated temperatures, a reduction in the number of hydrogen bonds is observed, indicating that thermal fluc-

tuations disrupt the intermolecular hydrogen bonding network. Since hydrogen bonding plays a key role in maintaining the structural cohesion of CPNT, its disruption at high temperatures leads to the breakdown of the tubular conformation, ultimately resulting in the instability of the nanotube.

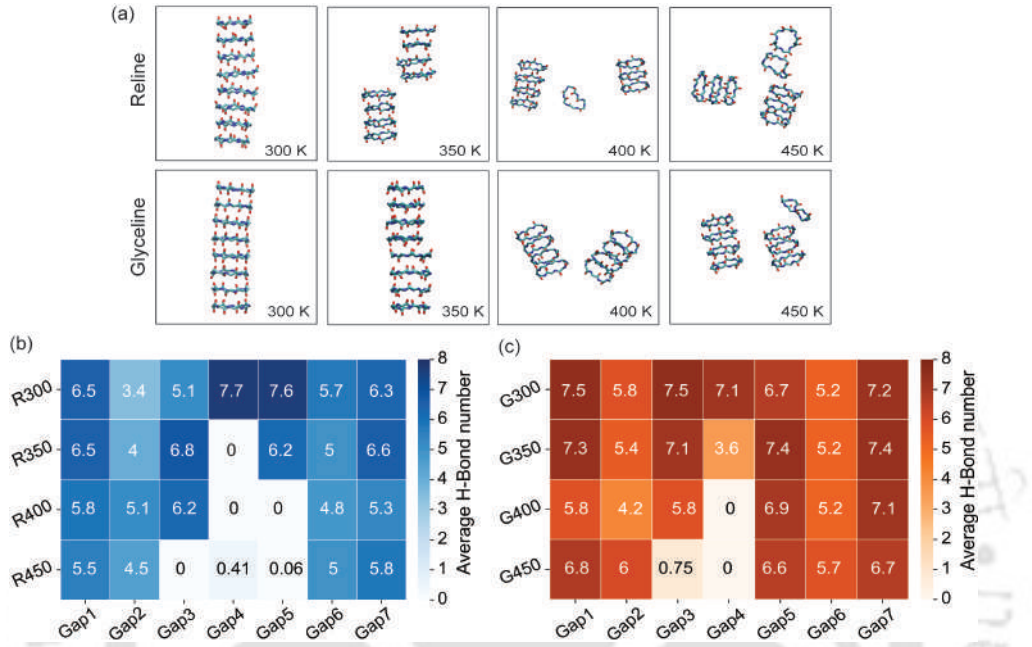

Figure 4.18: *(a) Snapshots of the CPNT after 500 ns simulation run in both DESs at four different temperatures. Average number of hydrogen bonds between the gaps of the CPNT in (b) reline and (c) glyceline at four different temperatures. Here the color bar indicates the average hydrogen bond values. Also, R300 and G300 stands for the systems R0 and G0 respectively.*

4.4 Discussion

This study presents an in-depth analysis of the structural behavior of an 8 × D$\underline{\text{L}}$K$\underline{\text{L}}_2$ cyclic peptide nanotube (CPNT) within deep eutectic solvents (DES) under varying hydration conditions. The findings highlight that the CPNT maintains its structural integrity when immersed in pure DES environments, specifically reline and glyceline. However, the introduction of water into these systems leads to a progressive disruption of the nanotube's tubular architecture, demonstrating a significant influence of hydration on its stability.

A notable observation from the study is that the CPNT exhibits greater structural

stability in glyceline compared to reline. This enhanced stability is attributed to the formation of higher number of backbone-backbone hydrogen bonds between the CP rings in the glyceline (G0) system compared to the reline (R0) system, as demonstrated in Figure 4.19a. The variation in stability between these two DES systems is primarily driven by the molecular characteristics of their respective components. In reline, urea serves as a fundamental constituent, whereas in glyceline, glycerol plays the corresponding role. Due to its smaller molecular size and higher polarity, urea exhibits a stronger tendency to interact with the backbone of the CPNT resulting in higher number of hydrogen bonds with backbone atoms compared to glycerol (Figure 4.19b). These interactions with urea molecules lead to a slight reduction in the number of intra-CPNT hydrogen bonds, which are crucial for maintaining the nanotube's structural integrity. Consequently, the CPNT demonstrates slightly lower stability in reline than in glyceline. Additionally, it is observed that the contribution of side chain hydrogen bonding between adjacent CP rings of the CPNT to its stability is almost negligible in both R0 and G0 systems. This finding contrasts with earlier reports, which suggested that side-chain hydrogen bonding, alongside backbone interactions, plays a significant role in stabilizing the nanotube structure[61, 62, 65]. The complete absence of side-chain hydrogen bonding between the adjacent CP rings in this study is likely due to their preferential hydrogen bonding with DES components, thereby limiting their availability to form hydrogen bonds among themselves, as shown in Figure 4.13b.

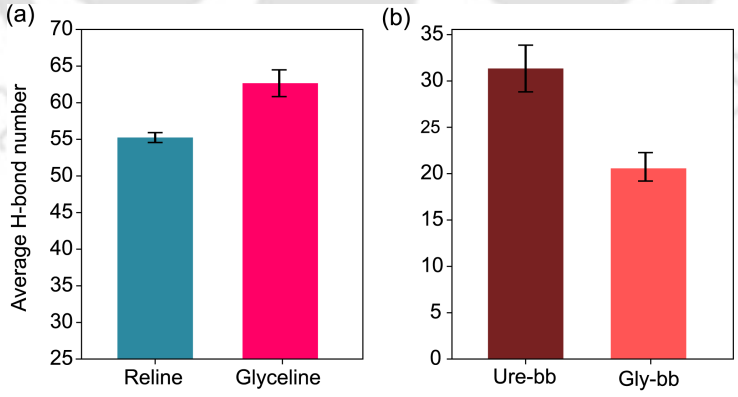

Figure 4.19: *(a) Average number of hydrogen bonds present between the backbone atoms of the CPNT in reline (R0) and glyceline (G0). (b) Average number of hydrogen bonds between urea in reline and glycerol in glyceline with the backbone atoms of the CPNT in R0 and G0 systems.*

Furthermore, the addition of water to the DES environment has a destabilizing effect on the CPNT structure, with a more pronounced impact observed in reline-based systems than in glyceline-based systems. The underlying mechanism behind this disruption lies in the competitive interactions between water molecules and the DES components with the CPNT. As water molecules infiltrate the system, they increasingly compete with DES molecules to engage in hydrogen bonding with the CPNT, leading to a gradual weakening of intra-CPNT hydrogen bond networks (Figure 4.6). This weakening ultimately results in the disintegration of the nanotube's tubular architecture. Additionally, the presence of water not only affects the stability of the CPNT but also contributes to the overall destabilization of the DES structure itself, further amplifying the loss of nanotube integrity (Figure 4.15). This observation aligns with previous studies indicating that hydration in DES gradually reduces the various interactions between the components of the DES[68, 69].

Temperature also emerges as a critical factor influencing the stability of the CPNT in DES environments. The study reveals that in glyceline, the CPNT maintains its structural integrity over a wider temperature range, remaining stable from 300 K up to 350 K without experiencing significant deformation. In contrast, in reline, the nanotube exhibits signs of structural instability upon reaching 350 K, where it begins to split into two distinct sections. As the temperature continues to rise, the CPNT undergoes more pronounced structural disruption, ultimately leading to its gradual disintegration. This temperature-dependent behavior can be linked to the reduction in hydrogen bond density at elevated temperatures. As thermal fluctuations intensify, they disrupt the intermolecular hydrogen bonding network, resulting in the breakage of the tubular conformation of the CPNT. Notably, in previous studies conducted in aqueous environments, this same CPNT failed to retain its tubular conformation even at 300 K[60]. In contrast, the use of DES significantly enhances its thermal stability, allowing the nanotube to remain structurally intact at higher temperatures.

In summary, the study explores the pivotal role played by the choice of DES, hydration levels, and temperature in dictating the structural stability of CPNTs. Glyceline provides a more favorable environment for CPNT stability compared to reline, owing to its molecular composition and ability to preserve intra-CPNT hydrogen bonding. However, the introduction of water leads to structural disintegration in both DES systems, with a more severe impact observed in reline. Additionally, temperature-induced fluctuations

further influence CPNT stability, with glyceline offering superior thermal resilience over a broader temperature range. These findings provide valuable insights into the fundamental interactions governing CPNT stability in complex solvent environments, paving the way for potential applications in nanotechnology and biomaterials.

4.5 Conclusion

In conclusion, this chapter provides valuable insights into the behavior of cyclic peptide nanotubes (CPNTs) in deep eutectic solvents (DES), offering important implications in the field of nanotechnology. The stability of the 8 × D$\underline{\text{L}}$K$\underline{\text{L}}_2$ nanotube in different DES environments demonstrates the potential of these solvents as media for nanostructure assembly and preservation. The superior stability of the CPNT in glyceline compared to reline highlights the importance of solvent selection in maintaining nanoscale architectures. Furthermore, the observed effects of hydration and temperature on CPNT integrity highlight the critical role of environmental conditions in nanostructure stability. These findings contribute to our understanding of how nanoscale assemblies interact with complex solvent environments, paving the way for the design of more robust and tunable nanostructures. As research in this field progresses, the interplay between nanostructures and deep eutectic solvents may open new avenues for creating functional materials with tailored properties at the nanoscale.

References

(1) Devi, M.; Moral, R.; Thakuria, S.; Mitra, A.; Paul, S. *ACS Omega* **2023**, *8*, 9702–9728.

(2) Cabezas, R.; Zurob, E.; Gomez, B.; Merlet, G.; Plaza, A.; Araya-Lopez, C.; Romero, J.; Olea, F.; Quijada-Maldonado, E.; Pino-Soto, L., et al. *Ind. Eng. Chem. Res.* **2022**, *61*, 17397–17422.

(3) Paiva, A.; Craveiro, R.; Aroso, I.; Martins, M.; Reis, R. L.; Duarte, A. R. C. *ACS Sus. Chem. Eng.* **2014**, *2*, 1063–1071.

(4) Smith, E. L.; Abbott, A. P.; Ryder, K. S. *Chem. Rev.* **2014**, *114*, 11060–11082.

(5) Pedro, S. N.; Freire, M. G.; Freire, C. S.; Silvestre, A. J. *Expert Opin. Drug Delivery* **2019**, *16*, 497–506.

(6) Mišan, A.; Nađpal, J.; Stupar, A.; Pojić, M.; Mandić, A.; Verpoorte, R.; Choi, Y. H. *Crit. Rev. Food Sci. Nutr.* **2020**, *60*, 2564–2592.

(7) Mbous, Y. P.; Hayyan, M.; Hayyan, A.; Wong, W. F.; Hashim, M. A.; Looi, C. Y. *Biotechnol. Adv.* **2017**, *35*, 105–134.

(8) Warrag, S. E.; Peters, C. J.; Kroon, M. C. *Curr. Opin. Green Sus. Chem.* **2017**, *5*, 55–60.

(9) Ünlü, A. E.; Arıkaya, A.; Takaç, S. *Green Process. Synth.* **2019**, *8*, 355–372.

(10) Jablonskỳ, M.; Škulcová, A.; Šima, J. *Molecules* **2019**, *24*, 3978.

(11) Millia, L.; Dall'Asta, V.; Ferrara, C.; Berbenni, V.; Quartarone, E.; Perna, F. M.; Capriati, V.; Mustarelli, P. *Solid State Ionics* **2018**, *323*, 44–48.

(12) Yadav, N.; Venkatesu, P. *Phys. Chem. Chem. Phys.* **2022**, *24*, 13474–13509.

(13) Sanchez-Fernandez, A.; Prevost, S.; Wahlgren, M. *Green Chem.* **2022**, *24*, 4437–4442.

(14) Tian, Y.; Zhu, M.; Hu, T.; Liu, C. *Int. J. Biol. Macromol.* **2023**, *247*, 125477.

(15) Yadav, N.; Bhakuni, K.; Bisht, M.; Bahadur, I.; Venkatesu, P. *ACS Sus. Chem. Eng.* **2020**, *8*, 10151–10160.

(16) Abo-Hamad, A.; Hayyan, M.; AlSaadi, M. A.; Hashim, M. A. *Chem. Eng. J.* **2015**, *273*, 551–567.

(17) Wagle, D. V.; Zhao, H.; Baker, G. A. *Acc. Chem. Res.* **2014**, *47*, 2299–2308.

(18) Tomé, L. I.; Baião, V.; da Silva, W.; Brett, C. M. *Appl. Mater. Today* **2018**, *10*, 30–50.

(19) Nam, N. N.; Do, H. D. K.; Trinh, K. T. L.; Lee, N. Y. *Nanomaterials* **2023**, *13*, 1164.

(20) Chen, Y. Y.; Walvekar, R.; Khalid, M.; Shahbaz, K.; Gupta, T. *Mater. Res. Express* **2017**, *4*, 075028.

(21) Rozas, S.; Atilhan, M.; Aparicio, S. *J. Phys. Chem. B* **2020**, *124*, 3556–3567.

(22) Jahanbakhsh-Bonab, P.; Esrafili, M. D.; Ebrahimzadeh, A. R.; Sardroodi, J. J. *J. Mol. Liq.* **2021**, *341*, 117277.

(23) Ghenaatian, H. R.; Shakourian-Fard, M.; Kamath, G.; Trant, J. F.; Mjalli, F. S. *J. Mol. Liq.* **2022**, *363*, 119855.

(24) Wen, Q.; Chen, J.-X.; Tang, Y.-L.; Wang, J.; Yang, Z. *Chemosphere* **2015**, *132*, 63–69.

(25) Hayyan, M.; Hashim, M. A.; Al-Saadi, M. A.; Hayyan, A.; AlNashef, I. M.; et. al. *Chemosphere* **2013**, *93*, 455–459.

(26) Azmi, S.; Koudahi, M. F.; Frackowiak, E. *Energy Environ. Sci.* **2022**, *15*, 1156–1171.

(27) Lapeña, D.; Lomba, L.; Artal, M.; Lafuente, C.; Giner, B. *J. Chem. Thermodyn.* **2019**, *128*, 164–172.

(28) Pal, S.; Paul, S. *J. Phys. Chem. C* **2019**, *123*, 11686–11698.

(29) Pal, S.; Roy, R.; Paul, S. *J. Phys. Chem. B* **2020**, *124*, 7598–7610.

(30) Silk, M. R.; Newman, J.; Ratcliffe, J. C.; White, J. F.; Caradoc-Davies, T.; Price, J. R.; Perrier, S.; Thompson, P. E.; Chalmers, D. K. *Chem. Commun.* **2017**, *53*, 6613–6616.

(31) Martínez, L.; Andrade, R.; Birgin, E. G.; Martínez, J. M. *J. Comput. Chem.* **2009**, *30*, 2157–2164.

(32) Maier, J. A.; Martinez, C.; Kasavajhala, K.; Wickstrom, L.; Hauser, K. E.; Simmerling, C. *J. Chem. Theory Comput.* **2015**, *11*, 3696–3713.

(33) Jorgensen, W. L.; Chandrasekhar, J.; Madura, J. D.; Impey, R. W.; Klein, M. L. *J. Chem. Phys.* **1983**, *79*, 926–935.

(34) Joung, I. S.; Cheatham III, T. E. *J. Phys. Chem. B* **2008**, *112*, 9020–9041.

(35) Frisch, M. J.; Trucks, G. W.; Schlegel, H. B.; Scuseria, G. E.; Robb, M. A.; Cheeseman, J. R.; et al. Gaussian 09, Revision A.02.; Gaussian, Inc., Wallingford, CT, 2009.

(36) Petersson, a.; Bennett, A.; Tensfeldt, T. G.; Al-Laham, M. A.; Shirley, W. A.; Mantzaris, J. *J. Chem. Phys.* **1988**, *89*, 2193–2218.

(37) Petersson, G.; Al-Laham, M. A. *J. Chem. Phys.* **1991**, *94*, 6081–6090.

(38) Bayly, C. I.; Cieplak, P.; Cornell, W.; Kollman, P. A. *J. Phys. Chem.* **1993**, *97*, 10269–10280.

(39) He, X.; Man, V. H.; Yang, W.; Lee, T.-S.; Wang, J. *J. Chem. Phys.* **2020**, *153*, 114502.

(40) Wang, J.; Wolf, R. M.; Caldwell, J. W.; Kollman, P. A.; Case, D. A. *J. Comput. Chem.* **2004**, *25*, 1157–1174.

(41) Sprenger, K.; Jaeger, V. W.; Pfaendtner, J. *J. Phys. Chem. B* **2015**, *119*, 5882–5895.

(42) Mamme, M. H.; Moors, S. L.; Terryn, H.; Deconinck, J.; Ustarroz, J.; De Proft, F. *J. Phys. Chem. Lett.* **2018**, *9*, 6296–6304.

(43) Fetisov, E. O.; Harwood, D. B.; Kuo, I.-F. W.; Warrag, S. E.; Kroon, M. C.; Peters, C. J.; Siepmann, J. I. *J. Phys. Chem. B* **2018**, *122*, 1245–1254.

(44) Shah, D.; Mjalli, F. S. *Phys. Chem. Chem. Phys.* **2014**, *16*, 23900–23907.

(45) Perkins, S. L.; Painter, P.; Colina, C. M. *J. Chem. Eng. Data* **2014**, *59*, 3652–3662.

(46) Perkins, S. L.; Painter, P.; Colina, C. M. *J. Phys. Chem. B* **2013**, *117*, 10250–10260.

(47) Case, D. A. et al. Amber 18., University of California: San Francisco, CA, 2018.

(48) Berendsen, H. J.; Postma, J. v.; Van Gunsteren, W. F.; DiNola, A.; Haak, J. R. *J. Chem. Phys.* **1984**, *81*, 3684–3690.

(49) Hünenberger, P. H. *Adv. Polym. Sci.* **2005**, 105–149.

(50) Ryckaert, J.-P.; Ciccotti, G.; Berendsen, H. J. *J. Comput. Phys.* **1977**, *23*, 327–341.

(51) Essmann, U.; Perera, L.; Berkowitz, M. L.; Darden, T.; Lee, H.; Pedersen, L. G. *J. Chem. Phys.* **1995**, *103*, 8577–8593.

(52) Roe, D. R.; Cheatham III, T. E. *J. Chem. Theory Comput.* **2013**, *9*, 3084–3095.

(53) Humphrey, W.; Dalke, A.; Schulten, K. *J. Mol. Graphics* **1996**, *14*, 33–38.

(54) Hunter, J. D. *Comput. Sci. Eng.* **2007**, *9*, 90–95.

(55) Gowers, R. J.; Linke, M.; Barnoud, J.; Reddy, T. J. E.; Melo, M. N.; Seyler, S. L.; Domanski, J.; Dotson, D. L.; Buchoux, S.; Kenney, I. M.; Oliver, B. *MDAnalysis: a Python package for the rapid analysis of molecular dynamics simulations*; tech. rep.; Los Alamos National Laboratory (LANL), Los Alamos, NM (United States), 2019.

(56) Michaud-Agrawal, N.; Denning, E. J.; Woolf, T. B.; Beckstein, O. *J. Comput. Chem.* **2011**, *32*, 2319–2327.

(57) Mitra, A.; Chattaraj, K. G.; Paul, S. *J. Phys. Chem. B* **2023**, *127*, 996–1012.

(58) Chattaraj, K. G.; Paul, S. *J. Chem. Phys.* **2019**, *150*, 064501.

(59) D'Agostino, C.; Harris, R. C.; Abbott, A. P.; Gladden, L. F.; Mantle, M. D. *Phys. Chem. Chem. Phys.* **2011**, *13*, 21383–21391.

(60) Moral, R.; Paul, S. *Phys. Chem. Chem. Phys.* **2023**, *25*, 5406–5422.

(61) Moral, R.; Paul, S. *J. Phys. Chem. B* **2025**, *129*, 3590–3603.

(62) Silk, M. R.; Price, J. R.; Mohanty, B.; Leiros, H.-K. S.; Lund, B. A.; Thompson, P. E.; Chalmers, D. K. *Chem. Eur. J.* **2021**, *27*, 14489–14500.

(63) Hartgerink, J. D.; Granja, J. R.; Milligan, R. A.; Ghadiri, M. R. *J. Am. Chem. Soc.* **1996**, *118*, 43–50.

(64) Vijayaraj, R.; Sundar Raman, S.; Mahesh Kumar, R.; Subramanian, V. *J. Phys. Chem. B* **2010**, *114*, 16574–16583.

(65) Vijayaraj, R.; Van Damme, S.; Bultinck, P.; Subramanian, V. *Phys. Chem. Chem. Phys.* **2012**, *14*, 15135–15144.

(66) Gao, Q.; Zhu, Y.; Ji, X.; Zhu, W.; Lu, L.; Lu, X. *Fluid Phase Equilib.* **2018**, *470*, 134–139.

(67) Hammond, O. S.; Bowron, D. T.; Edler, K. J. *Angew. Chem. Int. Ed.* **2017**, *129*, 9914–9917.

(68) Nolasco, M. M.; Pedro, S. N.; Vilela, C.; Vaz, P. D.; Ribeiro-Claro, P.; Rudić, S.; Parker, S. F.; Freire, C. S. R.; Freire, M. G.; Silvestre, A. J. D. *Front. Phys.* **2022**, *10*, 834571.

(69) Kumari, P.; Shobhna, n.; Kaur, S.; Kashyap, H. K. *ACS Omega* **2018**, *3*, 15246–15255.

Chapter 5

Interaction of Cyclic Peptide Nanotubes with Lipid Bilayers and Water Transport Dynamics

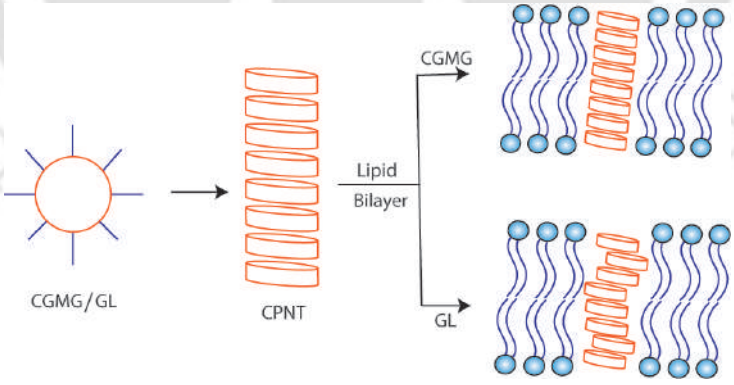

Overview

To evaluate the potential of CPNTs as artificial transmembrane channels, this chapter focuses on the structural stability and membrane integration of two distinct CPNTs, namely 8 × [(Cys-D-Gly-Met-D-Gly)$_2$] and 8 × [(Gly-D-Leu)$_4$] within different biologically relevant lipid bilayers. This includes 1-palmitoyl-2-oleoyl-sn-glycero-3-phosphocholine (POPC), a mixed model membrane (POPE/POPG), and a realistic yeast model membrane. The results demonstrate that both CPNTs maintain their tubular structures in all lipid bilayers, with [(Cys-D-Gly-Met-D-Gly)$_2$] showing increased stability over an extended period in these lipid membranes. The insertion of CPNTs shows negligible impact on lipid bilayer properties, including area per lipid, volume per lipid, and bilayer thickness. The study demonstrates that the CPNT preserves its two-line water movement pattern within all the lipid membranes, reaffirming their potential as water channels. The MSD curves further reveal that the dynamics of water molecules inside the nanotube are similar for all the bilayer systems with minor differences that arise due to different lipid environments.

5.1 Introduction

Over the previous chapters, the structural stability and self-assembly of CPNTs have been explored under various bulk-phase environments, including aqueous solvents, high salt concentrations, elevated temperatures, solvents with varying polarity, and deep eutectic solvents (DESs). These studies highlighted the sensitivity of CPNTs to their surrounding medium and the conditions necessary to promote or hinder their assembly. While such environments provided valuable insights into their aggregation tendency and conformational behavior, a comprehensive understanding of CPNT functionality requires extending this investigation into biologically relevant systems.

A critical next step involves studying how CPNTs behave when interfaced with lipid bilayers, which are fundamental structural components of all living cells. In biological systems, the transport of water, ions, and small molecules across membranes is mediated by protein channels and pores[1–3]. Mimicking these functions using synthetic channels like CPNTs presents a compelling opportunity in nanomedicine and biotechnology. To that end, understanding how CPNTs insert into, interact with, and remain stable within lipid membranes is essential for evaluating their potential as transmembrane channels.

Several synthetic nanotubular materials such as carbon, boron nitride, and silica nanotubes have been proposed for membrane channel applications. Carbon nanotubes, for example, exhibit exceptional mechanical strength and electrical conductivity[4], yet their poor biocompatibility and potential toxicity have limited their use in biological contexts[5–7]. Boron nitride nanotubes, while promising, present challenges in synthesis and exhibit reactivity that may interfere with membrane integration[8]. Silica nanotubes, although more tunable through surface modification, suffer from non-biodegradability, raising safety concerns for in vivo applications[9]. These limitations underscore the need for biologically compatible and structurally tunable alternatives.

In this regard, CPNTs offer an alluring alternative, underscored by their inherent biocompatibility[9], customizable surface functionalities[9–11], and the potential for versatile modular designs[12]. Their capacity to span diverse environments as nanochannels embedded within lipid bilayers positions them as a potent candidate for revolutionizing biomimetic systems. They possess the ability to compete with antimicrobial peptides[13–15] whose mode of action involves the barrel-stave mechanism[16, 17]-a mechanism re-

sembling that of CPNTs integrated into lipid membranes. Consequently, CPNTs have the potential to emerge as a suitable candidate to address the escalating issue of antibiotic resistance[15, 18, 19] in today's world. Hence, the distinctive attributes of CPNTs surmount the constraints associated with conventional nanotube materials, making them an attractive prospect for intricate molecular transport dynamics.

Following the pioneering synthesis of CPNT in 1993[20], extensive efforts have been directed towards optimizing these nanotubes as potential nanochannels. An array of investigations has delved into the interactions between water and peptide nanotubes. The dynamics of water within these structures were explored by Engles and colleagues[21], revealing a distinctive 1-2-1-2 water chain pattern. This observation was subsequently corroborated by the studies of Tarak et al.[22] and Liu et al.[23, 24]. Beyond water, the transport of ions through CPNTs has also garnered attention. The transportation of cations such as K^+[25–28], Na^+[25–29], Ca^{2+}[25], and $NH4^+$[30] in CPNTs composed of varying peptides and configurations has been investigated using molecular dynamics simulations. Moreover, the movement of molecules including O_2[31], CO_2[31], NH_3[30, 31], methane[32], methanol[32, 33], ethanol[32, 34], glucose[35], chloroform[33], ascorbic acid[36], lactic acid[37], and drugs like 5-fluorouracil[38, 39] through CPNTs has been reported in the later years. Notably, many of these transport studies involved CPNTs embedded within lipid bilayers, predominantly within POPE bilayers. Hence, ensuring the stability of a specific CPNT within a particular lipid bilayer becomes of paramount importance for facilitating efficient ion and molecule transportation. Addressing this concern, Maroli and Kolandaivel[40] conducted a comprehensive investigation into the stability of CPNTs across five distinct pure lipid bilayers: POPA, POPE, POPS, POPG, and POPC. Their study revealed comparable stability of the nanotube across all these lipid bilayers. However, the stability assessment of CPNTs in more intricate biological membrane systems remains an unexplored territory, despite the manifold possibilities associated with employing CPNTs as artificial channels.

This chapter aims to elucidate the stability of two CPNTs across three distinct lipid bilayer membranes. The first membrane is a pure lipid system comprising 1-palmitoyl-2-oleoyl-sn-glycero-3-phosphocholine (POPC). The second is a model membrane, mimicking the composition of gram-negative bacterial membranes, consisting of a 3:1 mixture of 1-palmitoyl-2-oleoyl-sn-glycero-3-phosphoethanolamine (POPE) and 1-palmitoyl-2-oleoyl-sn-glycero-3-phosphoglycerol (POPG)[41]. Lastly, the third is a realistic yeast

model membrane, consisting of 1,2-dioleoyl-sn-glycero-3-phosphocholine (DOPC), POPE, 1,2-dipalmitoyl-sn-glycero-3-phosphocholine (DPPC), 1-palmitoyl-2-oleoyl-sn-glycero-3-phosphate (POPA), 1-palmitoyl-2-oleoyl-sn-glycero-3-phospho-L-serine (POPS), and cholesterol (CHL). The composition of the yeast model membrane is based on the work by Sunhwan et al.[42]. We conducted 500 ns MD simulations for each system to evaluate the stability of CPNT within the lipid bilayers. Additionally, we examined the structural characteristics of the lipid bilayers with and without the CPNT. Finally, we investigated the dynamics of water within the CPNT when embedded in lipid membranes.

5.2 Materials and Methods

5.2.1 Construction of Stable CPNT Structure

The initial geometry of the cyclic peptide (CP) ring was taken from the previous chapter and random substitutions of amino acids were made to obtain different CP rings. Cyclic peptide nanotubes (CPNTs) were created by stacking eight distinct, minimized peptide rings in precise arrangements using PACKMOL [43]. To ensure the stability and avoid unfavorable contacts, the CPNTs were immersed in either polar (water) or non-polar (chloroform) solvents depending on the nature of the amino acid residues of the CP rings and subjected to energy minimization, heating, and equilibration using AMBER18 package [44]. Subsequent 100 ns simulation runs were conducted for each CPNT to observe their dynamics. The final stable structures of the nanotubes were then extracted for further simulation run.

5.2.2 System Setup for Lipid Simulation

The CPNT structure obtained from above simulation was embedded within three different model lipid bilayers, generated using the CHARMM-GUI membrane builder module [45, 46]. Detailed descriptions of these systems are provided in Table 5.1. Each lipid bilayer's upper and lower leaflets were symmetrically populated with an equal number of lipid molecules. The CPNT was placed at the bilayer membrane's center and oriented perpendicular to the principal axis (along the Z-axis). To ensure a realistic biological environment, each system was solvated with 50 TIP3P [47] water molecules per lipid, forming a water layer on top and bottom of the bilayers. Additionally, a salt concentra-

tion of 0.15 M KCl was included in each system, as K^+ ions are more prevalent inside cells compared to Na^+ ions. Furthermore, to neutralize negatively charged lipid molecules, an equivalent number of K^+ ions were added. Figure 5.1 depicts the system setup of a CPNT embedded in a lipid bilayer. The preparation of all systems in AMBER format, including their topology and coordinates, was accomplished using CHARMM-GUI. For the CPNTs and lipid models, the ff14SB [48] and lipid17 [49] force fields were employed, respectively, ensuring accurate and reliable simulations. The ion parameters developed by Joung and Chetham[50] were considered for K^+ and Cl^- ions.

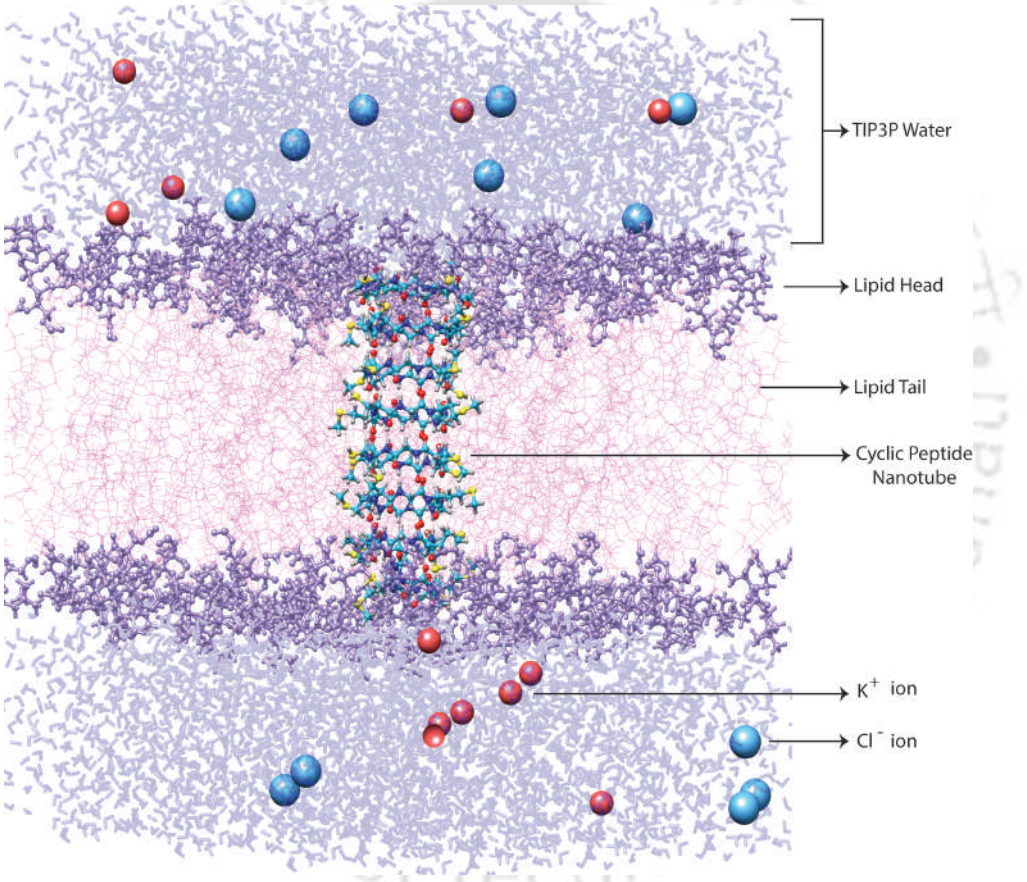

Figure 5.1: *Snapshot of the 8 × [Cys-D-Gly-Met-D-Gly]$_2$ nanotube embedded in hydrated yeast bilayer. Here, the CPNT is represented in ball and stick style, the head groups of the lipid bilayer are depicted in purple ball-stick style, lipid tails are in pink wire style, and water are in fadded light purple stick style. The K^+ and Cl^- ions are represented in red and blue spheres respectively.*

After the initial setup, all systems underwent two stages of energy minimization. Firstly, a 20,000-step minimization was conducted, where the lipid bilayer and CPNT

were kept under position restraints to minimize water within the systems effectively. Subsequently, another 20000-step minimization was performed without any restraints to optimize the entire systems. For the minimization process, first 10000 steps were carried out using steepest descent method and last 10000 steps were done using conjugate gradient method. Next, a gradual heating process elevated the system temperature to 303.15 K which is above the phase-transition temperature of all lipid bilayers. The systems were then maintained in the NPT ensemble for 1 ns at a target temperature of 303.15 K and a target pressure of 1.0 atm. Throughout this phase, the lipid bilayer and CPNT were held under weak position restraints. This restraint force was decreased gradually from 10 to 5 kcal/mol$Å^2$. Following these, a 4 ns NPT equilibration was carried out for each system without any position restraints. The desired pressure and temperature were regulated using the Monte Carlo barostat [51] with a pressure relaxation time of 2 ps and the Langevin thermostat [52] with a collision frequency of 1 ps^{-1}, respectively. Furthermore, semiisotropic pressure scaling is implemented, and a constant surface tension is applied with interfaces situated in the XY plane[53, 54]. To preserve the covalent bonds involving hydrogen atoms without affecting other degrees of freedom, the SHAKE algorithm [55] was applied. Simulations were conducted using a timestep of 2 fs, and all short-ranged non-bonded interactions were restricted within a cutoff distance of 10.0 Å . For the estimation of long-ranged electrostatic interactions, the particle mesh Ewald (PME) method [56] was employed. To eliminate edge effects, all simulations were carried out using periodic boundary conditions (PBC) in all three directions. Finally, a 500 ns production run was executed for all systems under the NPT ensemble.

The trajectories were analyzed using CPPTRAJ[57] module of Amber18 package. Some analyses were performed using in-house FORTRAN 95 codes. Visual Molecular Dynamics (VMD)[58] and UCSF-Chimera[59] were used for visualization purposes.

Table. 5.1: *Detailed information of all the systems that are studied in this work. Here CGMG refers to [(Cys-D-Gly-Met-D-Gly)$_2$] and GLrefers to [(Gly-D-Leu)$_4$].*

CPNT	Lipid Bilayer	Lipid Type	Number of lipids	Ratio of Molecules (CPNT:Lipid:Water)	Box Dimensions (Å× Å× Å)
	POPC	POPC	128	1:128:6400	65.54 × 65.54 × 83.93
8 × CGMG	Mixed	POPE,POPG	96,32	1:128:6400	62.05 × 62.05 × 91.95
	Yeast	DPPC,POPA, DOPC, POPS, POPE, CHL	20,20, 100,10, 60,60	1:270:13500	84.01 × 84.01 × 101.11
	POPC	POPC	128	1:128:6400	64.48 × 64.48 × 86.98
8 × GL	Mixed	POPE,POPG	96,32	1:128:6400	62.84 × 62.84 × 89.65
	Yeast	DPPC,POPA, DOPC, POPS, POPE, CHL	20,20, 100,10, 60,60	1:270:13500	87.04 × 87.04 × 94.82

5.2.3 System Setup for Water Dynamics Calculation

The mean square displacement (MSD) of water molecules along the channel was calculated for the CGMG nanotube placed in all the three lipid bilayers. For that, the final configuration of the systems obtained from the previous 500 ns NPT simulation were further equilibrated for 10 ns in NVT ensemble. The equilibrated systems (with fixed box dimensions) were subjected to an additional 32 ns production run in micro-canonical ensemble (NVE). The data from the final 12 ns of the NVE run was divided into three blocks, each spanning 4 ns. We performed the MSD analysis on these trajectory blocks and then computed their averages and standard deviations to ensure the accuracy of our results for each system. Again, to calculate hydrogen bond lifetime of the water molecules present inside the CPNT, the NVE systems were further simulated for 200 ps and the coordinates were recorded at 10 fs intervals.

5.3 Results and Discussions

In our quest to examine the stability of CPNTs in various lipid bilayers, we generate several CPNT variants by randomly substituting amino acid residues in the CP rings. Among the tested CPNTs, those exhibiting amphiphilic characteristics, such as 8 × [(Asp-D-Gly-Lys-D-Gly)$_2$], 8 × [(Asp-D-Ala-Lys-D-Ala)$_2$], and 8 × [(Asp-D-Leu-Lys-D-Leu)$_2$], display instability in all three different lipid bilayers. On the other hand, the hydrophobic CPNTs, including 8 × [(Gly-D-Leu)$_4$], 8 × [(Ala-D-Leu)$_4$], 8 × [(Ile-D-Leu)$_4$], and 8 × [(Trp-D-Leu)$_4$], show decreasing stability with their increasing hydrophobicity. It can be seen from the time evolution plots of RMSD and Rg values of backbone atoms of hydrophobic CPNTs (Figure 5.2).

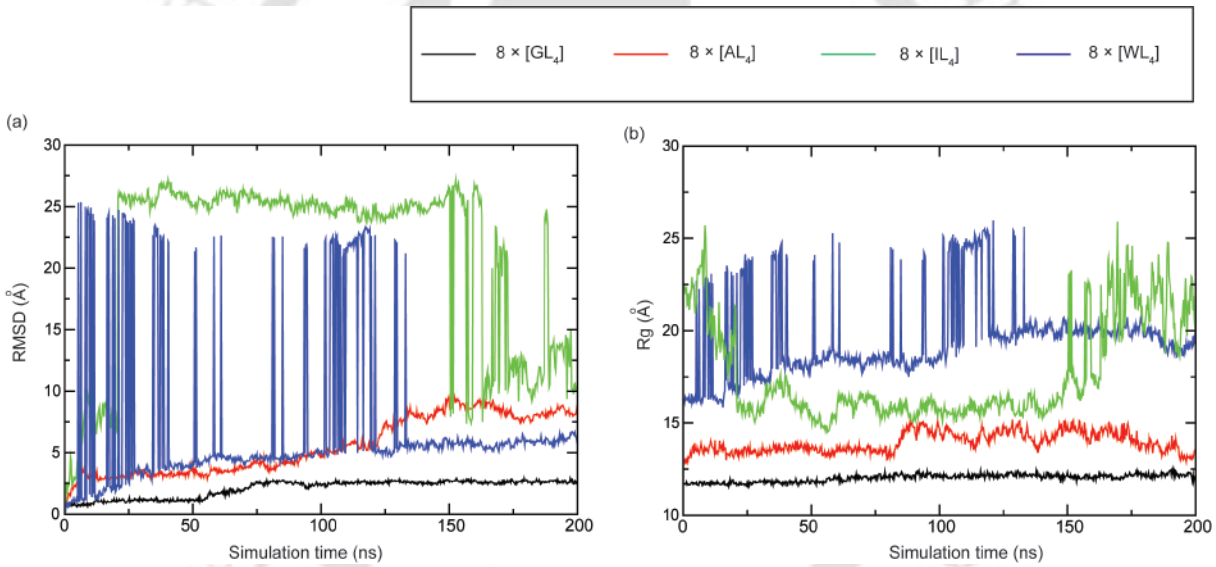

Figure 5.2: *(a) Root mean square deviation (RMSD) and (b) Radius of gyration (Rg) of backbone atoms of hydrophobic CPNTs namely 8 × [GL]$_4$, 8 × [AL]$_4$, 8 × [IL]$_4$, and 8 × [WL]$_4$.*

Notably, out of all CPNTs, 8 × [(Gly-D-Leu)$_4$] emerges as the most stable and is chosen for further investigations. Additionally, we consider 8 × [(Cys-D-Gly-Met-D-Gly)$_2$] nanotube[40], known for its stability in pure lipid model membranes, as a potential candidate to explore its stability properties in mixed and yeast lipid membranes. Henceforth, CPNT 8 × [(Cys-D-Gly-Met-D-Gly)$_2$] and 8 × [(Gly-D-Leu)$_4$] are termed as C<u>G</u>M<u>G</u> and G<u>L</u> respectively.

5.3.1 Structural Stability of CPNTs in Different Lipid Bilayers

The structural stability of both CPNTs within the three lipid bilayers is assessed using Root Mean Square Displacement (RMSD) and Root Mean Square Fluctuation (RMSF) analyses. Additionally, the compactness of the nanotubes is determined through Radius of Gyration (Rg) values. Figure 5.3(a and b) illustrates the RMSD variation of the backbone atoms of CP rings in CGMG and GL nanotubes over simulation time across the three lipid bilayers. Notably, the average RMSD values remain consistent among the three lipid bilayers for the CGMG nanotube, specifically 1.14 ± 0.1 Å for POPC, 1.30 ± 0.3 Å for mixed, and 1.08 ± 0.2 Å for yeast. These findings imply minimal deviation of the nanotube structure from their initial positions throughout the simulation. Conversely, the RMSD values for the GL nanotube show increasing trend after 200 ns simulation run for all the three lipid membranes. Further, the RMSF of the Cα atoms (Figure 5.3c) within CGMG nanotube exhibits lower fluctuations in all the bilayers, with exceptions seen between atom numbers 500 to 600 in POPC and yeast bilayers. However, higher fluctuations, notably around atom numbers 50 to 200, are observed for the GL nanotube (Figure 5.3d), primarily in the POPC bilayer, indicating structural distortions of terminal rings compared to the inner CP rings. To delve into the compactness of both nanotubes within the lipid bilayers, Rg values are computed (Figure 5.3 e and f). Notably, the CGMG nanotube displays robust stability in all three bilayers. In contrast, compared to CGMG, the GL nanotube exhibits relatively lower stability across all the bilayers considered.

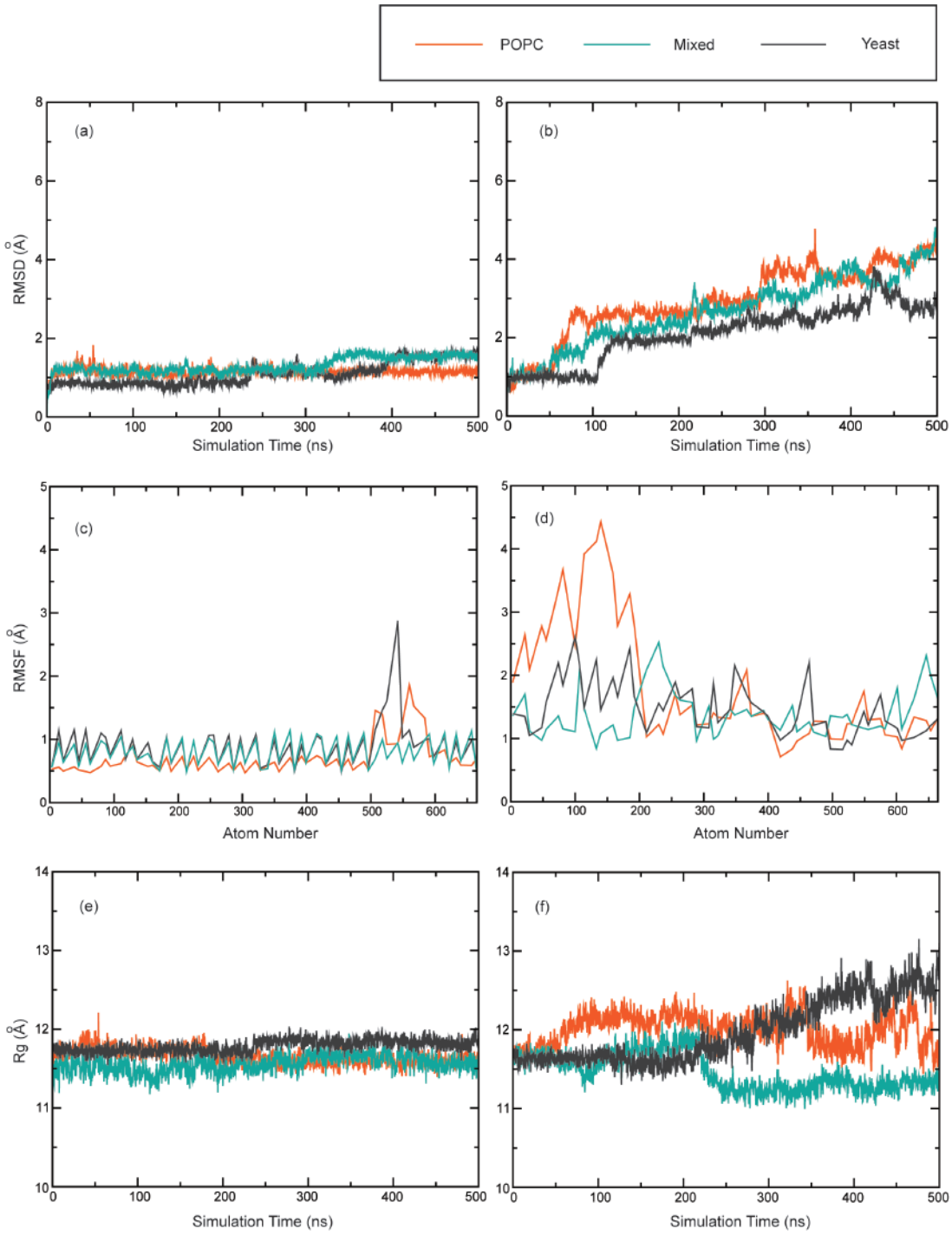

Figure 5.3: *Root mean square deviation (RMSD) of backbone atoms of the CPNTs (a) CGMG and (b) GL versus time, root mean square fluctuation (RMSF) of C-α atoms of (c) CGMG and (d) GL versus time, radius of gyration (Rg) of backbone atoms of (e) CGMG and (f) GL versus time embedded in POPC, mixed, and yeast membranes.*

Figure 5.4 illustrates the inter-ring center of mass distance for the two nanotubes within the yeast environment. Notably, the average distance between the center of mass of adjacent CP rings is 4.72 ± 0.06 Å for the CGMG nanotube, while the GL nanotube exhibits a slightly larger value of 4.87 ± 0.53 Å . However, in the GL nanotube, the inter-CP ring distances for the pairs 2 and 3, 4 and 5, and 6 and 7 exhibits substantial deviations from the average distance value, particularly beyond 200 ns. This pronounced change suggests that this hydrophobic nanotube is not stable within the yeast membrane over extended simulation periods.

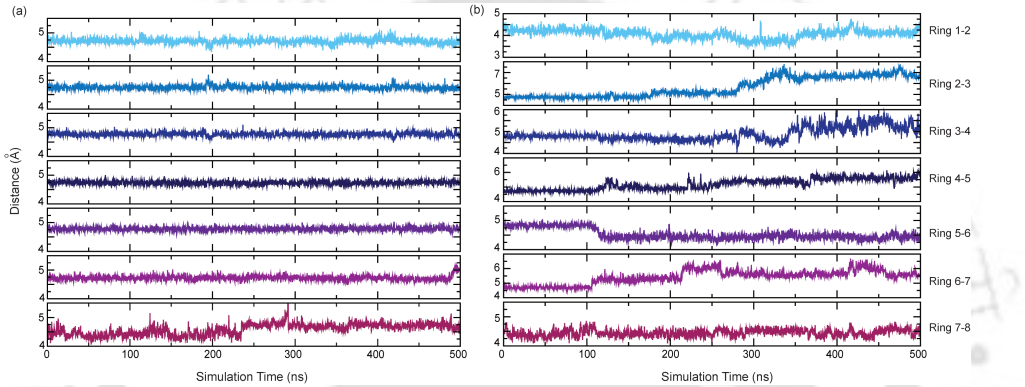

Figure 5.4: *Distance between the center of mass versus time of two adjacent CP rings of the CPNTs (a) CGMG and (b) GL embedded in yeast bilayer.*

Moreover, the inter-ring distances of CGMG and GL nanotubes within the POPC and mixed lipid bilayers are presented in Figure 5.5. The trend observed in the yeast membrane is also evident in both POPC and mixed bilayers. For the CGMG nanotube, the inter-ring distances remain nearly constant throughout the entire simulation period. In contrast, the GL nanotube exhibits noticeable deviations beyond 200 ns, with the first two inter-ring gaps showing more pronounced fluctuations in the POPC bilayer.

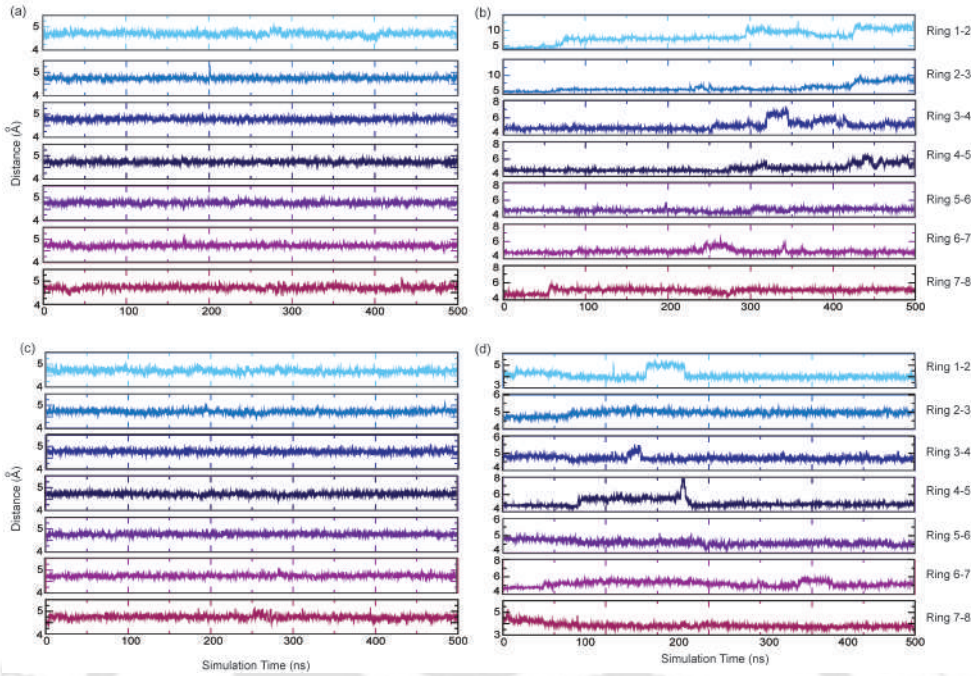

Figure 5.5: *Distance between the center of mass versus time of two adjacent CP rings of the CPNTs CGMG embedded in POPC (a) and mixed (c) bilayer, and GL embedded in POPC (b) and mixed (d) bilayer.*

In order to have a better understanding of these nanotubes' stability, we decomposed the total interactions between the adjacent CP rings of the nanotubes into electrostatic and van der Waals components. Figure 5.6 provides an insight into the non-bonded interactions between adjacent CP rings within the CGMG and GL nanotubes, specifically embedded in the yeast membrane as function of simulation time. For the POPC and mixed membranes, detailed interaction energy profiles are available in Figures 5.7 and 5.8 respectively. In the context of the CGMG nanotube, a nearly constant pattern of interaction energies prevail between adjacent CP rings suggesting its consistant stability throughout the simulation time in all the lipid bilayers. Conversely, for the GLnanotube, the CP ring pairs 2 and 3, 4 and 5, and 6 and 7 show less elctrostatic interactions (more unfavorable) among themselves after around 200 ns (Figure 5.6b) indicating lower stability.

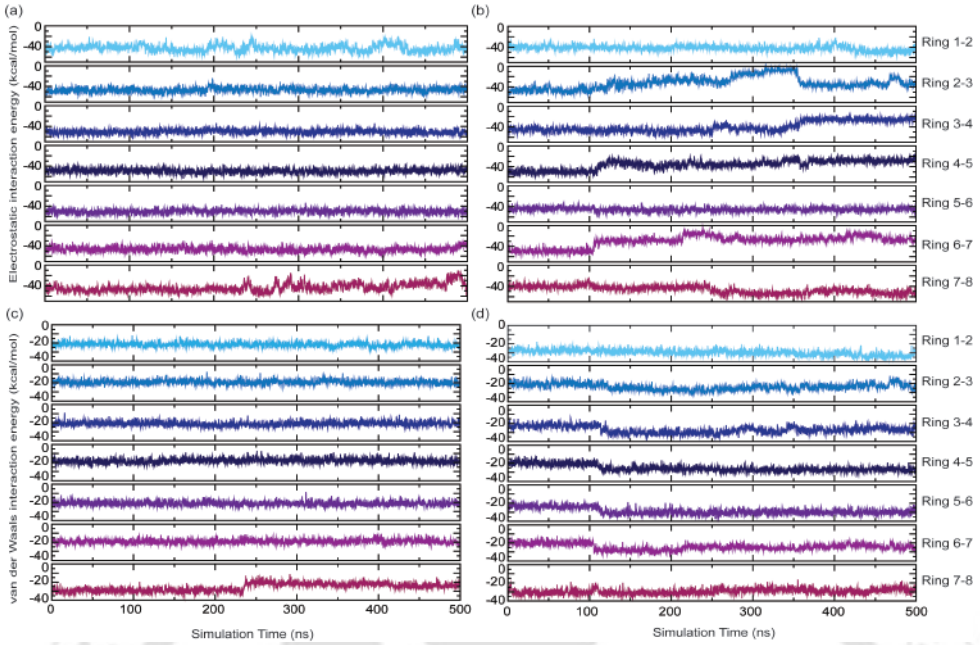

Figure 5.6: *Electrostatic interaction energies of the adjacent CP rings versus time of (a) CGMG and (b) GL, and van der Waals interaction energies of the adjacent CP rings versus time of (c) CGMG and (d) GL embedded in yeast bilayer. Here, both non-bonded interaction energies are expressed in kcal/mol.*

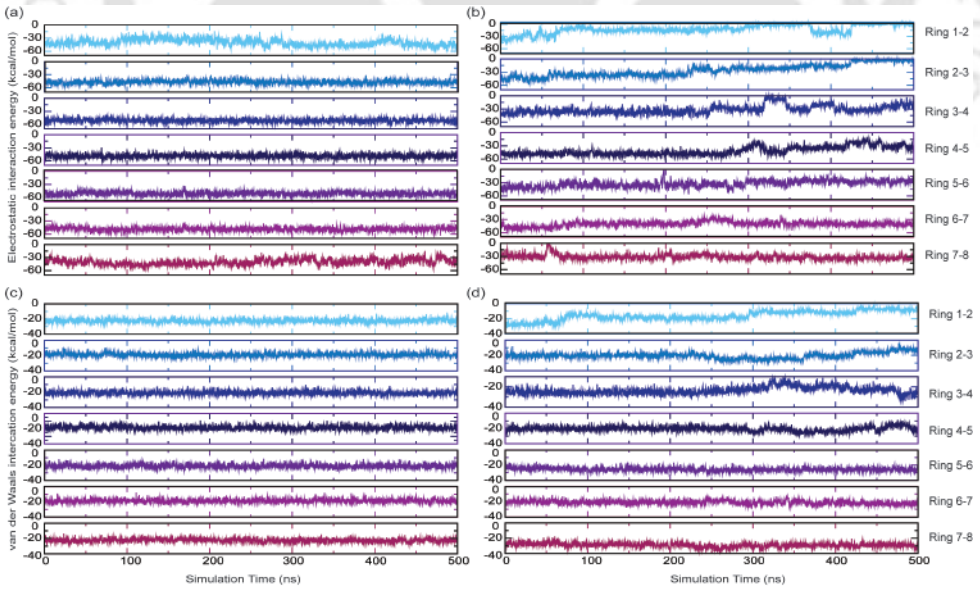

Figure 5.7: *Electrostatic interaction energies of the adjacent CP rings versus time of (a) CGMG and (b) GL, and van der Waals interaction energies of the adjacent CP rings versus time of (c) CGMG and (d) GL embedded in POPC bilayer. Here, both non-bonded interaction energies are expressed in kcal/mol.*

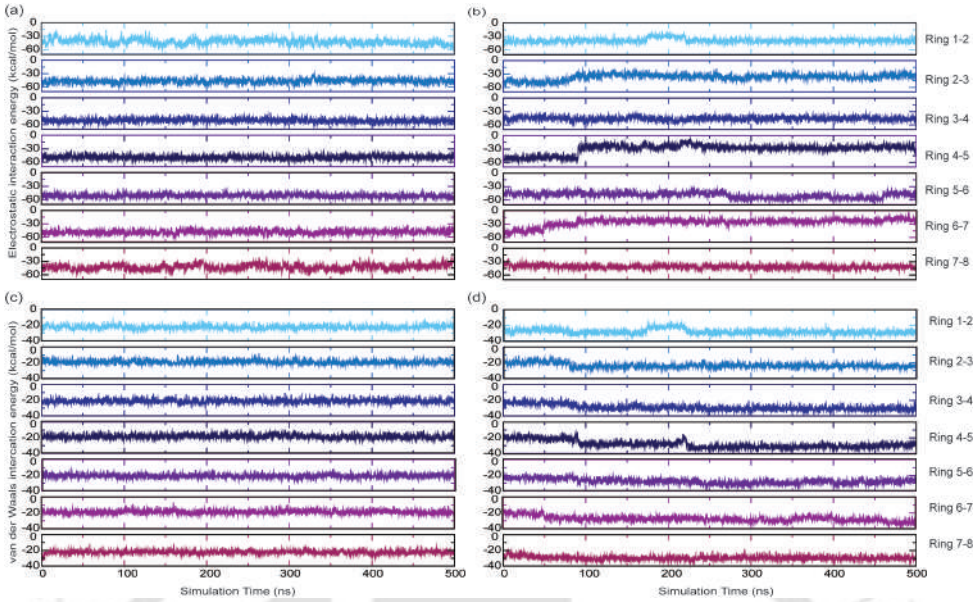

Figure 5.8: *Electrostatic interaction energies of the adjacent CP rings versus time of (a) CGMG and (b) GL, and van der Waals interaction energies of the adjacent CP rings versus time of (c) CGMG and (d) GL embedded in mixed bilayer. Here, both non-bonded interaction energies are expressed in kcal/mol.*

Table 5.2 comprehensively presents the average non-bonded interaction energies characterizing the interaction between the CPNTs and all the lipid bilayers. It is to be noted that the presence of polar groups within the CGMG nanotube results stronger interactions with all three membranes, distinguishing it from the GLnanotube.

Table. 5.2: *Average non-bonded interaction energies between the CPNTs and the lipid membranes. Here, 'Elec' represents Electrostatic Energy and 'vdW' represents van der Waals Energy. All the units are expressed in kcal/mol.*

	POPC		Mixed		Yeast	
	Elec	vdW	Elec	vdW	Elec	vdW
8 × CGMG	-107.92	-359.20	-95.29	-362.45	-101.70	-364.54
8 × GL	-84.15	-310.25	-24.55	-297.17	-56.12	-331.39

Moreover, it has been well-documented that CPNT stability relies significantly on intermolecular hydrogen bonds, particularly between NH and CO groups of adjacent CP rings[60]. The number of hydrogen bonds established between the backbone atoms of neighboring CP rings within the two CPNTs embedded in the yeast bilayer is depicted in

Figure 5.9(a and b). The criteria for characterizing hydrogen bonds is already mentioned in Chapter 1 (Section 1.4.3). The average number of hydrogen bonds between rings of C<u>G</u>M<u>G</u> and G<u>L</u> nanotubes stand at 7.04 ± 0.70 and 6.20 ± 0.92, respectively. The terminal rings of the C<u>G</u>M<u>G</u> nanotube exhibit less hydrogen bonding, whereas the G<u>L</u> nanotube shows a relatively low number of hydrogen bonds for all its rings, suggesting its lower stability.

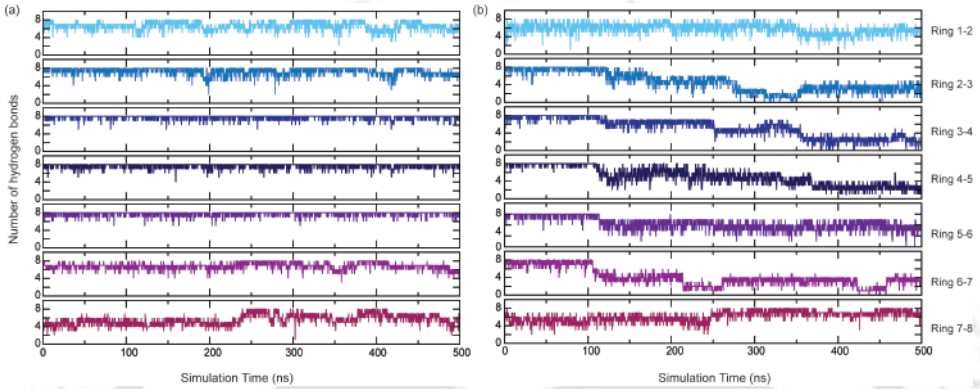

Figure 5.9: *Number of hydrogen bonds that are formed between the backbone atoms of the adjacent CP rings versus time of the (a) C<u>G</u>M<u>G</u> and (b) G<u>L</u> embedded in yeast bilayer.*

Consistent with the observations in the yeast membrane, the C<u>G</u>M<u>G</u> system maintains a stable number of hydrogen bonds throughout the simulation time, indicating preserved structural integrity (Figure 5.10). In contrast, the G<u>L</u> nanotube displays a noticeable reduction in hydrogen bonding, particularly within the initial few gaps. This decline is more prominent in the POPC bilayer, suggesting a compromised hydrogen bonding network and potential structural instability under this membrane environment.

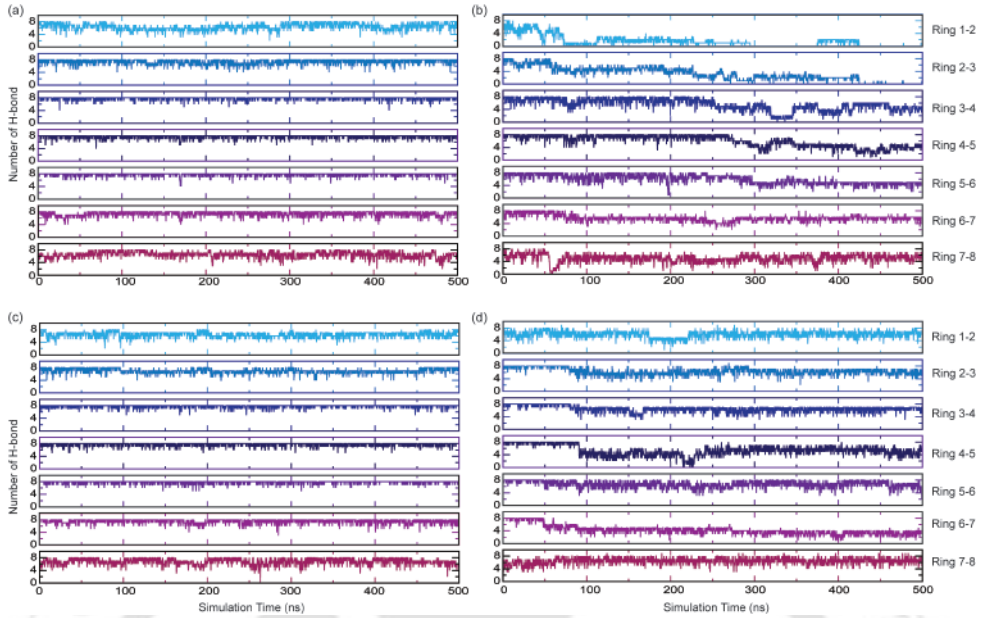

Figure 5.10: *Number of hydrogen bonds that are formed between the backbone atoms of the adjacent CP rings versus time of the CGMG embedded in POPC (a) and mixed (c) bilayer, and GL embedded in POPC (b) mixed (d) bilayer.*

Furthermore, Table 5.3 showcases the average hydrogen bond number involving the backbone atoms of the two CPNTs across all three lipid membranes. Notably, the yeast membrane exhibits the highest number of hydrogen bonds, while the mixed membrane records the lowest count for both CGMG and GLnanotubes.

Table. 5.3: *Average number of hydrogen bonds that were formed between the backbone atoms of the CPNTs in all the three lipid bilayers.*

	POPC	Mixed	Yeast
8 × CGMG	43.50	36.22	49.11
8 × GL	32.09	26.64	36.64

Consequently, it is evident that the CGMG nanotube exhibits a higher level of stability compared to the GL nanotube in all three lipid bilayers. The enhanced stability of CGMG can be attributed to the presence of polar sidechain groups, which tend to interact more with each other when placed in hydrophobic lipid environments. In contrast, the hydrophobic sidechains of the GL nanotube interact with the hydrophobic lipid environments, posing a challenge to sustaining its tubular structure over an extended pe-

riod. Additionally, the observed increase in hydrogen bonding (Figure 5.9, and 5.10) and non-bonded interaction energies (Figure 5.6, 5.7, and 5.8) between adjacent CP rings of CGMG nanotube further supports this observation.

5.3.2 Effect of CPNTs over Lipid Bilayer Properties

In this section, our try to examine how does the introduction of CPNTs during the simulation processes influence the stability of the model lipid bilayer structures. To achieve this, assessments are made on variables such as area per lipid, volume per lipid, and bilayer thickness. These evaluations are carried out on both pure lipid systems as well as the systems containing the nanotubes, and the findings are presented in Table 5.4. Area per lipid is determined by calculating the product of the average box dimensions in the x and y-directions, and then dividing this value by the number of lipids per layer. Similarly, volume per lipid is determined using the dimensions of the respective simulation box and substracting the volume of water molecules estimated based on a 50 ns NPT ensemble simulation of 6400/13500 TIP3P water molecules following a procedure analogous to that of the bilayer simulations[61]. To assess bilayer thickness, the distance between the peaks of the electron density profiles of the membranes in different systems is determined[61, 62]. Importantly, the values of area and volume per lipid for the pure lipid bilayer align with previously established findings[41, 63–66]. Likewise, the thickness of the pure bilayers correlate with prior research[67–71].

Referring to Table 5.4, it is evident that the incorporation of CPNTs into the lipid bilayers have minimal impact on their bulk properties. Although there is a slight increase in both area per lipid and volume per lipid with CPNT insertion, the bilayer thickness remain unaltered. This leads to the conclusion that the structural stability of all three lipid bilayers remain intact following the introduction of CPNTs throughout the simulation. Generally, introducing a transmembrane protein segment into a lipid membrane leads to hydrophobic mismatch, acting as a versatile factor influencing membrane organization [72]. Adjustments occur when the protein segment is longer or shorter than the hydrophobic thickness of the lipid bilayer. In our investigation, the incorporation of CPNTs into the lipid bilayers results in the tilting of the nanotube channel axis. We observed tilts of 5 °, 4.8 °, and 3.9 ° from the initial CGMG nanotube channel axis in POPC, mixed, and yeast membranes, respectively. The tilt angle of the axis of the GLnanotube is not

calculated since it does not maintain its tubular structure for an extended simulation time.

Table. 5.4: *Lipid Bilayer Structural Properties for all the systems. The values are reported as average ± standard deviation.*

	Area per lipid ($Å^2$)	Volume per lipid ($Å^3$)	Thickness (Å)
POPC	65.28 ± 0.60	1189.57 ± 0.12	38.74 ± 0.01
CGMG-POPC	66.67 ± 0.62	1242.10 ± 0.22	38.49 ± 0.01
GL-POPC	68.23 ± 0.51	1250.35 ± 0.10	38.74 ± 0.01
Mixed	57.72 ± 0.49	1134.52 ± 0.31	41.49 ± 0.01
CGMG-Mixed	60.29 ± 0.60	1182.18 ± 0.29	40.74 ± 0.01
GL-Mixed	60.37 ± 0.52	1195.22 ± 0.22	41.24 ± 0.01
Yeast	53.51 ± 0.49	1058.06 ± 0.11	42.49 ± 0.01
CGMG-Yeast	53.87 ± 0.55	1078.66 ± 0.10	41.74 ± 0.01
GL-Yeast	54.06 ± 0.51	1051.15 ± 0.12	42.24 ± 0.01

Again, order parameters play a vital role in assessing the structural stability of lipid bilayers. Therefore, the alterations in the order parameters of the lipid tail within these model lipid bilayers, both in comparison to the pure lipid bilayers and the corresponding bilayers containing the CPNTs are calculated (Figure 5.11). It should be noted that each model lipid bilayer comprises two lipid chains: lipid chain 1 (sn1) and lipid chain 2 (sn2). The determination of these lipid acyl chain ordering can be achieved through the calculation of the order parameter S_{CH}. S_{CH} serves as an indicator of the relative alignment of the C-H bond vector with respect to the bilayer's normal axis (typically the Z-axis) averaged over total number of lipids and the sampling time[73]. It is calculated by using the following formula[61, 62, 73, 74]:

$$S_{CH} = \frac{1}{2}\left\langle 3cos^2\theta - 1 \right\rangle \tag{5.1}$$

Here, θ signifies the angle formed between the bilayer's normal axis and the C-H bond vector while the angular brackets denotes the molecular and temporal ensemble averages[61, 73, 74]. The order parameter (S_{CH}) can vary between its minimum value, $S_{min} = -0.5$, which occurs when the bonds are consistently oriented parallel to the bilayer

plane, and its maximum value, $S_{max} = 1$, when the bonds are consistently oriented parallel to the bilayer normal[75].

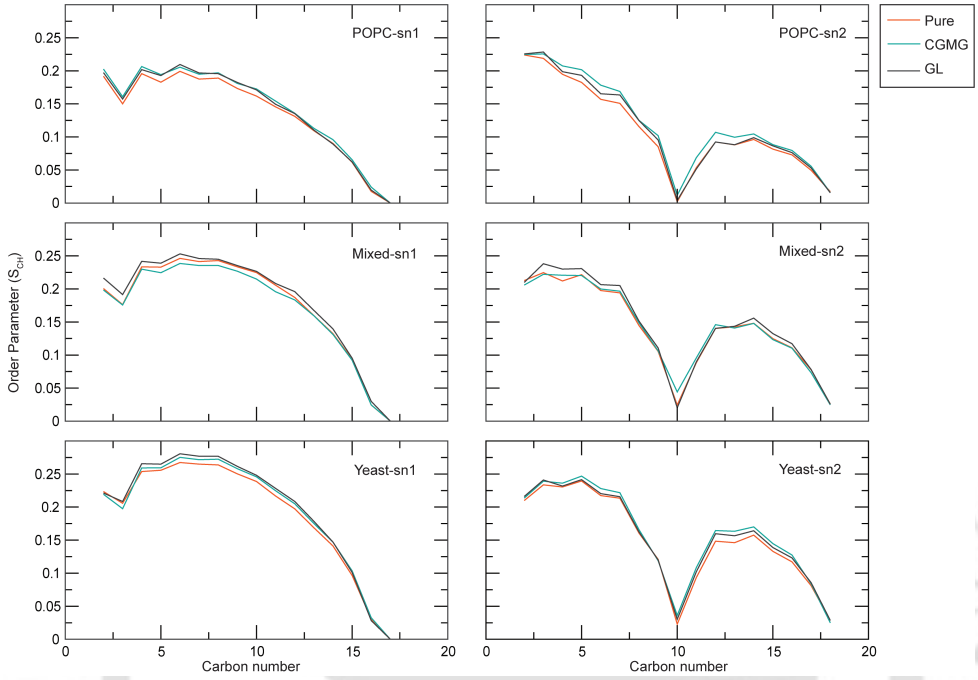

Figure 5.11: *sn1 and sn2 chain order parameters (S_{CH}) for POPC, mixed, and yeast bilayer in the presence and absence of CPNTs.*

Figure 5.11 depicts the lipid order parameters, S_{CH} as a function of carbon number (C_n) of that particular chain across all the lipid bilayer systems. Upon the insertion of CPNTs into the lipid bilayers, it becomes evident that the order parameters for both chains (sn1 and sn2) within these model membranes remain relatively unchanged. Notably, in all membranes, the carbon-2 atom of the sn1 and sn2 chains display distinct order parameter profiles due to variations in acyl chain alignment within those segments. Furthermore, the lipid membranes exhibits a noticeable separation in S_{CH} values between the sn2 and sn1 chains. The unsaturated chain present in all three lipid membranes demonstrates a distinct decrease at the carbon-9 and carbon-10 positions due to the presence of a *cis* double bond[61]. As a whole, the consistent S_{CH} values for both sn1 and sn2 chains across all systems, irrespective of the presence or absence of CPNTs, strongly indicate that the model lipid membranes remain structurally stable in the presence of CPNTs.

5.3.3 CPNT as Water Channels

Given that CPNTs function as artificial channels within lipid membranes, this section focuses on exploring the behaviour and dynamics of water molecules within these nanotubes. Given our findings which indicate that the GL nanotube struggles to sustain its tubular structure over prolonged intervals, this section of our study focuses exclusively on investigating the water dynamics within the CGMG nanotube. As illustrated in Figure 5.12(a, b, and c) snapshots reveal the pattern of water movement within the CGMG nanotube embedded in all the lipid membranes. Notably, the water movement exhibits a repeating 1-2-1-2 pattern, consistent with observations of prior studies[22, 24]. The number density profiles of water inside CGMG embedded in the lipid bilayers along the channel axis coordinate (z-axis) are illustrated in Figure 5.12 (d, e, and f). Sharp peaks are observed between two adjacent CP rings i.e. in the mid-Cα planes, while the peaks in the Cα planes are approximately half the height of those between the CP rings. This pattern suggests that the water density in the mid-Cα planes of the nanotube is nearly doubled as compared to the Cα planes in all the lipid bilayers.

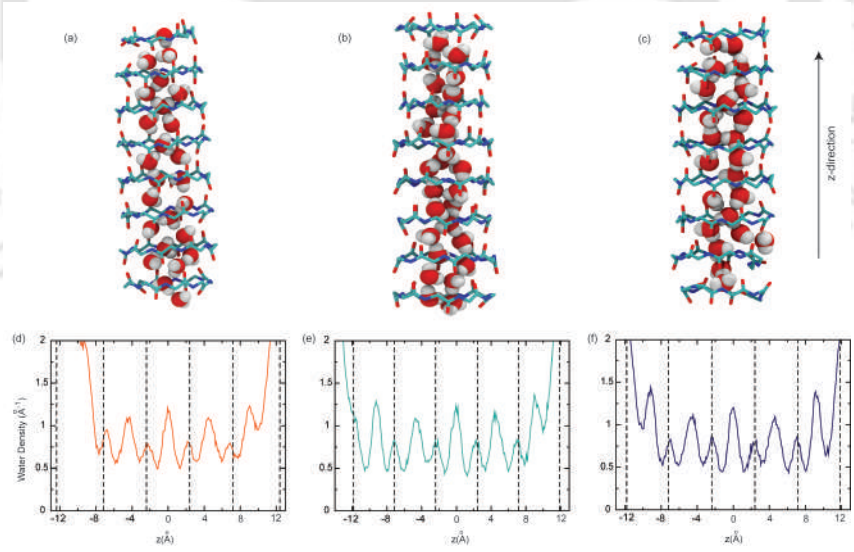

Figure 5.12: *The 1-2-1-2 movement pattern of water inside CGMG embedded in (a) POPC, (b) mixed, and (c) yeast bilayer. Here, CPNT is represented in ball-stick style and the hydrogen and oxygen atoms of water molecules are represented in white and red spheres respectively. The number density profiles (in Å $^{-1}$) of water present inside CGMG embedded in (d) POPC, (e) mixed, and (f) yeast bilayer. Here, the dotted black vertical lines represent the positions of the Cα planes of the nanotube.*

Next, we estimate the average number of hydrogen bonds that are formed between CPNTs and water molecules present inside the nanotube (Table 5.5). Two potential forms of hydrogen bonds between water within a nanotube and the peptide backbone are possible. In one scenario, water molecules act as donors and the carbonyl groups of the peptide backbone serve as acceptors, while the opposite holds true in the other case, i.e., water molecules act as acceptors and the amino groups of the peptide backbone function as donors[76]. Across all lipid bilayers, the former type of hydrogen bond dominates over the latter. Table 5.5 lists the average number of hydrogen bonds formed per gap of C$\underline{G}$M$\underline{G}$ between water molecules enclosed within the nanotube and the carbonyl/amide groups of the backbone of the CP rings.

Table. 5.5: *The average number of hydrogen bonds (per gap) formed between backbone atoms of C$\underline{G}$M$\underline{G}$ and water molecules present inside the nanotubes. Here, HB_{CO-HW} denotes hydrogen bond between carbonyl group of C$\underline{G}$M$\underline{G}$ backbone and hydrogen atom of water and HB_{NH-OW} denotes hydrogen bond between amide group of C$\underline{G}$M$\underline{G}$ backbone and oxygen atom of water.*

	H-Bond	POPC	Mixed	Yeast
8 × C$\underline{G}$M$\underline{G}$	HB_{CO-HW}	1.12	1.16	1.19
	HB_{NH-OW}	0.14	0.13	0.15

Furthermore, to examine the translational movement of water molecules within the nanotube, we computed the mean square displacement (MSD) of water molecules over time. This calculation can be expressed using the following equation:[24, 77]

$$MSD(t) =< r^2(t) >= \left\langle |r_{wat}(t) - r_{wat}(0)|^2 \right\rangle \tag{5.2}$$

In equation (2), t and r_{wat} denotes the correlation time and the coordinate vector of the oxygen atom of water respectively. The term "r_{wat}(t)-r_{wat}(0)" represents the distance covered by water over the time interval t. The slope of MSD versus time plot defines the self-diffusion constant (D) as per Einstein's equation[77]:

$$D = \lim_{\Delta t \to \infty} \frac{\langle \Delta r^2 \rangle}{2d\Delta t} \tag{5.3}$$

Here, d is the dimensionality of the co-ordinate system.

Figure 5.13 depicts the MSD profiles of water molecules present inside the CGMG nanotube in the x, y, and z directions across all three lipid bilayers. Notably, water molecules exhibit their predominant movement along the z-direction, which coincides with the nanotube's orientation in each lipid bilayer. For the POPC bilayer, MSD(x) and MSD(y) are equivalent, but in the mixed and yeast bilayers, they diverge slightly. This anisotropy in the MSD values in the xy-plane can be attributed to the shape of the CP rings within these two bilayers. As the simulation progresses, CP rings of CGMG in the mixed and yeast bilayers transform to a nearly elliptical shape from their initial circular shape. The slopes of the MSD(z) plots are calculated after linear fitting in the time range of 200 to 800 ps.

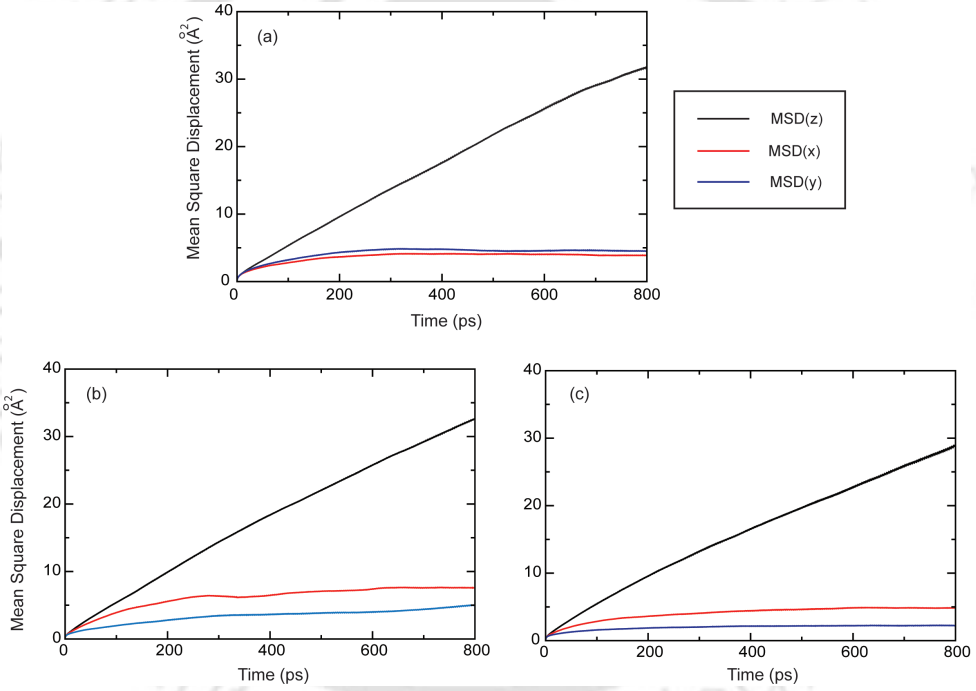

Figure 5.13: *Mean square displacement (MSD) plots of water molecules present inside CGMG embedded in (a) POPC, (b) mixed, and (c) yeast bilayer. The MSDs were calculated in parallel (z-axis) and perpendicular (x and y-axes) directions, respectively.*

The diffusion coefficient values (D) of water present inside the CGMG nanotube in all the lipid bilayers are listed in Table 5.6. The D_x and D_y values in the POPC bilayer are nearly identical, whereas, in the other two bilayers, they differ due to alterations in the shape of the CP rings within those bilayers. The higher D_z values observed in all the bilayers signify that the primary motion of water molecules predominantly occurs along

the z-direction which is also evident in the MSD profiles (Figure 5.13). Furthermore, the variation in diffusion coefficient values indicates that altering the lipid environment surrounding the CPNT affects its permeability, consistent with the findings of Liu et al.[23].

Table. 5.6: *The diffusion coefficients (D) of water inside CGMG nanotube embedded in all the three lipid bilayers. Here, D_x, D_y, and D_z stands for diffusion coefficient values along x, y, and z directions respectively. The values are reported as average ± standard deviation. The value of D for bulk water is provided for comparison.Units are expressed in $Å^2$ ns^{-1}.*

	POPC	Mixed	Yeast
D_z	19.04 ± 8.79	18.74 ± 7.01	15.88 ± 1.67
D_x	0.07 ± 0.01	2.67 ± 0.95	0.99 ± 0.09
D_y	0.06 ± 0.02	1.42 ± 0.74	0.02 ± 0.05
D	480 (Bulk water)[78]		

In our concluding analysis, we computed the lifespan of hydrogen bonds formed among water molecules inside the CGMG nanotube across all three lipid bilayers. This was achieved using the continuous hydrogen bond time correlation function (TCF), $S_{HB}(t)$. In our analysis, we randomly selected ten water molecules that are present within the nanotube channel for the entire 200 ps NVE simulation.

We calculated individual decay functions, $S_{HB}(t)$, over time for each molecule and subsequently averaged them. Notably, certain water molecules exhibites slightly different decay curves compared to others within the nanotube channel for all the three lipid bilayers. The lifetime values ($<\tau_{HB}>$) of these specific water molecules are comparatively higher, attributed to their simultaneous hydrogen bonding with the CPNT backbone atoms. These bound water molecules are less mobile, forming stronger hydrogen bonds with neighboring water molecules, resulting in increased lifetime values. Figure 5.14 illustrates the decay functions, $S_{HB}(t)$, depicting the time evolution of water-water hydrogen bonds within the nanotube channel for two different types of water molecules across all three lipid bilayers.

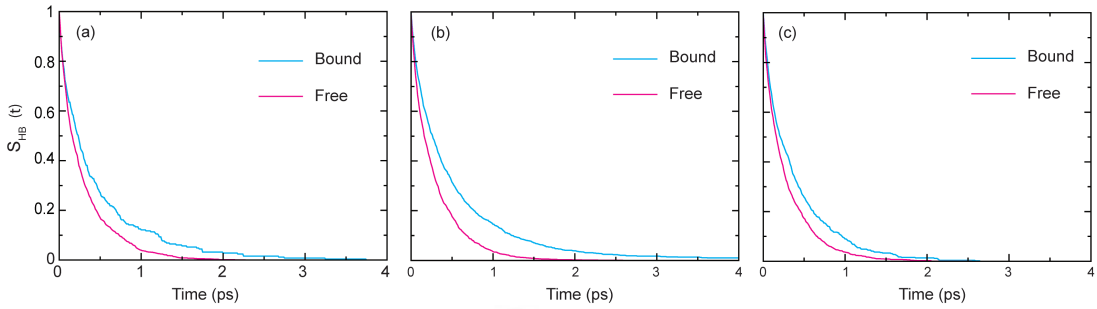

Figure 5.14: *The continuous hydrogen bond correlation functions for free and bound water-water hydrogen bonding pairs inside the CPNT channel placed within (a) POPC, (b) mixed, and (c) yeast bilayer.*

Table 5.7 provides details on the average number of water-water hydrogen bonds per water (<n_{HB}>), the average lifetime values of water-water continuous hydrogen bonds for free and bound water molecules within the CPNT in all three lipid bilayers. To extract lifetime information, we applied biexponential fits to the decay curves for the water molecules that are bound to the peptide backbone and single exponential fits to the decay curves of other water molecules. The average lifetime of free water-water hydrogen bonds is relatively similar to the bulk TIP3P water which is approximately 0.27 ps[78]. However, bound water molecules exhibit significantly higher hydrogen bond lifetimes compared to bulk water. The <n_{HB}> values are marginally lower than pure water[79] as water molecules can form hydrogen bonds simultaneously with backbone atoms of the CPNT.

Table. 5.7: *The average number of water-water hydrogen bonds per water (<n_{HB}>), the average lifetime values (<τ_{HB}>) of free and bound water-water hydrogen bonds inside CPNT placed in the three lipid bilayers. All the lifetime values are expressed in ps.*

	<n_{HB}>	Average lifetime value (<τ_{HB}>)	
		Free Water	Bound Water
POPC	2.99	0.30	0.43
Mixed	3.03	0.28	0.52
Yeast	3.09	0.29	0.37
Bulk	3.16[79]	0.27[78]	

5.4 Conclusion

This study delves into the behavior of two CPNTs, specifically 8 × [(Cys-D-Gly-Met-D-Gly)$_2$] and 8 × [(Gly-D-Leu)$_4$], within three distinct lipid bilayers: POPC, POPC/POPG (mixed), and a realistic yeast membrane. Through classical molecular dynamics simulations, it has been found that both the CPNTs have maintained their tubular structure across all lipid bilayers, with [(Cys-D-Gly-Met-D-Gly)$_2$] (C$\underline{\text{G}}$M$\underline{\text{G}}$) exhibiting enhanced stability due to higher interaction among the adjacent CP rings when placed in hydrophobic lipid environments. G$\underline{\text{L}}$ nanotube, on the other hand, fails to retain its tubular structure over an extended period of simulation time.

The average length of both nanotubes ranges from 32 to 33 Å with an intersubunit distance of approximately 4.72-4.87 Å between the adjacent CP rings. Again, constant pattern of non-bonded interaction energies between adjacent CP rings in C$\underline{\text{G}}$M$\underline{\text{G}}$ suggests its stability over the G$\underline{\text{L}}$ nanotube. Furthermore, the inherent polarity of the sidechains of C$\underline{\text{G}}$M$\underline{\text{G}}$ nanotube intensifies the non-bonded interactions across all membranes, distinguishing it from the hydrophobic G$\underline{\text{L}}$ nanotube. The average hydrogen bonds between C$\underline{\text{G}}$M$\underline{\text{G}}$ and G$\underline{\text{L}}$ nanotube rings tally at 7.04 ± 0.70 and 6.20 ± 0.92, respectively. Impressively, the yeast membrane exhibits the highest hydrogen bond count, while the mixed POPE/POPG membrane records the lowest, irrespective of the CPNT type.

Assessment of CPNTs' influence on lipid bilayer properties indicates minimal impact on area per lipid, volume per lipid, thickness, and order parameters upon their introduction. These results accentuate the structural stability of the lipid bilayers in the presence of both CPNTs.

Furthermore, our study confirms the presence of the characteristic 1-2-1-2 pattern of water movement within the C$\underline{\text{G}}$M$\underline{\text{G}}$ nanotube in all the lipid membranes. This pattern is consistently observed in system snapshots and water density plots. The MSD plots reveal that the dynamics of water inside the nanotube are similar for all the bilayer systems. The difference in diffusion coefficient values shows that the lipid environment can alter the permeability of water through the CPNT. Moreover, a scrutiny of hydrogen bonding dynamics within CPNT reveals that, despite the average lifetimes of water-water hydrogen bonds inside the channel being nearly similar to those of bulk water, specific backbone-bound water molecules display elevated hydrogen bond lifetime values.

Collectively, these findings illuminate the stability of CPNTs within realistic yeast and bacterial membranes, extending beyond pure lipid models. Furthermore, the retention of the specific water movement pattern in the realistic lipid membranes implies their suitability as water channels. This opens new avenues for CPNTs to serve as potential ion and drug delivery channels in these biologically relevant environments.

References

(1) Agre, P.; Preston, G. M.; Smith, B. L.; Jung, J. S.; Raina, S.; Moon, C.; Guggino, W. B.; Nielsen, S. *Am. J. Physiol. Renal Physiol.* **1993**, *265*, F463–F476.

(2) Hille, B. *Biophys. J.* **1978**, *22*, 283–294.

(3) Gouaux, E.; MacKinnon, R. *Sci.* **2005**, *310*, 1461–1465.

(4) Dresselhaus, M. S.; Dresselhaus, G.; Eklund, P.; Rao, A., *Carbon nanotubes*; Springer: 2000.

(5) Poland, C. A.; Duffin, R.; Kinloch, I.; Maynard, A.; Wallace, W. A. H.; Seaton, A.; Stone, V.; Brown, S.; MacNee, W.; Donaldson, K. *Nat. Nanotechnol.* **2008**, *3*, 423–428.

(6) Lam, C.-W.; James, J. T.; McCluskey, R.; Hunter, R. L. *Toxicol. Sci.* **2004**, *77*, 126–134.

(7) Muller, J.; Huaux, F.; Moreau, N.; Misson, P.; Heilier, J.-F.; Delos, M.; Arras, M.; Fonseca, A.; Nagy, J. B.; Lison, D. *Toxicol. Appl. Pharmacol.* **2005**, *207*, 221–231.

(8) Kodali, V.; Roberts, J. R.; Glassford, E.; Gill, R.; Friend, S.; Dunn, K. L.; Erdely, A. *J. Mater. Res.* **2022**, *37*, 4620–4638.

(9) Hsieh, W.-H.; Liaw, J. *J. Food Drug Anal.* **2019**, *27*, 32–47.

(10) Hamley, I. W. *Angew. Chem. Int. Ed.* **2014**, *53*, 6866–6881.

(11) Khazanovich, N.; Granja, J. R.; McRee, D. E.; Milligan, R. A.; Ghadiri, M. R. *J. Am. Chem. Soc.* **1994**, *116*, 6011–6012.

(12) Chapman, R.; Danial, M.; Koh, M. L.; Jolliffe, K. A.; Perrier, S. *Chem. Soc. Rev.* **2012**, *41*, 6023–6041.

(13) Ramamoorthy, A. *Solid State Nucl. Magn. Reson.* **2009**, *35*, 201–207.

(14) Wang, C.; Hong, T.; Cui, P.; Wang, J.; Xia, J. *Adv. Drug Deliv. Rev.* **2021**, *175*, 113818.

(15) Hoskin, D. W.; Ramamoorthy, A. *Biochim. Biophys. Acta.* **2008**, *1778*, 357–375.

(16) Li, X.; Zuo, S.; Wang, B.; Zhang, K.; Wang, Y. *Molecules* **2022**, *27*, 2675.

(17) Epand, R. F.; Ramamoorthy, A.; Epand, R. M. *Protein Pept. Lett.* **2006**, *13*, 1–5.

(18) Sarma, H.; Kiewhuo, K.; Jamir, E.; Sastry, G. N. *Biophys. Chem.* **2023**, 107070.

(19) Epand, R. M.; Vogel, H. J. *Biochim. Biophys. Acta* **1999**, *1462*, 11–28.

(20) Ghadiri, M. R.; Granja, J. R.; Milligan, R. A.; McRee, D. E.; Khazanovich, N. *Nature* **1993**, *366*, 324–327.

(21) Engels, M.; Bashford, D.; Ghadiri, M. R. *J. Am. Chem. Soc.* **1995**, *117*, 9151–9158.

(22) Tarek, M.; Maigret, B.; Chipot, C. *Biophys. J.* **2003**, *85*, 2287–2298.

(23) Liu, J.; Fan, J.; Cen, M.; Song, X.; Liu, D.; Zhou, W.; Liu, Z.; Yan, J. *J. Chem. Inf. Model.* **2012**, *52*, 2132–2138.

(24) Liu, J.; Fan, J.; Tang, M.; Cen, M.; Yan, J.; Liu, Z.; Zhou, W. *J. Phys. Chem. B* **2010**, *114*, 12183–12192.

(25) Yan, X.; Fan, J.; Yu, Y.; Xu, J.; Zhang, M. *J. Chem. Inf. Model.* **2015**, *55*, 998–1011.

(26) Carvajal-Diaz, J. A.; Cagin, T. *J. Phys. Chem. B* **2016**, *120*, 7872–7879.

(27) Hwang, H.; Schatz, G. C.; Ratner, M. A. *J. Phys. Chem. B* **2006**, *110*, 26448–26460.

(28) Song, Y.; Lee, J. H.; Hwang, H.; Schatz, G. C.; Hwang, H. *J. Phys. Chem. B* **2016**, *120*, 11912–11922.

(29) Song, X.; Fan, J.; Liu, D.; Li, H.; Li, R. *J. Mol. Model.* **2013**, *19*, 4271–4282.

(30) Zhang, M.; Fan, J.; Xu, J.; Weng, P.; Lin, H. *J. Mol. Model.* **2016**, *22*, 1–12.

(31) Li, R.; Fan, J.; Li, H.; Yan, X.; Yu, Y. *J. Phys. Chem. B* **2013**, *117*, 14916–14927.

(32) Xu, J.; Fan, J. F.; Zhang, M. M.; Weng, P. P.; Lin, H. F. *J. Mol. Model.* **2016**, *22*, 1–12.

(33) Montenegro, J.; Ghadiri, M. R.; Granja, J. R. *Acc. Chem. Res.* **2013**, *46*, 2955–2965.

(34) Li, R.; Fan, J.; Li, H.; Yan, X.; Yu, Y. *J. Chem. Phys.* **2015**, *143*.

(35) Khavani, M.; Izadyar, M.; Housaindokht, M. R. *J. Mol. Graph. Model.* **2017**, *71*, 28–39.

(36) Joozdani, F. A.; Taghdir, M. *J. Mol. Liq.* **2022**, *349*, 118136.

(37) Farrokhpour, H.; Mansouri, A.; Najafi Chermahini, A. *J. Phys. Chem. C* **2017**, *121*, 8165–8176.

(38) Liu, H.; Chen, J.; Shen, Q.; Fu, W.; Wu, W. *Mol. Pharmaceutics* **2010**, *7*, 1985–1994.

(39) Vijayaraj, R.; Van Damme, S.; Bultinck, P.; Subramanian, V. *Phys. Chem. Chem. Phys.* **2013**, *15*, 1260–1270.

(40) Maroli, N.; Kolandaivel, P. *J. Biomol. Struct. Dyn.* **2020**, *38*, 186–199.

(41) Mukherjee, S.; Kar, R. K.; Nanga, R. P. R.; Mroue, K. H.; Ramamoorthy, A.; Bhunia, A. *Phys. Chem. Chem. Phys.* **2017**, *19*, 19289–19299.

(42) Daum, G.; Tuller, G.; Nemec, T.; Hrastnik, C.; Balliano, G.; Cattel, L.; Milla, P.; Rocco, F.; Conzelmann, A.; Vionnet, C.; et. al. *Yeast* **1999**, *15*, 601–614.

(43) Martínez, L.; Andrade, R.; Birgin, E. G.; Martínez, J. M. *J. Comput. Chem.* **2009**, *30*, 2157–2164.

(44) Case, D. A. et al. Amber 18., University of California: San Francisco, CA, 2018.

(45) Jo, S.; Lim, J. B.; Klauda, J. B.; Im, W. *Biophys. J.* **2009**, *97*, 50–58.

(46) Wu, E. L.; Cheng, X.; Jo, S.; Rui, H.; Song, K. C.; Dàvila-Contreras, E. M.; Qi, Y.; Lee, J.; Monje-Galvan, V.; Venable, R. M.; Klauda, J. B.; Im, W. *J. Comput. Chem.* **2014**, *35*, 1997–2004.

(47) Jorgensen, W. L.; Chandrasekhar, J.; Madura, J. D.; Impey, R. W.; Klein, M. L. *J. Chem. Phys.* **1983**, *79*, 926–935.

(48) Maier, J. A.; Martinez, C.; Kasavajhala, K.; Wickstrom, L.; Hauser, K. E.; Simmerling, C. *J. Chem. Theory Comput.* **2015**, *11*, 3696–3713.

(49) Gould, I.; Skjevik, A.; Dickson, C.; Madej, B.; Walker, R. *Manuscript in preparation* **2018**.

(50) Joung, I. S.; Cheatham III, T. E. *J. Phys. Chem. B* **2008**, *112*, 9020–9041.

(51) Åqvist, J.; Wennerström, P.; Nervall, M.; Bjelic, S.; Brandsdal, B. O. *Chem. Phys. Lett.* **2004**, *384*, 288–294.

(52) Hünenberger, P. H. *Adv. Polym. Sci.* **2005**, 105–149.

(53) Omelyan, I.; Kovalenko, A. *J. Chem. Phys.* **2013**, *139*, 224106.

(54) Zhang, Y.; Feller, S. E.; Brooks, B. R.; Pastor, R. W. *J. Chem. Phys.* **1995**, *103*, 10252–10266.

(55) Ryckaert, J.-P.; Ciccotti, G.; Berendsen, H. J. *J. Comput. Phys.* **1977**, *23*, 327–341.

(56) Essmann, U.; Perera, L.; Berkowitz, M. L.; Darden, T.; Lee, H.; Pedersen, L. G. *J. Chem. Phys.* **1995**, *103*, 8577–8593.

(57) Roe, D. R.; Cheatham III, T. E. *J. Chem. Theory Comput.* **2013**, *9*, 3084–3095.

(58) Humphrey, W.; Dalke, A.; Schulten, K. *J. Mol. Graphics* **1996**, *14*, 33–38.

(59) Pettersen, E. F.; Goddard, T. D.; Huang, C. C.; Couch, G. S.; Greenblatt, D. M.; Meng, E. C.; Ferrin, T. E. *J. Comput. Chem.* **2004**, *25*, 1605–1612.

(60) Silk, M. R.; Newman, J.; Ratcliffe, J. C.; White, J. F.; Caradoc-Davies, T.; Price, J. R.; Perrier, S.; Thompson, P. E.; Chalmers, D. K. *Chem. Commun.* **2017**, *53*, 6613–6616.

(61) Dickson, C. J.; Madej, B. D.; Skjevik, Å. A.; Betz, R. M.; Teigen, K.; Gould, I. R.; Walker, R. C. *J. Chem. Theory Comput.* **2014**, *10*, 865–879.

(62) Dickson, C. J.; Walker, R. C.; Gould, I. R. *J. Chem. Theory Comput.* **2022**, *18*, 1726–1736.

(63) Kučerka, N.; Nagle, J. F.; Sachs, J. N.; Feller, S. E.; Pencer, J.; Jackson, A.; Katsaras, J. *Biophys. J.* **2008**, *95*, 2356–2367.

(64) Kučerka, N.; Tristram-Nagle, S.; Nagle, J. F. *J. Membr. Biol.* **2006**, *208*, 193–202.

(65) Rappolt, M.; Hickel, A.; Bringezu, F.; Lohner, K. *Biophys. J.* **2003**, *84*, 3111–3122.

(66) Skjevik, Å. A.; Madej, B. D.; Dickson, C. J.; Lin, C.; Teigen, K.; Walker, R. C.; Gould, I. R. *Phys. Chem. Chem. Phys.* **2016**, *18*, 10573–10584.

(67) Lee, J.; Cheng, X.; Jo, S.; MacKerell, A. D.; Klauda, J. B.; Im, W. *Biophys. J.* **2016**, *110*, 641a.

(68) Venable, R. M.; Brown, F. L.; Pastor, R. W. *Chem. Phys. Lipids* **2015**, *192*, 60–74.

(69) Pluhackova, K.; Kirsch, S. A.; Han, J.; Sun, L.; Jiang, Z.; Unruh, T.; Böckmann, R. A. *J. Phys. Chem. B* **2016**, *120*, 3888–3903.

(70) Kučerka, N.; Nieh, M.-P.; Katsaras, J. *Biochim. Biophys. Acta, Biomembr.* **2011**, *1808*, 2761–2771.

(71) Kučerka, N.; van Oosten, B.; Pan, J.; Heberle, F. A.; Harroun, T. A.; Katsaras, J. *J. Phys. Chem. B* **2015**, *119*, 1947–1956.

(72) De Planque, M. R. R.; Killian, J. A. *Mol. Membr. Biol.* **2003**, *20*, 271–284.

(73) Piggot, T. J.; Allison, J. R.; Sessions, R. B.; Essex, J. W. *J. Chem. Theory Comput.* **2017**, *13*, 5683–5696.

(74) Paul, R.; Paul, S. *Langmuir* **2021**, *37*, 10376–10387.

(75) Rabinovich, A. L.; Lyubartsev, A. P. In *J. Phys. Conf. Ser.* 2014; Vol. 510, p 012022.

(76) Liu, J.; Fan, J.; Tang, M.; Zhou, W. *J. Phys. Chem. A* **2010**, *114*, 2376–2383.

(77) Paul, R.; Mitra, A.; Paul, S. *Phys. Chem. Chem. Phys.* **2021**, *23*, 22703–22717.

(78) Pal, S.; Chakraborty, K.; Khatua, P.; Bandyopadhyay, S. *J. Chem. Phys.* **2015**, *142*.

(79) Ong, E. E.; Liow, J.-L. *Fluid Phase Equilib.* **2019**, *481*, 55–65.

Chapter 6

Ion Transportation Through Cyclic Peptide Nanotube Embedded in Lipid Bilayer

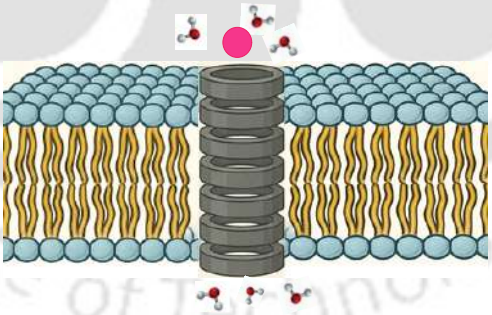

Overview

Cyclic peptide nanotubes (CPNTs) have emerged as promising synthetic channels for selective ion transport due to their structural tunability and biomimetic properties. In this chapter, the transport behavior of three cations: Na^+, K^+, and Cs^+, and two anions: Cl^- and HCO_3^- was investigated through a CPNT composed of eight stacked rings of cyclo-[Cys-D-Gly-Met-D-Gly]$_2$ embedded in a biologically realistic yeast lipid bilayer using molecular dynamics simulations. Potential of mean force (PMF) profiles reveal a strong preference for cation permeation, with Na^+ and K^+ encountering moderate energy barriers, while Cs^+ shows signs of getting trapped inside the channel due to higher entry and exit barriers. In contrast, both anions face significant energetic constraints, effectively preventing their entry or translocation through the channel. Electrostatic interaction energies further highlight the favorable interaction of cations with the CPNT backbone and the unfavorable interactions of anions. Hydration analysis shows that spatial confinement in the CPNT alters the solvation shell, with Na^+ retaining more hydration and interacting with the CPNT backbone via water bridges, followed by K^+, and Cs^+ forming more direct interactions with backbone carbonyl groups. Water structure and dynamics inside the nanotube are also modulated by the presence of cations, disrupting the typical 1-2-1-2 arrangement and reducing axial water diffusion, most notably in the presence of Na^+. Dipole angle distributions of the channel water oxygen atoms indicate strong ion-induced ordering of water molecules without the formation of L- or D-type defects. These findings offer valuable insights into the size- and charge-dependent selectivity of CPNTs, reinforcing their potential in the design of artificial nanochannels for targeted ion transport applications.

6.1 Introduction

In the previous chapter, the potential of CPNTs as water channels embedded within different lipid membranes was explored, along with an investigation of the associated water dynamics. In the present chapter, we shift focus to examine the ion selectivity of CPNTs and analyze the transport behavior of various ions through the nanotube channel.

Efficient and selective transport of ions, biopolymers, and metabolites across biological membranes is essential for maintaining cell vitality[1]. In nature, ion channels enable this selective transport across lipid bilayers. However, natural ion channels are large and complex membrane proteins that are expensive to produce, susceptible to denaturation, and challenging to isolate in their native form. As an alternative, artificial ion channels offer a promising solution due to their simpler and more cost-effective synthetic routes[2, 3]. These synthetic channels can be easily modified to enhance ion selectivity and adapt their properties for specific applications[3].

Numerous theoretical and experimental investigations have established that CPNTs are highly effective artificial channels for transporting small molecules, including water[4–6] and various ions[2, 6–8]. The foundational studies by Ghadiri and colleagues revealed that CPNTs can facilitate the movement of cations such as Na^+ and K^+ at rates exceeding those observed in natural channels like gramicidin A[9]. This discovery sparked significant interest in understanding the mechanisms that drive ion selectivity in these artificial channels. Subsequent MD simulations have shed light on the factors that govern cation transport through CPNTs. Key determinants include the diameter of the channel, the size and charge of the ion, and the specific interactions between the ion and the channel environment. For example, steered molecular dynamics work by Hwang et al.[10] provided some of the earliest detailed free-energy landscapes for Na^+ and K^+ ions tansversing a CPNT in water, revealing distinct conductance profiles for each ion and highlighting the nuanced interplay of ion-channel interactions. In continuation to this understanding, Sumiya et al.[11] designed a minimalistic CPNT composed of glycine residues, demonstrating that while the channel readily accommodates cations, its structural stability is compromised when anions such as F^- attempt to pass through. This finding underscores the inherent cation selectivity of CPNTs. Complementary studies by Choi et al.[12], employing advanced sampling techniques, showed that Na^+ and K^+ ions encounter favorable

energetic environments within the nanotube, whereas Cl^- ions face significant barriers, reinforcing the selective nature of these channels. Work by Granja and collaborators[13] expanded on these observations by examining the transport of various electrolyte solutions through self-assembled α,γ-peptide nanotubes, consistently finding a preference for alkaline metal ions. Additional studies have delved into how the position of an ion within the CPNT affects the surrounding water structure, with both the density and orientation of water molecules shifting depending on the ion's location along the channel axis[14, 15]. Again, Yan et al.[7] have compared the transport properties of Na^+, K^+, and Ca^{2+} ions through a CPNT embedded in POPE, revealing that while monovalent cations traverse the channel with moderate energy barriers, divalent ions like Ca^{2+} face much greater resistance due to their higher charge and stronger hydration shells. Zhang et al.[16] have further demonstrated that the application of strong electric fields can enable the entry of Li^+ ions into the CPNT, while Na^+ ions can permeate even under less intense conditions. In a recent study by Gong and Fan[17], transportation of water and K^+ through terminally charged CPNTs were studied. They observed that end-charges enhanced the nanotube stability and modulated K^+ permeation by altering the internal electrostatic environment.

While CPNTs have been widely studied for their cation transport properties, particularly for Na^+ and K^+, the role of ion size and hydration in modulating permeation remains an active area of investigation. Larger alkali ions like Cs^+ are less explored, and studies directly comparing ions of different sizes under identical conditions are limited. Moreover, the transport of anions through CPNTs remains virtually unaddressed, despite their biological relevance.

In this chapter, the permeation behavior of three cations: Na^+, K^+, and Cs^+, and two anions: Cl^- and $HCO_3{}^-$, through the CPNT cyclo-[Cys-D-Gly-Met-D-Gly]$_2$ embedded in a yeast lipid bilayer is investigated. Sodium and potassium are vital physiological cations involved in maintaining membrane potential and facilitating cellular signaling, while cesium, due to its larger ionic radius, serves as a model for assessing the effect of ion size on transport. Chloride is the most abundant biological anion, essential for osmotic balance and electrical neutrality, whereas bicarbonate plays a crucial role in cellular pH regulation and metabolic buffering. By comparing both cations and anions within the same biologically relevant membrane environment, this study aims to provide insights into how ion size, charge, and hydration collectively influence transport through CPNTs.

6.2 Materials and Methods

6.2.1 System Setup

To investigate the ion transport properties through CPNT, we have considered the previous eight-membered cyclo-[Cys-D-Gly-Met-D-Gly]$_2$ nanotube, abbreviated as [C$\underline{\text{G}}$M$\underline{\text{G}}_2$]$_8$. This CPNT was constructed by stacking eight (C$\underline{\text{G}}$M$\underline{\text{G}}$)$_2$ rings in an antiparallel arrangement using PACKMOL[18]. The assembled nanotube was then embedded within a model yeast lipid bilayer generated using the membrane builder module of CHARMM-GUI[19, 20]. This particular CPNT was chosen based on the observations of our previous chapter (Chapter 5), where it demonstrated superior structural stability and retained its tubular conformation within a yeast bilayer environment. The lipid bilayer model consists of 1,2-dioleoyl-sn-glycero-3-phosphocholine (DOPC), 1-palmitoyl-2-oleoyl-sn-glycero -3-phosphoethanolamine (POPE), 1,2-dipalmitoyl-sn-glycero-3-phosphocholine (DPPC), 1-palmitoyl-2-oleoyl-sn-glycero-3-phosphate (POPA), 1-palmitoyl-2-oleoyl-sn-glycero-3-phospho-L-serine (POPS), and cholesterol (CHL). The composition of this yeast model membrane follows the lipid ratio reported by Sunhwan et al.[21], comprising 100 DOPC, 60 POPE, 20 DPPC, 10 POPA, 20 POPS, and 60 CHL molecules.

For system setup, the lipid bilayer was constructed with a symmetric distribution of lipid molecules between the upper and lower leaflets. The CPNT was positioned at the center of the bilayer and oriented perpendicular to the membrane plane, along the Z-axis. To mimic a realistic biological environment, each system was solvated with 50 TIP3P water[22] molecules per lipid, resulting in aqueous layers above and below the membrane. To account for ionic conditions relevant to transport studies, a salt concentration of 0.15 M MX (M = Na^+, K^+, Cs^+; X = Cl^-) was included, depending on the specific ion being studied. For systems involving bicarbonate (HCO_3^-) transport, 0.024 M $NaHCO_3$ and 0.126 M NaCl were added, to mimic physiological conditions corresponding to a total of 0.15 M Na^+. The $NaHCO_3$ concentration reflects the physiological plasma bicarbonate level, typically ranging from 0.022-0.027 M[23, 24].

For systems involving bicarbonate (HCO_3^-) transport, 0.024 M $NaHCO_3$ and 0.15 M NaCl were added. Additionally, to neutralize the negatively charged lipid headgroups, an appropriate number of counterions were introduced. All systems were prepared in AMBER[25] format, including topology and coordinate files, using CHARMM-GUI. The

ff19SB[26] and lipid21[27] force fields were applied for the CPNT and lipid molecules, respectively, ensuring accurate molecular representation during simulations. Parameters for Na^+, K^+, Cs^+, and Cl^- ions were taken from the Joung and Cheatham ion models[28]. For the HCO_3^- anion, geometry optimization was performed using Hartree-Fock (HF) with the 6-31G* basis set in Gaussian09[29]. The electrostatic potential was then used to derive atomic partial charges using the RESP (Restrained Electrostatic Potential) method[30] implemented in the AMBER18 package[25]. The remaining force field parameters for the anion were generated using the General AMBER Force Field (GAFF)[31] with the ANTECHAMBER module[32].

6.2.2 Simulation Protocols

All molecular dynamics simulations were performed using the AMBER18 package[25]. Visual Molecular Dynamics (VMD)[33] and UCSF-Chimera[34] were used for visualization purposes. The system temperature was maintained at 303 K using a Langevin thermostat[35] with a collision frequency of 1 ps^{-1}, and the pressure was regulated at 1 atm using a Monte Carlo barostat[36] with a pressure relaxation time of 2 ps. Semiisotropic pressure scaling was applied, along with a constant surface tension, with the membrane interfaces defined in the XY plane[37, 38]. To constrain covalent bonds involving hydrogen atoms without affecting other degrees of freedom, the SHAKE algorithm[39] was used. Simulations were conducted with a timestep of 2 fs. Short-range non-bonded interactions were calculated using a cutoff of 10.0 Å and long-range electrostatics were handled using the particle mesh Ewald (PME) method[40]. Periodic boundary conditions (PBC) were applied in all three dimensions to eliminate edge effects.

Steered Molecular Dynamics (SMD)

To investigate ion passage through the CPNT channel, constant-velocity steered molecular dynamics (cv-SMD) simulations were carried out. This approach, widely recognized for capturing transport events in confined systems like nanotubes, allowed us to observe the ion translocation process in a dynamic setting. Moreover, the configurations obtained from these simulations served as suitable initial structures for subsequent umbrella sampling calculations aimed at generating the potential of mean force (PMF) profiles.

To investigate ion translocation through the nanotube channel, a single ion of interest was initially positioned at z = −20 Å (close to the entrance of the CPNT) along the longitudinal axis (Z-axis) of the CPNT (Figure 6.1). The system was then subjected to energy minimization, beginning with 5000 steps of the steepest descent algorithm followed by 5000 steps of conjugate gradient minimization. Subsequently, the system was gradually heated to a temperature of 303.15 K and equilibrated under NVT conditions. During both the minimization and NVT equilibration phase, positional restraints were applied to the lipid bilayer, the CPNT, and the ion located at z = −20 Å to maintain structural stability. Following equilibration, a harmonic pulling force was applied to the ion to pull it along the Z-axis through the lumen of the CPNT, from its initial position at z = −20 Å to a final position at z = +20 Å . A constant pulling velocity of 2×10^{-3} Å ps^{-1} was employed. To prevent excessive drift of the nanotube during the pulling simulation, a positional restraint with a force constant of 20 kcal/mol $\cdot$ $Å^{-2}$ was applied to all C-α atoms of the CPNT backbone and the lipid membrane. The steered molecular dynamics (cv-SMD) simulation was carried out for 20 ns, and trajectories were collected throughout for subsequent data analysis.

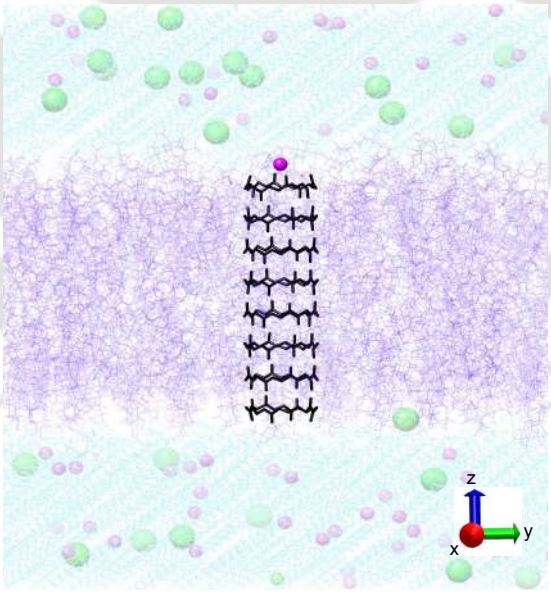

Figure 6.1: *Snapshot of the 8 × [Cys-D-Gly-Met-D-Gly]$_2$ nanotube embedded in a hydrated yeast bilayer with one Na^+ ion positioned at z = −20 Å. The CPNT is shown in black wire style, and the lipid bilayer is represented in blue wire style. Na^+ and Cl^- ions are depicted as pink and green spheres, respectively, while water molecules are shown in cyan wire style. Except for the CPNT backbone and the Na^+ ion at z = −20 Å, all other components are rendered in faded colors to enhance visual clarity.*

Potential of Mean Force (PMF)

The PMF profiles were created with the help of the umbrella sampling (US) method via the weighted histogram analysis method (WHAM)[41, 42]. After completing the cv-SMD simulation from −20 Å to +20 Å along the Z-axis, the trajectory was processed to extract the coordinates at every 1 Å interval of the ion displacement. These system coordinates of the whole system containing the ion displacement in each window serve as the starting points for umbrella sampling. Umbrella sampling simulations were then carried out by subdividing each window into four sub-windows with a width of 0.25 Å thereby improving sampling resolution and overlap. This resulted in a total of 161 bins covering the entire range from −20 Å to +20 Å . A harmonic restraint with a force constant of 2.5 kcal/mol $\cdot$ Å^{-2} was applied between the ion and the center of mass of the CPNT along the Z-axis to maintain the ion at the target position. Each US window was then introduced to minimization, equilibration, followed by 5 ns of NPT production run simulation. The resulting distance distributions were compiled into histograms and analyzed using the WHAM to reconstruct the potential of mean force (PMF) profile for ion translocation through the CPNT. Throughout the US simulations, the backbone of the CPNT and the lipid membrane were held under positional restraints. To improve statistical accuracy, the PMF data from both sides of the CPNT were averaged, assuming symmetry of the systems.

Water Dynamics Calculation

To calculate the mean square displacement (MSD) of water molecules along the channel of the CPNT in the presence of a cation, the respective cation was first placed at the center of the nanotube. The system was then equilibrated for 10 ns under the NVT ensemble, with positional restraints applied to the ion to keep it fixed at the center of the channel. Following equilibration, a 32 ns unrestrained production simulation was performed in the microcanonical (NVE) ensemble. The final 12 ns of this NVE trajectory were divided into three equal blocks of 4 ns each. MSD analysis was carried out on each of these blocks independently, and the resulting values were averaged. Standard deviations were also computed to assess the statistical reliability and consistency of the results across different systems.

6.3 Results and Discussions

6.3.1 PMF Profiles of the Ions Through the CPNT

The potential of mean force (PMF) profiles for the transport of five different ions, namely Na^+, K^+, Cs^+, Cl^-, and HCO_3^- across the CPNT channel are shown in Figure 6.2. These profiles reveal distinct patterns of ion selectivity during translocation through the nanotube. The PMF profile for Na^+ (Figure 6.2a) shows moderate energy fluctuations ranging from 0 to about 9 kcal/mol, with several small energy barriers between 2-5 kcal/mol along the channel axis. The K^+ profile (Figure 6.2b) displays a similar trend, but with slightly lower barriers suggesting a somewhat more favorable translocation compared to Na^+. This observation is consistent with earlier studies by Hwang et al.[10] and Yan et al.[7], where it was reported that Na^+ tends to remain longer inside the CPNT compared to K^+, indicating stronger interactions between Na^+ and the peptide backbone. Both Na^+ and K^+ profiles show repeating local minima near the α-planes and maxima in the regions between the planes. These features are a result of the regular and periodic arrangement of cyclic peptide rings in the CPNT structure. Additionally, shallow energy wells are observed between gap 2 and gap 7 (around $z = \pm 16$ Å), similar to findings by Dehez et al.[15]. These weaker minima likely occur when the ion is positioned between two adjacent peptide rings at nearly equal distances. In the case of Cs^+ (Figure 6.2c), the PMF profile shows a different behavior. High energy barriers, exceeding 10 kcal/mol, are present at the entry and exit points of the nanotube (around $z = \pm 15$-20 Å). If Cs^+ somehow manages to cross these barriers and enter the channel, it becomes trapped due to a deep energy well located near the center of the nanotube (from $z = 0$ to ± 4 Å).

For anions, the transport energetics suggest strong exclusion by the CPNT channel. The PMF profile for Cl^- (Figure 6.2d) shows a highly periodic pattern, with alternating energy barriers reaching 10-11 kcal/mol and deep wells dropping close to 0 kcal/mol. These repeating features appear at positions that match the locations of the cyclic peptide rings (indicated by red dashed lines), suggesting strong electrostatic repulsion between the negatively charged chloride ion and the backbone of the CPNT. This behavior agrees with earlier results by Choi et al.[12], who reported that while Na^+ and K^+ ions experience favorable free energy wells inside a CPNT nanotube, Cl^- faces energy barriers, highlighting the channel's preference for cations over anions. The PMF profile for HCO_3^-

(Figure 6.2e) shows even stronger exclusion. Entry barriers at the channel opening and exit exceed 20-22 kcal/mol, which makes it energetically unfavorable for the bicarbonate ion to enter the lumen. This is likely due to its larger size and higher charge density compared to Cl^-. No significant energy wells are observed along the channel interior, indicating that HCO_3^- is unable to form stable interactions within the CPNT.

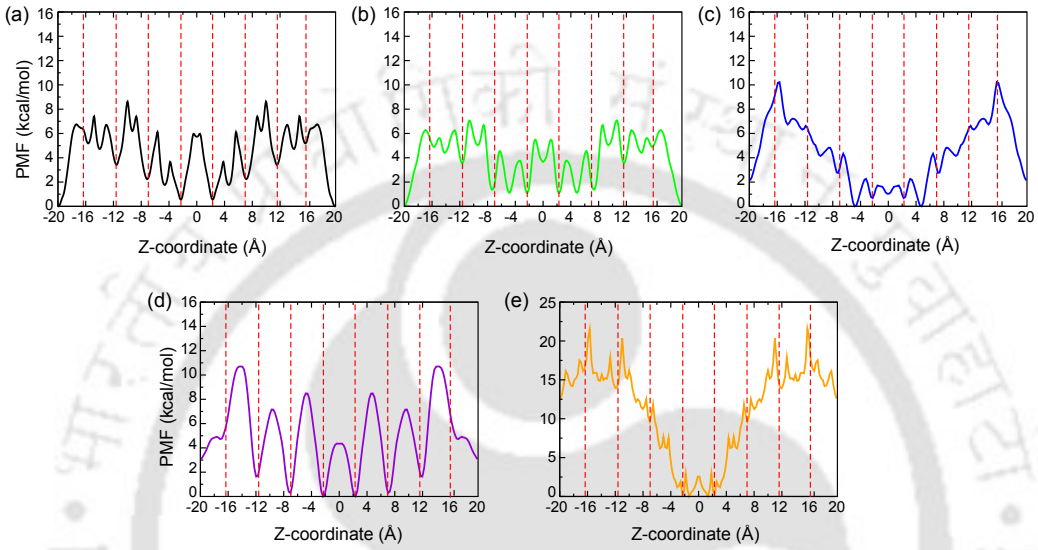

Figure 6.2: *The PMF profiles of (a) Na^+, (b) K^+, (c) Cs^+, (d) Cl^-, and (e) HCO_3^- ions moving through the CPNT. The red vertical dashed lines indicate the positions of the eight CP rings of the nanotube. The Z-axis is aligned along the major axis of the CPNT.*

6.3.2 Non-Bonded Interactions of the Ions with the Backbone of the CPNT and Channel Water

The non-bonded interaction energy profiles (Figure 6.3) provide valuable insights into how each ion interacts with the CPNT's backbone and the surrounding water molecules during its journey through the channel. To generate these plots, a single ion from each system was placed at multiple positions along the tube axis (z-axis), including the α-planes (z = ±16.33, ±11.61, ±6.98, ±2.28 Å) and the mid α-planes (z = ±23, ±20.7, ±18.4, ±13.8, ±9.2, ±4.6, and 0 Å). At each site, a 2 ns simulation was performed with a 1 fs time step, where the first 1 ns was used for equilibration and the second 1 ns for data collection.

For the cations (Na^+, K^+, and Cs^+), the electrostatic interaction with the peptide backbone (black line) is strongly attractive, ranging between −100 and −150 kcal/mol

across the lumen. In comparison, the van der Waals interaction with the backbone (red line) remains almost flat and close to zero, indicating that electrostatic forces are the primary contributors to cation-backbone stabilization. The electrostatic interaction between the cations and the neighboring water molecules (blue line) is also attractive, with the magnitude of this interaction being greatest for Na^+, followed by K^+, and weakest for Cs^+. This trend reflects the differences in size and charge density among these ions, with Na^+, as the most highly hydrated cation, exhibiting the strongest interaction with channel water, followed by K^+, while Cs^+, being the least hydrated, shows the weakest interaction among all three. The van der Waals interactions between the cations and water molecules (green line) are minimal and nearly unfavorable across the channel, suggesting that these forces contribute negligibly to the overall stabilization of the cations within the nanotube.

In contrast, the anions Cl^- and HCO_3^- display a different pattern (Figure 6.3d and e). The electrostatic interaction with the backbone is repulsive (black line), with positive values that peak near the center of the nanotube, indicating that the carbonyl-rich interior disfavors anion entry. The electrostatic interaction with water (blue line) remains attractive, but the overall energy landscape is less favorable for anion transport compared to cations. Notably, for HCO_3^-, the repulsive backbone interaction is even more pronounced, resulting in a high energy barrier that effectively prevents the anion from entering or traversing the nanotube.

These interaction energy profiles reveal that the selectivity of the CPNT arises primarily from the electrostatic interactions between the ions and the peptide backbone. Cations are stabilized by strong attractive forces with the backbone carbonyl groups, while anions are excluded due to electrostatic repulsion. The minor contribution of van der Waals interactions further emphasizes the dominant role of electrostatics in governing ion transport through the CPNT.

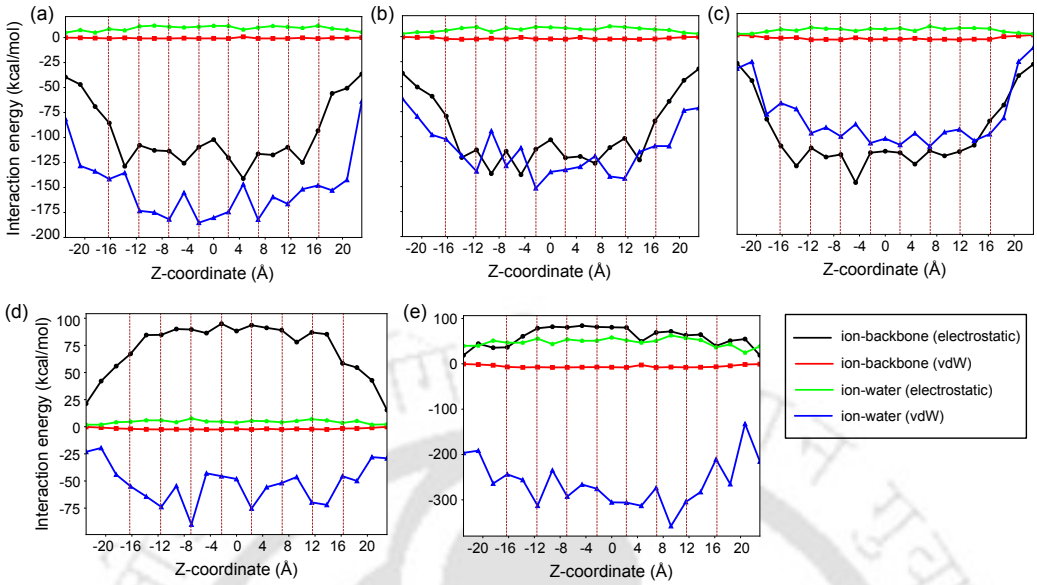

Figure 6.3: *Electrostatic and van der Waals interactions of (a) Na^+, (b) K^+, (c) Cs^+, (d) Cl^-, and (e) HCO_3^- ions with the CPNt backbone and the channel water. The red vertical dashed lines indicate the positions of the eight CP rings of the nanotube.*

6.3.3 Cation Interactions with the CPNT Lumen

Based on the PMF profiles and non-bonded interaction energy analyses, it is evident that the CPNT used in this study exhibits strong cation selectivity, effectively excluding anions such as Cl^- and HCO_3^- from entering the nanotube lumen. Given this selectivity, it is important to explore how the three studied cations: Na^+, K^+, and Cs^+, interact differently with the CPNT. This section focuses on how Na^+, K^+, and Cs^+ interact with the CPNT during translocation, highlighting the differences in their interaction patterns with the peptide backbone that influence their passage through the channel.

In this study, we examined two types of interactions between the cations and the backbone of the CPNT. The first type is direct coordinations (DCs), where the cations directly interact with the carbonyl oxygen atoms of the peptide backbone. The second type involves water-bridged interactions (WBs), where water molecules act as intermediaries between the cations and the backbone carbonyl atoms. These interactions were analyzed by examining the trajectories from the 20 ns SMD simulations of each cation moving through the CPNT channel.

Direct coordinations (DC) were identified by checking whether the carbonyl oxygen

atoms of the CPNT backbone were located within the first coordination shell of the cation. The cutoff distances used for this determination were specific to each ion: 3.1 Å for Na^+, 3.5 Å for K^+, and 3.9 Å for Cs^+ ion. For water-bridged (WB) interactions, a set of geometric criteria was applied. A water bridge was considered present when a hydrogen atom from a water molecule was within 3 Å of a backbone carbonyl oxygen atom, and the angle formed by the water oxygen, its bonded hydrogen, and the carbonyl oxygen was greater than 160°[7]. Additionally, the water molecule involved in bridging had to reside within the ion's first hydration shell to ensure it was directly associated with the cation.

Figure 6.4 presents the time evolution of the number of direct coordinations (DCs) and water-bridged interactions (WBs) formed between each cation and the CPNT backbone over the course of 20 ns SMD simulations. For Na^+, the number of DCs fluctuates between one and three, with occasional short-lived peaks up to five. In contrast, the WB interactions for Na^+ are more frequent and persistent throughout the simulation, indicating that Na^+ often remains hydrated while interacting indirectly with the backbone via water molecules. K^+ displays a slightly different pattern: the DC count is relatively stable, often ranging from two to four, suggesting a stronger tendency for direct contact with the backbone compared to Na^+. WBs are still present but somewhat reduced in frequency. Cs^+ shows the highest number of DCs, frequently maintaining four or more direct contacts, while WBs are sparse and intermittent. This trend reflects a shift from water-mediated to direct interaction as the cation radius increases. The smaller, highly hydrated Na^+ prefers WB interactions to maintain its solvation shell, whereas the larger, weakly hydrated Cs^+ tends to lose hydration and form more stable direct interactions with the carbonyl oxygens of the CPNT backbone. K^+ exhibits intermediate behavior between these two extremes.

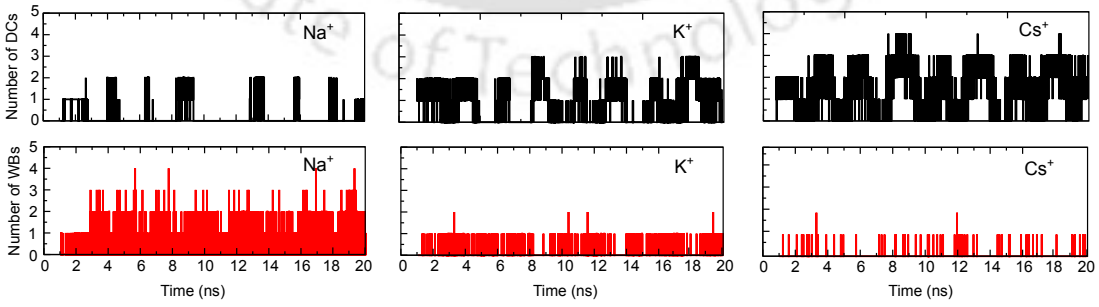

Figure 6.4: *Temporal profiles of direct coordination (DC, black) and water bridge (WB, red) interactions between Na^+, K^+, and Cs^+ ions and the CPNT framework over a 20-ns SMD pulling simulation.*

6.3.4 Radial Distributions of the Cations within the CPNT Channel

In this section, the radial distributions of a cation, channel water oxygen atoms (O_W), and backbone carbonyl oxygen atoms ($O_{C=O}$) of the CPNT were analyzed to gain a clearer understanding of the interaction between the cation and its surrounding environment. To perform this analysis, one cation from each respective system was initially restrained at the center of the CPNT and equilibrated for 2 ns. Following equilibration, the positional restraint was removed, and the cation was allowed to move freely during a 40 ns molecular dynamics simulation in the NVT ensemble. The radial distribution was calculated using the equation:

$$r = \sqrt{x^2 + y^2} \tag{6.1}$$

where r denotes the distance of the cation from the major axis (z-axis) of the CPNT, and x and y are the coordinates of the cation within the channel cross-section. As shown in Figure 6.5, all three cations tend to reside near the central axis of the channel, with Na^+ being the closest to the axis, followed by K^+ and then Cs^+. The radial distribution of Na^+ is broader than that of K^+ and Cs^+, suggesting that Na^+ exhibits greater mobility within the channel.

Interestingly, the presence of the cations does not significantly alter the radial distributions of water oxygen or carbonyl oxygen atoms, indicating that the overall spatial organization of the channel remains intact. Among the three cations, Na^+ shows the greatest overlap with the water oxygen distribution, implying that it primarily interacts with the CPNT backbone via water-mediated coordination. In contrast, Cs^+ shows a slight overlap with the carbonyl oxygen distribution, suggesting a greater tendency to form direct coordinations (DCs) with the peptide backbone compared to Na^+ and K^+.

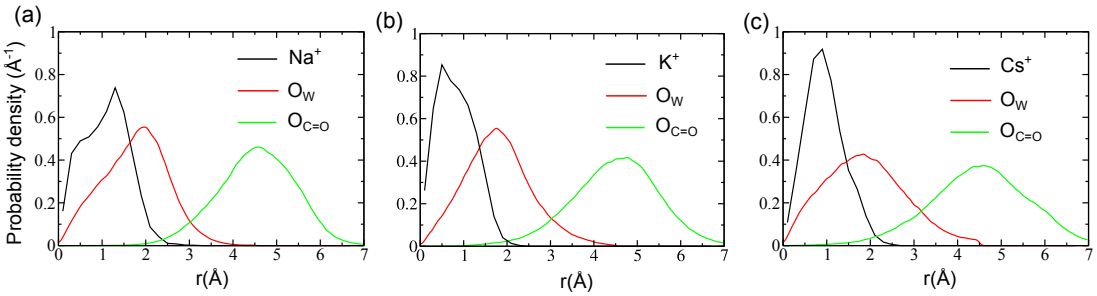

Figure 6.5: *Radial distributions of Na^+, K^+, Cs^+ ions, channel water oxygen atoms (O_W) and the backbone carbonyl oxygens ($O_{C=O}$) atoms of the CPNT.*

6.3.5 Distribution of Water Along the Lumen of the CPNT in Presence of Cations

As previously reported in the literature, water molecules inside the CPNT tend to follow a regular 1-2-1-2 arrangement along the channel axis[4, 43]. However, the presence of a cation inside the nanotube significantly disrupts this ordered water chain structure. Figure 6.6a and b show the axial density distribution of water molecules within the CPNT when a single cation is placed either at the center (mid-plane) or at an α-plane region ($z = 6.98$ Å), respectively. In both cases, the characteristic water pattern is lost, and two prominent density peaks appear symmetrically around the cation.

Interestingly, the peak heights are slightly higher when the cation is positioned in the α-plane region compared to when it is placed at the center of the channel. This difference can be attributed to spatial constraints: when the cation is located at the center of the CPNT, fewer water molecules from adjacent α-planes can accumulate around it due to limited space. In contrast, when the cation resides in an α-plane zone, more water molecules can approach and interact with it, leading to increased local density and higher peak heights. These observations are further supported by the structural snapshots shown in Figure 6.6, which clearly illustrate greater water accumulation around the cation in the α-plane region compared to the mid-plane location.

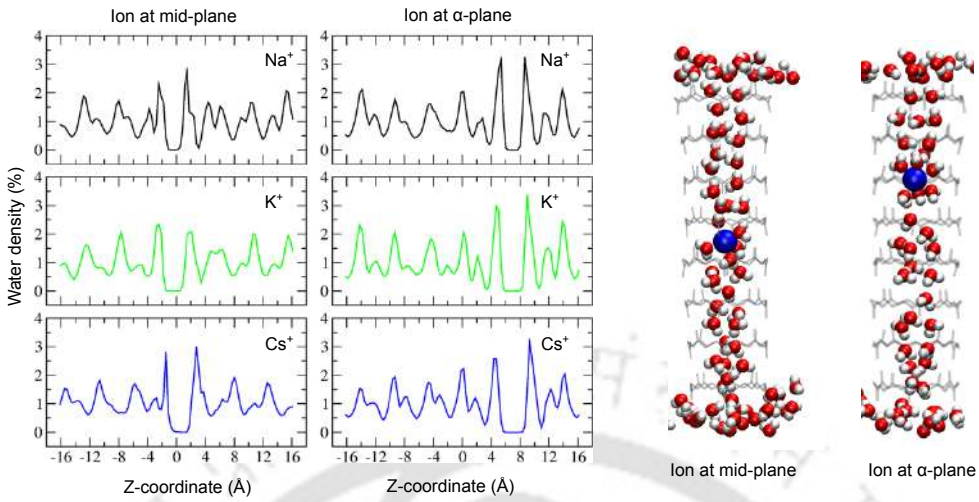

Figure 6.6: *Axial water density profiles (in %) inside the CPNT with Na^+, K^+, and Cs^+ ions placed at two distinct locations: the mid-plane ($z = 0$ Å) and the α-plane region ($z = 6.98$ Å). The corresponding snapshots illustrate the arrangement of channel water molecules for each ion position.*

6.3.6 Effect of Cations on the Translational Dynamics of Water Inside the CPNT

In addition to disrupting the axial distribution of water molecules, the presence of a cation inside the CPNT also alters the translational dynamics of water. To assess how water mobility is affected, we calculated the mean square displacement (MSD) of water molecules over time. It captures the extent of water molecule movement along the channel as a function of time, computed using the equation below:[4, 44]

$$MSD(t) = \left\langle |r_{\text{wat}}(t) - r_{\text{wat}}(0)|^2 \right\rangle \tag{6.2}$$

Here, t represents the correlation time, and r_{wat} is the coordinate vector of the oxygen atom of a water molecule. The term $r_{\text{wat}}(t) - r_{\text{wat}}(0)$ corresponds to the displacement of the water molecule over the time interval t. The slope of the MSD versus time plot yields the self-diffusion coefficient (D) according to Einstein's relation:[44]

$$D = \lim_{\Delta t \to \infty} \frac{\langle \Delta r^2 \rangle}{2d\Delta t} \tag{6.3}$$

where d denotes the dimensionality of the system. In this case, diffusion was analyzed along the z-axis of the CPNT. Figure 6.7 presents the MSD profiles of water molecules inside the CPNT in the presence of Na^+, K^+, and Cs^+ ions. The nearly linear increase of MSD with time indicates that, despite the presence of a cation, water molecules continue to exhibit one-dimensional diffusion along the channel axis. The calculated diffusion coefficients (D) of water in the presence of Na^+, K^+, and Cs^+ are 3.86 ± 0.44, 5.33 ± 1.3, and 8.41 ± 1.7 $Å^2$/ns, respectively.

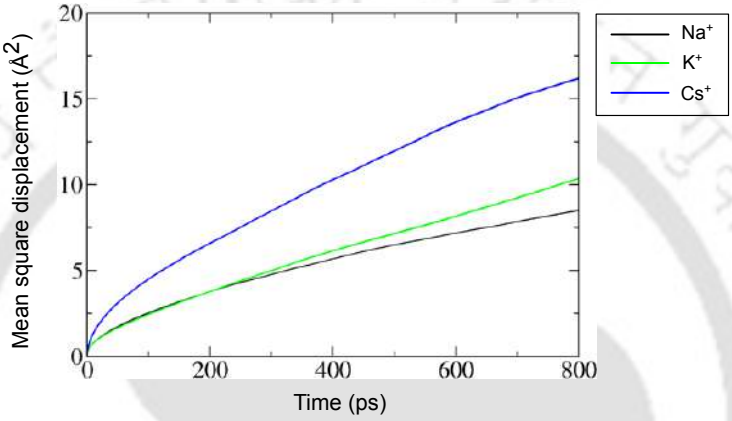

Figure 6.7: *Mean square displacement (MSD) plot of channel water molecules when Na^+, K^+, and Cs^+ ion is placed inside the CPNT.*

This increasing trend in diffusion coefficients: $Na^+ < K^+ < Cs^+$, highlights how each cation differently influences water mobility inside the confined environment of the nanotube. Na^+, with the smallest radius and highest charge density, forms a compact and stable hydration shell that tightly binds nearby water molecules. This disrupts the native water structure and reduces the overall mobility of water along the channel. K^+, having a larger radius and lower charge density, interacts less strongly with water, resulting in a less restrictive hydration environment and moderately increased water diffusion. Cs^+, the largest and least strongly hydrated of the three, exerts minimal influence on surrounding water molecules, allowing them to move more freely and leading to the highest observed diffusion coefficient. These results suggest that water mobility inside the CPNT is inversely related to the strength of ion-water interactions, with more weakly hydrated cations having a less inhibitory effect on water transport.

In comparison to our previous study (Chapter 5), where no ion was placed inside the CPNT, the diffusion coefficient of water was considerably higher, measured at 15.88

$\pm$ 1.67 Å^2/ns. This stark contrast highlights that the presence of a cation within the nanotube significantly slows down water movement. The reduction in mobility can be attributed to the disruption of the native water chain by the ion and the formation of strong ion-water and ion-channel interactions, which hinder the otherwise rapid one-dimensional diffusion of water molecules through the CPNT.

6.3.7 Dipole Moment of Channel Water in the Presence of Cations

The presence of a cation inside the lumen of the CPNT not only influences the axial arrangement and diffusion of channel water molecules but also alters their dipole moment orientations. In the present study, the dipole orientation of water was described by the angle θ, defined as the angle between the dipole vector of an individual water molecule and the longitudinal axis (z-axis) of the CPNT.

In the presence of a cation, the nearby water molecules tend to reorient: their oxygen atoms are drawn toward the ion due to electrostatic attraction, while the hydrogen atoms are correspondingly oriented away. This reorganization is reflected in the distribution of θ. Figure 6.8 presents the angular distribution profiles of channel water dipole orientations in individual inter-ring gaps of the CPNT, for systems where a single Na^+, K^+, or Cs^+ is located either at the channel center i.e., at z=0 Å (mid-plane) or at z= +6.9 Å (α-plane). The differences in these profiles reveal how ion identity and position modulate the orientational behavior of confined water within the nanotube.

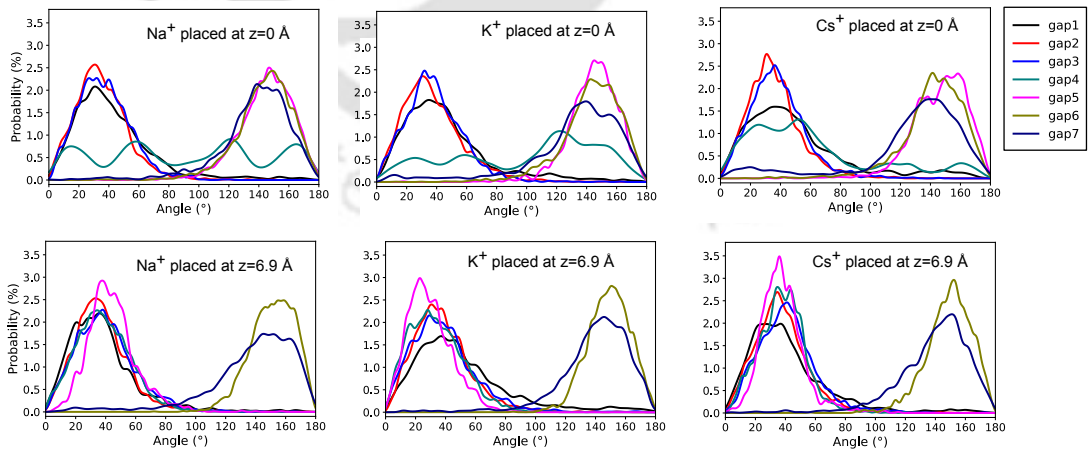

Figure 6.8: *Dipole orientation angle (θ) distributions of channel water molecules inside the CPNT in the presence of Na^+, K^+, and Cs^+ ions positioned at the mid-plane ($z = 0$ Å) and at the α-plane ($z = +6.9$ Å).*

As illustrated in Figure 6.8, the incorporation of a cation at the center of the CPNT channel induces strong dipolar orientation in channel water molecules across all gaps except for gap 4, where the ion is located. This is reflected by prominent peaks in the dipole angle distributions around $\theta \approx 30°$ and $\theta \approx 150°$, indicating a well-ordered arrangement in which the oxygen atoms of water molecules point toward the cation, while the hydrogen atoms orient away. In gap 4, the dipole orientation varies depending on the type of cation present. This difference arises due to the variation in the number of water molecules that can be accommodated within the central region (-2.7 Å $\leq z \leq 2.7$ Å), which is influenced by the ionic radius. The larger Cs^+ ion (~ 1.8 Å) restricts the available space and typically allows only one water molecule to occupy gap 4. In comparison, K^+ (~ 1.5 Å) and Na^+ (~ 1.1 Å) can accommodate approximately three and four water molecules, respectively. These differences in local hydration environments result in distinct dipole angle profiles for each cation.

On the other hand, when the cations are placed in the α-plane ($z = +6.9$ Å), all three cations exhibit a similar trend in dipole orientation angles across the gaps. Gaps 1 to 4 show water molecules with dipole angles oriented around $\theta \approx 30°$, indicating a consistent alignment pattern. In gap 5, a slight deviation is observed, as the cation is positioned between gaps 5 and 6, partially influencing the orientation of nearby water molecules. Gaps 6 and 7 display dipole angles centered around $\theta \approx 150°$, suggesting that water molecules in these regions orient in the opposite direction compared to those in the preceding gaps. Interestingly, no L- or D-type hydrogen bond defects are observed in any of the systems within gap 1 and gap 7. This is in contrast to the findings of Yan et al.[7], who reported the occurrence of such defects at the terminal regions of the channel in similar systems. The absence of these defects in the present study suggests a more stable and coherent dipolar alignment of water molecules near the channel openings, possibly due to differences in the peptide sequence of the CPNT, ion positioning, or membrane environment.

6.3.8 Effect of Confinement on Cation Hydration Shells

In confined systems such as CPNTs, the structure and stability of the hydration shell of the cations can differ significantly from that in bulk water due to spatial restrictions. To assess this, radial distribution functions, g(r) of water oxygen atoms (O_W) around

Na^+, K^+, and Cs^+ were calculated both inside the CPNT and in bulk water. Figure 6.9 presents the radial distribution functions $g(r)$ of water oxygen atoms (O_W) around Na^+, K^+, and Cs^+ within the CPNT channel and in bulk water. Inside the CPNT, all three cations display distinct hydration behaviors influenced by the geometric confinement of the channel. Na^+ exhibits the most pronounced and structured hydration shell, with a peak around 2.3 Å, indicating strong and localized interactions with surrounding water molecules. K^+ shows a broader and less intense peak at approximately 2.7 Å, while Cs^+ displays a weak peak near 3.1 Å, reflecting its poor hydration within the confined space compared to the other two ions. Notably, the radial distribution functions inside the CPNT decay toward zero beyond the channel radius, as no water molecules are found at larger radial distances due to the spatial restriction of the nanotube.

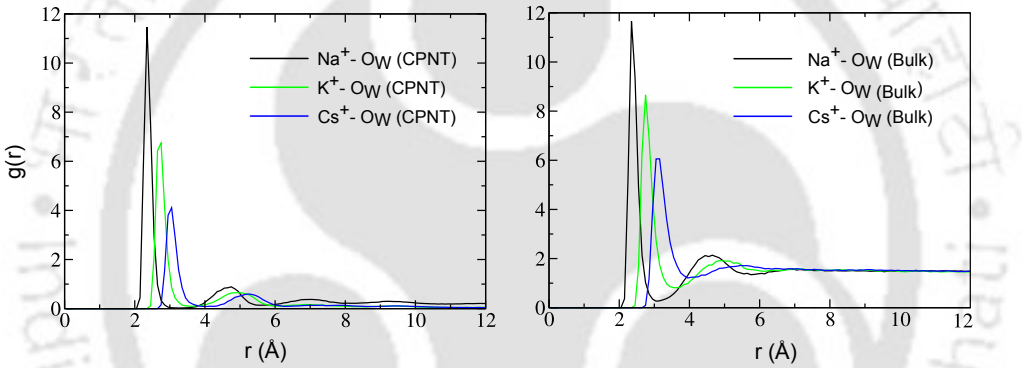

Figure 6.9: *Radial distribution functions (RDFs) between Na^+, K^+, and Cs^+ ions and water oxygen atoms (O_W), computed during their random motion inside the CPNT. For comparison, RDFs for the same ions with water oxygen atoms in bulk solution are also shown.*

In contrast, in bulk water, all three cations maintain their expected hydration shells with sharper and better-defined peaks. Na^+ again shows the strongest first-shell peak at $\sim$ 2.3 Å, followed by K^+ and Cs^+, consistent with their decreasing charge densities and increasing ionic radii. Unlike inside CPNT, the bulk RDFs converge to 1 at long distances, reflecting the uniform and unbounded nature of the solvent environment. These trends highlight that Na^+ retains stable hydration in both environments, while the hydration of Cs^+ is significantly disrupted under confinement, underscoring the selective compatibility of smaller cations with the CPNT interior.

The water coordination numbers (CN_W) for Na^+, K^+, and Cs^+ in the water phase and inside the CPNT are presented in Table 6.1. $CN_W(1)$ refers to the number of water

Table 6.1: *Average water coordination numbers for Na^+, K^+, and Cs^+ in both inside the CPNT and in the bulk environment. Here, $N_W(1)$ and $N_W(2)$ denotes the first and the second solvation shells of the cations.*

	$N_W(1)$		$N_W(2)$	
	CPNT	Bulk	CPNT	Bulk
Na^+	3.98	5.03	7.82	21.71
K^+	3.78	6.91	7.34	26.23
Cs^+	3.44	8.21	6.85	32.43

molecules in the first solvation shell, while $CN_W(2)$ denotes the number of water molecules in the second solvation shell. Across all three cations, the coordination numbers are significantly reduced inside the CPNT compared to the water phase, reflecting the spatial confinement imposed by the narrow CPNT channel. In the bulk environment, the coordination numbers increase with ionic size, following the trend $Cs^+ > K^+ > Na^+$, as larger ions tend to accommodate more water molecules in their hydration shells due to their larger size, despite having lower charge density and weaker electrostatic attraction[45, 46]. Experimental studies report first-shell hydration numbers of approximately 5-6 for Na^+, 6-7 for K^+, and 8 for Cs^+ [46–48]. These values are comparable to the $CN_W(1)$ obtained in the simulations.. However, this trend is partially reversed under confinement. Inside the CPNT, Na^+ retains the largest number of coordinating water molecules in both $CN_W(1)$ and $CN_W(2)$, followed by K^+ and then Cs^+. The drop in coordination is most pronounced for Cs^+, whose $CN_W(1)$ decreases from 8.21 in water phase to 3.44 inside the CPNT. This indicates that Cs^+, due to its larger ionic radius, experiences severe steric hindrance within the channel and loses a substantial portion of its hydration shell. In contrast, Na^+ maintains a relatively stable hydration structure under confinement. The corresponding dehydration energy costs, estimated from the change in first-shell coordination numbers, follow the order $Na^+ < K^+ < Cs^+$, with values of 6.3, 12.52, and 14.28 kcal/mol, respectively. Despite having the strongest per-water binding affinity, Na^+ incurs the lowest penalty because its hydration shell is only marginally perturbed within the CPNT. In contrast, K^+ and especially Cs^+ lose a larger fraction of their coordinating waters, leading to substantially higher dehydration costs. These observations reinforce the idea that CPNTs are structurally more compatible with smaller, more strongly hydrated cations like Na^+, while larger ions like Cs^+ are less favorably accommodated.

6.4 Summary and Conclusion

This chapter systematically investigates the selective ion transport behavior of three cations: Na^+, K^+, and Cs^+, and two anions: Cl^- and HCO_3^-, through a CPNT composed of eight stacked rings of cyclo-[Cys-D-Gly-Met-D-Gly]$_2$, embedded in a biologically realistic yeast lipid bilayer. Potential of mean force (PMF) profiles clearly demonstrate the CPNT's intrinsic preference for cation over anion transport, consistent with prior theoretical and experimental studies [11, 12]. Among the cations, Na^+ and K^+ encounter moderate energy barriers and are able to permeate the nanotube efficiently. Cs^+, however, faces higher energy barriers at both the entry and exit regions, indicating possible transient trapping within the channel. In contrast, anion permeation is energetically unfavorable: Cl^- becomes trapped in deep energy wells, while HCO_3^- encounters prohibitively high entry barriers, preventing access to the lumen. Electrostatic energy profiles further support these trends; cations exhibit favorable interactions with the CPNT backbone, whereas anions experience repulsive or destabilizing forces.

Hydration structure analysis highlights ion-size-dependent behavior. Na^+, being the smallest and most strongly hydrated, remains centrally located and primarily interacts through water bridges with the CPNT backbone. Cs^+, in contrast, due to its larger ionic radius and weaker hydration, tends to shift toward the channel wall compared to Na^+ and forms more direct contacts with backbone carbonyl oxygens. Radial distribution functions and water coordination analysis confirm that confinement within the CPNT disrupts hydration shells more severely for larger ions. Notably, the presence of cations does not significantly affect the spatial distribution of water or carbonyl oxygen atoms along the channel wall.

The introduction of cations also alters water structure and dynamics within the CPNT. Water density decreases in the presence of ions, and the characteristic 1-2-1-2 single-file water arrangement is disrupted. Water mobility is lowest with Na^+, intermediate with K^+, and highest with Cs^+, reflecting an inverse correlation between ion-water interaction strength and water diffusion under confinement. Dipole angle distribution profiles of channel water across individual gaps further show ion-dependent water alignment without the presence of L- or D-type hydrogen bond defects, indicating uninterrupted dipole ordering within the channel.

In summary, this study underscores the importance of ionic size, hydration properties, and electrostatic interactions in governing ion transport through CPNTs. The findings reaffirm the CPNT's selectivity for smaller, more strongly hydrated cations, while demonstrating its near-impermeability to anions under the conditions studied. These insights enhance our understanding of selective transport in artificial nanochannels and offer valuable guidance for the rational design of bioinspired systems for ion separation, sensing, and therapeutic delivery.

References

(1) Stein, W. D.; Litman, T., *Channels, carriers, and pumps: an introduction to membrane transport*; Elsevier: 2014.

(2) Carvajal-Diaz, J. A.; Cagin, T. *J. Phys. Chem. B* **2016**, *120*, 7872–7879.

(3) Zheng, S.-p.; Huang, L.-b.; Sun, Z.; Barboiu, M. *Angew. Chem. Int. Ed.* **2021**, *60*, 566–597.

(4) Liu, J.; Fan, J.; Tang, M.; Cen, M.; Yan, J.; Liu, Z.; Zhou, W. *J. Phys. Chem. B* **2010**, *114*, 12183–12192.

(5) Li, H.; Fan, J. F.; Li, R.; Yu, Y.; Yan, X. L. *J. Mol. Model.* **2014**, *20*, 1–11.

(6) Shan, T.; Zhao, X.; Liang, H. *Mater. Res. Express* **2020**, *7*, 065010.

(7) Yan, X.; Fan, J.; Yu, Y.; Xu, J.; Zhang, M. *J. Chem. Inf. Model.* **2015**, *55*, 998–1011.

(8) Zhang, M.; Fan, J.; Xu, J.; Weng, P.; Lin, H. *J. Mol. Model.* **2016**, *22*, 1–12.

(9) Ghadiri, M. R.; Granja, J. R.; Buehler, L. K. *Nature* **1994**, *369*, 301–304.

(10) Hwang, H.; Schatz, G. C.; Ratner, M. A. *J. Phys. Chem. B* **2006**, *110*, 26448–26460.

(11) Sumiya, N.; Igami, D.; Takeda, K. In *AIP Conf. Proc.* 2011; Vol. 1399, pp 1055–1056.

(12) Choi, K.-M.; Kwon, C.-H.; Kim, H.-L.; Hwang, H.-S. *Bull. Korean Chem. Soc.* **2012**, *33*, 911–916.

(13) Garcia-Fandino, R.; Amorin, M.; Castedo, L.; Granja, J. R. *Chem. Sci.* **2012**, *3*, 3280–3285.

(14) Song, X.; Fan, J.; Liu, D.; Li, H.; Li, R. *J. Mol. Model.* **2013**, *19*, 4271–4282.

(15) Dehez, F.; Tarek, M.; Chipot, C. *J. Phys. Chem. B* **2007**, *111*, 10633–10635.

(16) Zhang, L.; Fan, J.; Qu, M. *J. Chem. Inf. Model.* **2018**, *59*, 170–180.

(17) Gong, T.; Fan, J. *J. Chem. Inf. Model.* **2021**, *61*, 2754–2765.

(18) Martínez, L.; Andrade, R.; Birgin, E. G.; Martínez, J. M. *J. Comput. Chem.* **2009**, *30*, 2157–2164.

(19) Jo, S.; Lim, J. B.; Klauda, J. B.; Im, W. *Biophys. J.* **2009**, *97*, 50–58.

(20) Wu, E. L.; Cheng, X.; Jo, S.; Rui, H.; Song, K. C.; Dàvila-Contreras, E. M.; Qi, Y.; Lee, J.; Monje-Galvan, V.; Venable, R. M.; Klauda, J. B.; Im, W. *J. Comput. Chem.* **2014**, *35*, 1997–2004.

(21) Daum, G.; Tuller, G.; Nemec, T.; Hrastnik, C.; Balliano, G.; Cattel, L.; Milla, P.; Rocco, F.; Conzelmann, A.; Vionnet, C.; et. al. *Yeast* **1999**, *15*, 601–614.

(22) Jorgensen, W. L.; Chandrasekhar, J.; Madura, J. D.; Impey, R. W.; Klein, M. L. *J. Chem. Phys.* **1983**, *79*, 926–935.

(23) Marques, P. A. A. P.; Magalhaes, M. C. F.; Correia, R. N. *Biomater.* **2003**, *24*, 1541–1548.

(24) Azinge, E. C. Discrepancies in interlaboratory plasma bicarbonate measurement., 2016.

(25) Case, D. A. et al. Amber 18., University of California: San Francisco, CA, 2018.

(26) Tian, C.; Kasavajhala, K.; Belfon, K. A.; Raguette, L.; Huang, H.; Migues, A. N.; Bickel, J.; Wang, Y.; Pincay, J.; Wu, Q., et al. *J. Chem. Theory Comput.* **2019**, *16*, 528–552.

(27) Dickson, C. J.; Walker, R. C.; Gould, I. R. *J. Chem. Theory Comput.* **2022**, *18*, 1726–1736.

(28) Li, P.; Song, L. F.; Merz Jr, K. M. *J. Chem. Theory Comput.* **2015**, *11*, 1645–1657.

(29) Frisch, M. J.; Trucks, G. W.; Schlegel, H. B.; Scuseria, G. E.; Robb, M. A.; Cheeseman, J. R.; et al. Gaussian 09, Revision A.02.; Gaussian, Inc., Wallingford, CT, 2009.

(30) Bayly, C. I.; Cieplak, P.; Cornell, W.; Kollman, P. A. *J. Phys. Chem.* **1993**, *97*, 10269–10280.

(31) He, X.; Man, V. H.; Yang, W.; Lee, T.-S.; Wang, J. *J. Chem. Phys.* **2020**, *153*, 114502.

(32) Wang, J.; Wang, W.; Kollman, P. A.; Case, D. A. *J. Mol. Graphics Modell.* **2006**, *25*, 247–260.

(33) Humphrey, W.; Dalke, A.; Schulten, K. *J. Mol. Graphics* **1996**, *14*, 33–38.

(34) Pettersen, E. F.; Goddard, T. D.; Huang, C. C.; Couch, G. S.; Greenblatt, D. M.; Meng, E. C.; Ferrin, T. E. *J. Comput. Chem.* **2004**, *25*, 1605–1612.

(35) Hünenberger, P. H. *Adv. Polym. Sci.* **2005**, 105–149.

(36) Åqvist, J.; Wennerström, P.; Nervall, M.; Bjelic, S.; Brandsdal, B. O. *Chem. Phys. Lett.* **2004**, *384*, 288–294.

(37) Omelyan, I.; Kovalenko, A. *J. Chem. Phys.* **2013**, *139*, 224106.

(38) Zhang, Y.; Feller, S. E.; Brooks, B. R.; Pastor, R. W. *J. Chem. Phys.* **1995**, *103*, 10252–10266.

(39) Ryckaert, J.-P.; Ciccotti, G.; Berendsen, H. J. *J. Comput. Phys.* **1977**, *23*, 327–341.

(40) Essmann, U.; Perera, L.; Berkowitz, M. L.; Darden, T.; Lee, H.; Pedersen, L. G. *J. Chem. Phys.* **1995**, *103*, 8577–8593.

(41) Kumar, S.; Rosenberg, J. M.; Bouzida, D.; Swendsen, R. H.; Kollman, P. A. *J. Comput. Chem.* **1992**, *13*, 1011–1021.

(42) Souaille, M.; Roux, B. *Comput. Phys. Commun.* **2001**, *135*, 40–57.

(43) Tarek, M.; Maigret, B.; Chipot, C. *Biophys. J.* **2003**, *85*, 2287–2298.

(44) Paul, R.; Mitra, A.; Paul, S. *Phys. Chem. Chem. Phys.* **2021**, *23*, 22703–22717.

(45) Hribar, B.; Southall, N. T.; Vlachy, V.; Dill, K. A. *J. Am. Chem. Soc.* **2002**, *124*, 12302–12311.

(46) Mahler, J.; Persson, I. *Inorg. Chem.* **2012**, *51*, 425–438.

(47) Liu, C.; Min, F.; Liu, L.; Chen, J. *Chem. Phys. Lett.* **2019**, *727*, 31–37.

(48) Hayamizu, K.; Chiba, Y.; Haishi, T. *Rsc Adv.* **2021**, *11*, 20252–20257.

Chapter 7

Summary and Our View on Cyclic Peptide Nanotubes

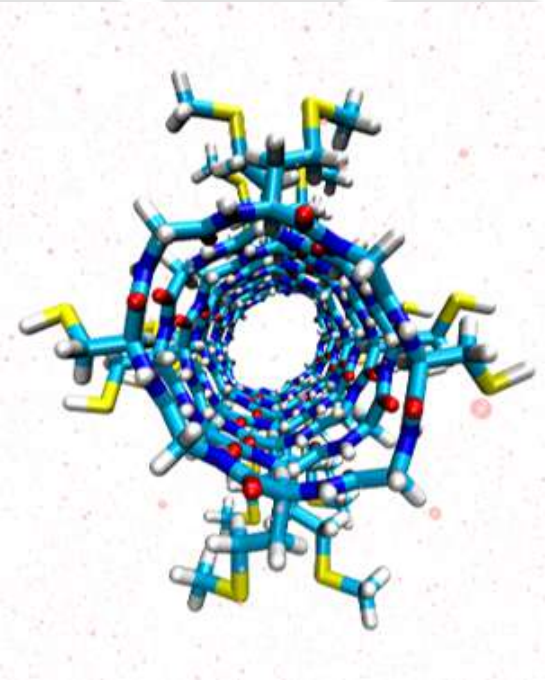

Since their discovery, cyclic peptide nanotubes (CPNTs) have quickly become a holy grail for the research community, owing to their unique architecture, biocompatibility, and highly tunable physicochemical properties. Their remarkable ability to self-assemble into stable, tubular nanostructures with defined internal cavities has positioned them at the forefront of nanotechnology and materials science. Recognizing the far-reaching possibilities of CPNTs' applictaions, this thesis undertakes a comprehensive investigation into the behavior of CPNTs, primarily focussing on the various factors that govern their self-assembly with the help of molecular dynamics simulation. Furthermore, the potential of using these nanotubes as synthetic channels for the transportation of water and different ions in lipid environment is also explored.

The first study of the thesis focuses on understanding the mechanism of self-assembly of cyclic peptides (CPs) in water under different salt concentrations. Lower concentration of NaCl promotes increase solubility of CPs (salting in) whereas at higher concentration, more association of CPs is observed (salting out). Additionally, the role of temperature in the self-assembly process is examined. It is found that low temperature favour the self-assembly process of CPs to form nanotube-like structures.

Following this, the role of solvent polarity and amino acid composition of the CP rings in governing the stability of CPNTs is examined. Results show that non-polar solvents provide stability to the CPNT structure compared to the polar solvents. Also, combination of hydrophilic and hydrophobic amino acids in alternate positions in the cyclic peptide ring helps in maintaining the circular shape of the CP subunits.

The study of solvents is then extended to deep eutectic solvents (DESs), where the behavior of CPNTs is evaluated under different solvent environment. The simulations revealed that DESs can significantly stabilize the nanotube conformation and with increase in hydration of DES and system temperature, this stability decreases. These results expand the understanding of CPNT behavior in green solvents and suggest that deep eutectic solvents could serve as novel media for the stabilization or functionalization of nanotube systems.

Moving towards biologically relevant environments, the interaction of CPNTs with diverse lipid bilayers is explored. The ability of CPNTs to integrate into lipid membranes, and the water transport dynamics through the nanotubes, are systematically studied. The findings show that insertion of CPNT within the lipid bilayers donot alter the properties

of the membranes and CPNT can be used as an synthetic water channel. The presence of the characteristic 1-2-1-2 pattern of water movement is also observed within the CGMG nanotube. Furthermore, the average lifetimes of water-water hydrogen bonds inside the channel is found to be nearly similar to those of bulk water. However, specific backbone-bound water molecules display elevated hydrogen bond lifetime values.

Finally, the transport of ions through CPNT embedded in yeast bilayer is investigated. Potential of mean force (PMF) profiles reveal a strong preference for cation permeation, with Na^+ and K^+ encountering moderate energy barriers, while Cs^+ shows signs of getting trapped inside the channel due to higher entry and exit barriers. In contrast, both anions face significant energetic constraints, effectively preventing their entry or translocation through the channel. Water structure and dynamics inside the nanotube are also modulated by the presence of cations, disrupting the typical 1-2-1-2 arrangement and reducing axial water diffusion, most notably in the presence of Na^+.

In summary, this thesis offers a thorough exploration of various physical and biological factors that are responsible for the stability of CPNTs. Additionally, the possibility of using these nanotubes as synthetic water and ion transport channels is explored which establishes a solid foundation for future innovations and applications of CPNTs in fields such as nanotechnology, biotechnology, and advanced materials science.

Looking ahead, several promising avenues emerge to further advance this work. Investigating the influence of solvent pH on CPNT stability may provide deeper insights into their environmental adaptability. Building on previous studies of drug transport, CPNTs could be evaluated for their potential in delivering a broader range of therapeutic molecules, opening new possibilities in targeted drug delivery. Finally, extending this research to include other classes of cyclic peptides, such as cyclic β-peptides and cyclic α-γ-peptides, could unlock new modes of self-assembly and functional diversity, reinforcing the position of CPNTs at the forefront of next-generation nanoscale materials.

Publications

1. Moral, R; Paul, S. Influence of salt and temperature on the self-assembly of cyclic peptides in water: a molecular dynamics study. *Phys. Chem. Chem. Phys.* **2023**, *25*, 5406-5422.

2. Moral, R; Paul, S. Exploring Cyclic Peptide Nanotube Stability Across Diverse Lipid Bilayers and Unveiling Water Transport Dynamics. *Langmuir* **2024**, *40*, 882-895.

3. Moral, R; Paul, S. Understanding the Role of Solvent Polarity and Amino Acid Composition of Cyclic Peptides on Nanotube Stability. *J. Phys. Chem. B* **2025**, *129 (14)*, 3590-3603.

4. Moral, R; Paul, S. Cyclic Peptide Nanotubes in Deep Eutectic Solvents: Insights into Stability, Hydration and Thermal Effects. *J. Phys. Chem. B* **2025**, *129 (31)*, 7861-7874.

5. Moral, R; Paul, S. Molecular Insights into the Selective Ion Permeation and Confined Water Behavior in a Transmembrane D/L-α Cyclic Peptide Nanotube. (Under Revision)

6. M. Devi, R. Moral, S. Thakuria, A. Mitra and S. Paul. Hydrophobic Deep Eutectic Solvents as Greener Substitutes for Conventional Extraction Media: Examples and Techniques. *ACS Omega* **2023**, *8*, 9702-9728. (Shared 1st author)

7. Medhi, D; Moral, R; Paul, S; Hazarika, S. From Monomer to Pentamer: Solvent-Driven Aggregation Pathways of Methylene Blue Investigated via Spectroscopy and Molecular Dynamics Simulations. (Under Revision)

8. Sannigrahi, A; Rai, V; Moral, R; Chakraborty, D; Kulshrestha, A; Maity, D; Challil, M. V.; De, N; Ayappa, K. G.; Paul, S; Roy, R. Ternary lipid membrane stimulates the membrane rupture by Cytolysin A by facilitating the conformational transitions during pore formation. (Under Preparation)

Conference and Workshops

1. Attended summer school on "Advanced Molecular Dynamics Simulation (AMDS-2021)", jointly organized by Department of Physics, Kathmandu University, Nepal; Department of Chemistry, IISER Pune, India; and Green Club of Thoughts, Kathmandu University, Nepal.

2. Presented a poster in the 17th "Theoretical Chemistry Symposium (TCS-2021)", organized by IISER Kolkata, IACS Kolkata, Kalyani University, and S.N. Bose National Centre for Basic Sciences, Kolkata.

3. Presented a poster in the "Research and Industrial Conclave (RIC-2022)", organized by SAB, IIT Guwahati and IIT Guwahati Research Park, Guwahati, Assam.

4. Presented a poster at the "Chemical Research Society of India 28th National Symposium in Chemistry (CRSI NSC-28)", organized by Department of Chemistry, IIT Guwahati, Assam.

5. Presented a poster in the conference "Frontiers in Chemical Sciences (FICS-2022)", organized by IIT Guwahati, Assam.

6. Presented a poster at the conference "Structure and Dynamics of Chemical and Biomolecular Systems (SDCBS-2023)", organized by Department of Chemistry, IIT Kanpur, Uttar Pradesh.